

# **Exploring the Interfacial Molecular Level Behavior of Biomacromolecules and Nanomaterials using Non-Linear Vibrational Spectroscopy**

**Doctoral Thesis**

by

**“Harsharan Kaur”**

**(2016BMZ0002)**



**DEPARTMENT OF BIOMEDICAL ENGINEERING  
INDIAN INSTITUTE OF TECHNOLOGY ROPAR**

**April, 2023**



# **Exploring the Interfacial Molecular Level Behavior of Biomacromolecules and Nanomaterials using Non-Linear Vibrational Spectroscopy**

A Thesis Submitted

In Partial Fulfillment of the Requirements

For the Degree of

**DOCTOR OF PHILOSOPHY**

by

**“Harsharan Kaur”**

**(2016BMZ0002)**



DEPARTMENT OF BIOMEDICAL ENGINEERING  
INDIAN INSTITUTE OF TECHNOLOGY ROPAR

April, 2023





Harsharan Kaur: *Exploring the Interfacial Molecular Level Behavior of Biomacromolecules and Nanomaterials using Non-Linear Vibrational Spectroscopy*

Copyright © 2023, Indian Institute of Technology Ropar

All Rights Reserved



**This thesis is  
Dedicated  
to  
my Family  
&  
Science**



## Declaration of Originality

I hereby declare that the work which is being presented in the thesis entitled **“EXPLORING THE INTERFACIAL MOLECULAR LEVEL BEHAVIOR OF BIOMACROMOLECULES AND NANOMATERIALS USING NON-LINEAR VIBRATIONAL SPECTROSCOPY”** has been solely authored by me. It presents the result of my own independent investigation/research conducted during the time period from July 2016 to December 2022 under the supervision of Dr. Kailash Chandra Jena, Associate Professor, Department of Physics and Dr. Narinder Singh, Professor, Department of Chemistry. To the best of my knowledge, it is an original work, both in terms of research content and narrative, and has not been submitted or accepted elsewhere, in part or in full, for the award of any degree, diploma, fellowship, associateship, or similar title of any university or institution. Further, due credit has been attributed to the relevant state-of-the-art and collaborations (if any) with appropriate citations and acknowledgments, in line with established ethical norms and practices. I also declare that any idea/data/fact/source stated in my thesis has not been fabricated/falsified/misrepresented. All the principles of academic honesty and integrity have been followed. I fully understand that if the thesis is found to be unoriginal, fabricated, or plagiarized, the Institute reserves the right to withdraw the thesis from its archive and revoke the associated Degree conferred. Additionally, the Institute also reserves the right to appraise all concerned sections of society of the matter for their information and necessary action (if any). If accepted, I hereby consent for my thesis to be available online in the Institute’s Open Access repository, inter-library loan, and the title & abstract to be made available to outside organizations.

*Harsharan Kaur*

Signature

Name: Harsharan Kaur

Entry Number: 2016BMZ0002

Program: PhD

Department: Biomedical Engineering

Indian Institute of Technology Ropar

Rupnagar, Punjab 140001

Date: 10-04-2023



## Certificate

This is to certify that the thesis entitled **Exploring the Interfacial Molecular Level Behavior of Biomacromolecules and Nanomaterials using Non-Linear Vibrational Spectroscopy**, submitted by **Harsharan Kaur (2016BMZ0002)** for the award of the degree of **Doctor of Philosophy** of Indian Institute of Technology Ropar, is a record of bonafide research work carried out under our guidance and supervision. To the best of our knowledge and belief, the work presented in this thesis is original and has not been submitted, either in part or full, for the award of any other degree, diploma, fellowship, associateship or similar title of any university or institution.

In our opinion, the thesis has reached the standard fulfilling the requirements of the regulations relating to the Degree.

Signature of the Supervisor(s)



**Dr. Kailash Chandra Jena**

Associate Professor

Department of Physics

Indian Institute of Technology Ropar

Rupnagar, Punjab 140001



**Dr. Narinder Singh**

Professor

Department of Chemistry

Indian Institute of Technology Ropar

Rupnagar, Punjab 140001

**Date:** 10-04-2023





## Acknowledgments

Any accomplishment that we attain in our life path is not the result of solely our hard work, but a team of people from both personal and professional network who remained our backbone and inspiration through the rough waters of life. I would like to embrace the fact that if I am able to expand my knowledge and see further beyond the horizon, it is only by standing on the shoulders of the giants. Hence, I would like to extend my appreciation to all those who made this journey successful.

Firstly, I would like to express my sincere gratitude to my academic supervisors, Dr. Kailash Chandra Jena and Dr. Narinder Singh for their guidance, constant encouragement, motivational words, and for believing in me at my lowest. While working with them, I feel highly obliged to gain exposure in working with lasers, optics, and concepts of nanomaterials and non-linear bio-photonics. They have been like the fundamental pillars for structuring and shaping my skills, knowledge and research articulates during my Doctoral tenure.

I offer my deepest appreciation to the members of my Doctoral Committee (DC): Dr. Yashveer Singh (DC Chairperson), Dr. Shubhrangshu Dasgupta, Dr. Ramjee Repaka, and Dr. Deepti Bathula for their timely help, sincere feedback and suggestions about my research work. I would like to genuinely thank my DC chairperson Dr. Yashveer Singh for being an inspiration and teaching me to confidently face the circumstances, inculcated a belief in my abilities and sincerely guiding me to work on my shortcomings constructively. I thank him from the bottom of my heart in providing me with immense knowledge as my teacher, departmental head, and doctoral chairperson of my research work. I also thank my teacher cum TA supervisor Dr. Srivastava Naidu for being a wonderful instructor who believed in me, encouraged me and taught me the necessary skills of cell culture and fundamentals of molecular biology techniques during the coursework.

I have a deep respect and gratitude towards my senior colleague Dr. Shilpi Chaudhary (post-doctoral research fellow) in teaching me with the necessary skills, knowledge, inquisitive outlook, and how a friendly collaboration can be made successful while staying grounded in your associations. She has been an active contributor in the protein related work as presented in Chapter 3 and 4 of this thesis work. I would like to humbly acknowledge our collaborators: Dr. Suman Singh (Principal Scientist) and Dr. Mayank Garg (Research Student) from CSIO-CSIR, Chandigarh, for providing with the quantum dots and protein molecules for addressing an interesting piece of research work related to biosensing activity at the interface, as discussed in Chapter 5 of this thesis work. I also appreciate the efforts and cooperation of Dr. Meenakshi Verma in teaching me the nanoparticle synthesis procedure and helping in carrying out the DNA binding work (being discussed in Chapter 6 of this thesis). These collaborative occasions undoubtedly

brought us together, not only was there a cross-section in knowledge sharing, but also applauding the efforts of each other.

I sincerely thank my fellow group members: Dr. Deepak Tomar for teaching me data analysis and taking care like a big brother; Dr. Harpreet Kaur for her tasty snacks, late night tea-breaks, motivational thoughts, research discussions, and being a supportive friend throughout; Dr. Monika Chaudhary for teaching me being brave and self-reliance; Bhawna Rana and Sarabjeet Kaur for insightful discussions and creating an entertaining ambience in lab. Sarabjeet Kaur needs a special mention for being my big supporter, motivator and the brightest light in my mundane life as my room-mate. I also thank my other group members: Ashay (summer intern), Shubham (M.Sc. Student), other PhDs: Sagar, Rakshith Kamath, Rakshit Singh, Tuhina, Meenu, Sitara, Yagyraj Subedi for their kind words and support.

I would like to thank all the staff members of Department of Biomedical Engineering and Department of Physics, IIT Ropar for their timely support and handling of documentation work. Also, I thank Mr. Harsimranjit Singh for his help in AFM characterizations.

Some friends stay in background, but they hold you, support you, and pray for you silently for your success, and don't make a big deal about it! I am highly thankful to my best buddies: Dr. Yashasvi Bansal, Dr. Anshul Sharma, Dr. Pooja Sharma, Prabhjot Kaur, and Kuldeep Kaur for always cheering me up through thick and thin and being there for me like a family. They taught me a very important lesson that gratitude is the key to manifest abundance.

Most importantly, I am highly indebted to my family for always encouraging me, celebrating my achievements, and bearing me during my long PhD tenure. Besides, there are many other people who helped me in one way or the other, and I am thankful to all those whose names I might have missed here but are not forgotten.

The journey of a mile starts with a small step which has to be taken by oneself. Finally, I want to take a moment to thank my past-self for fighting through the insecurities and putting in the hard work, the rewards of which I am still reaping today. It is learnt the hard way that it is not only the steps forward that we must accept, but the stumbles and trials that we must appreciate during the journey. For this I would like to thank the Almighty for providing me the courage, new opportunities, wonderful experiences, people, wealth of knowledge and inculcating strength and patience in me. This is the journey worth to remember and difficult to forget.

**Date:** 10-04-2023

**Harsharan Kaur**

## **Abstract**

### **Exploring the Interfacial Molecular Level Behavior of Biomacromolecules and Nanomaterials using Non-Linear Vibrational Spectroscopy**

Harsharan Kaur

Department of Biomedical Engineering, IIT Ropar

Doctor of Philosophy

Biomolecular adsorption is an important process which arises over the surface of several different biomedical devices and sensing surfaces. Nanotechnology involves a rich study of materials with modified physico-chemical, electrical, and optical properties. Amalgamating biomolecules with nanomaterials is ubiquitously involved in sensor chip designs or biomedical devices or in-vivo theragnostic. Hence, it is crucial to know the interfacial behavior and molecular conformation of biomolecules and nanoparticles distinctively in order to correlate the fundamental attributes of their complexation. We have worked with protein and DNA, both of which provide adaptability, structural flexibility, amphiphilicity, and site-specificity. DNA and protein molecules proffer a suitable opportunity to understand the bottom-up oriented approach of biomolecular interfaces and nano-bio interactions. The present thesis work encompasses the importance of interfaces in decoding the molecular-scale phenomena involving phase-separation, surface tensiometry perturbations, surface adsorption propensity, molecular kinetics, understanding binding interactions at interface, surface density, molecular orientation, and the role of the surrounding environment in modulating the molecular structure. Several research works done in analyzing the biomolecular fundamentals and nano-bio interactions have been performed using surface-specific spectroscopic techniques like surface plasmon resonance, mass spectrometry, X-ray diffraction, or surface-enhanced Raman spectroscopy. However, they involved vacuum-aided functioning, need of crystallite sample, sample labeling or modification, and sophisticated high-energy synchrotron sources which could change the morphology and molecular associations under analysis. Our main aim is to study these processes with minimal modification procedures and under pristine conditions without utilizing strong perturbates. These parameters are crucial in utilizing biomolecules or employing nano-bio complexes to develop fine-tuned functional surfaces/interfaces, which could be potentially

characterized by an interface-sensitive label-free detection approach of sum frequency generation vibrational spectroscopy (SFG-VS). It is capable of providing information of only highly aligned molecular systems which are both IR- and Raman-active. Information regarding structural composition, molecular interaction, kinetics, orientation, and impact on neighboring environment can be explored simultaneously in one experimental configuration itself at the interface. Hence, this work could provide a fresh look to the existing knowledge related to biomolecular mechanism and nano-bio interactions, which has yet not been explored fully in the SFG community itself. We have also extended our studies on tensiometry, dynamic light scattering, zeta-potential, and ATR-FTIR spectroscopy to gather information related to the bulk-features. We have characterized the biomolecular adsorption and kinetics, molecularly-imprinted surfaces for BHB recognition, complex interaction between two protein molecules with quantum dots, and hydrophobically-modified organic nanoparticle behavior at interface and with dsDNA. From the research work performed, we conclude that the interfacial directionality of molecular groups is determined by the interplay of different intermolecular forces such as electrostatic, van der Waals, and hydrogen bonding. These events decide the fine-tuning of the interfacial properties and its dynamics. Our work could offer significant contribution towards the rapidly growing domains of bio-mimicking systems, soft functional materials, micro-fluidic device fabrications and biomolecular sensing applications. Thus, it provides an exploratory research domain in the area of interfacial science, which could be evaluated in a variety of experimental sets further.

**Keywords:** Interface; sum frequency generation vibrational spectroscopy (SFG-VS); interfacial water structure; nanomaterials; nano-bio interactions; molecular recognition; biomolecular adsorption; hydrogen bonding.

# Table of Contents

<b>Acknowledgments</b> .....	<b>i</b>
<b>Abstract</b> .....	<b>iii</b>
<b>Table of Contents</b> .....	<b>v</b>
<b>List of Symbols and Abbreviations</b> .....	<b>ix</b>
<b>List of Figures</b> .....	<b>xi</b>
<b>List of Tables</b> .....	<b>xxv</b>
<b>Chapter 1: Introduction</b> .....	<b>1</b>
1.1 Phases and Interfaces .....	1
1.2 Techniques Characterizing Surfaces or Interfaces .....	3
1.3 Biomolecules and Nanomaterials at Interface.....	5
1.4 Literature Review Based on Interfacial SFG Studies.....	9
1.4.1 SFG Studies on Interfacial Influence of Protein Molecules .....	9
1.4.2 SFG Studies on Interfacial Influence of DNA Molecules .....	19
1.4.3 Studying Nanomaterials at Interface using SFG-VS .....	23
1.4.4 Probing the Interfacial Influence of Nano-Bio Interactions .....	27
1.5 Research Gaps and Motivation .....	29
1.6 Aim and Objectives .....	30
1.7 Outline of the Thesis .....	31
<b>Chapter 2: Experimental theory and methods</b> .....	<b>37</b>
2.1 Interaction of optical radiation with matter.....	37
2.1.1 Generation of linear vs non-linear optical response .....	37
2.2 Origin of sum frequency vibrational response .....	41
2.2.1 Optical polarization-dependent molecular orientation analysis of methyl functional groups .....	45
2.2.2 Instrumental details of SFG .....	50
2.2.3 Methodology and cleaning procedure for SFG experimentation.....	52
2.3 ATR-FTIR vibrational spectroscopy.....	52
2.3.1 Instrumental details and experimental protocol.....	57
2.4 Surface tensiometry: Wilhelmy plate method.....	59
2.5 Zeta-sizer and potentiometry measurements.....	62
2.6 Other experimental characterization techniques .....	65

2.6.1	Nuclear magnetic resonance (NMR) spectroscopy.....	65
2.6.2	Scanning electron microscopy (SEM) .....	65
2.6.3	Atomic force microscopy (AFM) .....	65
<b>Chapter 3: Probing interfacial adsorption of biomacromolecules and their impact on water molecular network at the air-water interface.....</b>		<b>67</b>
3.1	Introduction .....	68
3.2	Experimental methods and procedures .....	69
3.2.1.	Material requirements .....	69
3.2.2.	Sample preparation method .....	69
3.2.3.	Surface tension measurements .....	70
3.2.4.	Sum frequency generation vibrational spectroscopy (SFG-VS).....	70
3.3	Probing the bovine hemoglobin adsorption process and its influence on interfacial water structure at the air-water interface.....	71
3.3.1	Background .....	71
3.3.2	Results and discussion .....	72
3.3.3	Conclusion .....	84
3.4	Investigating the molecular structure of double-stranded DNA and the influence of hydrogen peroxide at the air-aqueous interface .....	84
3.4.1	Background.....	84
3.4.2	Results and discussion .....	88
3.4.3	Conclusion .....	94
<b>Chapter 4: Characterization of molecularly imprinted polymer and its protein recognition ability using sum frequency generation vibrational spectroscopy .....</b>		<b>95</b>
4.1	Introduction .....	96
4.2	Experimental Methods and Procedure .....	99
4.2.1	Material Requirements.....	99
4.2.2	Fabrication Procedure for NIPs and MIPs .....	99
4.2.3	UV-Visible Spectrophotometer .....	100
4.2.4	Atomic Force Microscopy (AFM) .....	100
4.2.5	Scanning Electron Microscopy (SEM) .....	100
4.2.6	Sum Frequency Generation Vibrational Spectroscopy .....	101
4.3	Results and Discussion.....	101
4.4	Conclusion.....	113
<b>Chapter 5: Monitoring the protein-protein interactions mediated by tungsten disulfide quantum dots at the air-aqueous interface .....</b>		<b>115</b>

5.1	Introduction .....	115
5.2	Experimental Methods and Procedure .....	118
5.2.1	Material Requirements .....	118
5.2.2	Synthesis and Preparation of WS <sub>2</sub> QDs .....	118
5.2.3	Sum Frequency Generation Vibrational Spectroscopy (SFG-VS) .....	119
5.2.4	SFG-VS Data Analysis .....	119
5.3	Results and Discussion.....	120
5.4	Conclusion.....	135
<b>Chapter 6: Elucidating the molecular structure of hydrophobically modified polyethylenimine nanoparticles and its potential implication for DNA binding .....</b>		<b>137</b>
6.1	Introduction .....	137
6.2	Experimental methods and procedure .....	140
6.2.1	Material requirements .....	140
6.2.2	Synthesis and preparation scheme of polymeric nanoparticles .....	140
6.2.3	Surface tensiometry .....	142
6.2.4	UV-Visible spectrophotometer .....	143
6.2.5	Viscometry measurements .....	143
6.2.6	Atomic force microscopy.....	143
6.2.7	Zeta-sizer and potentiometry measurements .....	143
6.2.8	ATR-FTIR vibrational spectroscopy .....	144
6.2.9	Sum frequency generation vibrational spectroscopy .....	144
6.3	Results and discussion.....	145
6.4	Conclusion.....	168
<b>Chapter 7: Conclusion.....</b>		<b>171</b>
7.1	Scope of research work .....	173
7.2	Future prospects .....	174
<b>References.....</b>		<b>175</b>
<b>Appendix A.....</b>		<b>195</b>
<b>Appendix B.....</b>		<b>199</b>
<b>Appendix C.....</b>		<b>201</b>
<b>Appendix D.....</b>		<b>205</b>
<b>Appendix E.....</b>		<b>211</b>
<b>List of publications.....</b>		<b>215</b>
<b>Conferences/Seminars/Workshops.....</b>		<b>217</b>

**Bio-Data of Author ..... 219**



## List of Symbols and Abbreviations

Symbol	Units	Description
$\epsilon_0$	$\text{Cm}^{-1}\text{V}^{-1}$	Vacuum permittivity
$\beta$	$\text{Cm}^3\text{V}^{-2}$	Molecular hyperpolarizability
E	$\text{Vm}^{-1}$	Electric field
P	$\text{Cm}^{-2}$	Polarization vector
$\chi^{(1)}$		Linear electric susceptibility
$\chi^{(2)}$		Second-order electric susceptibility
$\chi^{(3)}$		Third-order electric susceptibility
$\omega$	$\text{cm}^{-1}$	Wavenumber
$^{\circ}\text{C}$		Degree Celsius
HWHM		Half-width at half maximum
$\Gamma$	$\text{cm}^{-1}$	Half width at half maximum (HWHM) or line-width
$\mu\text{m}$		Micrometer
a.u.		Arbitrary unit
$\phi$		Azimuthal angle
$\Psi$		Rotation or twist angle
$\theta$		Tilt angle
$\eta$		Viscosity
$\gamma$		Surface tension
$\Gamma'$		Surface excess
$T_m$		Melting temperature
$\zeta$		Zeta
NEXAFS		Near-Edge X-ray Absorption Fine Structure spectroscopy
XPS		X-ray Photoelectron Spectroscopy
XRD		X-ray Diffraction
ATR-FTIR		Attenuated Total Reflection Fourier Transform Infrared
SERS		Surface-Enhanced Raman Scattering
VSFG		Vibrational Sum Frequency Generation
SFG-VS		Sum Frequency Generation Vibrational Spectroscopy
SANS		Small-Angle Neutron Scattering

AFM		Atomic Force Microscopy
CARS		Coherent Anti-Stokes Raman Scattering
SPR		Surface Plasmon Resonance
ToF-SIMS		Time of Flight Secondary Ion Mass Spectrometry
SEM		Scanning Electron Microscopy
DLS		Dynamic Light Scattering
UV		Ultraviolet
IR		Infrared
ST		Surface Tension
PEI		Polyethylenimine
PMMA		Poly (methyl methacrylate)
PEG		Poly (ethylene glycol)
PDA		Polydopamine
AuNPs		Gold Nanoparticles
MD		Molecular Dynamics
H-bond		Hydrogen-bond
ONPs		Organic Nanoparticles
SHG		Second-Harmonic Generation
DFG		Difference Frequency Generation
BBO		$\beta$ -barium borate
OPO		Optical Parametric Oscillation
DMSO		Dimethyl sulfoxide
BHb		Bovine Hemoglobin
dsDNA		double stranded Deoxyribonucleic acid
H <sub>2</sub> O <sub>2</sub>		Hydrogen Peroxide
NIP		Non-Imprinted Polymer
MIP		Molecularly-Imprinted Polymer
Ag		Antigen
Ab		Antibody
PPIs		Protein-Protein Interactions
WS <sub>2</sub>		Tungsten disulfide
CDCl <sub>3</sub>		Deuterated Chloroform

## List of Figures

- Figure 1.1** Illustration of the molecular arrangement at the junction of the two distinct interfaces i.e., solid (needle)-water and air-water interface. The isotropic and anisotropic behavior of water molecules are depicted at the bulk-phase and interface, respectively, via the surface tension phenomenon. .... 2
- Figure 1.2** Schematic representation of the broad applications of biomolecules, nanoparticles, and nano-bio interactions at the interfacial region. .... 6
- Figure 1.3** Representation of the fundamental processes occurring among the molecular systems at or near surface or interface, and an associated influence of the surrounding environment. These phenomena are principally derived by fundamental forces of interaction occurring at the molecular-scale. .... 8
- Figure 1.4** Modelled illustration of the methyl group orientation of (A) lysozyme, (B) fibrinogen, and (C) BSA protein molecules adsorbed at the hydrophilic silica surface as a function of protein concentration. Reprinted with permission from Kim and Somorjai, J. Am. Chem. Soc. **125**, 3150-3158 (2003). Copyright (2003) American Chemical Society.<sup>60</sup> ..... 11
- Figure 1.5** Chemical structure of (A) peptoid 1 and (B) peptoid 2 utilized for nanosheet formation. (C) Model depiction of the attractive and repulsive interactions of peptoid monolayers. Reprinted with permission from Robertson et al., Proc. Natl. Acad. Sci. **111**, 13284-13289 (2014). Published by the National Academy of Sciences.<sup>38</sup> ..... 12
- Figure 1.6** Schematic of water molecular orientation in aqueous media in presence of (A) negatively charged proteins with pH above IEP, and (B) positively charged protein in aqueous pH below IEP, for interface-adsorbed BLG proteins. (C) SFG-VS spectra of adsorbed BLG protein molecules in CH- and OH-stretch regions. Reprinted with

permission from Engelhardt et al., *Langmuir* **29**, 11646-11655 (2013). Copyright (2013) American Chemical Society.<sup>66</sup>..... 13

**Figure 1.7** Interfacial conformation and orientation determination of lysozyme protein molecules using SFG spectroscopy experiments and MD approach, as a function of solution pH. Reprinted with permission from Alamdari et al., *Langmuir* **36**, 11855-11865 (2020). Copyright (2020) American Chemical Society.<sup>68</sup> ..... 14

**Figure 1.8** (A) SFG-VS spectra of AFP-III at air-water interface as a function of concentration (0-90  $\mu\text{M}$ ) with solution pH of 7.8 in CH- and OH-stretch regions. (B) SFG-VS spectra of BSA, inactive AFP-III, active AFP-III at lower (3  $\mu\text{M}$ ) and higher (94  $\mu\text{M}$ ) concentrations at air-water interface. Reprinted with permission from Meister et al., *Proc. Natl. Acad. Sci.* **111**, 17732-17736 (2014). Published by the National Academy of Sciences.<sup>71</sup> ..... 16

**Figure 1.9** Illustration of the salting-up process of BSA protein molecules at the air-salt interface as a variation of time, observed in real-time using SFG kinetics measurements. Reprinted with permission from Li et al., *Langmuir* **35**, 13815-13820 (2019). Copyright (2019) American Chemical Society.<sup>73</sup> ..... 17

**Figure 1.10** Illustration of the experimentally determined structural arrangement and membrane orientation of (A)  $G\beta_1\gamma_2$ , and (B)  $G\alpha_i\beta_1\gamma_2$ . The  $G\alpha_i\beta_1\gamma_2$  protein complex is represented in two views, images arranged at  $90^\circ$  with respect to each other. The membrane plane is shown in blue rectangle form. Reprinted with permission from Yang et al., *J. Am. Chem. Soc.* **135**, 5044-5051 (2013). Copyright (2013) American Chemical Society.<sup>63</sup> ..... 18

**Figure 1.11** Graphical image of (A) hydrophobic, and hydrophilic bacteria in (B) absence, and (C) presence of BSA-coated ODT-SAM surface. SFG spectra shown towards the right side for the respective stages of bacteria interactions with surface.

Reprinted with permission from Bulard et al., *Langmuir* **28**, 17001-17010 (2012).  
 Copyright (2012) American Chemical Society.<sup>74</sup> ..... 18

**Figure 1.12** Pictorial depiction of the arrangement of thymine DNA single strands associated with the CaF<sub>2</sub> substrate towards air and in D<sub>2</sub>O, at the interfacial region. Reprinted with permission from Howell et al., *Biointerphases* **3**, FC47-FC51 (2008). Copyright (2008), American Vacuum Society.<sup>35</sup> ..... 20

**Figure 1.13** Scheme for studying the linker monolayer structural ordering as a function of ssDNA geometry in presence of (A) monovalent cations, and (B) divalent cations. Reprinted with permission from Asanuma et al., *J. Am. Chem. Soc.* **130**, 8016-8022 (2008). Copyright (2008) American Chemical Society.<sup>78</sup> ..... 21

**Figure 1.14** (A) Pictorial illustration of the probable structural arrangement and collapse of T<sub>40</sub> ssDNA in presence of Mg<sup>2+</sup> ion binding. (B) SFG-VS spectra of ssDNA as a function of Mg<sup>2+</sup> concentration. Here, the blue dotted peak fit depicts symmetric methyl stretch and red dotted fit represents asymmetric methyl stretch mode. (C) Quantitative plot of the symmetric and asymmetric peak ratios with Mg<sup>2+</sup> addition. The inset in this panel shows plotted points for T<sub>40</sub> ssDNA (red points) and linker (green points). Reprinted with permission from Walter et al., *J. Am. Chem. Soc.* **135**, 17339-17348 (2013). Copyright (2013) American Chemical Society.<sup>79</sup> ..... 22

**Figure 1.15** Illustration of the dodecanethiol ligand chain length bound over the spherical gold nanoparticle surface, representing the conical space occupied by the gauche defect formation. The SFG spectra shown towards right depicts the size-dependent SSP spectra of dodecanethiol bound to nanoparticles in CH-stretch region. Reprinted with permission from Weeraman et al., *J. Am. Chem. Soc.* **128**, 14244-14245 (2006). Copyright (2006) American Chemical Society.<sup>86</sup> ..... 25

**Figure 1.16** SFG-VS characterization of the binding structure and the oxidation state mechanism of CNP surfaces on binding deuterated acetic acid in an aqueous media, at the solid-aqueous interface. The graphical representation suggests the bidentate bridging and chelating modes of interaction of carboxylate group with CNPs. Reprinted with permission from Lu et al., *J. Phys. Chem. C* **117**, 24329-24338 (2013). Copyright (2013) American Chemical Society.<sup>87</sup> ..... 26

**Figure 1.17** Schematic of the experimental investigation of CdSe QDs fabricated surface and the sensitivity of SFG to the introduction of disorder of ligand molecules upon subjecting to surface washing. Reprinted from *J. Colloid. Interface Sci.* **537**, Watson et al., Probing ligand removal and ordering at quantum dot surfaces using vibrational sum frequency generation spectroscopy, 389-395, Copyright (2019), with permission from Elsevier.<sup>88</sup> ..... 27

**Figure 1.18** SFG-VS spectra in TIR mode of the assembled AuNPs, BioSH-adsorbed AuNPs, BioSH-adsorbed AuNPs immersed in avidin solution, pre-saturated with biotin, and immersed in BSA only. Reprinted and modified with permission from Springer Nature, *J. Mater. Sci.* **44**, 24329-24338 (2009). Close-packed array of gold nanoparticles and sum frequency generation spectroscopy in total internal reflection: a platform for studying biomolecules and biosensors, Tourillon et al., Copyright (2009).<sup>99</sup> ..... 29

**Figure 2.1** (A) Schematic representation of the SFG generation in the reflection mode at the air-water interface in a co-propagating geometry. (B) Energy-level diagram of the process of SFG generation, which results from the resonant transitions occurring from ground vibrational state ( $\nu_0$ ) to the first excited vibrational state ( $\nu_1$ ) via IR photon, which is further upshifted to higher virtual electronic state by excitation through visible photon. The SFG is generated as a result of an anti-stokes raman process, where the absorbed photon energy relaxes back to the ground state. .... 43

**Figure 2.2** Arrangement of the functional methyl group, attached to methylene moieties, in the molecular coordinate system (a, b, c) and lab-frame coordinate system (X, Y, Z) respectively. The principal axis of methyl group and surface normal is depicted by c and Z, respectively. Three molecular orientation angles are showcased for methyl group arrangement i.e., azimuthal angle  $\phi$  about Z-axis, rotation (twist) angle  $\psi$  about c-axis, and tilt angle  $\theta$  about the Z-axis..... 46

**Figure 2.3** Theoretical plots with  $\delta$ -distribution function depicting the variation in the SFG intensity values with respect to the tilt angle (in degrees) in SSP and PPP polarization schemes for the (A) methyl symmetric stretch and (B) methyl asymmetric stretch modes, respectively. .... 48

**Figure 2.4** Simulated orientation curves plotted using Gaussian distribution function with distribution width ( $\sigma$ ) by considering the absolute values of susceptibility ratios of SSP and PPP polarization modes with respect to the methyl group tilt angle ( $\theta$ ) variation..... 49

**Figure 2.5** Schematic illustration of the SFG experimental set-up depicting the beam path across the picosecond Nd:YAG laser, second harmonic generation (SHG) unit, optical parametric generation (OPG), optical parametric amplification (OPA), difference frequency generation (DFG), and the detection unit (monochromator and photomultiplier tube: PMT). Abbreviated labels include M1-M6: mirrors, L1-L3: focusing lens, F1-F2: filters, HWP1-HWP2: half-wave plates, GP: glan prism. .... 51

**Figure 2.6** (A) Schematic of the path of optical beam across the multiple reflection internal reflection element (IRE) geometry of the ATR-FTIR spectrometer. Reprinted with permission from Kaur et al. Springer Nature Singapore Pte Ltd. 2021.<sup>30</sup> Implementation of Beer's law in ATR-FTIR spectroscopy data acquisition for (B) bovine hemoglobin (BHb) protein, and (C) polymeric nanoparticles (NPEI-ONPs) studied in this thesis work as a function of concentration in aqueous media. (D) Calibration curve plot

for BHb protein and NPEI-ONPs obtained using peak intensities at 1645 and 1238  $\text{cm}^{-1}$  absorption bands respectively. The offset noted in the calibration curve of BHb protein depicts the contribution of bending vibrational mode from residual water molecules around 1645  $\text{cm}^{-1}$ . While, NPEI-ONPs demonstrated minimal interference from the water absorption bands in 1238  $\text{cm}^{-1}$  region after performing spectrum subtraction with water spectra as reference. .... 54

**Figure 2.7** (A) Digital photograph of the ATR-FTIR spectroscopic instrument in lab facility used in the present thesis work. (B) Optical layout of ATR-FTIR spectrometer attached with a variable-angle horizontal ATR accessory mounted with the trapezoidal ATR crystal, and the spectrometer interfacing with the OPUS software for data analysis. Reprinted with permission from Kaur et al. Springer Nature Singapore Pte Ltd. 2021.<sup>30</sup> 58

**Figure 2.8** Sketch of Wilhelmy plate method for surface tension measurement of sample. .... 61

**Figure 2.9** (A) Picture of the zeta-sizer instrument ZS90 from Malvern used for the study. (B) Schematic optical layout of the ZS90 set-up for measuring particle size and electrophoretic mobility of the particles within sample. The scheme showcase the particle size measurement plot with intensity depicting the average values. (C) Illustration of the charged particle under the influence of applied voltage across the gold plated electrodes to analyse the electrophoretic mobility and zeta-potential values (in mV) over the particle surface. .... 63

**Figure 3.1** (A) SFG-VS spectra of BHb protein molecules as a function of concentration at air water interface in OH-stretch region. (B) Contour plot of the observed red-shift in the  $\sim 3225 \text{ cm}^{-1}$  wavenumber intensity with an increment in BHb concentration. The color bars are respectively associated with the observed SFG intensity from lower (black) towards higher (red) values. (C) SFG spectra of 10 ppm BHb concentration at air-water



and air-D<sub>2</sub>O interface obtained after achieving equilibrium at ~5000s, in both OH- and aromatic CH-stretch modes. (D) SFG-VS spectra of BHb protein with increasing bulk concentration (0–800 ppm) observed in CH-stretch region at air-water interface. The solid lines here represent the fitting data and scattered points depict experimental values. Reprinted with permission from Chaudhary and Kaur et al. *Appl. Spectrosc.* **75**, 1497-1509 (2021).<sup>129</sup> ..... 74

**Figure 3.2** SFG-VS spectra of the temporal-state evolution in the OH-stretch region for (A) 5 ppm, and (B) 10 ppm BHb concentration, observed at the air-water interface. Reprinted with permission from Chaudhary and Kaur et al. *Appl. Spectrosc.* **75**, 1497-1509 (2021).<sup>129</sup> ..... 78

**Figure 3.3** in situ real-time SFG measurements for observing changes in the SFG intensity with time for methyl symmetric stretch (CH<sub>3SS</sub>) mode at 2875 cm<sup>-1</sup> and OH-stretch of strongly H-bonded water molecules at 3200 cm<sup>-1</sup> for (A) 5 ppm, and (B) 10 ppm BHb concentrations. Real-time measurements for 5 ppm BHb concentrations of CH<sub>3SS</sub> mode with (C) OH-stretch at 3160 cm<sup>-1</sup>, and (D) OH-stretch mode for weakly H-bonded water molecules at 3400 cm<sup>-1</sup>. Reprinted with permission from Chaudhary and Kaur et al. *Appl. Spectrosc.* **75**, 1497-1509 (2021).<sup>129</sup> ..... 79

**Figure 3.4** Surface tension measurements of BHb protein molecules (A) as a function of its bulk concentration, and (B) observing the surface tension kinetics for BHb concentrations of 5 ppm, 10 ppm, and 20 ppm. Reprinted with permission from Chaudhary and Kaur et al. *Appl. Spectrosc.* **75**, 1497-1509 (2021).<sup>129</sup> ..... 81

**Figure 3.5** Predicted model representation of the protein surface adsorption and structural re-arrangement process and its influence on the interfacial water molecular structure at the air-water interface at working pH of 5.8±0.1. The size of molecular entities represented in

this model does not represent the actual space occupied by them. Reprinted with permission from Chaudhary and Kaur et al. *Appl. Spectrosc.* **75**, 1497-1509 (2021).<sup>129</sup>.. 83

**Figure 3.6** SFG-VS spectra of pristine water, Tris-HCl buffer (at pH 7.4), and dsDNA solution at two concentrations (100 and 300 ppm) observed in (A) SSP, (B) PPP, and (C) SPS polarization schemes at the air-aqueous interface. .... 89

**Figure 3.7** Influence of hydrogen peroxide ( $H_2O_2$ ) as a function of its volume concentration on the interfacial molecular features of dsDNA (300 ppm) in (A) SSP and (B) PPP polarization combinations at the air-aqueous interface. .... 92

**Figure 4.1** (A) Chemical Structure of dopamine (DA) monomer (here only polar hydrogen atoms are shown for clarity purpose). (B) Illustration of the PDA properties and their relationship with domain-specific applications. .... 97

**Figure 4.2** Distinct fabrication schemes followed for (A) non-imprinted PDA polymerization, and (B) molecularly-imprinted PDA polymerization procedure. .... 100

**Figure 4.3** (A) Digital images of PDA fabricated  $SiO_2$  substrates (NIP films), (B) SEM imaging, and (C) Film thickness evaluation by AFM with distinct polymerization time durations of NIP for (I) 3-hrs, (II) 6-hrs, and (III) 24-hrs respectively. (C) Subpanel (IV) represents the histogram of the film thickness evaluated by AFM. .... 102

**Figure 4.4** (A) Plausible molecular structure of the polydopamine (PDA) formed after the polymerization from dopamine (DA) monomers. (B) Possible arrangements of the PDA fabrication over  $SiO_2$  substrates and BHb protein association. .... 104

**Figure 4.5** (A) Fitted VSFG spectra of NIP films fabricated with 3-, 6-, 9-, and 24-hrs duration of polymerization. (B) SFG spectra of 3-hr NIP film in SSP and PPP polarization combinations. (C) Peak intensity ratios of  $P_1$  and  $P_2$  for the fitted SFG spectra of NIP films fabricated at distinct time-scales. .... 106

**Figure 4.6** (A) Fitted VSFG profile of MIP thin films with polymerization duration of 3-, 6-, 9-, and 24-hours. (B) Polarization-dependent VSFG spectra of BHB protein molecules fabricated as a thin-film over SiO<sub>2</sub> substrate. (C) Peak intensity ratio trend of d<sup>+</sup>/r<sup>+</sup> ratio values and R<sub>0</sub> (I<sub>CH3FR</sub>/I<sub>CH3SS</sub>) ratio values observed for MIP fabrications of distinct polymerization durations. .... 108

**Figure 4.7** (A) Fitted VSFG spectra, and (B) peak intensity profile of d<sup>+</sup>/r<sup>+</sup> (CH<sub>2SS</sub>/CH<sub>3SS</sub>) ratio values plotted for the 6-hrs MIP film evaluated after a sequence of washing cycles (in SSP polarization mode). .... 111

**Figure 4.8** (A) Fitted VSFG spectra, and (B) histogram profile of cavity bearing 6-hr MIP surface and after BHB-cavity re-binding. (C) Comparative VSFG profile of 6-hrs NIP fabrication before and after subjecting to systemic washing and BHB re-binding processes. (D) UV-Visible absorption spectra of the residual solution from 6-hrs NIP and MIP fabrications respectively after conducting the BHB re-binding experiment. .... 112

**Figure 5.1** Synthesis scheme for tungsten disulfide quantum dots (WS<sub>2</sub> QDs)..... 118

**Figure 5.2** VSFG spectra of pristine water-air interface in (A) SSP, (B) PPP, and (C) SPS polarization schemes. .... 122

**Figure 5.3** VSFG spectra in CH-stretch region (2750-3050 cm<sup>-1</sup>) of individual proteins under pristine condition and in presence of WS<sub>2</sub> QDs respectively at the higher protein concentration in (A) SSP, (B) PPP, and (C) SPS polarization schemes. .... 124

**Figure 5.4** VSFG spectra in CH-stretch region (2750-3050 cm<sup>-1</sup>) of individual proteins under pristine condition and in presence of WS<sub>2</sub> QDs respectively at the lower protein concentration in (A) SSP and (B) PPP polarization schemes. .... 126

**Figure 5.5** Polarization-dependent VSFG spectra in OH-stretch region (3050-3750 cm<sup>-1</sup>) of individual proteins under pristine condition and in presence of WS<sub>2</sub> QDs respectively at the higher (panel A and B) and lower (panel C and D) protein concentrations..... 127

**Figure 5.6** Polarization-dependent VSFG spectra in CH-stretch region (2750-3050 cm<sup>-1</sup>) of lower (set-I) (panel A and B) and higher (set-II) (panel C and D) concentration combination of PPIs in absence and presence of WS<sub>2</sub> QDs. .... 130

**Figure 5.7** A bar-graph representation of VSFG intensity ratio values of CH<sub>3FR</sub> (r<sup>+FR</sup>) and CH<sub>3SS</sub> (r<sup>+</sup>) modes for lower (set-I) and higher (set-II) PPI concentration sets with WS<sub>2</sub> QDs. .... 132

**Figure 5.8** Polarization-dependent VSFG spectra in OH-stretch region (3050-3750 cm<sup>-1</sup>) of lower (set-I) (panel A and B) and higher (set-II) (panel C and D) concentration combination of PPIs in absence and presence of WS<sub>2</sub> QDs. .... 133

**Figure 5.9** (A) Theoretical plot of  $|\chi^{(2)}_{SSP,SS}/\chi^{(2)}_{PPP,AS}|$  ratios corresponding to the tilt angle ( $\theta$ ) values with the theoretical curves of the angular distribution width ( $\sigma$ ). (B) The trend of  $\theta$  variation at  $\sigma = 0^\circ$  (for  $\delta$ -distribution function) of the terminal methyl groups, as determined from the intersection points of the sample peak ratios obtained with the theoretical curve..... 135

**Figure 5.10** Schematic illustration of PPIs in absence and presence of WS<sub>2</sub> QDs, showcasing the modulation in antibody and antigen binding strength, increased polar alignment of interfacial water molecules, and the observed molecular orientational changes of methyl residues, observed using SFG spectroscopy. This model represents the protein molecules at lower concentration combination, which tend to show surface propensity in presence of WS<sub>2</sub> QDs..... 136

**Figure 6.1** (A) Reaction scheme of the synthesis of naphthalimide modified polyethylenimine (NPEI) polymer. (B) Pictorial illustration of the preparation of NPEI organic nanoparticles (NPEI-ONPs) in buffered solution. Reprinted with permission from Kaur et al., *Langmuir* **38**, 13456–13468 (2022). Copyright (2022) American Chemical Society.<sup>276</sup>..... 142

**Figure 6.2** (A)  $^1\text{H}$  NMR and (B)  $^{13}\text{C}$  NMR spectra in  $\text{CDCl}_3$  of the synthesized NPEI polymer. The chemical structure of NPEI polymer is provided along for clarity. Reprinted with permission from Kaur et al., *Langmuir* **38**, 13456–13468 (2022). Copyright (2022) American Chemical Society.<sup>276</sup> ..... 147

**Figure 6.3** (A) Histogram representation of the measured NPEI-ONP particle size. (B) Morphological determination by AFM imaging of the prepared NPEI-ONPs. (C) Zeta potential measurements with NPEI-ONP concentration variation. (D) ATR-FTIR absorbance profile of b-PEI polymer and prepared NPEI-ONPs in the aqueous media. Reprinted with permission from Kaur et al., *Langmuir* **38**, 13456–13468 (2022). Copyright (2022) American Chemical Society.<sup>276</sup> ..... 148

**Figure 6.4** Variations in the (A) mean surface tension of aqueous media, and (B) formulated molecular surface excess ( $\Gamma'$ ) plot as a function of NPEI-ONP concentration. Reprinted with permission from Kaur et al., *Langmuir* **38**, 13456–13468 (2022). Copyright (2022) American Chemical Society.<sup>276</sup> ..... 151

**Figure 6.5** (A) SFG spectrum of pristine water-air interface at pH 5.8 along with peak assignments. (B) Comparative sum frequency spectra of aqueous media taken for reference. Reprinted with permission from Kaur et al., *Langmuir* **38**, 13456–13468 (2022). Copyright (2022) American Chemical Society.<sup>276</sup> ..... 152

**Figure 6.6** SFG spectra in SSP polarization scheme for (A) b-PEI (1.4 mM) and (B) 1,8-naphthalic anhydride (0.04  $\mu\text{M}$ ). Solid lines are indicative of the fitted curve for the symbol-marked experimental data points. Reprinted with permission from Kaur et al., *Langmuir* **38**, 13456–13468 (2022). Copyright (2022) American Chemical Society.<sup>276</sup> 153

**Figure 6.7** (A) Sum frequency spectra of NPEI-ONPs as a function of concentration variation at air-aqueous interface, (B) represent histogram profile of  $3450\text{ cm}^{-1}$  and  $3225\text{ cm}^{-1}$  peak intensity ratios, and (C) depicts peak amplitude variation at  $3073\text{ cm}^{-1}$  aromatic

peak feature, in SSP polarization combination with inset illustrating aromatic ring ordering. (D) SFG spectra of NPEI-ONPs at selective concentrations in PPP polarization scheme. (E) SFG spectra of NPEI-ONPs prepared in buffered D<sub>2</sub>O media for selective concentrations. (F) Concentration-dependent profile of NPEI polymer in buffer system. In SFG spectra, the solid lines depict fitting lines of the experimental data points represented in symbols. Reprinted with permission from Kaur et al., *Langmuir* **38**, 13456–13468 (2022). Copyright (2022) American Chemical Society.<sup>276</sup> ..... 155

**Figure 6.8** Pictorial illustration of the possible NPEI-ONP molecular behavior at the air-aqueous interface. .... 158

**Figure 6.9** Chemical structure of (A) prepared NPEI-ONPs and (B) dsDNA.<sup>276,281</sup> ..... 159

**Figure 6.10** (A) Viscosity measurements of dsDNA in pristine conditions and under NPEI-ONP influence added to fixed dsDNA concentration. (B) The melting temperature (T<sub>m</sub>) profile of dsDNA observed at its characteristic 260 nm absorbance wavelength with and without NPEI-ONP addition to aqueous media. Reprinted with permission from Kaur et al., *Langmuir* **38**, 13456–13468 (2022). Copyright (2022) American Chemical Society.<sup>276</sup> ..... 160

**Figure 6.11** (A) Mean particle size evaluation, (C) ζ-potential and (D) electrophoretic mobility measurements, and (E) conductivity (σ) analysis of NPEI-ONPs, compared with respect to dsDNA and ONP concentration ratios. Reprinted with permission from Kaur et al., *Langmuir* **38**, 13456–13468 (2022). Copyright (2022) American Chemical Society.<sup>276</sup> ..... 163

**Figure 6.12** ATR-FTIR absorbance spectra in bending region (900-1300 cm<sup>-1</sup>) of dsDNA and NPEI-ONP with concentration ratios (A) 1:1, (B) 3.33:1, and (C) 33.33:1. (D) ATR-FTIR spectra in CH- and OH-region (2700-3800 cm<sup>-1</sup>) of NPEI-ONPs, DNA, and their respective concentration ratios. Arrows depicts variations in intensity and peak shifting.

Reprinted with permission from Kaur et al., Langmuir **38**, 13456–13468 (2022).

Copyright (2022) American Chemical Society.<sup>276</sup>..... 165

**Figure 6.13** Sum frequency spectra of (A) dsDNA (0.03 mg.mL<sup>-1</sup>) comparative to pristine water, (B) b-PEI (at 1.4 mM concentration) and (C) 1,8-naphthalic anhydride (NA, 0.04 μM) with dsDNA concentration variation respectively in SSP polarization scheme. Solid lines represent fitted lines of experimental data points denoted in symbol form. Reprinted with permission from Kaur et al., Langmuir **38**, 13456–13468 (2022).

Copyright (2022) American Chemical Society.<sup>276</sup>..... 166

**Figure 6.14** SFG spectra of NPEI-ONPs with increasing dsDNA concentration in μg.mL<sup>-1</sup> in (A) SSP and (B) PPP polarization schemes in CH- and OH-stretch region. (C) Intensity ratio plot of fitted data peaks centred at ~3450 cm<sup>-1</sup> and ~3225 cm<sup>-1</sup> wavenumber value with added dsDNA of fitted SSP polarization data. (D) SFG spectra in bending mode region (in ssp polarization scheme) for NPEI-ONPs with varying dsDNA concentration at the air-aqueous interface. Pristine dsDNA spectra at 3.68 μg.mL<sup>-1</sup> concentration is shown for reference. Reprinted with permission from Kaur et al., Langmuir **38**, 13456–13468 (2022). Copyright (2022) American Chemical Society.<sup>276</sup> 168

**Figure 6.15** Characterizing the molecular-level activities of hydrophobically modified polymeric nanoparticles as a variation of its concentration and under the influence of double-stranded DNA at the air-aqueous interface. Reprinted with permission from Kaur et al., Langmuir **38**, 13456–13468 (2022). Copyright (2022) American Chemical Society.<sup>276</sup>..... 169





## List of Tables

<b>Table 2.1</b> Description of ZnSe ATR crystal properties. Reprinted with permission from Kaur et al. Springer Nature Singapore Pte Ltd. 2021. <sup>29,30,114,118,119</sup> .....	56
<b>Table 6.2</b> <sup>1</sup> H and <sup>13</sup> C NMR peak designations of NPEI polymer. Reprinted with permission from Kaur et al., Langmuir <b>38</b> , 13456–13468 (2022). Copyright (2022) American Chemical Society. <sup>276</sup> .....	146
<b>Table 6.3</b> ATR-FTIR absorption profile peak designations and assignments for b-PEI polymer and NPEI-ONPs in aqueous media. Reprinted with permission from Kaur et al., Langmuir <b>38</b> , 13456–13468 (2022). Copyright (2022) American Chemical Society. <sup>276</sup>	149



# Chapter 1

## Introduction

In this chapter, the fundamentals of surface, interface, bio-interface, and the correlation among the nanomaterials and biomolecules is being discussed and presented in details. In-depth information along with the research support is provided to build an understanding about how the notion of combining the nanomaterials and biomolecules (which come from the similar dimension scales) would open a new window towards several different technological perspectives. This chapter also elaborates about the fundamental inter-molecular forces of interactions which are entailed universally in several different type of molecular-level associations. A brief discussion is given over different bulk-/linear-optics-based experiments, the interface-sensitive non-linear (NL) optical tools and the sum-frequency generation vibrational spectroscopy (SFG-VS) based on second-order NL process along with their corresponding literature survey specific towards the protein and DNA molecules as model biomacromolecules, nanomaterials, and nano-bio associations. Further, various application-based domains enrolling the nano-bio associations and biomolecules at interface are also being explored. The last section of the chapter confers about the aim and objectives of the research work performed, and provides a glimpse towards the overall structure of the thesis work to be discussed.

### 1.1 Phases and Interfaces

Phases are composed of a homogenous system where the intrinsic properties of the system for instance, density, volume, melting/boiling point, etc. are continuous throughout the system.<sup>1</sup> Whenever there is a disruption in the homogeneity of the system via compositional changes or the occurrence of phase boundary region, an interface emerges. Thus, an interface is simply a region which lies at the boundary of two distinct phases, segregating the two homogenous systems. Understanding it from the molecular-level perspective by taking the example of the air-water interface (Figure 1.1), the bulk-phase of the system (i.e., the homogenous system of water molecules) constitutes the molecules which are under a constant random Brownian motion and experience a compensating force in magnitude from all directions, hence averaging out the net

intermolecular force to be zero. However, the molecules at the interfacial region are surrounded unevenly by the neighboring molecular units with the resultant force directing towards the bulk of the liquid. At the interface, the liquid media tends to reduce the area which is exposed-off towards the air, as much as possible. As a result, the surface tension ‘ $\gamma$ ’ property arises which is one such phenomena occurring at the air-water interface where the water molecules are inclined to occupy minimum surface area.<sup>1</sup> Moreover, several properties like composition of media, density, and even molecular ordering could be distinct for bulk and interface respectively. The interfacial molecules are associated with the molecules existing in three distinct localities i.e., the molecules lying in the bulk media beneath the interface, molecules co-existing at the surface/interface, and lastly, the molecules of the interacting environment (for example molecules of air or solid media interacting with interfacial molecules of liquid media at air-liquid and solid-liquid interface respectively) as shown in Figure 1.1.<sup>1,2</sup> Hence, any kind of perturbation of the interface could readily modulate the behavior of molecular system underneath. These molecular disturbances and interfacial perturbations at both micro- and macroscopic levels are exerted by certain intermolecular forces segregated to attractive and repulsive forces, strong and weak forces, short- and long-range forces.<sup>1-3</sup> These molecular forces are responsible for impacting the molecular structure, function, molecular orientation, re-organization, and molecular adsorption at the anisotropic media (i.e., an interface) than that in the isotropic bulk-phase.<sup>2-4</sup>

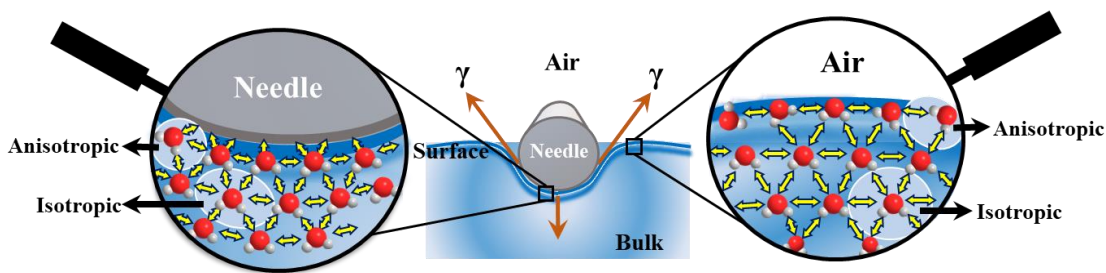


**Figure 1.1** Illustration of the molecular arrangement at the junction of the two distinct interfaces i.e., solid (needle)-water and air-water interface. The isotropic and anisotropic behavior of water molecules are depicted at the bulk-phase and interface, respectively, via the surface tension phenomenon.

A special interest in studying interfaces has increased primarily to gain a deeper understanding about the various natural phenomena and molecular interactions occurring ubiquitously. For instance, living organisms comprise majorly of water making the air-liquid or solid-liquid or liquid-liquid interface a common site within the physiological

systems in terms of maintaining cellular shape, membrane integrity, cellular compartmentalization, molecular functionality, etc.<sup>3,5,6</sup> Another interfacial phenomenon enrolls the process of cloud formation where the water molecular nucleation encircling the dust particles rely on the surface effects.<sup>2,7</sup> The property of emulsions, food quality, detergents, and foam generation are largely governed by the liquid-liquid interfaces.<sup>2,8,9</sup> Several technological applications viz., material lubrication, wetting properties, composite material production, and thin-film casting are often mediated by surface/interfacial effects.<sup>2,6,10-12</sup> In lieu of an extensive practicality of the interfacial milieu, the investigation of interfacial processes become pivotal to improve upon the system's efficiency and efficacy. This thesis work involves a primitive interpretation about biomolecular interfacial behavior which is extended to be utilized for understanding the influence of their association with nanomaterials within its vicinity, regulating the structure and molecular recognition by ensuing molecular-level perturbations. Henceforth, we will focus our discussion ahead more on the biomolecules and nanomaterial influence over the surface properties of the aqueous media and as thin-film fabrications, and the respective technological implementations commonly pursued in the research community.

## **1.2 Techniques Characterizing Surfaces or Interfaces**

The development of an understanding of modern science relies on the fundamental principles and working of the instrument which could readily investigate the physico-chemical processes of distinct molecular systems. Quoting an excerpt of Sir Humphrey Davy (a re-known chemist of his times):<sup>13</sup>

*“Nothing tends so much to the advancement of knowledge as the application of a new instrument.”*

It can be emphasized that the development of new instruments and technologies has predated and undeniably revolutionized the existing concepts of science. Monitoring interfacial molecular structures and environment with adequate selectivity and sensitivity, whose expressions are distinct from the bulk features, is a daunting task which is encountered by several conventional techniques. Besides, much of the interfacial information about the structural properties of biomolecule and nanomaterials, gathered to date arise majorly from an enormous collection of indirect evidences obtained from different surface-probing techniques, which include: colorimetric assays,<sup>14,15</sup> surface

tensiometry or contact angle measurements,<sup>15,16</sup> quartz crystal microbalance (QCM),<sup>15,17</sup> and atomic force microscopy (AFM).<sup>15,17,18</sup> Considering a rise in demand for employing label-free approaches to probe the biomolecular and nanomaterial physical characteristics without perturbing their native state, these techniques provide a label-free information about the surface properties (hydrophilic/hydrophobic), surface roughness, molecular adsorption, quantification, and binding kinetics in real-time. Nevertheless, they come with certain limitations such as temperature and medium sensitivity, the requirement of the conductive interface, cost, the need for large sample quantity, difficulty with analyzing soft samples and limited spatial information.<sup>15</sup>

Spectroscopic approaches are selectively appealing as they encompass broad range of information on the hidden interfaces and resonating molecular features. Electrochemical impedance spectrometry display resolved data of biomolecular immobilization and modification over the electrode surface which is observed in terms of potential differences.<sup>15,19,20</sup> But, it is cumbersome here to differentiate among the specific and non-specific binding events and often require a rigorous in-built control data value for comparison and reliability. Other routinely used powerful spectroscopies like surface plasmon resonance (SPR), scanning tunneling spectroscopy (STS), time-of-flight secondary ions mass spectrometry (ToF-SIMS), X-ray diffraction (XRD), and near edge X-ray absorption fine structure spectroscopy (NEXAFS, with 6-200 nm sensitivity) are known to characterize the biomolecular structural aspects and surface composition profiling of the sample.<sup>15,21-26</sup> Moreover, NEXAFS is known to examine the orientation of thiol-modified DNA strands compared to the unmodified DNA over the substrate.<sup>27</sup> Yet, they require a vacuum-aided functioning, need of crystallite sample, and sophisticated high-energy synchrotron sources which could change the morphology and molecular associations under analysis. Hence, these systems are refrained from being employed for in-situ investigations particularly of soft molecular systems like protein and DNA. Most of these techniques offer characterization of samples in the non-aqueous system. However, for all the biomolecules and bio-applicable nanomaterials, aqueous systems are indispensable if we intend to understand their architecture and functionality in native state. In lieu of this, both, attenuated total reflection Fourier transform infrared (ATR-FTIR) spectroscopy and surface enhanced Raman spectroscopy (SERS) can be employed for in-situ and ex-situ molecular-level investigations in aqueous media. Both spectroscopies are based on the vibrational spectroscopic technique. In ATR-FTIR, the

molecular vibration modes are probed for solid samples and at solid-liquid interfaces reaching a probing depth of a few micro-meters.<sup>15,28-30</sup> On the other hand, the SERS experimental tool examines the polarizability derivative i.e., degree of polarizability changes observed during molecular vibration of the molecular groups of samples in liquid state or as thin-film coatings.<sup>15,20</sup> However, SERS require sample deposition procedures which may hinder the native state of different biomolecules under study. Thus, an effective experimental instrument is required to readily offer composition-specific information along with the molecular-level orientation and their association with the surrounding environment/media properties. These aspects have been successfully fulfilled by a second-order non-linear optical process i.e., sum frequency generation vibration spectroscopy (SFG-VS), which uniquely allows the in-situ as well as ex-situ probing of molecules which are both IR- and Raman-active at the interface with the probing depth corresponding up to which the centro-symmetry is broken at the interface.<sup>12,31,32</sup> SFG-VS is an interface-specific approach for studying the resonant vibrational patterns of molecular functional groups at the interface where the media's centro-symmetry is broken, in comparison to traditional techniques, without the requirement for sample labelling or structural modifications.<sup>8,12,31-33</sup> As a result, it appears to be a perfect tool for exploring and extracting the structural organization, composition, and orientational parameter of molecules and related groups at various interfaces/surfaces. SFG-VS has significantly contributed to understanding the molecular underpinnings of many surfaces i.e., solid-solid, solid-liquid, liquid-liquid, air-solid, and air-liquid interfaces.<sup>8,12,31-35</sup> Proteins, DNA, and phospholipids have all been examined in various interfacial settings using SFG spectroscopic tool.<sup>8,34-39</sup> In the following sections of this chapter, we will overview the literature on various studies using the SFG spectroscopic approach to investigate the interfacial molecular structures of various biomolecules (specific to proteins and DNA molecules) and nanomaterials in different environments. We have further evaluated the fundamentals forces involved in the process of nano-bio interactions and their impact on the interfacial architecture.

### **1.3 Biomolecules and Nanomaterials at Interface**

Physiological systems have naturally evolved by making a profound utilization of surfaces/interfaces to conduct several biological reactions and phenomena, while maintaining the cellular integrity. Interface arises at different levels within the biological

system (depicted in Figure 1.2) viz., during molecular recognition, transmembrane proteins segregated among two distinct phases across the cellular membrane, lung alveoli membrane region at the air-liquid interface and preventing lung collapse, cellular phase separation, or regulating the emergence of a disease.<sup>3,5,6,40-42</sup> These interfacial systems are associated directly with conformational transitions and molecular environments, thereby governing the biomolecular functionality. Biomolecules are broadly categorized into five subsets: proteins (including single amino acids, peptides, aggregates), lipids (including membrane mono- or bi-layer, lipidic vesicles), carbohydrates (saccharides), nucleotides (DNA, RNA, nucleic bases), and composite molecules formed by the combination of two or more molecular units.<sup>23,34</sup> The biomolecular response at the molecular scale remains elusive, often when the system is delineated in terms of bulk and interfacial activity where the concept of short-range intermolecular forces enrolled in perturbing dielectric properties at the interface comes into the picture.

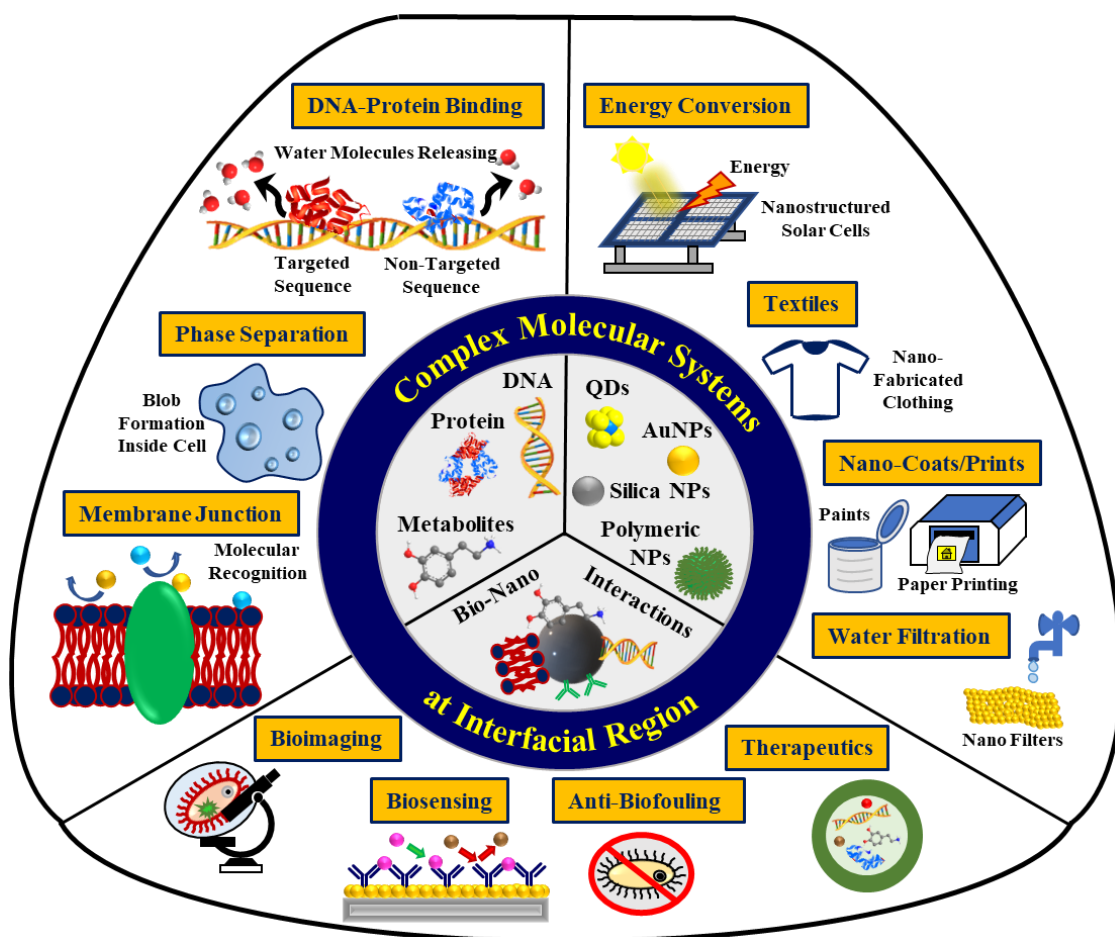


**Figure 1.2** Schematic representation of the broad applications of biomolecules, nanoparticles, and nano-bio interactions at the interfacial region.



Similarly, nanotechnology involves a rich study of materials bearing large surface area to volume ratio and offering modified physico-chemical, electrical, and optical properties.<sup>43,44</sup> As a result, they have been widely applied in varied fields such as drug-delivery, diagnostics, device fabrications for opto-electronic applications, surface-protective coatings, etc. (shown in Figure 1.2).<sup>23,43,45,46</sup> Often, different classic nanomaterials/particles are amalgamated with the nano-scaled biomolecules which offers unique properties to each element, reshaping their ultimate functionality.<sup>43-45</sup> The specificity, functionality, and bio-compatibility are adapted from biological molecules by associating them with distinct nanomaterials for various technological applications (see Figure 1.2). These offer a sustainable alternative to conventional synthetic methodologies that involve a non-specific ligand for interactions under arduous conditions.<sup>45</sup> Thus, a correlation between the structure, dynamics and behavior of both biomacromolecules and nanomaterials is the mainspring for understanding key biophysical aspects involved in numerous bio-combinatorial approaches. The nano-bio interactions are often indulged in dynamically affecting the interface by three-different contributions: (i) biomolecular conformation and dynamics, (ii) physico-chemical characteristics and composition of nanoparticles, and (iii) influence of individual physico-chemical properties of nanomaterial and biomolecules during their association.<sup>44,45</sup> Here, the interfacial molecular re-structuring of the surrounding medium could attribute to the molecular dissolution or molecular phase transition, especially for samples prepared in the aqueous phase.<sup>44,45,47,48</sup> In all these scenarios, the process of interfacial molecular adsorption is a primitive step that is determined by the fundamental forces ensuing during molecular interactions and their surface coverage, thus affecting the surface free energy (Figure 1.3). Biomolecules i.e., protein and DNA molecules, are amphiphilic (carrying both hydrophilic and hydrophobic properties) in nature due to which they gravitate towards the hydrophilic-hydrophobic interfacial region. The adsorption process brings about some conformational changes in the biomolecules as well as influence the interfacial environment, which is known to decide the subsequent biological fate of macromolecules. Thus, biomolecular adsorption is a necessary process which arises over the surface of different biomedical devices. These include long-range forces originating from the attractive van der Waals (vdW) and repulsive electrostatic interactions; short-range forces resulting from steric, solvent interactions, and charge-based association (represented in Figure 1.3).<sup>44,47,48</sup> These result in certain important interfacial attributes (shown in Figure 1.3) viz., molecular kinetics, hydrophilicity, hydrophobicity, viscosity, molecular phase-

separation, self-assembly of molecules, micellar formation, surface tension changes, surface adsorbing tendency, molecular condensation, molecular orientation, etc. Thus, it is crucial to know the interfacial behavior and molecular conformation of biomolecules and nanoparticles distinctively.

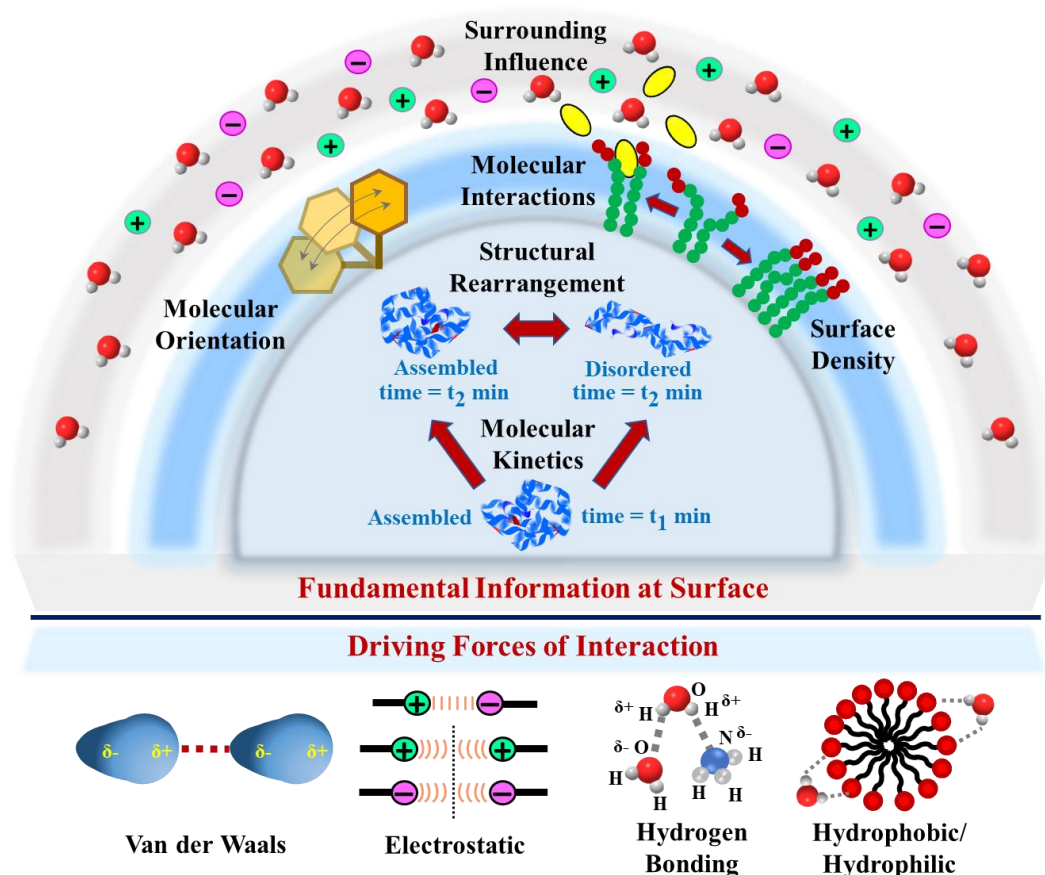


**Figure 1.3** Representation of the fundamental processes occurring among the molecular systems at or near surface or interface, and an associated influence of the surrounding environment. These phenomena are principally derived by fundamental forces of interaction occurring at the molecular-scale.

The natural inquisitiveness of a human being has always existed in dissecting things to their smallest level of existence to understand the bigger picture. Thus, we must address a problem from the ‘first principles’ approach, as stated by Francis Crick (a famous molecular biophysicist) in his book ‘What mad pursuit’:<sup>49</sup>

*“Almost all aspects of life are engineered at the molecular level, and without understanding molecules we can have a very sketchy understanding of life itself.”*

Out of the enlisted biomolecules, we have worked with protein and DNA, both of which provide adaptability, structural flexibility, amphiphilicity, and site-specificity.

DNA and protein molecules proffer a suitable opportunity to understand the bottom-up oriented approach of biomolecular interfaces and nano-bio interactions. Using SFG-VS, the molecular expression of both protein and DNA molecules can be observed via their hydrophobic CH-domains, vibrational bending features of protein's amide bond, DNA's phosphate bond, and by observing their impact over the neighboring water structure. Henceforth, we will initially present the literature on exploring the individual properties of biomolecules (protein and DNA) and nanomaterials impacting distinct interfaces using SFG-VS technique and then delve into understanding the complexity of nano-bio interactions and their combined influence over the interfacial architecture.

## **1.4 Literature Review Based on Interfacial SFG Studies**

### **1.4.1 SFG Studies on Interfacial Influence of Protein Molecules**

**Studying protein conformational dynamics at the interface.** Next to water, protein molecules are ubiquitously found in the human body. Protein's adsorption and activity is critical for its functioning within the biological system and for several industrial and biomedical-based applications.<sup>11,23,34,40,46</sup> Numerous studies have been performed to develop an understanding about its complex behavior ensuing during adsorption process from a variety of perspectives, including concentration-based adsorption, adsorption kinetics, structural changes and conformational reversibility.<sup>23,34,50-53</sup>

Wang et al. investigated the conformational variations of bovine serum albumin (BSA) protein molecules, by SFG spectroscopy, as a function of their molecular surface coverage at the air-water interface. They concluded that the protein's concentration is a primary determinant of its unfolding state (at low concentration) and a partially folded state (at higher protein concentration) at the interface. Here, the rate of adsorption for lower and higher protein concentrations depicted a time-dependent dynamic process.<sup>54</sup> Further studies were conducted by the same group on observing the BSA protein adsorption on distinct substrates forming an air-solid and liquid-solid interface for protein adsorption.<sup>55,56</sup> The substrates employed were silica, polystyrene (PS), and polymethylmethacrylate (PMMA), which were interfaced with varied chemical constituents, including air, water, carbon tetrachloride (CCl<sub>4</sub>), benzene, and a hydrophobic fluorinated solvent. It was observed that the exposed off residues of BSA

protein arrange distinctively, exhibiting varying conformational state for the protein molecule relative to the contacting media-interface conditions. A hydrophobic conformation of BSA forms across hydrophobic media, while a hydrophilic protein configuration persists interfacing two hydrophilic media.<sup>55,56</sup> These studies were performed in the C-H stretching range (i.e., 2800-3100  $\text{cm}^{-1}$ ) and summarized the occurrence of interfacial protein adsorption to be an implication of the protein's hydrophobic effect. Chen group studied the concentration- and time-dependent interfacial behavior of two different antibody molecules at the silicone oil-aqueous interface.<sup>57,58</sup> They concluded that a distinct surface hydrophobicity of the two proteins under study is responsible for their differential adsorbing tendency, forming an ordered structure at the silicon oil-aqueous interface.

Characterizing the surface-bound protein molecules has an essential implication in studying the biological response during the cellular attachment, bio-crystallization, and bio-film coatings, as well as in various immuno-diagnostic assay procedures.<sup>6,23</sup> Here, the macroscopic adsorbing tendency of proteins intimately governs the spatial orientation of the protein's molecular units. Hence, developing an understanding about the protein's surface coverage, orientation, and conformation after their surface attachment is necessary. Utilizing a thin-film model for BSA molecules, Wang et al. demonstrated a quantitative interpretation in terms of the orientational distribution of the protein's methyl groups to explain the conformational differences incurred by protein molecules at the air-solid and solid-liquid interfaces (i.e., BSA at fused silica-air and fused silica-solution; PMMA-BSA solution interface).<sup>59</sup> They suggested from their work that the adsorbed protein film is generally of several nanometer thickness at the interface. Therefore, the SFG signal originates from the adsorbed protein layer, ruling out the inclusion of any non-local contributions towards the generated SFG signal.<sup>59</sup> Kim and Somorjai investigated the surface structure and molecular packing of three different proteins (lysozyme, fibrinogen, and BSA) adsorbed on the silica (hydrophilic) and PS (hydrophobic) surfaces, as a function of their concentration, using SFG and fluorescence microscopy.<sup>60</sup> Their results showcased that the methyl group orientation differs among protein molecules due to their relative tendency to denature and the thickness of the film formed when their adsorbing concentration is raised. Figure 1.4 represents different models proposed for protein adsorption over silica substrate. Considering the idea of a soft and hard protein molecules, the lysozyme protein shows a concentration-independent

methyl intensity such that the protein molecules occupy the surface with dimension near to its native molecular axis due to the negligible denaturation of lysozyme. Contrarily, fibrinogen and BSA (being soft proteins) form a thin layer with their molecular arrangement parallel to the silica surface, showing a concentration-dependent increment in methyl intensity.<sup>60</sup> With the experimentally obtained methyl response ratio of symmetric and anti-symmetric stretch modes, the molecular tilt angle distribution was also evaluated for the protein molecules. All these protein molecules, however, arrange more randomly over the PS surface, generating a weaker methyl feature in SFG spectra. The differential ordering of the phenyl groups of the three proteins studied indicated that BSA gets significantly affected upon binding with the hydrophobic PS substrate than lysozyme and fibrinogen.<sup>60</sup> This study depicts the structure-dependent differential adsorbing tendency of protein molecules at the air-solid interface.

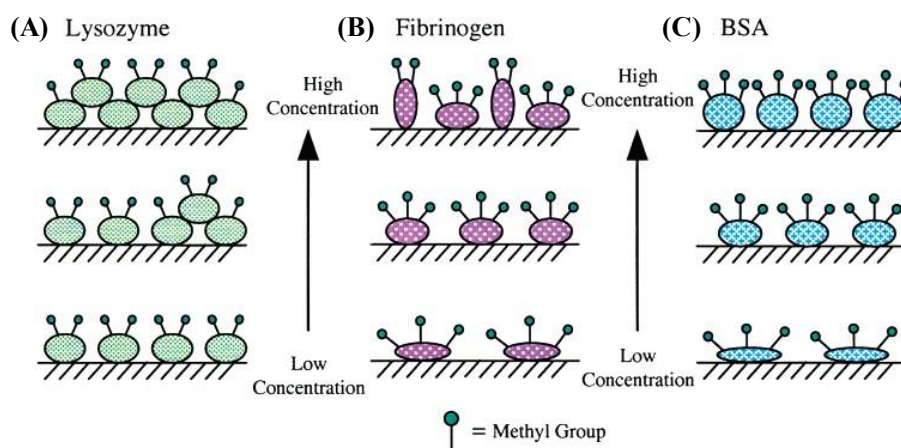


**Figure 1.4** Modelled illustration of the methyl group orientation of (A) lysozyme, (B) fibrinogen, and (C) BSA protein molecules adsorbed at the hydrophilic silica surface as a function of protein concentration. Reprinted with permission from Kim and Somorjai, J. Am. Chem. Soc. **125**, 3150-3158 (2003). Copyright (2003) American Chemical Society.<sup>60</sup>

Robertson et al. investigated the self-assembly based formation of 2D nanosheet structures after the adsorption of peptides at the oil-water interface.<sup>38</sup> The potential utility of these peptoid nanosheets lies in the domain of molecular sensing, bio-mimetic devices, or as model membrane structures, etc., as they tend to cover the lateral dimensions of the surface up to hundreds of micrometers. Two peptides with distinct chemical structures (Figure 1.5, panel A and B) i.e., peptoid 1 with both amine and carboxyl analogs, and peptoid 2 with only carboxyl analogs in the sequence, were studied in CH-OH stretch and the carboxylate regions respectively. At the working pH of 8, the peptoid 1 sustained both positive and negative charges, while the peptoid 2 carried only the negative charge.

Through the interfacial SFG spectral analysis, the authors elucidated that the peptoid 1 formed a packed ordered layer covering the interface, occurring due to the attractive associations among the oppositely charged amine and carboxylate residues of the peptoid 1. However, peptoid 2 assembled into a loosely packed monolayer owing to the occurrence of electrostatic repulsions among negatively charged carboxylates at the interface (see Figure 1.5C). This was evident from the broad methylene features observed for peptoid 2 and a slightly red-shifted carboxylate feature in comparison to the peptoid 1 feature, which depicted an increased involvement of carboxylates with water molecules via H-bonding for peptoid 2 nanostructures. This study highlighted the importance of fundamental molecular forces in the formation of self-assembled organic nanostructures at the interface.<sup>38</sup>

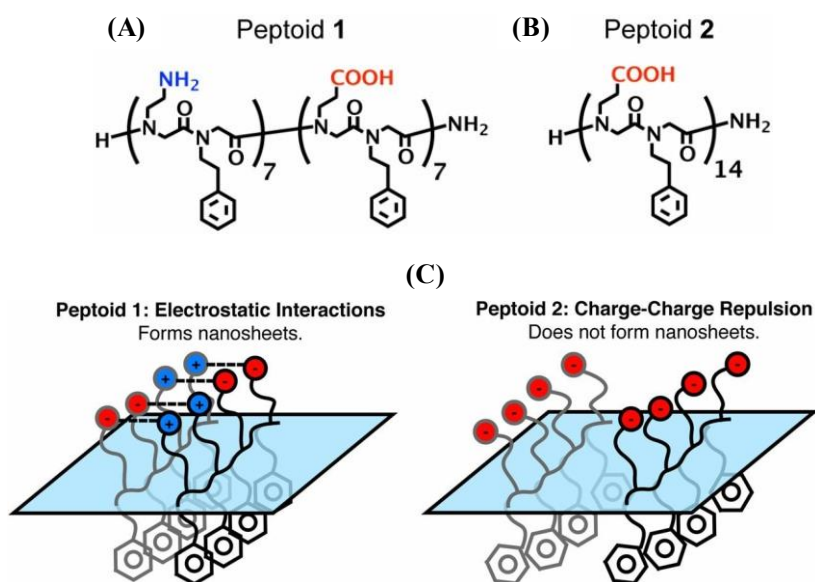


**Figure 1.5** Chemical structure of (A) peptoid 1 and (B) peptoid 2 utilized for nanosheet formation. (C) Model depiction of the attractive and repulsive interactions of peptoid monolayers. Reprinted with permission from Robertson et al., *Proc. Natl. Acad. Sci.* **111**, 13284-13289 (2014). Published by the National Academy of Sciences.<sup>38</sup>

**Impact of protein structure and environment on interfacial protein adsorption.** The surface adsorbing characteristics of protein molecules are predominantly influenced by interfacial surroundings. Interfacial parameters can be readily attuned by varying the ionic strength, temperature, solution pH, surface pressure of the aqueous media or protein interactions with differentially functionalized surfaces.<sup>8,42,61-63</sup> It also depends on the sample properties, such as sample age, protein sequence, and side-chain groups.<sup>61,64,65</sup>

Engelhardt et al. conducted SFG experiments on BSA protein solution as a function of pH at the air-water interface. Their studies reveal a pH-dependent polar ordering of the BSA protein and water molecules due to the charged interface formed by the adsorbed protein molecules. Through the SFG results, a net molecular disordering is observed in both CH- and OH-stretch regions near the isoelectric point (IEP) of protein molecules, which aided in forming an agglomerated network of BSA protein molecules. Considering this, it was deduced from their work that the IEP of the BSA at the interface is nearby to that observed for the BSA present in bulk i.e., pH  $\sim$ 5.<sup>8</sup> Another study by the similar group, was performed on  $\beta$ -lactoglobulin (BLG) protein molecules at the air-water interface as function solution pH, using surface rheology and SFG-VS. At the IEP of BLG, the results depicted a lower molecular ordering and higher dilatation elasticity of the protein multilayers formed at the interface due to the absence of an electric-field. Depending on the net overall charge present on the protein molecule beyond its IEP value (positive or negative), a strong ordering in the interfacial water molecular structure is observed. Here, they explained that the water dipoles for the negatively charged interface points towards the air, while the dipoles point towards the bulk phase for the positively charged interface (as presented in Figure 1.6).<sup>66</sup>

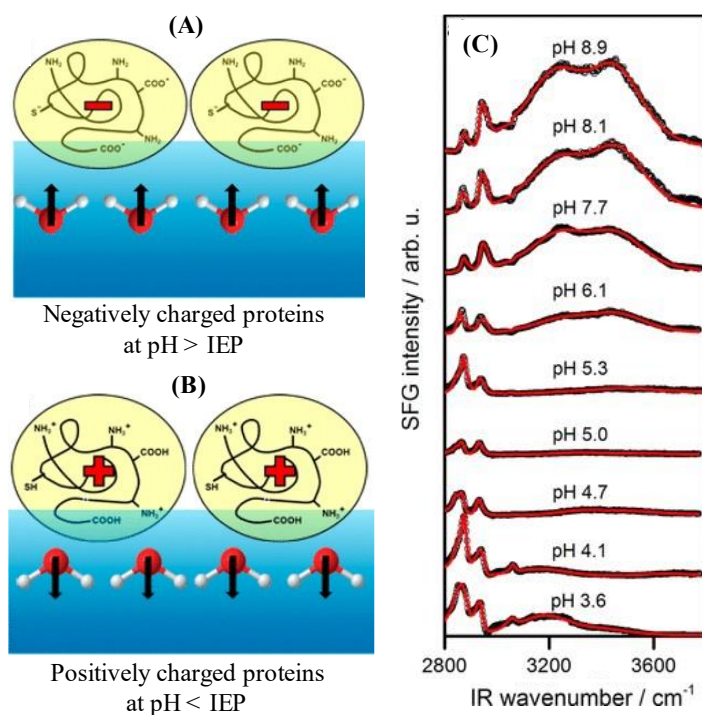


**Figure 1.6** Schematic of water molecular orientation in aqueous media in presence of (A) negatively charged proteins with pH above IEP, and (B) positively charged protein in aqueous pH below IEP, for interface-adsorbed BLG proteins. (C) SFG-VS spectra of



adsorbed BLG protein molecules in CH- and OH-stretch regions. Reprinted with permission from Engelhardt et al., *Langmuir* **29**, 11646-11655 (2013). Copyright (2013) American Chemical Society.<sup>66</sup>

Contrastingly, Devineau et al. reported the phase-dependent studies on hemoglobin (Hb) protein molecules and showcased that the IEP of Hb is 1 unit lower at the interface than that observed in bulk phase for Hb molecules. They assigned this observation to the protein conformational changes which occur due to the interfacial adsorption of Hb molecules.<sup>67</sup> Another work, reported by Alamdari et al. using SFG experiments and molecular dynamics (MD) simulations, determined the orientational tendency of lysozyme protein molecules at pH 7 and pH 11 (at IEP). They validated from their experimental and theoretical findings that the lysozyme adopts a head-on orientation at the interface at pH 7, while near IEP, it adopts a side-on conformation during lysozyme adsorption at the air-water interface (presented in Figure 1.7).<sup>68</sup> York et al. examined the impact of ionic strength of phosphate buffered saline (PBS) over the peptide adsorption and conformational state on silica and PS surfaces studied via SFG spectroscopy at the buffer-substrate interface. It was observed that the peptide molecules project N-H modes only at high ionic strength after adsorbing at the hydrophilic silica substrate (which depicts a stable secondary structure of the peptide). The hydrophobic PS surface presented the C-H modes to be independent of ionic strength variation, while the OH-stretch modes rise as the ionic strength gets reduced.<sup>69</sup>

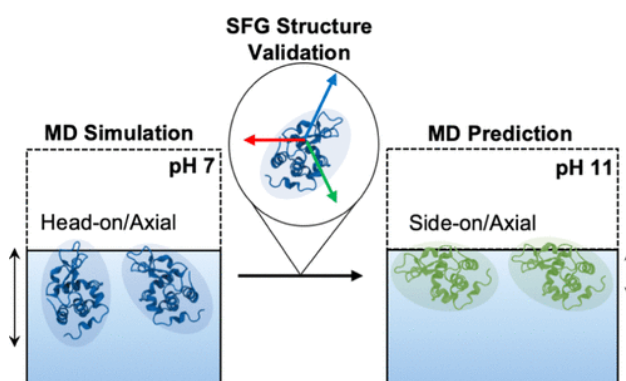


**Figure 1.7** Interfacial conformation and orientation determination of lysozyme protein molecules using SFG spectroscopy experiments and MD approach, as a function of solution pH. Reprinted with permission from Alamdari et al., *Langmuir* **36**, 11855-11865 (2020). Copyright (2020) American Chemical Society.<sup>68</sup>

Studies on LK peptides of varying chain length, side-chain character and amino acid sequence (i.e., LK<sub>14</sub>, LK<sub>7 $\alpha$</sub>  and LK<sub>7 $\beta$</sub> ) were carried out by Phillips et al. to understand its impact on peptide chain adsorption behavior at hydrophilic (silica) and



hydrophobic (PS) substrates.<sup>64</sup> Here,  $\alpha$  and  $\beta$  carries different amino acid sequence. The peptide adsorption on silica represented no well-defined peptide features, except for LK<sub>14</sub> where N-H features were seen in SFG spectra. PS substrate shows C-H modes of peptide hydrophobic moieties, where the amino acid-specific sensitivity towards molecular orientation changes could be observed. Their results concluded that the SFG potentially could demonstrate the amino acid-specific ordering tendency of peptides at PS, while a secondary structure ordering is seen at the silica-water interface.<sup>64</sup> Li et al. constituted a combined study using SFG and MD simulations to determine the influence of surface chemistry over the enzyme surface coverage, orientation and its catalytic activity after immobilization.<sup>70</sup> They deduced that on increasing the surface hydrophilicity of the substrate, the enzyme surface coverage gets reduced and increases the catalytic activity. Their results aimed to improve upon the enzyme-substrate interactions and provided crucial information on the substrate-specific optimizations to enhance the protein catalytic activity. Xiao et al. reported a detailed account of interactions of a short peptide chain (having varied mutational sequences) with MoS<sub>2</sub>, which described the nature of dominant amino acid of the peptide as a major factor in governing the adsorption sensitivity of peptide molecules on the MoS<sub>2</sub> surface.<sup>65</sup> They evaluated the emergence and disappearance of the amide mode of protein backbone in SFG spectra as an indicator of the highly ordered and flat conformation of protein molecules respectively. Their results focused on the protein sequence-optimizations to improve the substrate-protein adsorption for developing biological assays.

Water molecules are considered not merely a secondary player but, they tend to enroll actively in various biological processes like protein folding, molecular adsorption, molecular interactions or binding, etc. The protein's structure- and sequence-dependent impact on the interfacial water structure were also examined by Meister et al., where they reported a differential expression of interfacial water molecules and their re-arrangement for the anti-freeze protein (AFP-III) molecules in comparison to their mutant inactive versions and BSA protein molecules. They showed that the mutant AFP molecules represented similar OH-stretch features as depicted by BSA, while the native AFP at higher concentration has a distinct expression at air-water interface (Figure 1.8). Their work represented the response of water molecules by forming the hydration shells or structure in vicinity of the respective protein molecules at the air-water interface.<sup>71</sup>

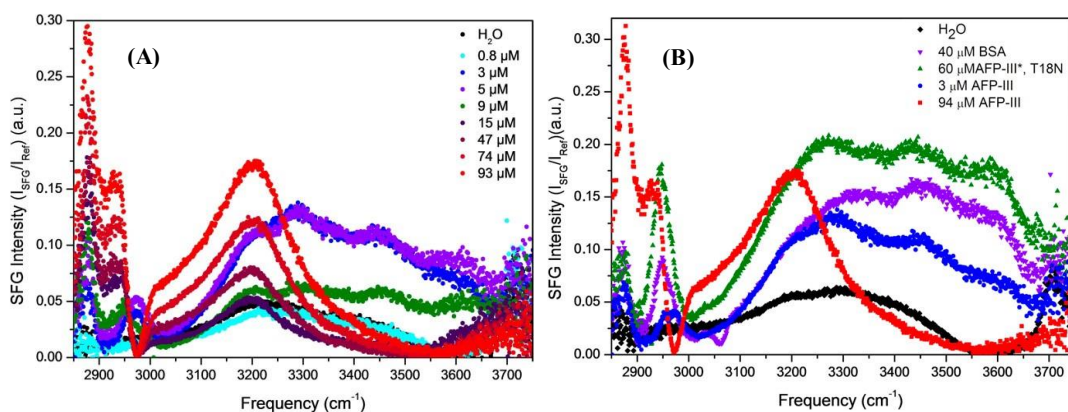


**Figure 1.8** (A) SFG-VS spectra of AFP-III at air-water interface as a function of concentration (0-90  $\mu\text{M}$ ) with solution pH of 7.8 in CH- and OH-stretch regions. (B) SFG-VS spectra of BSA, inactive AFP-III, active AFP-III at lower (3  $\mu\text{M}$ ) and higher (94  $\mu\text{M}$ ) concentrations at air-water interface. Reprinted with permission from Meister et al., Proc. Natl. Acad. Sci. **111**, 17732-17736 (2014). Published by the National Academy of Sciences.<sup>71</sup>

**Protein adsorption for surface bioengineering applications.** The protein interfacial adsorption does not only cause protein structural re-arrangement and the differential interfacial conditions, but it has also captured the attention in understanding the fundamental mechanisms. Jung et al.<sup>72</sup> examined the molecular-level information of the protein displacement process (Vroman effect) from the surface of silica substrate by secondary protein molecules present in aqueous media at physiological pH. They worked with human plasma fibrinogen (HPF), whose  $\alpha\text{C}$  domain formed weaker interactions via electrostatic bonding with the underlying deprotonated silanol groups of silica substrate. On conducting pH cycling towards the acidic state, the  $\alpha\text{C}$  domain gets positively charged and due to its weaker interaction with silica substrate, providing an opportunity for its ready displacement from the substrate surface. This is displayed from the observed N-H and lowering of OH-stretch feature in SFG spectra, representing aligned molecular groups at interface. In contrast, at physiological pH, the  $\alpha\text{C}$  domain gets removed and the remaining subunits of HPF interact strongly via H-bonding, vdW and hydrophobic interactions with the silica surface. This represented diminished contribution from N-H modes in SFG spectra.<sup>72</sup> Their results hinted towards the role of  $\alpha\text{C}$  domain in keeping HPF soluble in the bloodstream before its utilization for blood clot formation, thus contributing towards the Vroman effect. A kinetics-based study of BSA protein adsorption at air-water interface in absence and presence of salts is carried out by Li et al. using SFG and surface pressure-based measurements.<sup>73</sup> It was aimed to understand the “salting-up” effect of protein molecules occurring at concentrations well-below the value

where the “salting-out” effect of protein molecules is observed. Their results showcased that the presence of salt accelerates the emergence of BSA at the air-water interface, as revealed by the SFG-kinetics results (illustrated in Figure 1.9). Although, no interfacial influence was observed for other rigid proteins studied i.e., lysozyme and lipase. Their work surmised that even though the “salting-up” and “salting-out” of protein molecules depends on the principle of volume exclusion in the presence of ions, “salting-up” is noticed to additionally rely on the structural flexibility of protein molecules. Also, no aggregates were formed in the bulk media, which is commonly noticed for the “salting-out” process of protein molecules.<sup>73</sup> Their investigation provided a new-type of salt-driven protein interfacial adsorption phenomenon, which is specific to certain class of protein molecules only, and could be identified using interface-sensitive SFG spectroscopic tool.

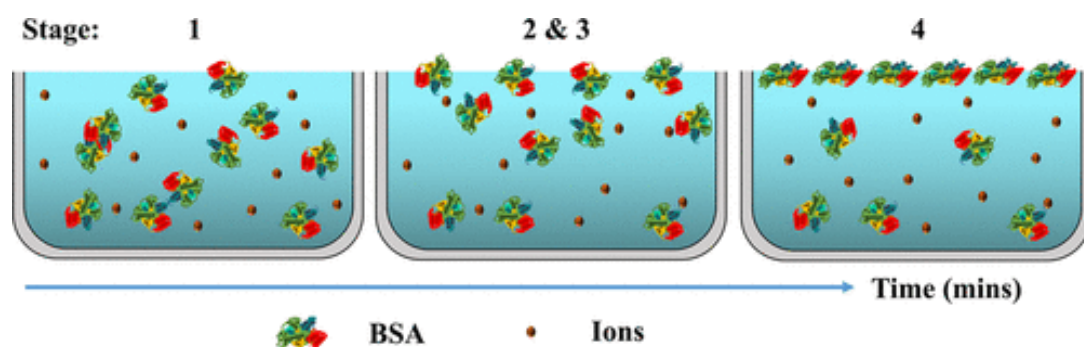


**Figure 1.9** Illustration of the salting-up process of BSA protein molecules at the air-salt interface as a variation of time, observed in real-time using SFG kinetics measurements. Reprinted with permission from Li et al., *Langmuir* **35**, 13815-13820 (2019). Copyright (2019) American Chemical Society.<sup>73</sup>

Yang et al. studied extensively the complex formation and orientation changes in a heterodimeric G-protein  $\beta_1\gamma_2$  subunits on associating with the  $G\alpha$ -subunit upon interacting on the model membrane coated over the  $\text{CaF}_2$  substrate at the solid-aqueous interface (represented in Figure 1.10). They introduced a methodology to study such membrane proteins in-situ and observed the subunit re-orientation in absence and presence of protein-protein interactions (PPIs) by observing the polarization-dependent amide region in SFG spectroscopy. They concluded that the PPIs do not show significant change in the orientation of the  $G\beta_1\gamma_2$  protein.<sup>63</sup> Their work provided an in-depth consideration of the orientational parameter significance during protein-protein and protein-lipid interactions in real time using both polarization-dependent SFG and ATR-FTIR spectroscopies.

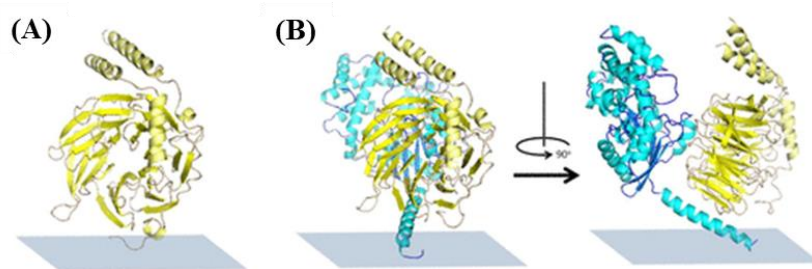


**Figure 1.10** Illustration of the experimentally determined structural arrangement and membrane orientation of (A)  $G\beta_1\gamma_2$ , and (B)  $G\alpha_i\beta_1\gamma_2$ . The  $G\alpha_i\beta_1\gamma_2$  protein complex is represented in two views, images arranged at  $90^\circ$  with respect to each other. The membrane plane is shown in blue rectangle form. Reprinted with permission from Yang et al., *J. Am. Chem. Soc.* **135**, 5044-5051 (2013). Copyright (2013) American Chemical Society.<sup>63</sup>

Another work performed with a more complex system encompass the competitive study between BSA adsorption and the adhesion of hydrophobic and hydrophilic bacteria on well-ordered octadecanethiol (ODT) self-assembled monolayer (SAM) coated substrate (Figure 1.11), studied using SFG and fluorescence microscopy.<sup>74</sup> The interaction of hydrophilic and hydrophobic bacteria with the ODT-SAM surface was differently observed in terms of the flattening or a rise in the terminal methyl contributions in the SFG spectra. With the presence of amphiphilic BSA coating over the ODT-SAM, the strength of bacterial adhesion on ODT-SAM substrate gets reduced, producing results similar to that of pristine BSA-coated ODT substrate. However, the pre-adsorbed BSA over hydrophobic bacterial cell wall helps in associating them with the BSA-coated ODT substrate, as observed from the reduction in the methyl flattening effect in comparison to that observed for bare bacteria and BSA-coated ODT interactions. Hence, they found that the BSA coated layer exhibits a potent antimicrobial effect, where they tend to compete positively with the bacteria to adhere over the ODT-SAM grafted surface.<sup>74</sup>

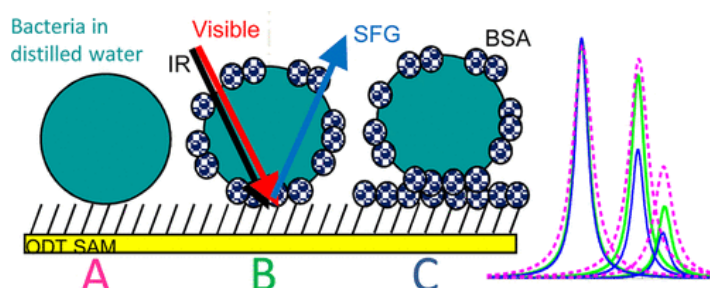


**Figure 1.11** Graphical image of (A) hydrophobic, and hydrophilic bacteria in (B) absence, and (C) presence of BSA-coated ODT-SAM surface. SFG spectra shown towards the right side for the respective stages of bacteria interactions with surface. Reprinted with permission from Bulard et al., *Langmuir* **28**, 17001-17010 (2012). Copyright (2012) American Chemical Society.<sup>74</sup>

Protein molecules are widely utilized for various analyte- or immuno-sensing applications and in identifying several molecular recognition events.<sup>11,36,39</sup> On similar road, Lis and Cecchet<sup>39</sup> demonstrated the potential of SFG spectroscopy to provide unique fingerprint features of the bio-recognition process. The antibody and antigen protein recognition were established over a solid-supported hybrid lipid bilayer platform. The approach of reconstructing a difference SFG spectra depicted the appearance of a new type of interactive vibrational mode at 3230 cm<sup>-1</sup> specific to the peptide bond frequency of antibody molecules. It was identified to have exclusively originated from the bio-recognition event, depicting a better organization of molecules after the molecular recognition.<sup>39</sup>

#### **1.4.2 SFG Studies on Interfacial Influence of DNA Molecules**

Deoxyribonucleic acid (DNA) is the basic foundation of all living beings. This double helical structure consists of spirally wound polynucleotide chains arranged in an antiparallel fashion. Each nucleotide consists of a phosphate group facing outwards, a deoxyribose sugar residue existing in the backbone and four different nucleic bases (adenine, guanine, cytosine and thymine) constituting its core.<sup>75</sup> It is the sequence in which these different nucleic bases are arranged that makes the DNA sequence unique with variable expression at the genetic level. The considerable flexibility of DNA in the physiologically relevant conditions allows the sequence of bases to be readily recognized by a variety of protein molecules, ligands (e.g., drugs or metabolites) and provides an indispensable opportunity to replicate and transcribe its coded information. Small local variations as a result of changes in the near neighborhood, i.e., under the influence of ions, temperature, or the presence of free radicals around the native B-form of DNA, ultimately lead to a large variety of geometries. Additionally, realizing DNA in terms of a programmable material and utilizing its molecular recognition properties for technological evolution provides an unprecedented approach toward developing highly structured materials for nanoscale applications. Thus, an understanding needs to be developed in the direction of how DNA dynamically organizes itself in the heterogeneous environment that it encounters.

**Identifying ssDNA and dsDNA arrangement.** SFG spectroscopic studies on DNA were initiated by Sartenaer et al.<sup>76</sup> by evaluating the monolayer of ssDNA coated over the

platinum (Pt) surface, with a view of the applying the obtained interfacial information for fabricating micro-arrays or developing DNA-based nanomachines. The DNA sample is prepared in phosphate buffer solution (PBS) and tris-EDTA (TE) solutions and the SFG spectra is acquired from the air-solid interface. The authors observed the intercalation of DNA monolayer with TE, while the PBS-immersed Pt coated with DNA monolayer represented the characteristic interfacial profile of DNA molecules observed using SFG. The analysis was performed in CH-stretch region based on the aliphatic chain ordering at the interface.<sup>76</sup> Howell and co-workers also probed the single-stranded DNA (ssDNA) monolayer, chemically adsorbed over gold wafers exposed to the air, D<sub>2</sub>O and PBS buffer.<sup>35</sup> A prism (half cylindrical CaF<sub>2</sub> crystal) geometry was localized on the top of the sample. A 5-member of nucleotide sequence of thymine (T<sub>5</sub>) and adenine (A<sub>5</sub>) were evaluated, and the contributions from the CH stretch as well as amide I regions, were analyzed. Based on the observed methyl stretching modes (in-plane and out-plane) and assessing the ratio of these modes for methyl orientation analysis, the thymine films were found to be highly ordered in air, slightly tilted in D<sub>2</sub>O solution (Figure 1.12), and randomly oriented in PBS. Contrarily, the adenine films presented a similar profile in D<sub>2</sub>O and PBS solution interfacing with the gold surface. They also carried out SFG studies to differentiate between the thiol and non-thiol linked modified T<sub>5</sub> films with respect to the arrangement and orientation of the carbonyl groups to the surface by probing the amide I region.<sup>35</sup> Hence, the significance of SFG was substantiated in extracting the information about molecular orientation of ssDNA fabricated films over the solid surface.

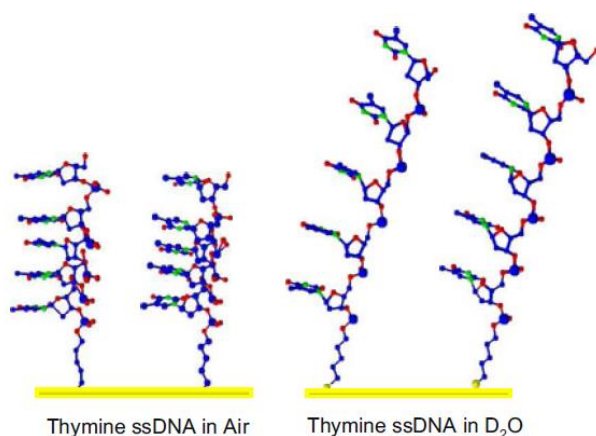


**Figure 1.12** Pictorial depiction of the arrangement of thymine DNA single strands associated with the CaF<sub>2</sub> substrate towards air and in D<sub>2</sub>O, at the interfacial region.



Reprinted with permission from Howell et al., *Biointerphases* **3**, FC47-FC51 (2008). Copyright (2008), American Vacuum Society.<sup>35</sup>

They further extended their work on DNA to understand the hybridization pattern of thymine and adenine homo- and di-block-oligonucleotides using SFG and secondary characterizing techniques.<sup>77</sup> By extracting the resonant SFG spectra in the CH-stretch region, the authors contemplated that the long T<sub>25</sub> chain depicted a loss in molecular ordering on the addition of complementary A<sub>15</sub> due to partial hybridization. The di-block A<sub>5</sub>T<sub>15</sub>, however, revealed an increase in ordering after hybridization.<sup>77</sup>

**Factors regulating DNA structural arrangement.** DNA hybridization and its functionality can be either hindered or initiated by several factors such as metal ion addition and temperature. Asanuma et al. investigated the extent of structural distortion of the silicon surfaces with the order of metal ion-DNA affinities.<sup>78</sup> This was done by probing the structural changes of DNA-linker monolayer on the silicon surface from the molecular orientations and conformational variation of DNA molecules over the linker monolayer through SFG spectroscopy. The analysis was based on the methyl and methylene peak intensity ratio values of the linker monolayer. Based upon the DNA-cation affinity ( $Mg^{2+} > Ca^{2+} > K^+ \sim Na^+$ ), they correlated that stronger the affinity of metal cations to DNA, more the structure of the underlying linker monolayer will be disrupted (Figure 1.13). Additionally, the effect of DNA hybridization showed a reverse trend in the presence of metal-cations on the integrity of the linker monolayer. Herein, they noted the major involvement of the divalent cations in masking the negative charges on the DNA backbone, which relatively minimized the disruption of the underlying surface. Thus, their approach mainly involved indirectly probing the effect of metal ions on the self-assembly of DNA molecules at the linker monolayer on the silicon surface.<sup>78</sup>

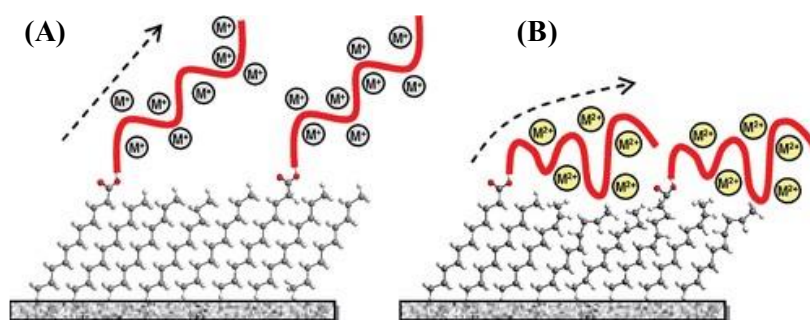


**Figure 1.13** Scheme for studying the linker monolayer structural ordering as a function of ssDNA geometry in presence of (A) monovalent cations, and (B) divalent cations.

Reprinted with permission from Asanuma et al., *J. Am. Chem. Soc.* **130**, 8016-8022 (2008). Copyright (2008) American Chemical Society.<sup>78</sup>

Walter and co-workers reported a first experimental quantification of the number of  $\text{Mg}^{2+}$  ions associating with the surface linker-functionalized thymine oligonucleotides ( $\text{T}_{40}$ ) in aqueous conditions.<sup>79</sup> They also evaluated the DNA duplex stabilizing tendency of  $\text{Mg}^{2+}$  ions and its role in the DNA hybridization process (Figure 1.14). Depending on the methyl group ordering, as interpreted through the SFG spectral peaks, the amplitude ratio of asymmetric to symmetric methylene groups were considered as a function of magnesium ion concentration. A noticeable drop in the intensity ratio was found for the  $\text{T}_{40}$  oligomers with the addition of magnesium ions, which was attributed to the structural re-ordering of the oligonucleotides. The results represented a collapsed structural state once  $\text{Mg}^{2+}$  binds with the oligonucleotide, causing minimization in the coulombic repulsions among DNA strands.<sup>79</sup>

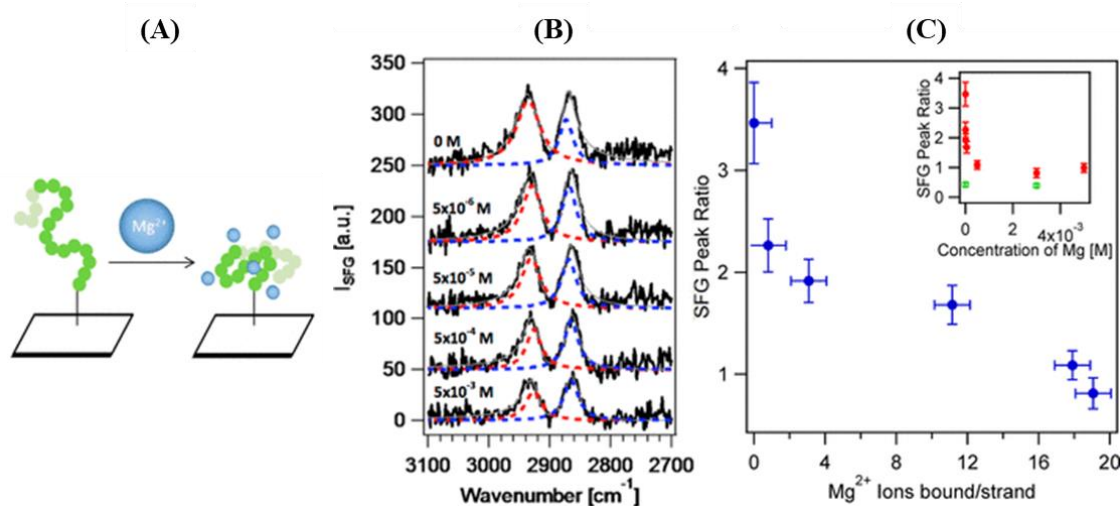


**Figure 1.14** (A) Pictorial illustration of the probable structural arrangement and collapse of  $\text{T}_{40}$  ssDNA in presence of  $\text{Mg}^{2+}$  ion binding. (B) SFG-VS spectra of ssDNA as a function of  $\text{Mg}^{2+}$  concentration. Here, the blue dotted peak fit depicts symmetric methyl stretch and red dotted fit represents asymmetric methyl stretch mode. (C) Quantitative plot of the symmetric and asymmetric peak ratios with  $\text{Mg}^{2+}$  addition. The inset in this panel shows plotted points for  $\text{T}_{40}$  ssDNA (red points) and linker (green points). Reprinted with permission from Walter et al., *J. Am. Chem. Soc.* **135**, 17339-17348 (2013). Copyright (2013) American Chemical Society.<sup>79</sup>

Several DNA immobilization technologies require a thermal cycling-based addition or removal of the strands from the surface or for analyte binding applications. This aspect was explored by Li and co-workers, where the thermal stability of the immobilized DNA strands was studied at the silica-buffer interface using SFG



spectroscopy.<sup>80</sup> They worked with the surface-linked polythymidine (T<sub>15</sub>) and its complementary polydeoxyadenosine (A<sub>15</sub>) and monitored the CH-stretching region. A significant methyl ordering for the single strand T<sub>15</sub> were observed at both the silica-air and silica-buffer interface in SFG spectra. The hybridization of T<sub>15</sub>-functionalized silica with A<sub>15</sub> at the silica-buffer interface showcased an enhancement in the methyl intensity contribution, which was related with an increased orientational ordering of thymine with its subsequent hybridization. The temperature-variation experiment (20°-60° C) displayed that the hybridized duplex (T<sub>15</sub>:A<sub>15</sub>) was more sensitive towards the temperature fluctuations, as the methyl fermi contribution decreased with the temperature increment. The duplex annealing was further monitored, demonstrating a change in intensity of respective methyl modes and was ascribed to an incomplete hybridization of the DNA strands.<sup>80</sup> McDermott et al. provided an unprecedented observation of the presence of a chiral superstructure of water molecules surrounding the double-helical DNA structure, as observed with a chiral SFG-VS technique.<sup>81</sup>

With the discussion of DNA-based work performed primarily using SFG spectroscopy, both the ssDNA orientation and the hybridization of the duplex were descriptively evaluated at distinct surfaces. These studies, however, can be further expanded to understand the duplex structure stabilization under various factors, several complex binding states of DNA, and the involvement of DNA in various mechanistic approaches at the interface (esp. at air-aqueous interface).

### **1.4.3 Studying Nanomaterials at Interface using SFG-VS**

Nanomaterials are considered as the small dimensioned materials/particles reigning between 1 to 1000 nm and hence, proffer an increased surface functionality in a particular volume due to its nano-scale dimensions.<sup>43,82</sup> Nanoparticles bear a high surface-to-volume ratio in comparison to the macroscopic materials, and as a result, project distinct surface energy and other physico-chemical properties.<sup>82,83</sup> Physically, nanoparticles are similar to biological molecules in size, and, therefore, are capable of altering their structure and chemical properties with respect to their immediate environment. These nano-dimensioned materials or particles tend to adsorb spontaneously at the high energy surfaces or interfaces, which ultimately lowers the free-energy state of nanomaterials.<sup>43,82,83</sup> Hence, it is necessary to understand the impact and tuning of the

surface or interface chemistry in the presence of nanoparticles or nanomaterials. Utilizing the monolayer and sub-monolayer sensitivity of the SFG-VS, many studies have been conducted by several research groups to characterize the nanoparticles at the interface.

Wang et al. studied the molecular moieties present on the nanoparticulate  $\text{TiO}_2$  freshly fabricated on the  $\text{CaF}_2$  substrate, probed by SFG-VS.<sup>84</sup> They were able to identify for the first time, the presence of a trace hydrocarbon layered over the  $\text{TiO}_2$  fabrication along with the surface hydroxyl groups (-OH), after conducting the fabrication procedure. The fabricated film was exposed to UV light to probe the characteristic variations of the film at the molecular-level. It was perceived that the UV treatment causes the hydrocarbon signatures observed in the CH-stretch region of the freshly prepared  $\text{TiO}_2$  film to vanish completely, which aligns with the  $\text{TiO}_2$ -based photocatalytic process. The OH-stretch region features, however, presents an enhanced contribution from the weakly coordinated OH-stretch region after UV-treatment, which arises due to the presence of low density of OH molecular groups over the film surface. This suggested the presence of surface heterogeneity of the fabricated nanoparticulate  $\text{TiO}_2$  films.<sup>84</sup> Another study on the globular sized particles (with 50-200 nm) of anatase  $\text{TiO}_2$  fabricated over  $\text{CaF}_2$  window is conducted by Hosseinpour et al. at the  $\text{TiO}_2$ -water interface.<sup>85</sup> Their phase-resolved SFG data also demonstrated the superhydrophilic character of  $\text{TiO}_2$  coated surface irradiated with UV light, where the dipole moments of OH-groups were found to orient oppositely. The ab initio MD analysis elaborated that the weakly donating H-bonds were attributed to the chemisorbed -OH groups, while the physisorbed water molecules are represented by the strongly donating H-bond. Thus, they were able to correlate the two types of adsorption schemes of water molecules via the strength of H-bonding interactions depicted over the  $\text{TiO}_2$ -coated surface.<sup>85</sup> Both of these studies indicated that the nanoparticle characterization at the interface is carried out either by observing the presence/absence of molecular contaminants or by discerning the spectral signatures of the molecular moieties adsorbed on the nanomaterial or nanoparticle surface, using SFG-VS. These parameters ultimately determine the electrical, chemical, biological or physical implications of nanoparticles, and also rely on the nanoparticle type i.e., organic or inorganic nanoparticles.<sup>82</sup>

Considering the importance of adsorbed organic molecules or molecular functionalities at the surface of nanoparticles, the influence of geometry of nanoparticles

over the chemisorbed alkanethiol conformation and vice-versa were examined by Weeraman and co-workers (shown in Figure 1.15).<sup>86</sup> They studied the spherical-shaped gold nanoparticles of different diameter, with SFG, and observed a clear trend of increment in the intensity ratio of methylene (CH<sub>2</sub>) vs methyl (CH<sub>3</sub>) symmetric stretches with respect to a reduction in the particle size of gold nanoparticles. This illustrates that as the surface curvature of gold nanoparticles gets reduced, the conformation of adsorbed dodecanethiol changes from an all-trans to gauche conformation. The insight would help in understanding the electron-transferring capability of functionalized nanoparticles with an optimum dimension for several applications.<sup>86</sup>

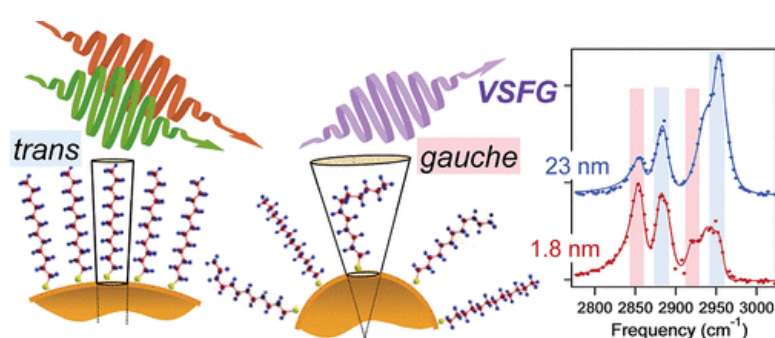


**Figure 1.15** Illustration of the dodecanethiol ligand chain length bound over the spherical gold nanoparticle surface, representing the conical space occupied by the gauche defect formation. The SFG spectra shown towards right depicts the size-dependent SSP spectra of dodecanethiol bound to nanoparticles in CH-stretch region. Reprinted with permission from Weeraman et al., *J. Am. Chem. Soc.* **128**, 14244-14245 (2006). Copyright (2006) American Chemical Society.<sup>86</sup>

Some oxide-based nanoparticles are known to involve in catalytic reactions due to their differing oxidation states in the aqueous media. Ceria nanoparticles (CNPs) were investigated by Lu et al.,<sup>87</sup> where the impact of different oxidation states of the nanoparticles on the ligand binding and the type of bonding involved were studied. These nanoparticles were fabricated over CaF<sub>2</sub> surface which is exposed to the deuterated acetic acid solution after assembling within the experimental cell. The spectral analysis in the bending region presented the deprotonation state of neutral acetic acid molecules at low pH value before adsorbing to oxidized Ce<sup>4+</sup> nanoparticle surface and the mixed oxidation state i.e., Ce<sup>3+</sup> and Ce<sup>4+</sup>. The polarization-dependent SFG spectra presented the symmetric stretching modes ascribed to the bidentate chelating and bridging binding species of the partially reduced nanoparticles, which could readily bind with the ligands. The chelated species signature gets reduced, however, for the fully oxidized ceria nanoparticles. Their results showcased the significance of SFG in comprehending the surface reactivity of

these nanoparticles and their combination with molecular adsorbates (as depicted in Figure 1.16).<sup>87</sup>

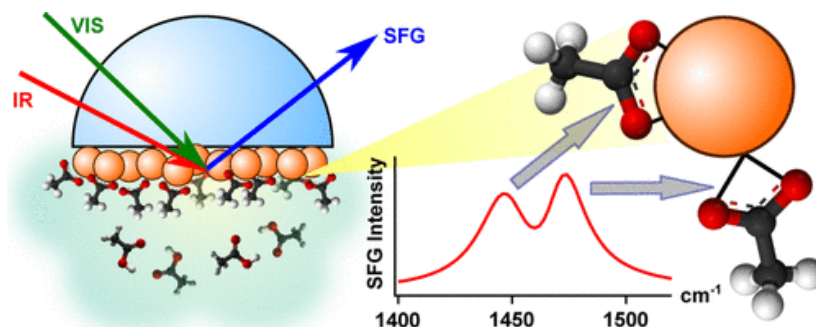


**Figure 1.16** SFG-VS characterization of the binding structure and the oxidation state mechanism of CNP surfaces on binding deuterated acetic acid in an aqueous media, at the solid-aqueous interface. The graphical representation suggests the bidentate bridging and chelating modes of interaction of carboxylate group with CNPs. Reprinted with permission from Lu et al., *J. Phys. Chem. C* **117**, 24329-24338 (2013). Copyright (2013) American Chemical Society.<sup>87</sup>

Considering the need to understand the arrangement of molecular species over nanomaterial surfaces for various technological applications, Watson and co-workers employed SFG-VS to probe the chemical features and interfacial ordering of octadecylamine ligands at the CdSe quantum dots (QDs) surface.<sup>88</sup> The washing of QD surface conducted (with polar protic and aprotic non-solvents) to remove the bound ligand molecules were sensitively probed using SFG-VS by analyzing the extend of disordering introduced into the packed ligand molecular structure, as observed in the CH-stretching region of the spectra based on the trans to gauche-conformation transition (see Figure 1.17). Their work demonstrated that even after multiple steps of washing, the ligand removal does not get completed, and the interfacial results thus, highlighted the significance of SFG in extracting the presence of surface-specific molecular entities in such kind of practical approaches.<sup>88</sup>

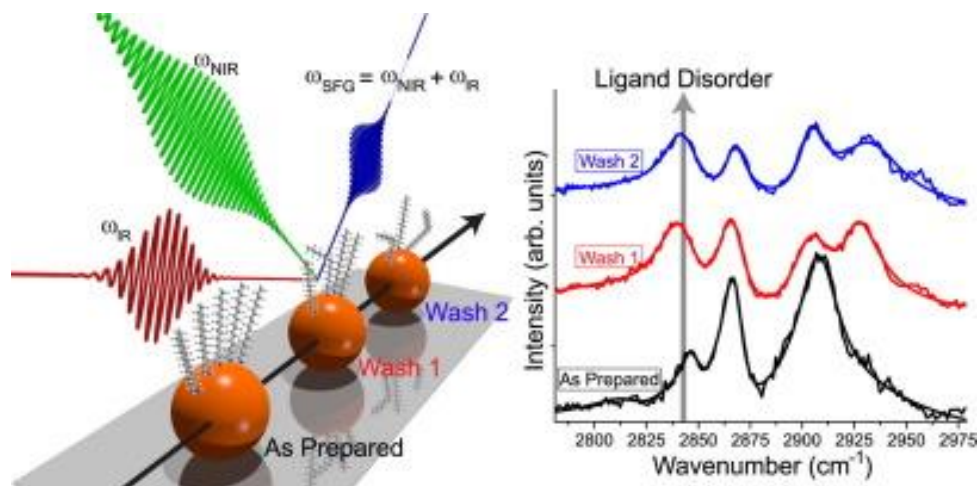


**Figure 1.17** Schematic of the experimental investigation of CdSe QDs fabricated surface and the sensitivity of SFG to the introduction of disorder of ligand molecules upon subjecting to surface washing. Reprinted from *J. Colloid. Interface Sci.* **537**, Watson et al., Probing ligand removal and ordering at quantum dot surfaces using vibrational sum frequency generation spectroscopy, 389-395, Copyright (2019), with permission from Elsevier.<sup>88</sup>

#### 1.4.4 Probing the Interfacial Influence of Nano-Bio Interactions

Studies related to nanoparticle characterization at interface discussed in previous section, highlighted the adaptability and potency of SFG spectroscopic tool in probing the structural and chemical state of nanomaterials, and the dynamic re-arrangement of bound ligands at distinct interfacial regions. In lieu of the practical usage of engineered nanoparticles for developing consumable goods, material coatings, energy technologies, environmental issues, or in bio-medical applications, it is vital to understand and evaluate their physico-chemical interactions with different biomolecules. The versatility of SFG-VS has prompted to investigate the role of these nanoparticles in realistic systems involving biological molecules, where they associate together to form complex interfaces. Most of the interfacial examination of nanoparticle interactions with biological systems have been performed with the modeled cell membranes or on lipid-supported framework.<sup>89-91</sup> These investigations explained an important role of the physico-chemical properties of nanoparticles in inducing the flip-flop of lipid molecules in a modeled cell membrane, influencing the structural re-organization both bilayer and associated water molecules, and impacting the surface geometry of the interfacially adsorbed surfactant monolayer. Although, a rigorous evaluation of nanoparticle interaction with lipid molecules or cell membrane model is in progress, not much studies have been conducted

in the direction of analyzing nanoparticle interactions with protein and DNA molecules at the interface.

Studies reported on the nanoparticle-protein and -DNA interactions evaluated the pH-dependent adsorption states of these biomolecules and their probable conformation on the nanoparticle surface.<sup>92-98</sup> These investigations enrolled surface/interface-specific techniques such as CARS, ATR-FTIR, synchrotron-based techniques, QCM, AFM, SPR, and LC-MS/MS analysis which offered the interfacial probing with a depth scale ranging from ~2-40 nm of the sample surface. SFG-VS could offer a simultaneous probing of the dynamic and the equilibrium states of the molecular species forming a non-centrosymmetric interfacial region. SFG-VS concomitantly gathers the structural information, spatial arrangement, and molecular orientation with ~1 nm scale specifically from the interface, in a single experimental model itself.<sup>32,34</sup> So far, there has been only one report where SFG-VS is employed in a total-internal reflection (TIR) configuration to obtain insights towards the biomolecular-recognition process and bio-sensing design by using gold nanoparticles (AuNPs), as published by Tourillon et al. in 2009.<sup>99</sup> They fabricated a well-assembled AuNP thin-film over the silane monolayer casted on the quartz surface. A biocytinylated thiol (BioSH) was then covalently associated with the AuNP fabricated surface, which is then utilized for recognizing avidin protein molecules. Depending on the molecular ordering and conformational sensitivity of SFG towards methyl features, the biocytin-avidin recognition process is probed (shown in Figure 1.18).<sup>99</sup> Apart from such studies, there is a need for more thorough investigations to be carried out for understanding the physico-chemical aspects of nano-bio interactions and their impact on the nearby surroundings (or vice-versa) at the interface, for their implication in several practical issues and to establish the potential of interface-specific SFG-VS tool for examining such complex interactions at distinct interfaces.

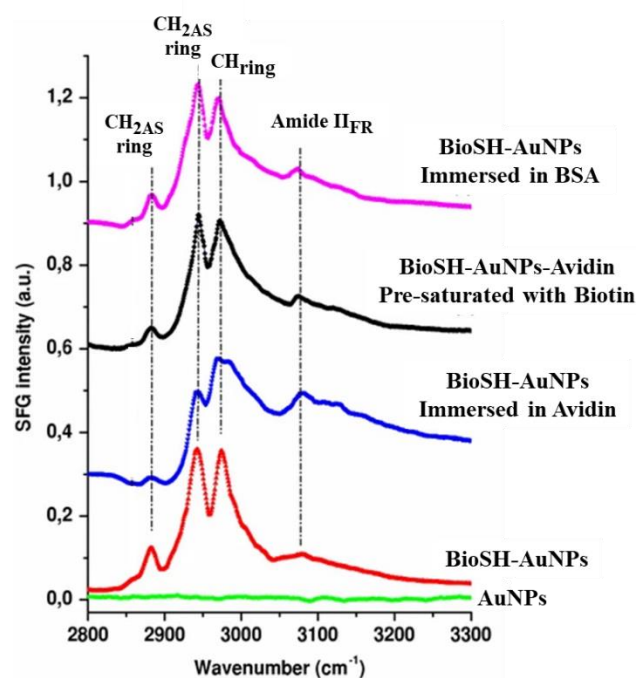


**Figure 1.18** SFG-VS spectra in TIR mode of the assembled AuNPs, BioSH-adsorbed AuNPs, BioSH-adsorbed AuNPs immersed in avidin solution, pre-saturated with biotin, and immersed in BSA only. Reprinted and modified with permission from Springer Nature, *J. Mater. Sci.* **44**, 24329-24338 (2009). Close-packed array of gold nanoparticles and sum frequency generation spectroscopy in total internal reflection: a platform for studying biomolecules and biosensors, Tourillon et al., Copyright (2009).<sup>99</sup>

## 1.5 Research Gaps and Motivation

In previous sections, we reviewed extensively the distinct behavior of biomolecules, nanomaterials and the impact of bio-nano bridging over the surrounding media at a variety of interfaces, studied using SFG-VS. Although the outcome of the investigations conducted has been compelling in understanding the fundamental molecular processes involved, several aspects yet remain unaddressed. Hence, understanding the structural organization of the basic biomolecules is highly important for their consideration as a programmable material in distinct device and surface coating applications for analyte recognition, where most of these biomolecules appear at the air-water interface. The potential aspects that remained to address include the followings:

- Localized protein adsorption dynamics in real-time at air-water interface, where the protein molecules are investigated in their native state i.e., without any buffering conditions.

- Understanding the probability of synchronization among the biomolecular (protein and DNA) interfacial adsorption (expressed through the characteristic vibrational modes of their hydrophobic moieties) and the structural perturbations in the interfacial water network.
- The interfacial molecular characterization of DNA adsorbed at air-aqueous interface is relatively unexplored much using SFG-VS within a broad IR spectral range including both CH- and OH-stretch regions.
- In-situ characterization of the molecular topology of imprinted surfaces constructed using protein molecules, where SFG-VS could directly substantiate the memory of imprinted surfaces for the molecular targets for sensor applications. This approach has not been conducted before with a macromolecule-based surface imprinting, using interface-sensitive spectroscopy.
- The characterization of nanoparticle (both organic and inorganic nanoparticles) behavior at air-aqueous interface has not been explored in details, which could be of paramount significance in determining their efficacy in various biomedical applications. Aqueous interfaces are ubiquitously enrolled in such aspects, and therefore of prime importance to explore in this arena.
- How do the nanoparticles modulate their physico-chemical properties and, the conformation and molecular orientation parameter of biomolecules during nano-bio interactions at the air-aqueous interface?
- The imprinting of these nano-bio associations could also be well understood secondarily by probing the impact of their interactions over the structure of water molecules at the interface. Studying such complex models could aid in understanding the crucial role of interfacial water molecules as a mediator and a reporter in steering the key molecular interactions.

## 1.6 Aim and Objectives

The key objective of our thesis work is to investigate the interfacial behavior of biomolecules from the fundamental perspective and their interactions at the modeled air-aqueous and air-solid interfaces. We have analyzed the biomolecules in presence of different nanomaterials i.e., nature-derived two-dimensionally fabricated nano-scale polymer, inorganic nanomaterials, and organic polymeric nanoparticles. An interface-dependent resonant molecular probing is regarded to be the essence of our work, since the



active molecular/functional groups are mostly projected at the surface/interface and decide the overall activity at the macro-level. Here, we targeted to specifically explore the nanomaterial behavior in presence of biomolecules in its vicinity, or vice-versa, at air-aqueous interface.

In order to extract the detailed molecular-level insights, we have employed vibrational sum frequency generation (VSFG) spectroscopy to probe both air-solid and air-aqueous interface. Additionally, VSFG spectroscopy exclusively provides information about the bio-nano-dependent impact over the water molecular network at the aqueous interface. We have also extended our studies on tensiometry, dynamic light scattering (DLS), zeta-potential, and ATR-FTIR spectroscopy to gather information related to the bulk-features. To achieve our objectives, the following plans have been designed for the current thesis work:

1. Interfacial adsorption mechanism of biomacromolecules (protein and double-stranded DNA) and their impact over the water molecular network at the air-water interface.
2. Fabricating two-dimensioned imprinted polymeric surfaces to recognize bovine hemoglobin protein molecules by probing the air-polymer interface.
3. Monitoring the interfacial recognition event among protein molecules mediated by tungsten disulfide quantum dots at the air-aqueous interface.
4. Elucidating the molecular adsorbing characteristics of polymeric nanoparticles and their implication for understanding binding properties with double-stranded DNA.

## **1.7 Outline of the Thesis**

The current thesis is organized into seven chapters which underlies the significant role of the interface and decoding the molecular-scale processes involved in phase-separation, molecular interactive forces, surface tensiometry perturbations, surface adsorption propensity, molecular kinetics, hydrophilic-hydrophobic tendency of molecules, etc. With this target, we have carried out our work to understand the biomolecular interfaces and interfacial wobbling during nano-bio associations using both bulk- and interface-specific techniques. To present this approach, the accomplished work has been structured into the following chapters within the thesis:

## **Chapter 1: Introduction**

This chapter involves a brief discussion about the surface and interface, distinguishing between bulk-phase and interface, bio-interfaces, and the correlation among the nanomaterials and biomolecules. A brief discussion is provided over different bulk-/linear-optics-based experiments, the interface-sensitive non-linear (NL) optical tools and sum-frequency generation vibrational spectroscopy (SFG-VS) based on the second-order NL optical process. A crucial view-point is presented about how the notion of bridging nanomaterials and biomolecules would open a new window towards several different technological perspectives. These implications enroll a basic understanding about the universal fundamental forces of interactions (inter- or intra-molecular). A literature survey specific to the protein and DNA molecules as model biomacromolecules, nanomaterials, and nano-bio associations is then presented which are investigated using SFG vibrational spectroscopic technique. The associated research questions are also discussed which are still unexplored in this field. The last section of this chapter confers the research objective and the organization of the current thesis work.

## **Chapter 2: Experimental theory and methods**

This chapter elaborates on different experimental techniques and the related theoretical details of their functioning which have been utilized to explore both the bulk-phase and interfacial behavior of biomolecules, nanomaterials and the impact of their association. Here, we have explained in-brief the linear and non-linear optical process, surface tensiometry, zeta-potentiometry set-up, ATR-FTIR, and SFG-VS, which are the potential techniques utilized in the current thesis work.

## **Chapter 3: Interfacial adsorption of biomacromolecules and their impact on water molecular network at the air-water interface**

This chapter includes the investigation of our first research problem involving the two bio-macromolecular system i.e., BHp protein molecules and double-stranded DNA (dsDNA) molecules. The study aims to recognize their interfacial molecular behavior, adsorption mechanism, and their kinetics. This chapter includes two sub-sections covering independent studies on both protein and DNA molecules, where we aim to address the following aspects:

- Real-time investigation of protein surface coverage and its influence over the interfacial arrangement of protein molecular structure in pristine conditions.
- Impact of real-time adsorption kinetics of BHB protein on the surrounding water structure at the interface, at the isoelectric point of the protein molecules.
- Probing the molecular signatures of dsDNA at the air-water interface in both CH- and OH-stretch regions. Here, the structural behavior of dsDNA is studied as a function of DNA concentration and under the influence of free-radical (i.e., hydrogen peroxide-  $\text{H}_2\text{O}_2$ ) concentration.
- Our target to probing the influence of  $\text{H}_2\text{O}_2$  on the interfacial adsorption dsDNA stems from the widely known analytical, radio-labeling, and micro-electrophoretic technologies, used for conducting DNA adsorption procedures for molecular separation or sensing procedures.<sup>100-102</sup> These procedures could render the generation of  $\text{H}_2\text{O}_2$  in the aqueous media due to the oxidation-reduction reaction process, as stated in several reports.<sup>103,104</sup>  $\text{H}_2\text{O}_2$  is known to potentially impact and break the dsDNA structure.<sup>105,106</sup> We aim to investigate here the direct influence of  $\text{H}_2\text{O}_2$  on the interfacial molecular behavior of dsDNA.

The results of BHB adsorption kinetics (discussed in section 3.3) with concentration displayed that the unfolding of the BHB molecule is significantly high for low surface coverage in comparison to the higher bulk concentration, which is limited due to increased protein-protein interaction. The time-dependent SFG studies at two different frequencies in the fingerprint region elucidated a synchronized behavior of protein adsorption with the structural variations among interfacial water molecules. However, the conformational changes in the protein structure due to the denaturation process stay for a long time, whereas the changes in water structure reconcile quickly.

The investigations of dsDNA structure at air-water interface (discussed in section 3.4) showcased a concentration-dependent surface coverage and molecular ordering of methyl features of DNA molecules. The surrounding water molecular arrangement also gets enhanced with DNA concentration. The alkyl features of DNA were seen to be disrupted significantly with  $\text{H}_2\text{O}_2$  addition, while the water molecular ordering showed subtle perturbation. These studies could ingrain the molecular-level insights and the dynamics of biomolecules (protein and dsDNA) at the air-water interface and could be potentially used for developing functional surfaces/interfaces.

## **Chapter 4: Fabricating molecularly imprinted polymeric surfaces for recognition of bovine hemoglobin protein molecules at the air-polymer interface**

This chapter explores the molecular-level underpinning in constructing a biomimetic surface for protein sensing applications. Here, we have constructed a bio-inspired polydopamine-based molecularly-imprinted polymer (MIP) substrates for imprinting the BHb protein as model template molecules. The BHb templates were then investigated for their recognition process over the cavity-laden MIP surfaces using SFG-VS. Since the molecular recognition of template molecule is largely governed by the organization of polymer matrix, molecular-level insight on the mechanism of MIP and non-imprinted polymer (NIP) formation at each step has been investigated at the interface. Here, we target to address the following parameters:

- Considering the time-dependent NIP and MIP film fabrication, we intend to tailor the specific functional groups of pre-polymerization solution and its subsequent fabrication is observed via SFG at the polymer-film interface, which is relevant for BHb imprinting.
- We aim to fabricate the biomimetic imprinted surface without utilizing strong radicals as initiators or without undergoing any substrate modification for efficient imprinting of the surface.

SFG-VS could directly probe the presence of protonated or non-protonated methyl group contribution in the spectra from MIP and NIP surfaces. The washing and subsequent re-binding potential of MIPs for templates were evaluated via methyl and methylene intensity ratio values indicating an appreciable template re-binding capacity observed within MIP cavities. The present study authenticates the potentiality of an interfacial-specific SFG-VS as a label-free technique for characterizing the biomolecular recognition process using biomimetic polymer surfaces with lesser sample amount and smaller fabricating surface area of the MIP substrates.

## **Chapter 5: Monitoring the protein-protein interactions mediated by tungsten disulfide quantum dots at the air-aqueous interface**

In this chapter, we advanced towards studying a complex model system involving protein-protein interactions (PPIs) and their modulation in the presence of a tungsten disulfide quantum dot (WS<sub>2</sub> QDs) at the air-water interface. We targeted to fulfill the following potential research gaps:

- Studies related to the interaction of WS<sub>2</sub> as quantum dots with protein molecules have not been explored yet. The majority of the investigation, revolves around WS<sub>2</sub> as two-dimensioned nanomaterials.
- Elucidating the modulation of PPIs under the influence of quantum dots has not been conducted as they pose to be a more complex system to investigate. We aim to investigate this paradigm with the interfacial-sensitivity and molecular orientational probing attribute of SFG-VS.
- Since water molecules are known as potential reporters or mediators in carrying out molecular interactions, it proves to be an essential indicator of nano-bio interactions.

Considering our goal, we conducted our study with antibody (Ab) and antigen (Ag) protein molecules as a function of their concentration in the presence and absence of WS<sub>2</sub> QDs. We also investigated the influence of nano-bio associations over the methyl group orientational pattern. Both binding selectivity and binding sensitivity of Ab and Ag proteins individually and in combination (as Ab-Ag) in presence of WS<sub>2</sub> QDs were observed in terms of prominence of methyl features and perturbations in water molecular ordering at the air-water interface. The orientational analysis depicted reorientation of hydrophobic methyl groups of Ab-Ag from  $\sim 40^\circ$  to  $\sim 28^\circ$  about the surface normal upon introducing WS<sub>2</sub> QDs, as observed at the air-water interface. The work aims to strongly build upon the fundamentals of nano-bio interactions for fine-tuned sensing applications.

## **Chapter 6: Elucidating the molecular structure of polymeric nanoparticles and its implication for DNA binding**

This chapter includes our final research work focusing on probing the behavior of hydrophobic modifications of a water-soluble polymer, branched polyethylenimine (b-PEI). Hydrophobic modification tends to regulate the physico-chemical properties of the molecules and is responsible for propelling various fundamental associations from bio-macromolecular assembly and protein folding to chemical reactions, material fabrication and designing. The interfacial adsorption process of the molecules is crucially involved in many application areas like drug loaded polyplex uptake via adsorptive endocytosis process, molecular encapsulation, cosmetic development, industrial-scale separation processes, microfabrication technologies and designing sensing or catalytically active surfaces, etc. Here, our prime rationale behind this work is:

- Understanding the interfacial behavior of the polymeric nanoparticles constructed from the widely used PEI polymer which is hydrophobically modified with the aromatic groups.
- Exploring the significance of tailored properties of polymeric nanoparticles in binding dsDNA in comparison with that of unmodified b-PEI polymer.

Hence, the modified polymer was assembled as organic nanoparticles (ONPs) in the buffered aqueous media, and was assessed for its surface/interfacial behavior using surface tensiometry and SFG-VS. The increased molecular surface coverage of ONPs were associated with an increased dipolar alignment of the interfacial water molecules. The ONPs were then evaluated for their DNA binding potency, and it was observed that varying the dsDNA concentration influenced the molecular structure and properties of NPEI-ONPs as observed from SFG-VS and zeta-potential measurements. The viscometry, DNA thermal denaturation, and ATR-FTIR measurements provided information about the conformational transitions in the DNA helical structure with the addition of ONPs. The work aims to strongly build some critical aspects of nano-bio interactions for their relevance in biomedical or sensing applications.

## **Chapter 7: Conclusion**

This chapter culminates and interconnects the research work presented descriptively in the preceding chapters. From the research work presented in previous chapters, we conclude that the interfacial directionality of molecular groups is determined by the interplay of different intermolecular forces such as electrostatic, van der Waals, and hydrogen bonding. These events decide the fine-tuning of the interfacial properties and its dynamics. In addition to the evaluation of the interfacial regime, the integration of complementing results via bulk-specific or linear optical tools further consolidates the fundamental understanding of the interfacial behavior of complex systems occurring during nano-bio associations. Our work could significantly contribute to the rapidly growing domains of bio-mimicking systems, soft functional materials, nano-bio-interfacing, and biomolecular sensing applications.

## Chapter 2

### Experimental theory and methods

The present chapter provides a brief discussion on the different experimental techniques and associated theories employed to study the bio-physico-chemical aspects of molecular behavior in bulk and at interfaces. Here, comparative details about the fundamentals of linear and non-linear optical processes are presented along with the instrumental details, their characteristics, and analytical and experimental approaches. The bulk-specific experimental methods involve surface tensiometry, zeta-sizer and -potentiometry, ATR-FTIR vibrational spectroscopy. However, the interface-specific characterizations were performed by vibrational sum frequency generation (VSFG) spectroscopy, which is based on a second-order non-linear optical process occurring during the light-matter interactions. Further, some other experimental techniques which have also been used in our studies are also discussed in this chapter. This is to bring to the notice that the description about the ATR-FTIR vibrational spectroscopy is a reflection of our publication as book chapter by H. Kaur et al.<sup>30</sup> in the book entitled “Modern Techniques of Spectroscopy: Basics, Instrumentation, and Applications”.

#### 2.1 Interaction of optical radiation with matter

Interaction of any optical radiation/light with matter leads to some perturbations among the internal elementary particles (i.e., electrons, protons, nuclei, ions) by influencing their motion and re-distribution within the material. During light propagation within the media, the processes like refraction, reflection, absorption, dispersion, and scattering come into the picture. The impinging light source projects certain force over the molecular valence electrons of the medium. These phenomena are interpreted in terms of a resultant electric field polarization is induced within the material after the radiation-matter interaction.<sup>12,33,107</sup>

##### 2.1.1 Generation of linear vs non-linear optical response

Many conventional optical sources project linear properties upon interaction with any material. When the molecule is placed in a weak electric field (conventional light

source), the induced electric dipole,  $\mu$ , is small and is proportional to the strength of the electric field  $E$ , given by:<sup>33,107</sup>

$$\mu = \mu_0 + \alpha E \quad (2.1)$$

where,  $\alpha$  is the polarizability of the electrons of a molecule, and  $\mu_0$  is referred as the static dipole moment value of the interacting material. The sum of electric dipoles within the molecular condensed phase constitutes the dipole moment per unit volume i.e., referred to as bulk polarisation 'P'. Hence, the polarisation induced within the material as an effect of an incident oscillating electric field from a linear/conventional light source is given by:<sup>33,107</sup>

$$P = \epsilon_0 \chi^{(1)} E \quad (2.2)$$

Here,  $\chi^{(1)}$  is the bulk macroscopic average of  $\alpha$  which is also referred to as a first-order linear susceptibility term. The vacuum permittivity is represented as  $\epsilon_0$ . An electric field originating from the conventional light source is of lower strength which makes it unable to impact the native force fields encountered by the electrons within the molecular system. Thus, during the linear optical response, the molecular dipoles induced by the electric field oscillations bear a frequency in proportion to that of the incident light. No coupling effects occur among the impinging light beams. Additionally, in the conventional optics regime, the refractive index ( $n_0$ ) of the material stay consistent as an independent entity irrespective of the incident beam intensity or its frequency.<sup>33,107</sup>

Contrarily, the non-linear optical response is described as a new phenomenon involving an intense coherent optical source (mainly laser source) capable to refining the intrinsic optical response of the material upon light interaction with matter. The significance of non-linear optics can be considered in terms of the strength of the applied electric field, which is responsible for inducing the non-linear effect in molecular systems. As a consequence, the electrons can oscillate at various frequencies depending on the frequency-mixing process. This produces a non-linearity within the material and the electrons under this situation do not respond harmonically to the applied electric field and the frequency-mixing processes could be readily observed. This way, certain higher-order terms corresponding to the electric field generated comes into the picture. Thus, the induced dipoles under non-linearity are defined by some additional non-linear terms as:<sup>12,33,107,108</sup>



$$\mu = \alpha E + \beta E^2 + \gamma E^3 + \dots \quad (2.3)$$

here,  $\beta$  and  $\gamma$  are the first- and second-order hyperpolarizabilities respectively. Thus, the generation of these novel effects within the bulk material depicts the polarisation in power series term as:<sup>12,33,107,108</sup>

$$P = \varepsilon_0(\chi^{(1)}E + \chi^{(2)}E^2 + \chi^{(3)}E^3 + \dots) \quad (2.4)$$

$$= P^{(1)} + P^{(2)} + P^{(3)} + \dots \quad (2.5)$$

where,  $\chi^{(2)}$  and  $\chi^{(3)}$  are the second- and third-order non-linear susceptibilities respectively, and are significantly lower in strength than the  $\chi^{(1)}$ , while  $P^{(1)}$ ,  $P^{(2)}$ , and  $P^{(3)}$  are the first-, second- and third-order polarizations respectively. Thus, fundamentally, the non-linear effects actuated within the material result in an induced dipole moment and perturbations among the molecules, and a secondary radiative wave is consequently emitted. Here, the frequency ( $\omega$ ) dependent term of the incident electromagnetic field ( $E$ ) could be identified as follows:<sup>12,33,107,108</sup>

$$E = E_1 \cos \omega t \quad (2.6)$$

The electric-field polarisation induced within the material is thus elaborated as:<sup>12,33,107</sup>

$$P = \varepsilon_0(\chi^{(1)}(E_1 \cos \omega t) + \chi^{(2)}(E_1 \cos \omega t)^2 + \chi^{(3)}(E_1 \cos \omega t)^3 + \dots) \quad (2.7)$$

This term can be expanded as:<sup>12,33,107,108</sup>

$$\begin{aligned} P = \varepsilon_0(\chi^{(1)}E_1 \cos \omega t + \frac{\chi^{(2)}}{2} E_1^2(1 \\ + \cos 2\omega t) + \frac{\chi^{(3)}}{4} E_1^3(3 \cos \omega t \\ + \cos 3\omega t) + \dots) \end{aligned} \quad (2.8)$$

The above equation depicts an induced polarisation term which elucidates that the output light beam consists of the terms which potentially oscillate at twice (second-harmonic generation,  $2\omega$ ), three times (third-harmonic generation,  $3\omega$ ), etc, with respect to the frequency ' $\omega$ ' of an incident field ' $E$ '.

The non-linear response of a material after laser-matter interaction mainly incorporates five different physical mechanisms occurring inside the media as follows:<sup>12,33,107,108</sup>

1. Electronic distortions – These occur as a result of external electric field-dependent perturbations in the electronic cloud within the molecular or atomic shells. This process happens to be faster taking an approximate duration of less than  $\sim 10^{-15}$ – $10^{-16}$  seconds.
2. Molecular-scale motions – It involves the intramolecular vibrations, rotations, etc. which emerge due to the optical field interactions with the molecular system, impacting the nuclei or ions constituting the molecular groups. The duration of this process is  $\sim 10^{-12}$ – $10^{-14}$  seconds.
3. Molecular orientations – This physical mechanism involves the electric-field induced polarization dependent variations in the angular distributions of molecular groups within an anisotropic media, which is arises within  $\sim 10^{-12}$ – $10^{-13}$  seconds of time-scale.
4. Acoustic motions – These enrol polarization contribution from the electric-field induced acoustic motions which depends partly on the molecular phase of the system (i.e., solid, liquid, or gas). The response time of the process is  $\sim 10^{-9}$ – $10^{-10}$  seconds.
5. Population reversal – The polarization contribution also arises from the molecular re-distribution and transitions occurring within the system principally due to photonic absorption or resonant transition processes. The time response in this case majorly relies on the properties of the molecular system involving transition and then relaxation processes and is generally considered to be a much slower process compared to above mechanisms.

Out of these possible mechanisms, which phenomenon is dominant and contributes towards the generation of the signal depending on the parameters of the incident field and the material characteristics. The duration of the impinging pulsed laser beam decides the relative occurrence/dominance of these mechanisms such that in case the incident pulsed laser source bears a longer duration than the time of response of any of the mechanism, then that respective mechanism could be included for its contribution towards the generated signal strength.<sup>108</sup>

The current thesis work predominantly involves the utilisation of sum frequency generation (SFG) vibrations spectroscopy which is based on a second-order non-linear optical process for characterizing the interfacial phenomena and molecular-scale behaviour at air-aqueous and air-solid interfaces. It is based on the second-order non-linear susceptibility ( $\chi^{(2)}$ ) process, which is surface and interface-sensitive, therefore, we will majorly confine our discussion towards this process further in this chapter.

## 2.2 Origin of sum frequency vibrational response

The theory of sum frequency generation (SFG) primarily follows the concept of electric dipole approximation to express the light-matter interactions, where the value of  $\chi^{(2)}$  gets nullified for the centrosymmetric/isotropic media. According to this approximation, the impact of optically generating magnetic fields and the inclusion of multipoles/quadrupoles is excluded. The contribution from the dipolar fields of neighbouring induced dipoles is also ignored and the induced impact of the propagating electric field is considered to be a macroscopic feature. For the SFG process to occur, the second-order polarisation term involved here,  $P^{(2)}$ , is expressed as the input and summation of the two distinct oscillating beams of  $\omega_1$  and  $\omega_2$  frequencies, which presents the following second-order polarization term as:<sup>12,33,107,108</sup>

$$P^{(2)} = \epsilon_0 \chi^{(2)} (E_1 \cos \omega_1 t + E_2 \cos \omega_2 t)^2 \quad (2.9)$$

Further expanding and rearranging the term, we obtain:<sup>12,33,107,108</sup>

$$\begin{aligned} P^{(2)} = \frac{1}{2} \epsilon_0 \chi^{(2)} [ & (E_1^2 + E_2^2) \\ & + (E_1^2 \cos 2\omega_1 t + E_2^2 \cos 2\omega_2 t) \\ & + (2E_1 E_2 \cos(\omega_1 - \omega_2)t) \\ & + (2E_1 E_2 \cos(\omega_1 + \omega_2)t) ] \end{aligned} \quad (2.10)$$

The two incident fields with frequencies  $\omega_1$  and  $\omega_2$  thus lead to the generation of a DC field (i.e., frequency independent field) generated at the surface, SHG for both input frequencies, difference frequency generation (DFG) i.e., the difference of the frequencies of the two input beams  $\omega_1 - \omega_2$ , and, the SFG beam which is generated at the sum of the two incident laser frequencies  $\omega_1 + \omega_2$ . Here,  $\chi^{(2)}$  (also known as the third-rank tensor component) basically embrace a three-wave mixing process.

Following a non-linear  $\chi^{(2)}$  process, SFG vibrational spectroscopy (SFG-VS) is intricately an interface-specific technique for characterizing the resonant vibrational patterns of molecular functional groups which are residing at the interfacial region. Thereby, it proves to be an ideal technique to explore and extract the structural organization, composition, as well as the orientational parameter of molecules and associated groups, which can be studied at different interfaces/surfaces.<sup>12,32-34,68,86,88,107,108</sup> Centred on the electric dipole approximation, the  $\chi^{(2)}$  dependent SFG-VS is generated from the interface/surface bearing non-centrosymmetric surroundings, i.e, where the inversion symmetry disintegrates. Thus, in order to be sensitive enough to produce SF beam, the molecules existing at the interface must acquire a net polar alignment with active polarizability. From here it could be inferred that only those molecular groups which are simultaneously IR and Raman active could sensitively generate a significant SFG signal strength at the resonant vibrational frequency. Thus, the molecules which do not carry a net orientation at the interface (i.e., indicative of their active polarity), the average molecular hyperpolarizability will get nullified. This provides valuable insight into the uniqueness of the SFG system towards selective probing of the molecular vibrational features at the interface. The resultant SFG signal entails the molecular-scale details from the interfacial regime with an approximate depth of 1 nm scale, which is influenced by the sample composition, charge, or the state of the sample (aqueous or solid-films, etc.).<sup>12,33,107,109</sup> The resultant SFG beam is an outcome of a resonant enhancement and upshifted in the visible range due to an incident fixed visible frequency (532 nm). For the successful production of the SFG beam, two primary conservation laws must be obeyed:

The energy conservation process, which is represented as,<sup>12,33,107</sup>

$$\omega_{\text{SFG}} = \omega_{\text{VIS}} + \omega_{\text{IR}} \quad (2.11)$$

and the conservation of phase-matching condition that is given by the wave vector components of the incident and reflected beams in the parallel direction ( $\vec{k}^{\parallel}$ ) to the incident plane,<sup>12,33,107</sup>

$$\vec{k}_{\text{SFG}}^{\parallel} = \vec{k}_{\text{VIS}}^{\parallel} + \vec{k}_{\text{IR}}^{\parallel} \quad (2.12)$$

Where,  $k = \frac{2n\pi}{\lambda}$  (here  $n$  is the material refractive index with respect to the incident field and  $\lambda$  is the beam wavelength), and the above equation can thus be expanded as below:<sup>12,33,107</sup>

$$n_{\text{SFG}}\omega_{\text{SFG}}\sin\theta_{\text{SFG}} = n_{\text{VIS}}\omega_{\text{VIS}}\sin\theta_{\text{VIS}} + n_{\text{IR}}\omega_{\text{IR}}\sin\theta_{\text{IR}} \quad (2.13)$$

This exemplifies that the angular dispersion of the SFG ( $\theta_{\text{SFG}}$ ) relies on the incident angles of the non-resonant visible ( $\theta_{\text{VIS}}$ ) and resonating IR beams ( $\theta_{\text{IR}}$ ) impinging over the sample, and can be readily calculated using the above formulation. The intensity of the generated SFG beam through the anti-stokes Raman process (as shown in Figure 2.1) is therefore presented as:<sup>12,33,107</sup>

$$I_{\text{SFG}} \propto |\chi^{(2)}|^2 I_{\text{VIS}} I_{\text{IR}} \quad (2.14)$$

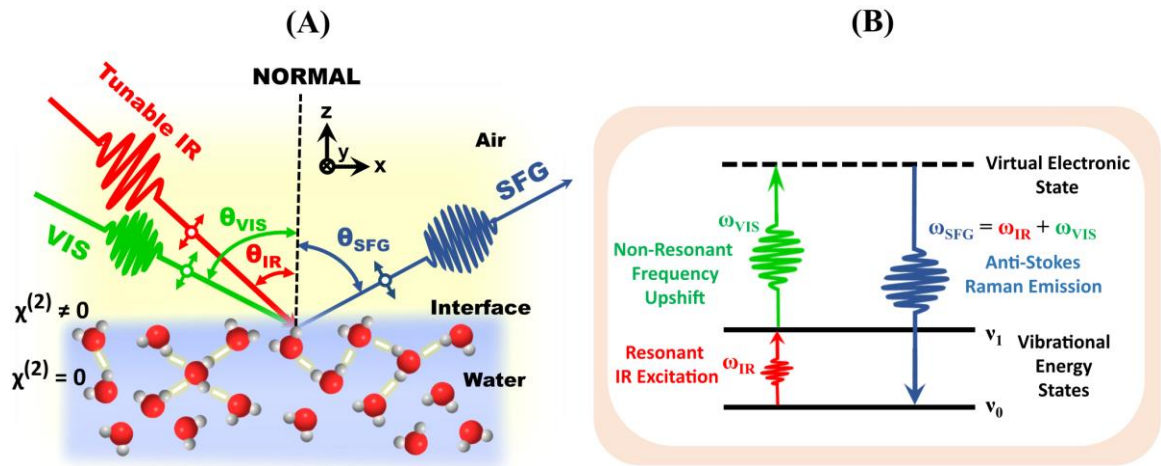


**Figure 2.1** (A) Schematic representation of the SFG generation in the reflection mode at the air-water interface in a co-propagating geometry. (B) Energy-level diagram of the process of SFG generation, which results from the resonant transitions occurring from ground vibrational state ( $v_0$ ) to the first excited vibrational state ( $v_1$ ) via IR photon, which is further upshifted to higher virtual electronic state by excitation through visible photon. The SFG is generated as a result of an anti-stokes raman process, where the absorbed photon energy relaxes back to the ground state.

The sensitivity of SFG towards the surface with non-centrosymmetric surroundings could be understood from the symmetry restrictions implemented over the third-rank tensor ' $\chi^{(2)}$ ', which is a material characteristic that is projected as a response to the interacting optical field. Being a polar tensor component,  $\chi^{(2)}$  has the propensity to showcase a sign reversal property during the molecular inversion (m) symmetry. This is

depicted as:  $\chi^{(2)}(-m) = -\chi^{(2)}(m)$  where the susceptibility component must reverse its sign upon molecular inversion. However, for the case of centrosymmetric surroundings (in bulk phase), the molecular system is seen as equal from all directions even after reversing the molecular axis which makes the susceptibility factor as:  $\chi^{(2)}(-m) = \chi^{(2)}(m)$ , as the opposite molecular directions become similar and the resultant sign value is not affected during inversion symmetry. For these cases to occur, the  $\chi^{(2)}(m)$  must be zero and the generation of SF beam is not possible under such circumstances since it is forbidden from the isotropic bulk media. While at the interface, the  $\chi^{(2)}(-m) = \chi^{(2)}(m)$  the relation is not feasible due to the asymmetrical environment which compels the interfacial molecules to be SFG active. Further, the response of  $\chi^{(2)}$  of SFG withholds the contribution of a non-resonant  $\chi_{NR}^{(2)}$  response and a resonant frequency-dependent response ( $\chi_R^{(2)}$ ) from the interfacial molecules, presented as:<sup>12,33,107-109</sup>

$$\chi^{(2)} = \chi_{NR}^{(2)} + \chi_R^{(2)} \quad (2.15)$$

$$\chi^{(2)} = \chi_{NR}^{(2)} + \sum_k \frac{A_k}{\omega_k - \omega_{IR} - i\Gamma_k} \quad (2.16)$$

where  $A_k$  is the amplitude of the  $k^{\text{th}}$  vibrational mode,  $\omega_{IR}$  is the frequency of the tuneable infrared beam,  $\omega_k$  is the frequency of the vibrational resonance and  $\Gamma_k$  is the damping or linewidth coefficient (i.e., half-width at half maximum, HWHM) of the resonating peak and here,  $i = \sqrt{-1}$ . The resonant amplitude of SFG is the product of  $\mu$ , the induced dipole moment, and  $\alpha$ , the polarizability. This indicates that the transition must be both IR and Raman active.<sup>12,33,107-109</sup> The non-resonant  $\chi_{NR}^{(2)}$  contribution specifically stems from the IR frequency-independent background signals involving multipolar or quadrupolar contributions and incident visible frequency (532 nm). This non-resonant involvement dominates significantly in the case of metals (gold, silver), and for other dielectric materials such as quartz, CaF<sub>2</sub> materials, fused silica, etc.<sup>33</sup> The resonant signal ( $\chi_R^{(2)}$ ) incorporates the material specific information which could be identified by probing the microscopic properties at the molecular-scale level constituting:<sup>12,33,107-111</sup>

$$\chi_R^{(2)} = \frac{N_S}{\epsilon_0} \langle \beta \rangle \quad (2.17)$$

Thus, the resonant factor directly relates with the number of SFG active molecular groups ( $N_s$ ) present at the interface, and orientation average of the molecular-scale hyperpolarizability factor denoted as  $\langle\beta\rangle$ . This orientational hyperpolarizability average further depends on:<sup>12,33,107-113</sup>

$$\langle\beta\rangle \propto \frac{\alpha_k \mu_k}{\omega_k - \omega_{IR} - i\Gamma_k} \quad (2.18)$$

Here,  $\alpha_k$  depicts Raman polarizability tensor, and  $\mu_k$  signifies net IR dipole moment. The fitting of the spectral data points obtained from the SFG-VS of a specific sample has been performed using the Lorentzian equation 2.16, which offered the information about the amplitude values at the resonating frequencies ' $\omega_k$ ' of a particular molecular ' $k^{\text{th}}$ ' vibrational mode.

### 2.2.1 Optical polarization-dependent molecular orientation analysis of methyl functional groups

The propagation of an electromagnetic light wave over the sample surface typically accompanies electric-field components which are polarized with respect to the plane of incidence of the beam at the sample surface. The polarization of light could be in parallel direction (represented as P-polarized) or in the perpendicular direction (designated as S-polarized) in correspondence with the incident axis plane. The electric-field component for the S-polarized light projects along the y-axis, while in case of P-polarized light the field component is extended towards both the x- and z-axis. Thus, the polarization state of the resonating input IR pump beam is very important to probe the orientation of the molecular group at the interfacial region, whether it is lying parallel to the plane of incidence or aligned with respect to the incident plane at a certain angle at the surface. Accounting for the incident and reflected light beam polarizations, the macroscopic-level information obtained as the non-linear susceptibility tensor components i.e.,  $\chi_{yyz}^{(2)}$ ,  $\chi_{zyy}^{(2)}$ ,  $\chi_{xxz}^{(2)}$ ,  $\chi_{zxx}^{(2)}$ ,  $\chi_{zzx}^{(2)}$ , and  $\chi_{zzz}^{(2)}$ , where x, y, and z are considered from the reference of the laboratory frame of coordinates. The macroscopic details could be transformed into the microscopic-level information about the molecular frame coordinate system as the second-order hyperpolarizability tensor element  $\beta_{abc}^{(2)}$ , where a, b, and c refer to the molecular coordinate framework, for specific polarization schemes with 'S' or 'P' polarization states.<sup>12,33,107-113</sup>

Our research work addresses the interfacial molecular re-orientation profile of the methyl groups with  $C_{3v}$  molecular symmetry. Considering a single methyl molecule/moiety, the molecular placement at the surface/interface arranges itself with a principal axis ‘c’ also referred to as the symmetry axis of a molecule within a molecular-coordinate frame. All the angular measurements for a particular molecular group are scaled with respect to the normal axis ‘z’ of the surface plane, which determines the lab-frame coordinate. As stated previously, both these coordinate systems can be effectively correlated by using Euler transformation, where the Euler angles, viz. azimuthal angle ( $\phi$ ), twist angle ( $\psi$ ), and tilt angle ( $\theta$ ) provides a complete information about the overall molecular rotation and placement at the interface. The tilt angle ‘ $\theta$ ’ is formed by the molecular moiety with respect to the normal axis at the surface extending to the molecular symmetry axis ‘c’ (demonstrated in Figure 2.2). Thus, the second-order susceptibility profile obtained in the lab-frame is correlated with the molecular-level hyperpolarizability for the ensemble average of the molecular groups in the molecular coordinate frame. This is illustrated as:<sup>12,33,107,108,110-112</sup>

$$\chi_{ijk}^{(2)} = \frac{N_s}{\epsilon_0} \sum \langle R_{ia}(\psi)R_{jb}(\theta)R_{kc}(\phi) \rangle \beta_{abc}^{(2)} \quad (2.19)$$

Where, the R components define the three-distinct rotational matrices associated with the respective molecular angular states (Euler angles) and the equation 2.19 itself represents the ensemble average of molecular tilt angle information as obtained from lab-frame to molecular-frame coordinate conversions.

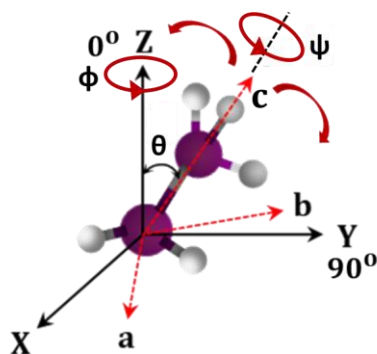


**Figure 2.2** Arrangement of the functional methyl group, attached to methylene moieties, in the molecular coordinate system (a, b, c) and lab-frame coordinate system (X, Y, Z) respectively. The principal axis of methyl group and surface normal is depicted by c and Z, respectively. Three molecular orientation angles are showcased for methyl group arrangement i.e., azimuthal angle  $\phi$  about Z-axis, rotation (twist) angle  $\psi$  about c-axis, and tilt angle  $\theta$  about the Z-axis.



To avoid the mathematical complexities towards analyzing the orientation analysis of methyl group, most of the research papers in general practice include only tilt angle analysis of the molecular c-axis and consider a random distribution for the other two angles i.e., azimuthal and twist angles at the interface.<sup>12,33,107,108,110-113</sup> Hence, in our study, we have considered the tilt angle analysis for SFG signal variation.

For a symmetric stretch of methyl groups:<sup>12,33,107,108,110-113</sup>

$$\chi_{xxz,SS}^{(2)} = \chi_{yyz,SS}^{(2)} = \frac{1}{2} N_S \beta_{ccc,SS} \{ (1+R) \langle \cos \theta_{CH_3} \rangle - (1-R) \langle \cos^3 \theta_{CH_3} \rangle \} \quad (2.20)$$

$$\begin{aligned} \chi_{xzx,SS}^{(2)} = \chi_{zxx,SS}^{(2)} = \chi_{yzy,SS}^{(2)} = \chi_{zyy,SS}^{(2)} \\ = \frac{1}{2} N_S \beta_{ccc,SS} (1-R) \{ \langle \cos \theta_{CH_3} \rangle - \langle \cos^3 \theta_{CH_3} \rangle \} \end{aligned} \quad (2.21)$$

$$\chi_{zzz,SS}^{(2)} = N_S \beta_{ccc,SS} \{ R \langle \cos \theta_{CH_3} \rangle + (1-R) \langle \cos^3 \theta_{CH_3} \rangle \} \quad (2.22)$$

For asymmetric stretch of methyl groups:<sup>12,33,107,108,110-113</sup>

$$\chi_{xxz,AS}^{(2)} = \chi_{yyz,AS}^{(2)} = -N_S \beta_{caa,AS} \{ \langle \cos \theta_{CH_3} \rangle - \langle \cos^3 \theta_{CH_3} \rangle \} \quad (2.23)$$

$$\chi_{xzx,AS}^{(2)} = \chi_{zxx,AS}^{(2)} = \chi_{yzy,AS}^{(2)} = \chi_{zyy,AS}^{(2)} = N_S \beta_{caa,AS} \langle \cos^3 \theta_{CH_3} \rangle \quad (2.24)$$

$$\chi_{zzz,AS}^{(2)} = 2N_S \beta_{caa,AS} \{ \langle \cos \theta_{CH_3} \rangle - \langle \cos^3 \theta_{CH_3} \rangle \} \quad (2.25)$$

where  $R = \left( \frac{\beta_{aac}}{\beta_{ccc}} \right)$  (also known as the hyperpolarizability ratio),  $\chi_{zzz}^{(2)} = \chi_{yyz}^{(2)}$ ;  $\chi_{xxz}^{(2)} = \chi_{yzy}^{(2)}$  and  $\chi_{zzz}^{(2)} = -2\chi_{yzy}^{(2)} = -2\chi_{xxz}^{(2)}$ .<sup>12,33,107,108,110-112</sup> Here,  $N_S$  depict the density of number of methyl groups under probe at the interface, and  $\langle \quad \rangle$  represents an ensemble average of all the possible molecular orientational values attained by the molecular group at the surface. The terms ‘SS’ and ‘AS’ designates the symmetric stretch and anti-symmetric stretch vibrational modes of the molecular groups under probing (here,  $CH_3$  groups are considered). Thus, both the second-order susceptibility and the hyperpolarizability factor interrelate to extract the molecular tilt angle ( $\theta$ ) information, which are widely calculated using two distinct distribution functions, i.e., the delta ( $\delta$ )- and Gaussian distribution functions. For the  $\delta$ -distribution function, the  $\langle \cos \theta \rangle \approx \cos \theta$  and  $\langle \cos^3 \theta \rangle \approx \cos^3 \theta$  values are used for calculations in reference to one molecular group under study. However, in the Gaussian distribution function, the molecular tilt

angle values are contemplated in form of the ensemble angular distribution, which is given by:<sup>12,110-113</sup>

$$f(\theta) = \frac{1}{\sigma\sqrt{2\pi}} \exp[-(\theta - \theta_0)^2/2\sigma^2] \quad (2.26)$$

$$\langle \cos \theta \rangle = \int_0^\pi f(\theta) \cos \theta \sin \theta \, d\theta \quad (2.27)$$

$$\langle \cos^3 \theta \rangle = \int_0^\pi f(\theta) \cos^3 \theta \sin \theta \, d\theta \quad (2.28)$$

Here  $\sigma$  is the root-mean-square of the distribution width that is referred to  $\sigma = 0^\circ$  for the  $\delta$ -distribution function,  $f(\theta)$  yields the molecular tilt angle ( $\theta$ ) distribution probability, and  $\theta_0$  is the average tilt angle. These mathematical evaluations offer a distinct quantitative information based on unique polarization-specific vibrational patterns attained by terminal methyl groups using SFG-VS as an interface-probing spectroscopic tool. By conducting the polarization-specific SFG study of a particular molecular system, one gathers the precise description about the predominant molecular stretching modes in a particular polarization combination. For instance, the SSP polarization scheme curtails signature from the symmetric stretching modes while the PPP and SPS showcase the principal contribution of anti-symmetric stretching modes of the molecular groups under probing,<sup>12,33,107-113</sup> as illustrated via theoretically plotted curves in Figure 2.3 considering the  $\delta$ -distribution function for the methyl stretch modes.

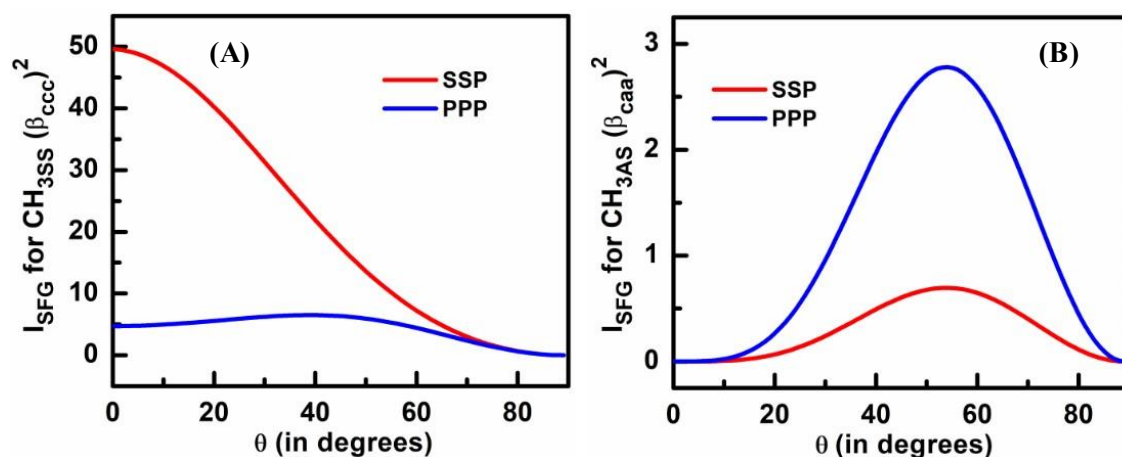


**Figure 2.3** Theoretical plots with  $\delta$ -distribution function depicting the variation in the SFG intensity values with respect to the tilt angle (in degrees) in SSP and PPP polarization schemes for the (A) methyl symmetric stretch and (B) methyl asymmetric stretch modes, respectively.

In order to accurately conduct these calculations, the amplitude ( $A_k$ ) values acquired from the Lorentzian data fitting of the SFG spectral profile were used in the formulations. This is realized from the relation among the second-order non-linear susceptibility with the resonating amplitude bearing a certain peak width (i.e., HWHM represented by ' $\Gamma_k$ '). The relation is given by:  $\chi_{xyz}^{(2)} \propto \frac{A_k}{\Gamma_k}$ . The calculations are further made convenient by assessing the susceptibility and correspondingly the amplitude ratios of different polarization schemes, for example, considering susceptibility ratio formulations for symmetric and asymmetric stretching modes of SSP and PPP polarization modes. For illustration purpose, Figure 2.4A represents the possible theoretical curve that could be simulated by varying the relative susceptibility ratio for calculating the methyl group tilt angle values, by using the Gaussian distribution function. Here, to ease the calculations, we have considered the followings:  $R = \frac{\beta_{aac}}{\beta_{ccc}} \approx 3$  and  $\frac{\beta_{caa}}{\beta_{aac}} \approx -1$ .<sup>12,110-113</sup> Here, the  $\sigma$  value are varied from  $0^\circ$ - $50^\circ$ . The experimentally measured susceptibility ratio values are plotted and extrapolated within these simulated theoretical curves for the respective susceptibility ratio plot. An example plot has been represented in panel B, where an experimentally obtained hypothetical value of susceptibility ratios between SSP symmetric and PPP asymmetric stretch modes has been extrapolated to identify the methyl tilt angle value at  $\sigma$  value of  $0^\circ$  to be equal to  $\sim 37^\circ$  corresponding to the x-axis.

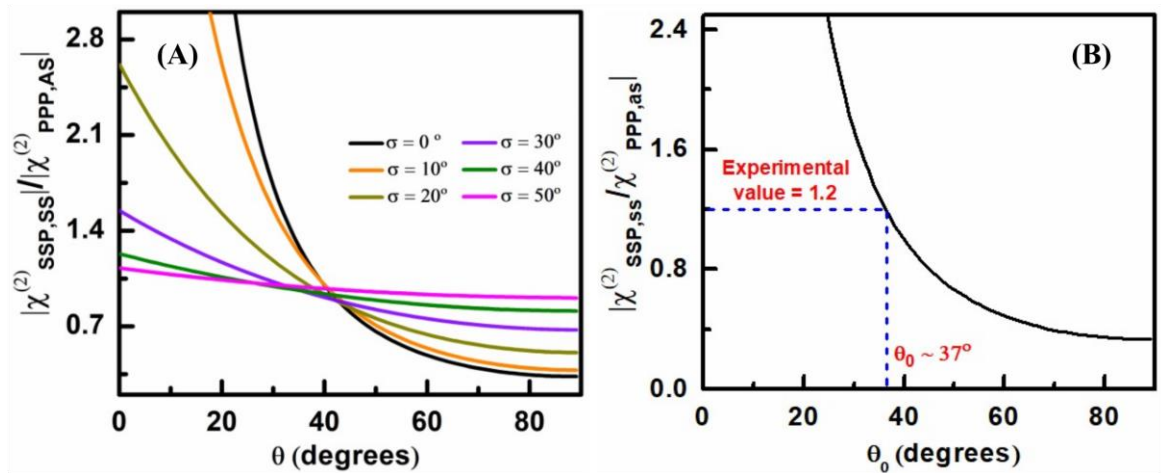


**Figure 2.4** Simulated orientation curves plotted using Gaussian distribution function with distribution width ( $\sigma$ ) by considering the absolute values of susceptibility ratios of SSP and PPP polarization modes with respect to the methyl group tilt angle ( $\theta$ ) variation.

### 2.2.2 Instrumental details of SFG

The vibrational sum frequency generation spectrometer utilised in our studies is procured from Ekspla (Lithuania). It is assembled by three-unit boxes consisting of aligned optics and a black box spectrometer (consisting of a sample compartment), as illustrated in Figure 2.5. It withholds a passively mode-locked Nd:YAG laser (Ekspla PL2231-50) source which capably triggers the production of 1064 nm wavelength of the coherent laser beam of diameter ~6mm. The laser beam emanating from the source bear a 30 picosecond of pulse duration with a 50 Hz repetition rate and ~40 mJ of the laser energy per pulse from the output port of the first unit. The resultant 1064 nm laser beam is then fed into the second unit called the second-harmonic unit (Ekspla SFGH500-2H) which, as the name suggests, proficiently generates two second-harmonic beams of 532 nm wavelength (i.e., twice the frequency of the seed laser input) via non-linear KD\*P (potassium di-deuterium phosphate) crystals. Thus, the output from the SH-unit consists of two 532 nm and the fundamental 1064 nm beam, which are then directed towards the third-unit which embody three distinct sections for the interplay with the coherent beam sources, viz., optical parametric oscillation (OPO), optical parametric amplification (OPA), and optical parametric generation within the parametric generation (PG) unit (Ekspla PG501/DFG2P). The 532 nm beam is fed to optically pump the non-linear BBO ( $\beta$  barium borate) crystals for conducting OPO and OPA processes which forms an idler beam with the wavelength range from 1064 nm–2300 nm. A specific range of wavelength from this idler beam (i.e., 1140 nm–1980 nm) is merged with the fundamental 1064 nm beam within the two different non-linear crystals in the DFG unit, AgGaS<sub>2</sub> (Silver Gallium Sulfide) or GaSe (Gallium (II) selenide). This intermixing of beams results in the generation of a spectral range of tunable IR spanning from 2300 nm-16000 nm (or 625 cm<sup>-1</sup>–4300 cm<sup>-1</sup>). This tunable IR range (diameter 150  $\mu$ m, with energy 235  $\mu$ J/pulse at 3000 nm) and the fixed 532 nm visible beam (diameter 200  $\mu$ m, energy 500  $\mu$ J/pulse) are impinged in a co-propagating scheme over a circular Teflon cell filled with the liquid sample with their respective incident angles of ~63° and ~56° respectively with respect to the surface normal. The overlapping of these two beams at the sample surface is performed by finely tuning with the adjustment knobs of focusing mirrors related to the spatial overlapping of guided laser for IR beam or visible beam and simultaneously observing the signal strength of the outgoing SFG beam at the resonating IR wavenumber with the help of LABVIEW software over the computer screen. The same software is

used to handle and regulate the motorization of some optical elements within the SFG units and for setting up the optimizing parameters for experimentation. The incident IR and Visible beams are temporally overlapped by means of interplaying with the visible delay line (installed in the SHG unit) through the software. Eventually, considering the laws of phase-matching and energy conservations, the sum of these two incident beams with respective frequencies is generated specifically from the sample interface as the SFG beam at  $\sim 61.5^\circ$  from the surface normal. The SFG beam is further aligned and focused towards the monochromator (MS2001i, SOL instruments Ltd.) which is sensitive in the wavelength region of 400-550 nm and bears a resolution of 0.06 nm. With some focusing optics, the involvement of the reflected visible and IR beam is filtered by spatial filters and the output refined beam is then directed towards the photomultiplier tube (Hamamatsu R7899, sensitive for the light in UV-Visible region) for additional signal amplification procedure. The SFG system is maintained with the constant lab temperature of  $\sim 22^\circ\text{C}$  and controlled lab humidity of  $\sim 35\text{-}45\%$  via a de-humidifier system. The laser is usually kept in a warming-up state for around 2 hours prior to its usage for conducting experiments.

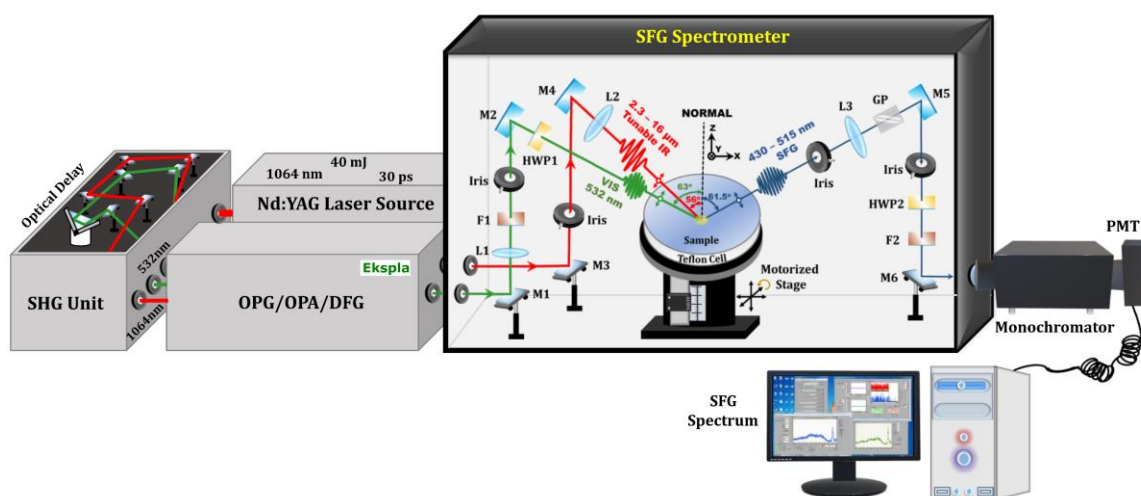


**Figure 2.5** Schematic illustration of the SFG experimental set-up depicting the beam path across the picosecond Nd:YAG laser, second harmonic generation (SHG) unit, optical parametric generation (OPG), optical parametric amplification (OPA), difference frequency generation (DFG), and the detection unit (monochromator and photomultiplier tube: PMT). Abbreviated labels include M1-M6: mirrors, L1-L3: focusing lens, F1-F2: filters, HWP1-HWP2: half-wave plates, GP: glan prism.

### 2.2.3 Methodology and cleaning procedure for SFG experimentation

The samples were prepared in type-1 millipore ultra-pure de-ionized water with a resistivity of 18.2 M $\Omega$ .cm and pH  $5.80 \pm 0.02$  at room temperature of  $\sim 22$  °C. The spectra were acquired in three distinct polarization schemes i.e., SSP, PPP, and SPS polarization combination, where S denotes the direction of electric field component perpendicular with respect to incident plane and P designates electric field component directing in parallel fashion to the plane of incidence over the sample surface. The incident and output beams are considered in different polarization combinations where in ‘SSP’, for example, the first letter ‘S’ in scheme presents the output polarization of SFG beam, second ‘S’ is the input polarization of visible beam, and the third letter ‘P’ is entitled as the polarized input of IR beam in sequence. The data acquisition for samples are done by averaging the data points to 200 pulses per step at the IR wavenumber step size of 2-5  $\text{cm}^{-1}$ . The work covered in the current thesis involves the spectral probing in the wavenumber range from 2750-3800  $\text{cm}^{-1}$  covering both the C-H stretch as well as O-H stretch region of vibrational resonance modes of samples.

The aqueous samples were studied in the circular Teflon assembly (45 mm diameter) capable of holding 7 mL of sample volume. While, the solid polymer film-based samples were coated over the SiO<sub>2</sub> glass slides (cut manually with approximate size of 2.5 x 2.5  $\text{cm}^2$ ). All the sample cells, storage vials, and glass slides were subjected to piranha treatment [with composition consisting of concentrated sulphuric acid (H<sub>2</sub>SO<sub>4</sub>):30% hydrogen peroxide (H<sub>2</sub>O<sub>2</sub>) in respective ratio of 3:1] and kept at 70°C over the hot plate for  $\sim 1$ – $2$  hours. Piranha solution is a highly reactive and corrosive solution mixture which is capable of rigorously removing any type of organic contaminants from the glasswares or sample cells for conducting contaminant-free interfacial studies. They were consecutively cleaned rigorously with de-ionized water and were then dried with warm air for some time prior to their usage. All the sample storage vials and sample bottles were covered and sealed by using Parafilm® in order to rule out the possibility of sample contamination and evaporation impact over the sample consistency.

### 2.3 ATR-FTIR vibrational spectroscopy

Attenuated total-internal reflectance Fourier transform infrared (ATR-FTIR) vibrational spectroscopy is a well-known spectroscopic tool used to investigate the

molecular conformation, chemical reactions, and dynamics of the species present in the molecular system.<sup>114-117</sup> As a result of a highly sensitive approach of ATR-FTIR vibrational spectroscopy towards the environment-aided fluctuations within the media, an information about the local framework of molecular interactions among the analytes prevailing in their distinct morphological states is easily analysed.<sup>114-117</sup>

The ATR-FTIR technique is governed by a reflectance phenomenon, where an internal reflection element (IRE) or ATR crystal plays a key role since it is generally interfaced in direct contact with the sample. The IR radiation emanating from its source is directed and is made to incident towards the ATR crystal where it gets total internally reflected (TIR) only when the incidence angle is above the critical angle ( $\theta_c$ ) of reflection as observed for the IRE crystal surface, kept in direct association with the sample. This critical angle is determined by commonly used formulation, Snell's law, given by:<sup>29,30,114,118</sup>

$$\theta_c = \sin^{-1} \left( \frac{n_2}{n_1} \right) \quad (2.29)$$

The impinging IR beam gets attenuated and/or absorbed by the molecular species within the sample which depends on their concentration, composition, or morphology, and the generated outgoing IR beam after reflection is of a relatively weaker intensity which is analyzed by the detector.<sup>29,30,114,117</sup> The molecules displaying vibrational resonance must signify a change in the dipole moment to be IR active for a significant absorption of an electromagnetic radiation in IR range to occur. Thus, the resultant IR absorbance ( $I_{Abs}$ ) of a molecule with changing dipole moment ( $d\mu$ ) across change in bond length ( $dx$ ) i.e.,  $\frac{d\mu}{dx} \neq 0$  is represented as:<sup>29,30,114,118</sup>

$$I_{Abs} \propto \left( \frac{d\mu}{dx} \right)^2 \quad (2.30)$$

Considering the different geometries of IREs for the ATR technique, the internal reflection could be conducted by either single or multiple reflection geometries, which differ in terms of number of reflection occurrence of the incident IR beam. Sample characterization and quantification information could be simply accessed through the detected IR peak absorbances and intensities which are in direct proportion to the solute concentration in the sample. The IR spectra is usually gathered in form of individual

reflections and depending on the IRE's configuration (Figure 2.6A), these are overall summated assuming negligible differences among individually reflected beams.<sup>29,30,114,118</sup>

Figure 2.6, panel B–D depicts the example of the obtained ATR-FTIR spectroscopic measurements and the corresponding calibration plots formulated with the concentration-dependent IR absorbance profile obtained experimentally.

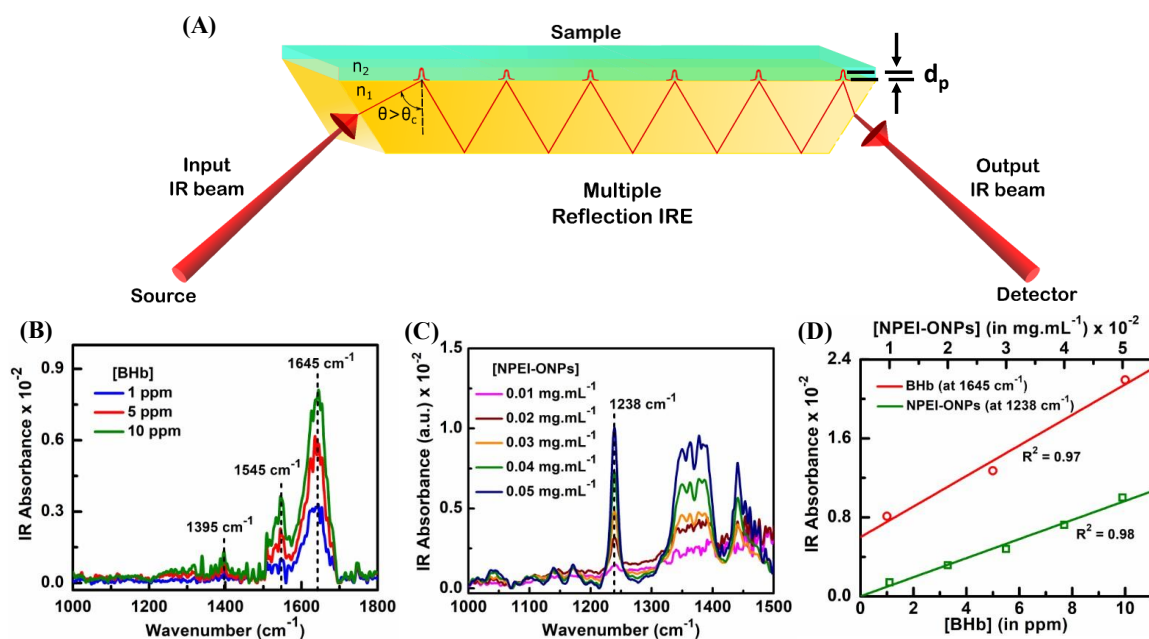


**Figure 2.6** (A) Schematic of the path of optical beam across the multiple reflection internal reflection element (IRE) geometry of the ATR-FTIR spectrometer. Reprinted with permission from Kaur et al. Springer Nature Singapore Pte Ltd. 2021.<sup>30</sup> Implementation of Beer's law in ATR-FTIR spectroscopy data acquisition for (B) bovine hemoglobin (BHB) protein, and (C) polymeric nanoparticles (NPEI-ONPs) studied in this thesis work as a function of concentration in aqueous media. (D) Calibration curve plot for BHB protein and NPEI-ONPs obtained using peak intensities at 1645 and 1238  $\text{cm}^{-1}$  absorption bands respectively. The offset noted in the calibration curve of BHB protein depicts the contribution of bending vibrational mode from residual water molecules around 1645  $\text{cm}^{-1}$ . While, NPEI-ONPs demonstrated minimal interference from the water absorption bands in 1238  $\text{cm}^{-1}$  region after performing spectrum subtraction with water spectra as reference.

The TIR process of an incident IR beam within the optically dense medium ( $n_1$ ) causes generation of an evanescent wave at the crystal boundary towards the optically rarer media ( $n_2$ ). The generated evanescent wave bears an electric field component of the incident IR radiation (E) which tends to exponentially decay in its strength with distance 'z' from the crystal surface facing towards the sample, and is depicted by following relation:<sup>29,30,114,118,119</sup>



$$E(z) = E_0 \exp\left(-\frac{z}{D_p}\right) \quad (2.31)$$

The beam penetration within the sample as a consequence of an evanescent wave bears a certain depth profiling (also called depth of beam penetration, 'D<sub>p</sub>') which is dictated by the distance 'z' where the amplitude of the electric field component of the incident IR radiation falls off with a factor of  $\left(\frac{1}{e}\right)$  times the electric field amplitude E<sub>0</sub> generated during initial evanescent wave occurrence, at the crystal-sample interface. The expression for 'D<sub>p</sub>' is given by:<sup>29,30,114,118,119</sup>

$$D_p = \left( 2\pi n_1 \omega_{IR(i)} \sqrt{\sin^2 \theta_i - \left(\frac{n_2}{n_1}\right)^2} \right)^{-1} = \frac{\lambda}{2\pi n_1 \sqrt{\sin^2 \theta_i - \left(\frac{n_2}{n_1}\right)^2}} \quad (2.32)$$

Here, n<sub>1</sub> and n<sub>2</sub> are the refractive indices of the crystal and sample media respectively, ω<sub>IR(i)</sub> represents the incident IR wavenumber, and θ<sub>i</sub> depicts the incident angle of the IR beam. Thus, D<sub>p</sub> is potentially influenced by the crystal and sample refractive index, and the incident angle of IR beam impinging over the crystal surface.

Thus, the ATR configuration successfully aids in the assessment of the water-based samples, since water is recognized to be a strong IR absorber making the experimentation difficult by conventional FTIR spectroscopy. This issue is addressed by probing the vibrational features with a reduced beam pathlength/beam penetrating depth within the sample, which is approximated to be of a few micrometers scale in the ATR mode.<sup>29,30,114</sup> These parameters are characteristic of the material property of which IREs are made off, and are required to be transparent for a specific IR wavelength range of probing majority of the molecular systems. Commonly used IRE materials are Germanium (Ge), Diamond, Silicon (Si), Zinc selenide (ZnSe), etc., and bear a characteristic refractive index (n<sub>1</sub>) and respective critical angle (θ<sub>c</sub>) depending on their intrinsic properties. Additionally, the net pathlength (L<sub>eff</sub>) of the absorbing component covered by the incident IR is determined by the product of the maximum number of internal reflections occurring within the ATR crystal and the D<sub>p</sub> of the incident beam, given by:<sup>29,30,114,118,119</sup>

$$L_{eff} = n_R \times D_p \quad (2.33)$$

where,  $n_R$  in the multi-reflection mode crystals is evaluated on basis of the crystal length ( $l_{IRE}$ ) and its thickness ( $t_{IRE}$ ), and the incident angle of IR radiation ( $\theta_i$ ).<sup>29,30,114,118,119</sup>

$$n_R = \frac{l_{IRE}}{2 \times t_{IRE} \times \tan \theta_i} \quad (2.34)$$

In our work, we have employed ZnSe IRE crystal material in a multiple-reflection mode within the variable angle ATR horizontal assembly for the acquisition of the IR absorbance data in the mid-IR region, where most of molecules show an active IR absorbance (crystal properties shown in Table 2.1). The total number of internal reflections happening within the ZnSe crystal with the surface facing the sample is calculated to be approximately 7 complete reflections (cumulatively 14 internal reflections), in accordance with the crystal dimensions (56 mm x 4 mm) being used.

**Table 2.1** Description of ZnSe ATR crystal properties. Reprinted with permission from Kaur et al. Springer Nature Singapore Pte Ltd. 2021.<sup>29,30,114,118,119</sup>

IRE Material	Refractive Index ( $n_1$ ) at 1000 $\text{cm}^{-1}$	Spectral Range ( $\text{cm}^{-1}$ )	Penetration Depth	Effective pH Range
			( $D_p$ ) in $\mu\text{m}$ at 1000 $\text{cm}^{-1}$ , $\theta_i = 45^\circ$ , $n_2$ (sample) = 1.4	
ZnSe	2.40	20,000-630	1.66	5-9

It is evident through equations 2.32–2.35 that the propagation of IR light from the crystal is predominantly steered by crystal properties, sample composition, etc. which simultaneously influences the effective absorbance of the resonating vibrational modes (i.e., both intensity and peak position). Thus, the transmission profile of the same sample does not correlate with the obtained absorbance spectra majorly due to inclusion of varying optical constant determinant throughout the absorbing incident wavenumber and the corresponding  $D_p$  of the electric field component within the obtained data profile. Therefore, the measured absorbance is subjected to exclusion and division by  $D_p$ ,  $n_R$ , and incident wavenumber to acquire a corrected spectral data. This factor is called an ATR correction factor ( $C_{ATR}$ ) denoted by:<sup>29,30,114,118,119</sup>

$$c_{ATR} \propto \frac{2n_1 \cos \theta_i}{n_R D_p \omega_{IR(i)}} \quad (2.35)$$

The IR spectra is treated by multiplying the obtained ATR absorbance ( $A_{ATR}$ ) with the  $c_{ATR}$  factor which is represented as:<sup>29,30,114,118,119</sup>

$$\text{Im}[\chi^{(1)}] = c_{ATR} A_{ATR} \quad (2.36)$$

Here, the  $\text{Im}[\chi^{(1)}]$  term is referred to the imaginary component of the electric field susceptibility, which is an indicative of the resonant absorbance of incident IR radiation by the respective molecular oscillators of the aqueous sample in direct contact with the ATR crystal.

### 2.3.1 Instrumental details and experimental protocol

The ATR-FTIR spectrometer (Bruker Optics Tensor II model, illustrated in Figure 2.7) used for conducting experiments constitutes one room temperature dependent deuterated L-alanine-doped triglycine sulfate (RT-DLaTGS) detector unit bearing a 6 mm aperture, included within the system. The sample scanning is performed with 7.5 kHz scanner velocity of the optics attached within spectrometer. The spectra were acquired using an ATRMax II variable angle horizontal ATR assembly with aligned highly focusing optics as procured from Pike technologies. An ATR crystal, trapezoidal ZnSe crystal is currently employed in our work with measured dimensions of around 56 mm x 10 mm x 4 mm (l x b x h or t) is mounted horizontally over the trough-based horizontal assembly. With the incident critical angle of impinging IR beam kept at  $\sim 45^\circ$ , the ZnSe crystal hence imparts total 14 internal reflections. The spectra are obtained in 900-1800  $\text{cm}^{-1}$  wavenumber range, spectral resolution  $\sim 2 \text{ cm}^{-1}$ , and the data points are averaged for 256 scans for 0.5 mL of sample volume, considering the atmospheric compensation parameter for both  $\text{H}_2\text{O}$  (as air moisture) and  $\text{CO}_2$ . These parameters could be manually incorporated and selected within a built-in OPUS software (version 7.5) and further data analysis could be performed readily including, spectral subtraction, smoothing of scattered data points by 13 smoothing number points, and spectral correction. Data smoothing enrolls the Savitzky-Golay filter algorithm. Spectral data correction involves implementation of three primary correction methods, viz., scattering correction, rubberband correction, and concave-rubberband correction. We have incorporated concave-rubberband correction method for spectral data processing and baseline

correction. The placement of FTIR spectrometer is within the air-conditioned room with temperature of  $22\text{ }^{\circ}\text{C} \pm 1\text{ }^{\circ}\text{C}$ . The spectrometer's humidity is maintained using silica beads in the range of 0–30%. The FTIR spectrometer is kept for warming-up and stabilization of the source, interferometer, and the detector for  $\sim 4\text{--}6$  hours of time before experimentation. The ATR crystal is subjected to rigorous cleaning initially with IPA (isopropyl alcohol), then with deionized water type-1 (resistivity  $18.2\text{ M}\Omega\cdot\text{cm}$  with pH 5.8), and were dried with warm air prior to their usage. The sequence of experimentation is adopted from the published procedure of Yang et al. to obtain reproducible and quality-based data.<sup>120</sup>

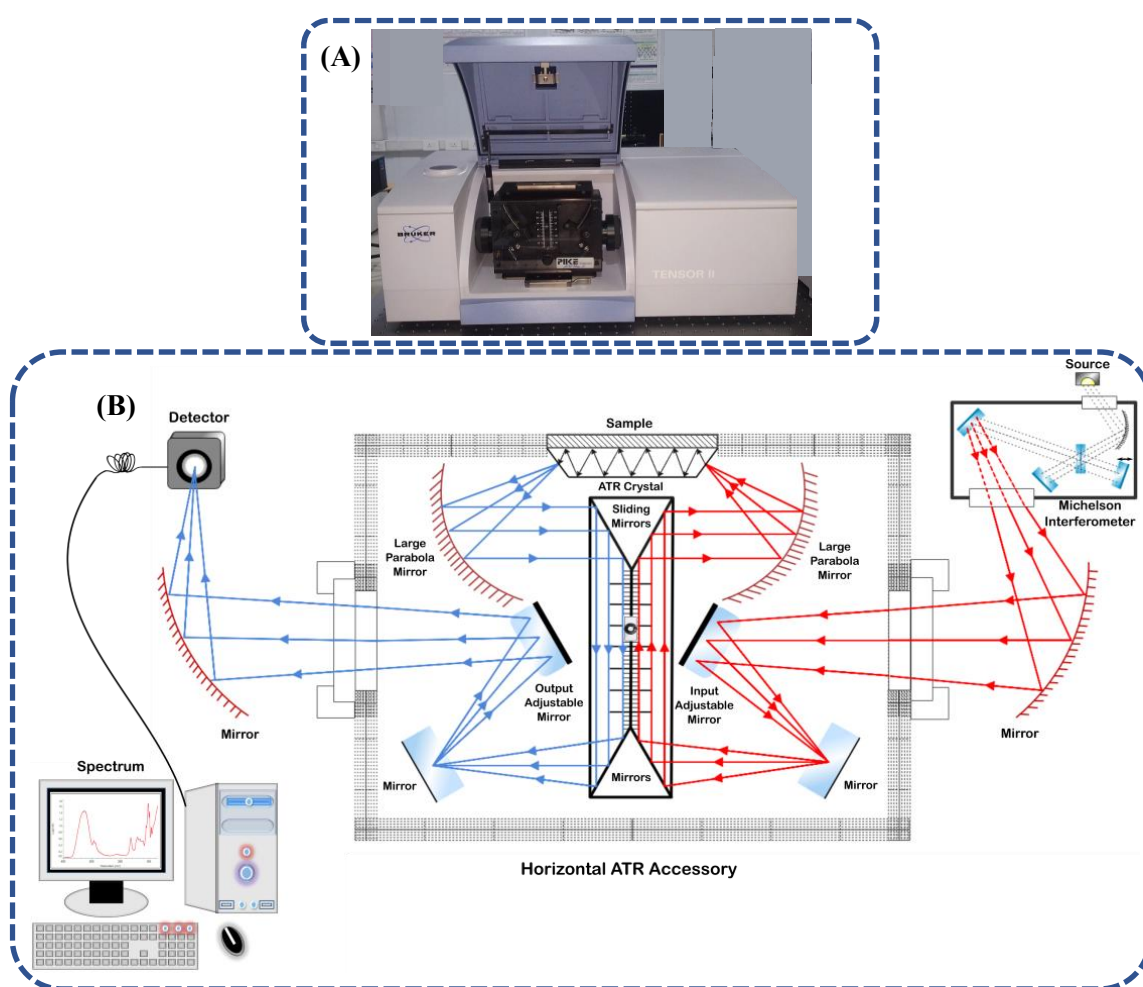


**Figure 2.7** (A) Digital photograph of the ATR-FTIR spectroscopic instrument in lab facility used in the present thesis work. (B) Optical layout of ATR-FTIR spectrometer attached with a variable-angle horizontal ATR accessory mounted with the trapezoidal ATR crystal, and the spectrometer interfacing with the OPUS software for data analysis. Reprinted with permission from Kaur et al. Springer Nature Singapore Pte Ltd. 2021.<sup>30</sup>

## 2.4 Surface tensiometry: Wilhelmy plate method

Surface tension (ST) measurements are a simple way to detect changes in the surface attributes of aqueous solutions, which can be used to forecast bulk-phase conditions. From the molecular-level perspective, it arises from the stronger cohesive forces experienced among the molecules and their near neighbour molecules present at the interface and below the surface region, in contrast to molecules residing within the bulk-phase. These surface/interfacial molecules projecting strong cohesive associations possess higher potential energy states than the molecules residing interiorly of the liquid system. As a result, these molecules tend to resist any force applied per unit length at right angles to the surface of the liquid. The net amount of work performed to equalize this potential energy barrier, where a certain amount of energy is expended to transfer the molecules underneath towards the interfacial region, defines the surface free energy of the liquid system per unit area of the surface expanded due to molecular movement across the two different phases (i.e., bulk and surface).<sup>121,122</sup> This property of the liquid sample is commonly known as the surface tension (ST).

The variation in ST values is a macroscopic response which essentially occurs due to surface adsorption of some molecular species and could be readily assessed experimentally. However, an active molecular adsorption requires the aqueous system to reach an equilibrium state in order to acquire a stable ST measurement. Therefore, the ST measurements are conducted by two different procedures depending on the compositional equilibrated state of the sample, i.e., steady-state ST (sample reached its equilibrated state) and dynamic ST measurements (ST changes monitored over time due to molecular re-distribution within the aqueous solution).<sup>121,122</sup> Steady-state ST is generally applicable for the large-sized particles/solutes, while dynamic ST is enrolled for studying molecular adsorption processes, induction time-scales (i.e., initiation of the surface adsorption process), energy barriers, adsorptive phase transitions, and for understanding the specific adsorption isotherms.<sup>123</sup> Dynamic ST is highly driven by the diffusion process of the molecular groups within the aqueous media from the bulk towards the surface. The dynamic activities are, however, largely influenced by the molecular composition/surface heterogeneities which eventually generates a longer surface tensiometry profile.

ST measurements are commonly known to be performed by various well-known classical methods/techniques which include capillary rise method, pendant drop method, spinning drop method, maximum bubble pressure method, Du Noüy ring method, and Wilhelmy plate method.<sup>121,122</sup> In our work, we have applied the Wilhelmy plate technique to perform both the static as well as dynamic ST measurements for distinct sample compositions. It is a microbalance-based technique that involves the immersion or withdrawal of the Wilhelmy plate (commonly platinum) to and from the liquid surface by applying an external vertical force to form an advancing or receding contact angle respectively. The ST will be applied on the plate in both the cases and is largely governed by the balancing among different forces acting on the plate at a time. In comparison to other methods, this method does not include any type of correction compensation, complex instrumental settings or methodologies, excludes capillary architectural-based heterogeneities, and can be conveniently used for general sample compositions in routine-use.<sup>121,122</sup>

Discussing about this method in depth, Wilhelmy plate method entails a thin vertical plate (made up of platinum (Pt), Pt-iridium alloy, mica, steel, or glass) which is initially kept in a stable position with respect to the horizontal plane of liquid surface. An external vertical force (F) applied over the plate is similar to the weight of the uplifted liquid meniscus formed in contact with the plate (i.e., the wetted length of the plate) as demonstrated in Figure 2.8. Therefore, quantification of this force (knowing the perimeter 'L' = 2(width 'w<sub>p</sub>' + thickness 't<sub>p</sub>') of the plate), is utilized to calculate the ST (γ) by using following relations:<sup>121,122</sup>

Force on the plate = Weight of plate + Surface tension force – Buoyant force, given by:

$$F = (m_p g) + 2(t_p + w_p)\gamma \cos \theta - \rho_t V_p g \quad (2.38)$$

$$F = 0 + 2(t_p + w_p)\gamma \cos \theta - 0 \quad (2.39)$$

$$\gamma = \frac{F}{L \cdot \cos \theta} \quad (2.40)$$

Here, 'θ' is the contact angle formed between the immersed plate and the liquid sample, 'g' is the force applied due to gravity, and 'm<sub>p</sub>' is the mass of the plate. The weight of the plate is initially set to a zero value while the impact of the buoyant force of the fluid is

removed by zeroing its impact over the plate at a certain depth of immersion performed manually.

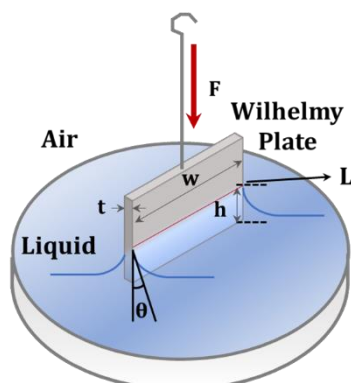


**Figure 2.8** Sketch of Wilhelmy plate method for surface tension measurement of sample.

This methodology conveniently allows the ST measurements of the samples contained in small-sized vessels/sample cells and hence require less sample volume to conduct measurements. However, the cleaning procedure needs to be taken care of, since there is a possibility of occurrence of errors during ST measurements due to some organic impurities in the laboratory environment. Therefore, prior to experimentation, the Wilhelmy plate is sufficiently cleaned with a good amount of organic solvents and de-ionized water to make sure the effectiveness of the measurements of the test samples, which are further repeated for establishing the reliability and consistency in the results. The occurrence of perturbations in the interfacial tension is strongly governed by the interfacial adsorption tendency of certain solutes present within the aqueous media primarily due to molecular diffusion process. Principally, the solute adsorbed at the air-liquid interface is quantitatively correlated in form of the Gibb's adsorption isotherm model. Incorporating simply the known ST values within the Gibb's equation, one can estimate the molecular surface excess property ( $\Gamma'$ ), which is given by:<sup>121-125</sup>

$$\Gamma' = -\frac{1}{nRT} \frac{\partial \gamma}{\partial \ln c_i} \quad (2.41)$$

where,  $\gamma$  represents the measured surface tension,  $n$  is referred to the number of adsorbate species present at the interface whose concentration is correlated with  $c_i$  (referred to the mole ratio of solute ( $n_i$ ) and solvent ( $n_1$ ) for dilute solutions),  $R$  is gas constant ( $8.314 \text{ J.mol}^{-1}.\text{K}^{-1}$ ), and  $T$  is the constant room temperature at which an experiment is being conducted. For ionic solutes,  $n$  is considered equivalent to 2.<sup>121,122,124</sup> Here, the molecular

surface excess ( $\Gamma'$ ) is defined as the difference between number of solute molecules occupying the interface and that present in the bulk-phase of the aqueous media, considering an equal occupancy of the solvent molecules in both the phases. [28-32] Thus, the above relation exhibits that the solute occupied interface ( $\Gamma' > 0$ ) reduces the ST, while for surface-inactive solutes ( $\Gamma' < 0$ ) ST increases even upon increasing the bulk amount of the solute molecules.<sup>121,122</sup>

Interfacial tension/surface tension (ST) determination could be readily conducted for any sample regardless of its chemical composition and the rate of interfacial adsorption depending on its molecular constituencies. ST deduction is widely applicable as predominant force in microfluidic flow channels, ST measurements of body fluids for medical diagnosis, identifying the effectiveness of coating materials, liquid purity, identifying critical micellar concentration point of solute molecules at industrial level, etc.<sup>121,122</sup>

## **2.5 Zeta-sizer and potentiometry measurements**

Both the size and potential measurements are estimated using Zetasizer Nano-ZS90 instrument (Malvern Panalytical Ltd.), which operates with a 4mW He-Ne laser power source generating an incident beam of 633 nm wavelength (Figure 2.9, panel A and B). The detection unit for analyzing the scattered light is aligned at 90° angle within the ZS90 system. The zeta potential measurements are formulated from the measured electrophoretic mobility data of the particles in an aqueous media at an applied voltage in Volts using majorly two different approximation models under Henry's function depending upon the particle size and sample characteristics, i.e., Hückel approximation (for non-polar systems with particle radius <10 nm), and Smoluchowski approximation (for ionic media like water, for particle radius >10 nm).<sup>126,127</sup> The measurement of average particle size distribution of different materials for instance nanoparticles, micelles, protein molecules, emulsions, etc. within the dispersed media is carried out on the principle of Brownian motion of the molecules and the acquisition of their scattered light. For the particles with size  $> 1/10^{\text{th}}$  of incident wavelength, angular variations are observed in the intensity of the scattered laser light through the sample which is in inverse relation with the particle size, viz., small sized particles scatter at large angles and large particles scatter light with smaller angular values. However, when the particle size is less



than  $1/10^{\text{th}}$  of the incident wavelength, the angular dependency of the scattered light is not there. Correspondingly, the relative intensity variation plot is obtained with respect to the particles of distinct sizes present within the aqueous media. The hydrodynamic radius ( $R_H$ ) of spherical particles can be readily calculated using the Stokes-Einstein equation as:<sup>126,127</sup>

$$R_H = \frac{k_B T}{6\pi\eta D_t} \quad (2.42)$$

Here, the  $R_H$  defines the average particle radius that is evaluated on the basis of the tendency of particles to diffuse in the fluidic system i.e., the translational diffusion coefficient ( $D_t$ ),  $k_B$  is the Boltzmann constant ( $1.381 \times 10^{-23}$  J/K), T, and  $\eta$  are represented as temperature and the absolute viscosity of the sample, respectively.

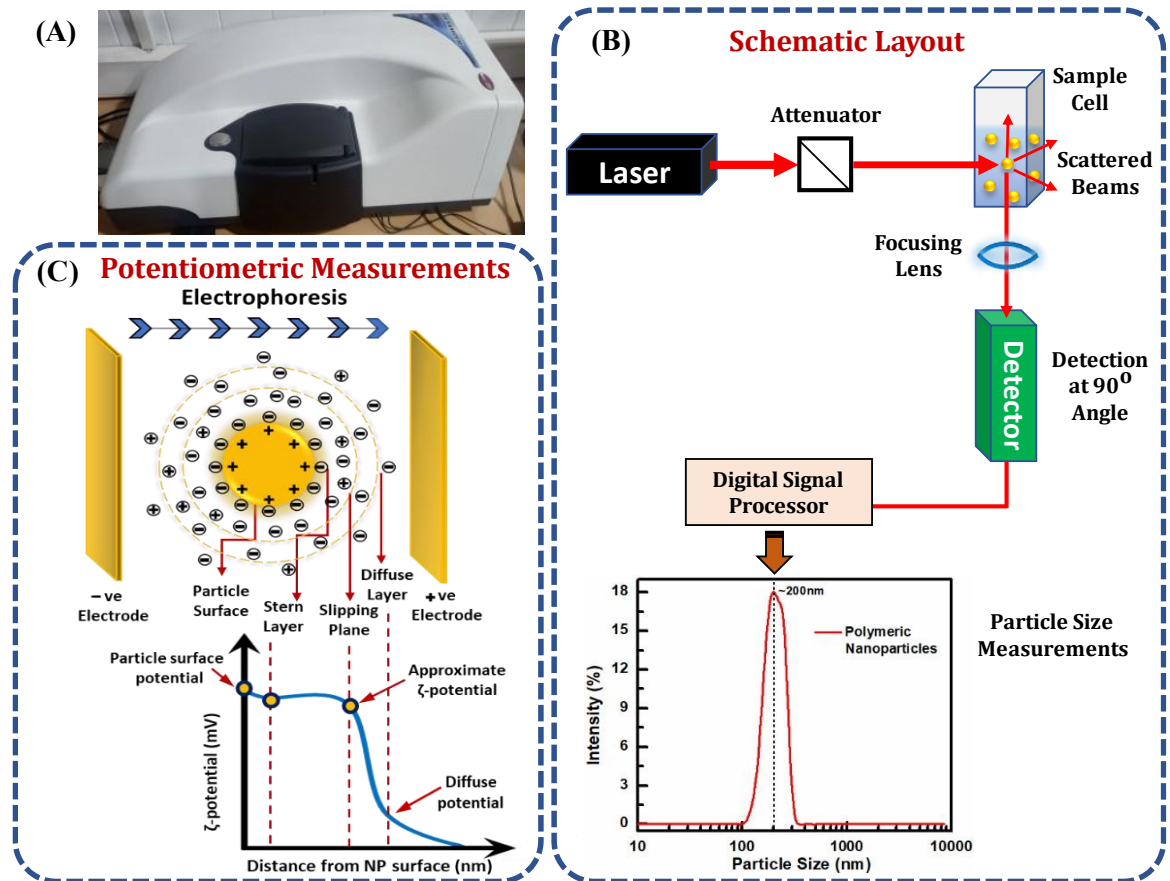


**Figure 2.9** (A) Picture of the zeta-sizer instrument ZS90 from Malvern used for the study. (B) Schematic optical layout of the ZS90 set-up for measuring particle size and electrophoretic mobility of the particles within sample. The scheme showcase the particle size measurement plot with intensity depicting the average values. (C) Illustration of the charged particle under the influence of applied voltage across the gold plated electrodes to analyse the electrophoretic mobility and zeta-potential values (in mV) over the particle surface.

The stability of dispersive media relies on the inter-particle interactions and the corresponding particle surface charge. Introducing any ligand into the dispersive media tends to alter the dielectric property of the suspension as well as the particle characteristics upon conjugation. The random motion and the momentum gained by the particles within the aqueous state is determined primarily by the particle size, such that, the larger particles tend to move slower while smaller particles acquire higher speed. An average charge sustained by a particle is measured indirectly through the evaluation of the particle mobility under an applied electric field, which is then utilized to theoretically quantify the zeta potential ( $\zeta$ ) values of the particle suspension.<sup>126,128</sup> Thus,  $\zeta$ -potential is considered to be an extrinsic property of the system under study which is governed by its composition, solvent ionic strength, material coating, and aqueous-phase conditions. It inspects the potential-dependent hydrodynamic shearing within the boundary of ions (slipping plane) existing in the inner stern (compact) region and outer diffuse region surrounding the particle, as illustrated in Figure 2.9C.<sup>126,128</sup> Thus, the measure of the  $\zeta$  value relies on the extension of discretely charged functional groups of the particle within its diffused boundary layer. Any changes incurring over the particle surface in terms of analyte adsorption, chemical conjugation, or interaction with dispersed ions within the solution; results in the variation of the magnitude or sign of obtained potentiometry values. Particles with zeta-potential (or electrophoretic mobility) values beyond  $\pm 30$  mV are referred to form highly stable dispersive media without any aggregation.<sup>126-128</sup> This arises due to predominance of electrostatic repulsions at higher potential magnitude which deters the aggregate formation. In our study, for characterizing nanomaterials in aqueous media, Helmholtz-Smoluchowski approximation model has been considered for potentiometric analysis, which is represented by the following equation as:<sup>126,127</sup>

$$U_{\text{elec}} = \frac{4\pi\epsilon\epsilon_0\zeta}{\eta_f} E \quad (2.43)$$

Here,  $\epsilon$  and  $\epsilon_0$  represents the dielectric constant of media and permittivity of free space respectively (in  $\text{kgmV}^{-2}\text{s}^{-2}$ ), while  $\eta_f$  depict the fluid viscosity ( $\text{kgm}^{-1}\text{s}^{-1}$ ) and  $U_{\text{elec}}$  is the particle velocity ( $\text{ms}^{-1}$ ) under the applied electric field  $E$  ( $\text{Vm}^{-1}$ ) across certain distance, where  $U_{\text{elec}}$  ratio  $E$  defines the electrophoretic mobility of the particles.

## **2.6 Other experimental characterization techniques**

### **2.6.1 Nuclear magnetic resonance (NMR) spectroscopy**

NMR spectroscopy is primarily used for the structural characterization of synthesized compounds in our study, by observing the impact of an externally incident magnetic field and radio frequencies over the sample. Depending upon the composition of the compound, the radio frequencies are characteristically absorbed by the nuclei of atoms bearing spin states of  $^1\text{H}$ ,  $^{13}\text{C}$ ,  $^{31}\text{P}$ , etc. In our work, we have employed  $^1\text{H}$  (at 400 MHz) and  $^{13}\text{C}$  (at 100 MHz) NMR. Before performing NMR experiments, the dried powdered sample is dissolved in the deuterated solvents ( $\text{CDCl}_3$ , deuterated chloroform in our work) in a thin round bottom cylindrical glass tubing. Sample tubes are placed inside the holder of the NMR spectrometer (JEOL JNM-ECS). The data is observed in terms of chemical shifts ( $\delta$ ) and the obtained NMR spectrum is evaluated as parts per million (ppm) which is done via the known chemical shift values of an internal standard tetramethylsilane [TMS,  $\text{Si}(\text{CH}_3)_4$ ,  $\delta=0$  ppm]. Analysis of the obtained NMR spectra involved integration of peaks using Delta processing software by JEOL USA, version 4.3.6.

### **2.6.2 Scanning electron microscopy (SEM)**

Imaging of the polymer film topography is done using SEM instrument (JEOL, model number 6610LV, Japan, with 10 kV operating voltage) at the 2  $\mu\text{m}$  scale. The glass slides with coated films were initially subjected to platinum sputtering to prepare a charged surface and acquire optimum images via electron beam scanning. The platinum coating is performed using sputter auto fine coater (JEOL JFC-1600).

### **2.6.3 Atomic force microscopy (AFM)**

The AFM instrument (MultiMode 8, Bruker, USA) is utilized in the experimental characterization of the solid polymer films for their approximate film thickness analysis and in identifying the morphology of the synthesized nanoparticles. The AFM technique is operated in a non-contact mode tapping mode for both thickness analysis and surface morphological characterizations. A silicon tip of  $\sim 10$  nm radius is used for tapping mode analysis. For film thickness measurements, the scratching method was performed.



### **Probing interfacial adsorption of biomacromolecules and their impact on water molecular network at the air-water interface**

In the foremost chapter of our research work, we will be presenting the fundamental studies of the molecular adsorption at the interface using SFG-VS and surface tension method of the two bio-macromolecules i.e., bovine hemoglobin (BHb) protein molecules and double-stranded DNA (dsDNA) molecules at the air-water interface. Our study aims to understand the interfacial molecular behavior, adsorption mechanism, and the kinetics of bio-macromolecules in an aqueous media. Biomolecular adsorption at interfaces is an intrinsic behavior of both the protein and DNA molecules due to their amphiphilic property. The adsorption process brings about some conformational changes in the biomolecules as well as influence the interfacial environment, which is known to decide the subsequent biological fate of macromolecules. Thus, biomolecular adsorption is a necessary process that arises over the surface of different biomedical devices. The result in certain important interfacial properties attributes viz., molecular kinetics, hydrophilicity, hydrophobicity, viscosity, molecular phase-separation, self-assembly of molecules, micellar formation, surface tension changes, surface adsorbing tendency, molecular condensation, molecular orientation, etc. Thus, knowing the interfacial behavior and molecular conformation of biomolecules are crucial. This chapter includes two sub-sections covering independent studies on protein (section 3.3) and DNA molecules (section 3.4). Here, in section 3.3 (work published: Chaudhary and Kaur et al. *Appl. Spectrosc.* 75, 1497-1509, 2021),<sup>129</sup> we have investigated the real-time interfacial adsorption dynamics of the BHb protein molecules and their influence on the interfacial water structure at the isoelectric point of BHb i.e., pH 5.8, by varying protein's concentration. In the second section 3.4 includes the study, where we are reporting the molecular signatures of dsDNA at physiological pH of 7.4 as a function of DNA concentration and in the presence of free-radical concentration.

### 3.1 Introduction

The molecular adsorption process at the interfacial region is simply defined as the accumulation of molecular entities at the surface or interface. The process of interfacial molecular adsorption is a primitive step that is governed by fundamental forces ensuing among the molecular groups during their surface coverage, thus affecting the surface free energy. It includes long-range forces originating from the attractive van der Waals (vdW) and repulsive electrostatic interactions; short-range forces resulting from steric, solvent interactions, and charge-based association. Protein and DNA molecules form the major constituent of the cell where, due to their intrinsic structural and functional flexibility, they enrol themselves in a variety of cellular functions such as gene expression, phase-transition, molecular condensate formation, signalling, molecular transport, binding, etc. During such events, they often encounter different interfaces and tend to undergo a spontaneous transition from their native three-dimensional architecture. This has a significant role in understanding the pre-biotic chemistry of such interface-adsorbing biomolecules. In addition to its biological implications, the adsorption of these bio-macromolecules at the interface is ubiquitous and plays an unprecedented role in a wide application area involving biomaterial implantation, bio-catalysis, bio-sensor fabrications, purification, drug design and its delivery.<sup>130-132</sup> The surface adsorption of these bio-macromolecules is highly governed by several factors like the nature of an interface, pH of the solution, concentration, temperature, sample age, and their native molecular structure or sequence.<sup>8,54,61,66,133</sup> Aqueous interfaces are the most studied systems for several biomedical engineering applications. The air-water interface is referred to as hydrophobic in nature and resultantly attracts the hydrophobic moieties readily towards the interface.<sup>54,134-136</sup> Water is considered as an active medium of biological system for playing a key role in the functionality, stability, structural changes, and dynamics of the biomolecules.<sup>54,67,134,137-139</sup> The precise influence of biomolecules on interfacial water structure is recognized primarily at the level of hydrogen bond strength, molecular hydrophobic propensity, and molecular crowding.<sup>134,138,139</sup> Thus, *in-situ* monitoring of the molecular structure of the protein and DNA molecules during the interfacial adsorption process in aqueous media is crucial to understand to be applied in many transdisciplinary areas of fundamental research.

## **3.2 Experimental methods and procedures**

### **3.2.1. Material requirements**

The BHb protein sample was procured from Sigma-Aldrich Co. Similarly, a low molecular weight Salmon sperm double-stranded DNA (dsDNA) was obtained from Sigma-Aldrich Co. These samples were used without further modification or purification. Both the samples were stored at 4°C temperature. The pre-defined crystals of Tris-HCl salt were purchased from Sigma-Aldrich. All the solvents and reagents used for the experimentation or cleaning purposes were purchased from Sigma-Aldrich Co. and MERCK. All samples were prepared in Millipore ultra-pure water type-1 with a resistivity of 18.2 MΩ.cm and pH  $5.8 \pm 0.1$  at 22°C. All glassware and Teflon sample cell used in the experiment were treated with piranha solution (sulphuric acid: hydrogen peroxide or H<sub>2</sub>SO<sub>4</sub>:H<sub>2</sub>O<sub>2</sub> in 3:1 ratio composition) and rinsed multiple times with Millipore water before their usage.

### **3.2.2. Sample preparation method**

To conduct the protein-based interfacial adsorption studies (for section 3.3 ahead), the BHb protein solution was prepared in the pristine water conditions (i.e., at pH 5.8), which is also rendered as the isoelectric point of BHb in the aqueous media. BHb concentration solutions were prepared by the dilution method from the freshly prepared concentrated stock solution of BHb of 1000 parts per million (ppm). This was done to maintain the consistency of the sample preparation time and minimize any concentration changes.

The studies on dsDNA (for section 3.4 ahead) were performed using the Salmon sperm DNA in powdered form and dissolving the sample in 20 mM of Tris-HCl buffer at the physiological pH of ~7.4. The experiments were performed at the two different concentrations i.e., 100 and 300 ppm. The diluted concentration was prepared from the stock solution sample of 300 ppm. The H<sub>2</sub>O<sub>2</sub> solution was added to the dsDNA concentration of 300 ppm in two volume percentages i.e., 0.1 and 0.2 v/v%, respectively.

### 3.2.3. Surface tension measurements

The surface tension (ST) measurements were performed using Biolin Scientific KSV NIMA LB apparatus. The samples of 7 mL volume were placed in a circular Teflon sample cell (45 mm diameter and 7 mm depth). The ST measurements were conducted with a Wilhelmy plate method with an interval of 300 sec between two consecutive readings. This experimental methodology was employed for the BHb protein characterization in an aqueous media (discussed in section 3.3). The ST value of pristine water has been taken as a reference and all the measurements were conducted at the room temperature of  $\sim 22 \pm 1^\circ\text{C}$ . The platinum Wilhelmy plate was thoroughly cleaned priorly with ethanol around 3–4 times, rinsed with ultrapure water, and then dried using warm air.

### 3.2.4. Sum frequency generation vibrational spectroscopy (SFG-VS)

The current study has been performed using a commercial SFG spectrometer (Ekspla, Lithuania). The details of the experimental set up are provided in chapter 2 (section 2.2.2). The samples (7 mL in volume) taken in a Teflon cell of 45 mm in diameter for SFG-VS evaluation. The SFG spectra were acquired for a broad region of  $2750\text{--}3800\text{ cm}^{-1}$  including both the CH- and OH-stretching regions. Experiments on BHb protein molecules were performed in SSP polarization combination, while the SFG experiments of dsDNA molecules were done in three polarization schemes i.e., SSP, PPP, and SPS. Here S and P denote electric field polarization of light to be perpendicular and parallel to the plane of incidence, respectively. The first letter denotes polarization mode of output SFG beam, second letter denotes polarization mode of the incident visible beam, and the third letter depicts the polarization mode of incident IR beam. The spectral data was gathered with average of 200 pulses per step and  $5\text{ cm}^{-1}$  step size. The experiments were performed at room temperature ( $\sim 22 \pm 1^\circ\text{C}$ ). The SFG spectra were evaluated and fitted using the Lorentzian expression (details can be seen in chapter 2, section 2.2, equation 2.16).



### **3.3 Probing the bovine hemoglobin adsorption process and its influence on interfacial water structure at the air-water interface**

#### **3.3.1 Background**

The complex structure of protein molecules, bearing both hydrophilic and hydrophobic residues, tend to occupy the interfaces and affect the water molecular network in their vicinity during the adsorption process at the air-water interface. This paradigm has been constantly the point focus in different research areas.<sup>134,138-142</sup> Most of the information about the protein structure has been extracted by spectroscopic tools such as nuclear magnetic resonance (NMR), fluorescence spectroscopy, circular dichroism, infrared and Raman spectroscopy.<sup>143-145</sup> The adsorption characteristics of protein molecules and their kinetics have been rigorously investigated by ellipsometry, rheology, thermodynamics, tensiometry and potential measurements in several potential studies.<sup>50,61,146,147</sup> Their results explained the relation of surface pressure, potential and thermodynamic energetics of water molecules with the anchoring of the protein molecules to the surface. These spectroscopic tools probe the structure of the protein in the bulk phase of the aqueous solution and provide the information about the ensemble average number of molecules, which represents the bulk-phase. Due to lack of their surface specificity and sensitivity, these spectroscopic tools depict a weaker potential to probe the protein structure and its kinetics in real time upon interfacial adsorption. Moreover, most of these techniques require harsh sample treatment, which dispose the biomolecules like proteins to either re-structure, modify, or denature prior to experimentation.

Utilizing SFG-VS as label-free technique, many fundamental studies related to protein structure and its behaviour have been evaluated at the aqueous interface. Wang et al. used SFG spectroscopy to investigate the conformational changes of bovine serum albumin (BSA) molecules by varying their surface coverage at air-water interface.<sup>54</sup> Yan et al. demonstrated through their work, by employing chiral SFG-VS to monitor the protein self-assembly process and the real-time kinetics of proton exchange among protein and water molecules at the air-water interface.<sup>50,56</sup> Subsequently, SFG studies on the protein molecules as function of pH were carried out which signified that the molecular-level re-structuring of the interfacial water molecules could depict the

isoelectric point of the proteins under study.<sup>8,56,133</sup> Later, Devineau et al.<sup>67</sup> reported a notable variation in the isoelectric point (IEP) of hemoglobin (Hb) upon adsorption at air-water interface relative to its bulk value by probing the orientational flipping of water molecules at the interface using heterodyne SFG spectroscopy. This change in IEP of protein molecules at the interface (as distinct from the bulk) was ascribed to the alteration in the protein structure. A kinetics-based study of BSA protein molecules using SFG and surface tensiometry was presented by Li et al.<sup>73</sup> at the air-water interface in absence and presence of salt with an aim to demonstrate the protein salting-up effect. It was illustrated through their work that the presence of salt accelerated the interfacial adsorption of BSA protein molecules as a function of time. Through the conscientious reviewing of various SFG-based studies targeting protein interfacial behavior, the kinetics of protein adsorption and the associated dynamics of interfacial water network at the point of zero net charge of protein molecules at the interface is still lacking and requires critical investigation. Here, the point of zero net charge-based investigation is crucial as it represents the pristine conditions of water where no salts or ions have been added to maintain the charge neutrality within the protein's structure. We have illustrated the steady-state and growth kinetics of the protein denaturation process upon adsorption and its effect on the hydrogen-bonding network of interfacial water molecules using SFG spectroscopy. Surface tension dynamics measurements were also conducted to probe the propensity of the protein molecules and their activities at the air-water interface.

### **3.3.2 Results and discussion**

#### **➤ Evaluating concentration-dependent BHb surface coverage by SFG-VS**

The interfacial adsorption process of BHb protein molecules were evaluated using SFG-VS in both CH- and OH-stretch regions as a function of BHb concentration varying from 1 to 800 ppm. The SFG measurements were carried out immediately after the preparation of the solution for required concentrations without waiting for the surface equilibrium. The CH-stretch region showcases the signature of hydrophobic moieties of protein molecules, while the OH-stretch region intends to probe the impact of protein adsorption on the hydrogen-bonding (H-bonding) network of the interfacial water structure.

All the SFG spectra have been fitted using Lorentzian equation as discussed in the experimental section 2.2, and the corresponding fitting tables are provided in the Appendix section A. Figure 3.1A represents the OH-stretch region of the SFG spectra. Here, the sharp distinct feature observed at  $3705\text{ cm}^{-1}$  is attributed to free OH-stretch mode (or dangling OH bond) of the interfacial water molecules facing towards the air.<sup>8,133,148,149</sup> The other two broad peaks located at  $\sim 3225\text{ cm}^{-1}$  and  $3400\text{ cm}^{-1}$  represent H-coordinated region depicting the strongly and weakly H-bonded water molecules, respectively. Here, we would like to elaborate a bit more on the concept of the OH-coordinated region assignment. Priorly, the origin of these broad spectral features in the OH-stretch region were assigned respectively as “ice-like” and “water-like” water molecules.<sup>8,133,150,151</sup> Later, Sovago et al.<sup>152</sup> presented a new insight about the origin of the double-peak features of water structure using SFG spectroscopy by considering the isotopic dilution experiment. It is revealed that the observed double-peak structure originated primarily due to the coupling effect between the OH-symmetric stretch and the overtone of OH-bending mode. Further, the notion of intramolecular or intermolecular coupling in OH-stretch region was equally supported by some theoretical and experimental findings of other groups.<sup>153-155</sup> Recently, it has been established that qualitatively, we can analyse our findings in OH-stretch region based on the relative intensities of both the peaks and the red shift in the lower frequency peak ( $\sim 3225\text{ cm}^{-1}$ ) to predict the strengthening of H-bonding among the water molecules at the interface.<sup>153,156,157</sup> With an increase in BHb concentration, we were able to notify a significant decrease in the intensities of both  $3450$  and  $3705\text{ cm}^{-1}$ . A decrease in the  $3450\text{ cm}^{-1}$  corresponds to a decrement in the contribution from the weakly H-bonded water molecules as the BHb concentration is raised. Similarly, lowering of the free OH feature at  $3705\text{ cm}^{-1}$  represents an increased molecular surface coverage. This clearly indicates the role of diffusion and the impact of surface coverage of the BHb protein molecules on the H-bonding environment of the interfacial water molecules. However, surprisingly for the strongly coordinated feature of water molecules (centered at  $\sim 3225\text{ cm}^{-1}$ ) depicted a red-shift in its peak position towards  $\sim 3160\text{ cm}^{-1}$ , which is clearly depicted in the contour plot represented in panel B. Here, based on the obtained SFG intensity values after fitting, the red colour bar indicates the maximum value seen corresponding to a particular wavenumber. This peak shift is attributed to the strengthening of the H-bonding of water molecules.

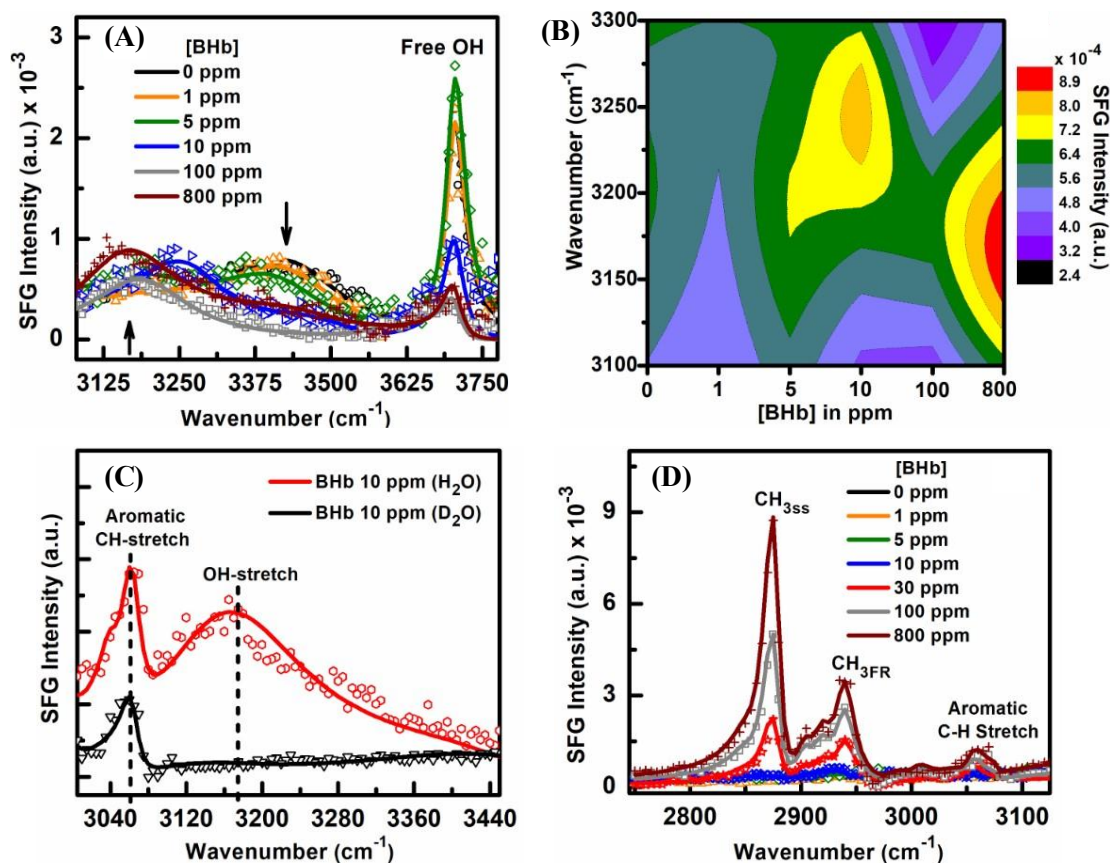


**Figure 3.1** (A) SFG-VS spectra of BHB protein molecules as a function of concentration at air water interface in OH-stretch region. (B) Contour plot of the observed red-shift in the  $\sim 3225\text{ cm}^{-1}$  wavenumber intensity with an increment in BHB concentration. The color bars are respectively associated with the observed SFG intensity from lower (black) towards higher (red) values. (C) SFG spectra of 10 ppm BHB concentration at air-water and air- $\text{D}_2\text{O}$  interface obtained after achieving equilibrium at  $\sim 5000\text{ s}$ , in both OH- and aromatic CH-stretch modes. (D) SFG-VS spectra of BHB protein with increasing bulk concentration (0–800 ppm) observed in CH-stretch region at air-water interface. The solid lines here represent the fitting data and scattered points depict experimental values. Reprinted with permission from Chaudhary and Kaur et al. *Appl. Spectrosc.* **75**, 1497-1509 (2021).<sup>129</sup>

However, the occurrence of peak red-shifting in the OH-stretch region could possibly be the cause of a contribution from either the aromatic CH-stretch or NH-stretch in the region of peak shifting, which also are the part of the molecular structure of the protein. This may arise due to the conformational changes of BHB molecules at the surface during or after adsorption. To confirm the exact origin of the feature, the SFG spectrum of BHB is acquired in the deuterated water ( $\text{D}_2\text{O}$ ) solution to suppress any interfering contribution from the OH-stretch features (Figure 3.1C). The SFG spectra shown in panel C is for 10 ppm BHB solution that is acquired after the surface equilibrium was reached (approximately after 5000 s). Interestingly, one could identify that the spectral signature observed for 10 ppm after surface equilibrium of 5000 s (panel C) is

very different than the SFG response recorded immediately after pouring the sample in the sample cell (panel A). Here, the term “equilibrium state” is intended to represent a state where no further changes are expected in the protein’s structural features or intensity in OH-stretch region in the SFG spectra at the interface. The differential spectral profile for the 10 ppm BHb has appeared primarily due to the change in molecular surface coverage with time and rearrangement of protein molecules at the interface. This aspect has been further elaborated in detail in the temporal state evolution (Figure 3.2).

From Figure 3.1C, we observed a prominent signature of the aromatic mode at  $\sim 3064\text{ cm}^{-1}$  that is assigned to  $\nu(\text{=CH})_{20b}$  representing the aromatic amino acids present in the protein structure (i.e., either from Tyr, Trp, or Phe). This feature is clearly visible for both  $\text{D}_2\text{O}$  and  $\text{H}_2\text{O}$  based SFG spectra of 10 ppm BHb. The NH-stretching modes tend to show a constructive interference as an overlapped resonant signal in region  $3100\text{--}3600\text{ cm}^{-1}$  and is usually identified around  $\sim 3150\text{ cm}^{-1}$  and  $\sim 3300\text{ cm}^{-1}$ .<sup>158-160</sup> This feature is absent in the 10 ppm BHb spectra in  $\text{D}_2\text{O}$ . Nevertheless, there could be a possibility of NH- to ND-stretch mode exchange after preparing the deuterated solution of protein sample. This observation has been demonstrated by Yan group using the chiral SFG spectroscopy platform.<sup>161</sup> Meister et al. also depicted the signature of NH-stretch mode from hydrophobin protein molecules by employing the conventional SFG spectroscopy at the air- $\text{D}_2\text{O}$  interface.<sup>162</sup> Yet, in our observed SFG spectral profile (panel C), we did not notice any feature from the NH-stretch mode from BHb protein in  $\text{D}_2\text{O}$  solution. Although it is not easy to detect the response of NH-stretch mode by using the conventional SFG spectroscopy, by considering a completely flat response in the NH-stretch region in our SFG spectrum, we have neglected the contribution of NH-stretch mode in our discussion. This conclusively suggests that the red-shifted peak appearing at the lower frequency side in the OH-stretch region is feasibly a signature from strongly H-bonded water molecules, which is a clear indication of the significant re-structuring of the interfacial water molecular network due to BHb adsorption. It is important to discuss here that the water molecular orientation and re-structuring is known to be quite sensitive towards the presence of any kind of interfacial or molecular-level charges or the occurrence of electrostatic interactions at the interface. Several studies have reported the presence of charge at the interface to be a major contributory factor in enhancing the water signal in OH-stretch region.<sup>8,56,133</sup> However, we did not observe any enhancement here which poses to be a clear signature of the existence of a point of zero net charge on

the protein molecular structure at our working pH of  $\sim 5.8 \pm 0.1$ , concerning the interface-based protein adsorption.

BHb is a tetrameric protein molecule (structure PDB 2QSP) which consists of two  $\alpha$ - and two  $\beta$ -chains carrying  $\sim 376$  methyl ( $\text{CH}_3$ ) groups and 50 aromatic residues in both the chains. The CH-stretch region is further interpreted in range  $2750\text{--}3150\text{ cm}^{-1}$ , to evaluate the occurrence of hydrophobic signatures (including both methyl and aromatic features) of BHb protein molecules at the interface as function of concentration (panel D). The methyl features are observed in range of  $2800\text{--}3000\text{ cm}^{-1}$ , while the aromatic CH-stretch is primarily seen in  $3000\text{--}3100\text{ cm}^{-1}$  region. No CH-stretch signatures were seen for lower concentrations of BHb protein i.e., 1, and 5 ppm, while slight perturbations are seen for 10 ppm in the CH-stretch region at the air-water interface. On raising the BHb bulk concentration further, remarkable changes were seen in the aliphatic and aromatic CH-stretch regions and simultaneously in OH-stretch region (panel A) for BHb concentration beyond 10 ppm. The appearance of the peak positions at  $2875\text{ cm}^{-1}$  and  $2940\text{ cm}^{-1}$  are ascribed to symmetric stretching ( $\text{CH}_{3\text{SS}}$ ) and Fermi resonance ( $\text{CH}_{3\text{FR}}$ ) modes of methyl groups, respectively.<sup>67</sup> The presence of vibrational modes from aromatic amino acid residues of BHb molecules is assigned to the peak contributions from  $3005\text{ cm}^{-1}$ ,  $3041\text{ cm}^{-1}$ , and  $3055\text{ cm}^{-1}$  and are attributed to  $2\nu(\text{C}=\text{C})_{\text{S}}$  (combination band of the aromatic C=C stretching mode),  $\nu(=\text{CH})_{20\text{a}}$ , and  $\nu(=\text{CH})_{20\text{b}}$ , respectively.<sup>158-160</sup> The details of the fitting parameters are given in Appendix A. The dominant presence of  $\text{CH}_{3\text{SS}}$  mode is an indication that the methyl entities are aligned along the surface normal, which is in accordance with the recent heterodyne-SFG measurements on Hb molecule at the air-water interface.<sup>67</sup>

Several experimental studies have reported the concentration-dependent protein molecular surface coverage to be nearly three times on raising protein concentration from 5 ppm to 1000 ppm.<sup>163,164</sup> Similar report suggested the surface coverage of Hb molecules to raise by five times on varying protein concentration from 6 ppm to 65 ppm to adsorb proteins at the quartz surface.<sup>165</sup> For the case of BSA protein molecules, it has been reported that the molecular surface coverage rises to  $0.2\text{ }\mu\text{g}\cdot\text{cm}^{-2}$  for 1000 ppm in comparison to the  $0.1\text{ }\mu\text{g}\cdot\text{cm}^{-2}$  for 5 ppm concentration.<sup>166,167</sup> From our results, we observed that according to the SFG intensity of  $\text{CH}_{3\text{SS}}$  mode, the intensity for 800 ppm concentration was approximately two times to that observed for 5 ppm BHb

concentration. Hence, our results indicate that the protein molecules may have unfolded significantly at lower concentrations as compared to higher protein concentrations. The lower concentrations provide sufficient spatial opportunity to the molecules to spread without encountering hinderance from the neighboring protein molecules at the interface.<sup>54</sup> The higher protein concentrations, however, tend to achieve limited unfolding or acquire a partially folded state, as the unfolding tends to be hindered by the presence of protein-protein interactions at the surface.<sup>136</sup>

### ➤ **Temporal evolution measurements of BHB adsorption by SFG-VS**

The BHB protein surface coverage was seen to be instantaneous for higher protein concentrations (viz., >10 ppm), while for lower concentrations (viz., 5 and 10 ppm) the interfacial adsorption and occurrence of molecular features at the interface were seen to take several minutes to hours. In order to evaluate in detail, the sequential perturbations in the water structure with the adsorbing protein molecules with time, we conducted a time interval-based SFG experiments on 5 and 10 ppm protein concentrations (shown in Figure 3.2, panel A and B). These time-dependent measurements at lower BHB concentrations showcase the importance of observing the temporal dynamics of the interfacial adsorption process of relevant species by providing distinct spectral features with respect to time.

The temporal measurements were accomplished in OH-stretch region for both 5 and 10 ppm concentrations. The spectra in Figure 3.2 presented different induction time period for 5 and 10 ppm respectively. The induction time period here is defined as the total time duration required for the molecules to become SFG sensitive such that we are able to observe some spectral changes (in terms of intensity or spectral shifts) in the SFG spectra. In both the panel A and B, we could observe the gradual appearance of a red-shift in the  $\sim 3225\text{ cm}^{-1}$  peak position depicting the existence of a strongly H-bonded water structure emanating with the adsorbing protein molecules at the interface as observed with time. Also, the  $3450\text{ cm}^{-1}$  feature tends to diminish slowly with time, suggesting the disappearance of the weakly H-bonded water structure due to interfacial protein adsorption. The disappearance of  $3450\text{ cm}^{-1}$  feature is seen to be significant for 10 ppm than 5 ppm protein concentration. These variations were seen to be in alignment with the observations monitored for the concentration-dependent SFG spectra variations in OH-stretch region in Figure 3.1A.

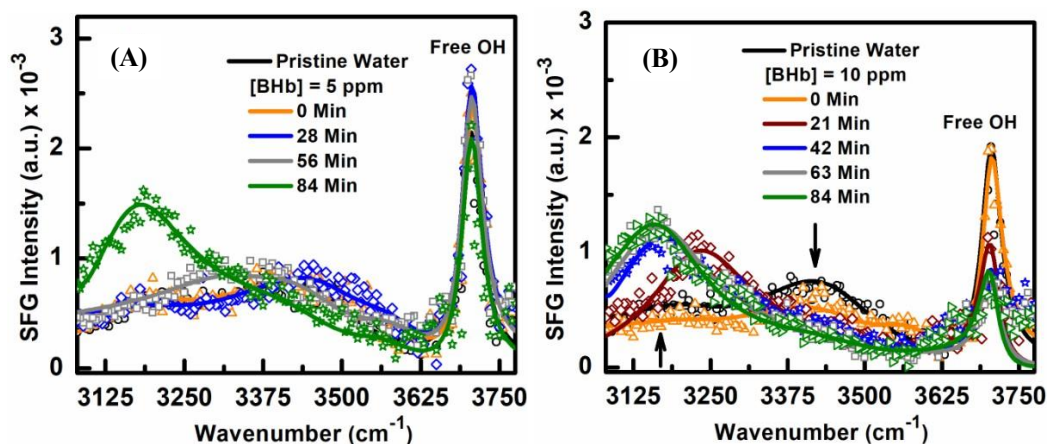


**Figure 3.2** SFG-VS spectra of the temporal-state evolution in the OH-stretch region for (A) 5 ppm, and (B) 10 ppm BHB concentration, observed at the air-water interface. Reprinted with permission from Chaudhary and Kaur et al. *Appl. Spectrosc.* **75**, 1497-1509 (2021).<sup>129</sup>

These interpretations suggest that a similar kind of dynamical variations are observed in the interfacial water structure with time, irrespective of the protein concentration added, to form a strongly H-bonded water network. The red-shift observed for  $\sim 3225\text{ cm}^{-1}$  towards  $3160\text{ cm}^{-1}$  in the OH-stretch region indicates a strong influence of the interfacial adsorption process of BHB protein on the interfacial water structure. This has been equally supported by the gradual decrease in the free OH response for both 5 and 10 ppm protein samples with time, which depicts an enhanced molecular surface coverage due to the diffusion of the protein molecules from the bulk phase towards the surface or interface.

➤ **In situ real-time dynamics of BHB adsorption at interface probed by SFG-VS**

The observations of temporal-state SFG results of BHB interfacial adsorption dynamics instigated its further investigation in terms of the real-time in situ analysis of the protein adsorption, protein re-structuring, and water molecular re-ordering at the air-water interface. Corresponding results are showcased in Figure 3.3 (panel A and B). Here, the SFG spectra for 5 ppm (panel A) and 10 ppm (panel B) protein concentrations were acquired at two specific wavenumbers i.e.,  $2875\text{ cm}^{-1}$  ( $\text{CH}_{3\text{SS}}$  mode) and  $3200\text{ cm}^{-1}$  (strong H-bonding water) as a variation of time in seconds. This real-time observation will be characteristic of the ongoing protein adsorption process and the resultant H-bonding network changes observed at each step with time. An enhancement in the  $2875\text{ cm}^{-1}$  and  $3200\text{ cm}^{-1}$  features were observed after the induction time period. Here, an enhanced water signal is well synchronized with the appearance of BHB methyl response



at the interface. Interestingly, the conformational changes in the protein structure continued for a longer time, whereas the changes in SFG intensity for the OH-stretch region reconcile quickly. The real-time monitoring of the growth in methyl features provide direct evidence of the diffusion-driven BHB interfacial adsorption and also hints towards the conformational-level alterations ongoing in the protein structure after adsorption at the air-water interface.

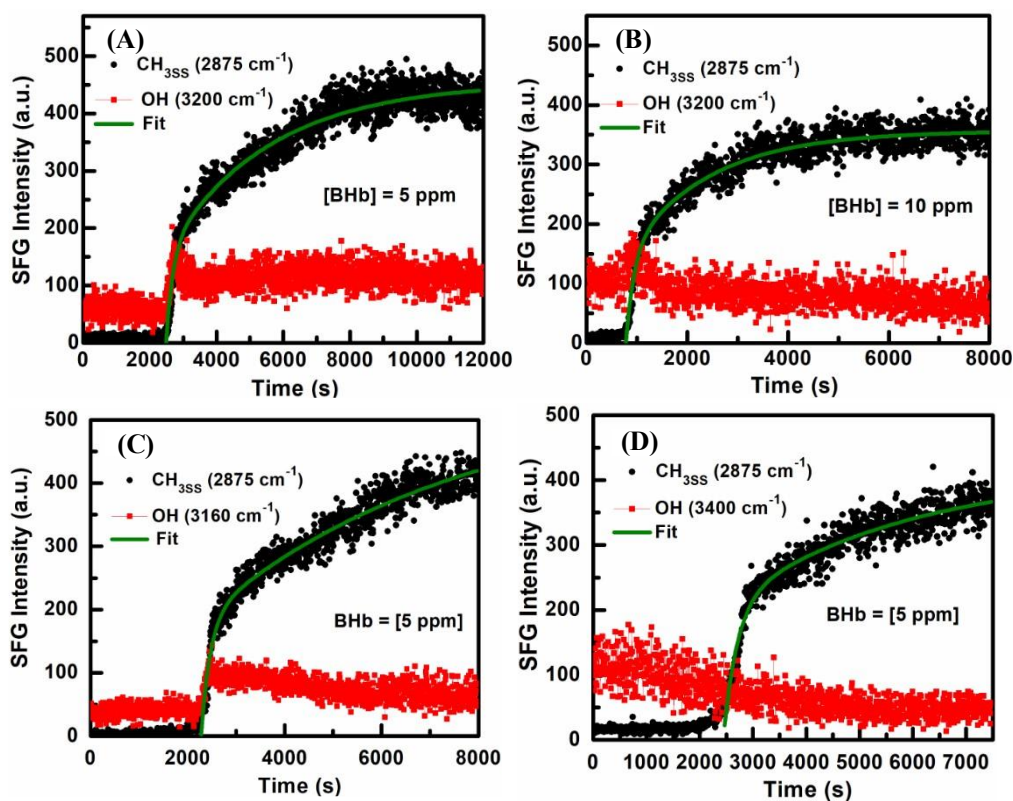


**Figure 3.3** in situ real-time SFG measurements for observing changes in the SFG intensity with time for methyl symmetric stretch ( $\text{CH}_{3\text{SS}}$ ) mode at  $2875\text{ cm}^{-1}$  and OH-stretch of strongly H-bonded water molecules at  $3200\text{ cm}^{-1}$  for (A) 5 ppm, and (B) 10 ppm BHB concentrations. Real-time measurements for 5 ppm BHB concentrations of  $\text{CH}_{3\text{SS}}$  mode with (C) OH-stretch at  $3160\text{ cm}^{-1}$ , and (D) OH-stretch mode for weakly H-bonded water molecules at  $3400\text{ cm}^{-1}$ . Reprinted with permission from Chaudhary and Kaur et al. *Appl. Spectrosc.* **75**, 1497-1509 (2021).<sup>129</sup>

Due to the protein diffusion process, the time periods of the fast- and slow-exponential growth of the  $\text{CH}_{3\text{SS}}$  mode were quantified by fitting the intensity rise using double exponential growth function which is given by:<sup>168</sup>

$$(I_{\text{SFG}})^{1/2} = A + A_1 \exp(-R_1 t) + A_2 \exp(-R_2 t) \quad (3.1)$$

where,  $A = (A_1 + A_2)$ ,  $A_1$ , and  $A_2$  are referred as constants, and  $R_1$  or  $(1/\tau_1)$  and  $R_2$  or  $(1/\tau_2)$  are defined as the rate constants of the growth profile with the characteristic time

period. Here for our results,  $R_1$  symbolizes the fast exponential rate while  $R_2$  symbolizes the slow exponential growth rate with their corresponding characteristic time periods.

By using the above equation number 3.1, the 5 ppm BHb concentration (in Figure 3.3A) presented a characteristic time ( $\tau_1$ ) of  $\sim 198 \pm 16$  s from the first exponential growth, suggesting the diffusion or initial adsorption time of the BHb molecules from the bulk-phase towards the air-water interface. The second characteristic time ( $\tau_2$ ) was calculated to be  $\sim 3120 \pm 103$  s depicting the second exponential growth, which corresponded to the time taken for the structural re-arrangement BHb molecules at the interface. The OH-stretch mode growth SFG plot was fitted with a single exponential growth function (fitted profile not shown for clarity purpose), and the observed  $\tau_1$  of the rising section of the  $3200 \text{ cm}^{-1}$  wavenumber was observed to be  $\sim 180 \pm 15$  s. By comparing the profiles of 5 ppm (panel A) and 10 ppm (panel B), we can readily discern from their respective growth kinetics profile that the characteristic time period decreases with a rise in the bulk concentration of BHb molecules to 10 ppm (seen in panel B). Here, we noticed the first and second characteristic time period to be  $\sim 143 \pm 9$  s and  $\sim 1624 \pm 37$  s, respectively. The trend of the growth kinetics for the OH-stretch mode for 10 ppm BHb concentration was noted with a characteristic time of  $\sim 132 \pm 8$  s.

From the temporal evolution SFG measurements of 5 and 10 ppm protein concentration (Figure 3.2) we observed a clear red-shift from  $\sim 3225 \text{ cm}^{-1}$  to  $3160 \text{ cm}^{-1}$  in the lower frequency region in the OH-stretch region during the protein adsorption process at the interface. Therefore, we have also acquired the real-time evolution at  $3160 \text{ cm}^{-1}$  peak position observed in OH-stretch region along with the evolution in the  $2875 \text{ cm}^{-1}$  peak position noticed in the CH-stretch region for 5 ppm sample (panel C). The enhancement in the SFG signal at  $3160 \text{ cm}^{-1}$  is monitored which was found to be well-synchronized with the initial growth phase observed for the  $\text{CH}_{3\text{SS}}$  mode of BHb molecules. Similarly, the weakly H-bonded region centered at  $3400 \text{ cm}^{-1}$  for 5 ppm concentration is seen to decrease in its SFG intensity as the methyl features rise in intensity in the real-time data (panel D). The findings from real-time dynamics SFG plots suggest that during the protein adsorption process, some concurrent changes in the interfacial water molecular structure are probably occurring by tumbling the population of weakly H-bonded water molecules.

### ➤ Surface tensiometry measurements of BHB adsorption

In order to understand and correlate the SFG findings of protein adsorption kinetics, we have performed the conventional surface tensiometry measurements in both static and dynamic evolution mode. Similar set of experimental protocols were followed for ST measurements, i.e., samples were evaluated immediately after their preparation. The observed ST value for pristine water was seen to be  $\sim 72$  mN/m, which was found to decrease with raising BHB concentration in the solution reaching up to the value of  $\sim 49.2$  mN/m at the maximum BHB concentration of 1000 ppm (Figure 3.4A). The ST kinetics measurements were further performed to evaluate the dynamic changes observed in the water ST values (Figure 3.4B). For this, three specific BHB concentrations were chosen viz., 5, 10, and 20 ppm. The induction time periods for the three concentrations were certainly different and we could identify a clear variation in their respective ST value changes. This suggests a significant difference in the surface coverage by the diffusion process and the resultant conformational changes of the BHB protein molecules at the air-water interface.

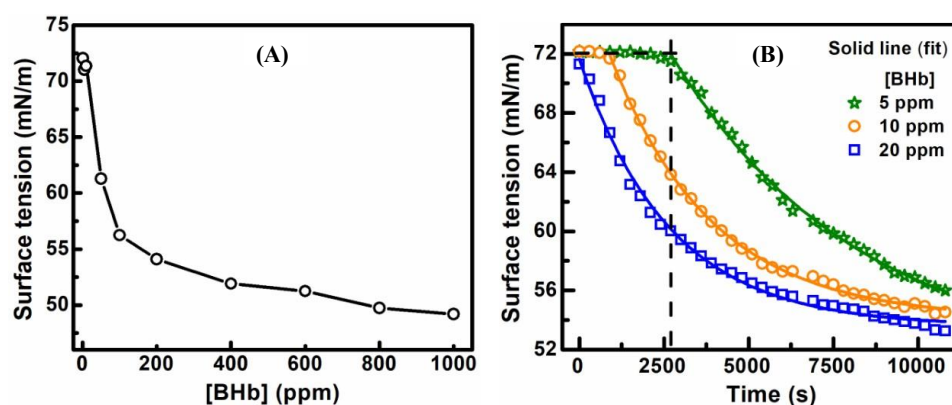


**Figure 3.4** Surface tension measurements of BHB protein molecules (A) as a function of its bulk concentration, and (B) observing the surface tension kinetics for BHB concentrations of 5 ppm, 10 ppm, and 20 ppm. Reprinted with permission from Chaudhary and Kaur et al. *Appl. Spectrosc.* **75**, 1497-1509 (2021).<sup>129</sup>

In terms of a quantitative evaluation, the induction time for 5 ppm was observed to be  $\sim 2500$  s, after which the ST values started decreasing steadily reaching up to  $\sim 56.0$  mN/m after the time period of 10,000 s. In the case of 10 ppm BHB, the marked difference in the ST values occurs at  $\sim 1000$  s (Figure 3.4B). Here, the vertical lines marked (in dash form) represent the induction time period when the ST values started decreasing steadily. The ST kinetic measurements were found to be in good alignment with the SFG intensity measurements for the time dynamics evolution of protein

adsorption process in real-time for both 5 and 10 ppm samples. For SFG measurements the induction time period, however, presented a sharp rise in the SFG intensity at selected resonant wavenumbers. However, the abrupt fast growth observed in case of SFG time dynamics is essentially absent in the steady decay profile observed in the ST-based measurements. These differences in the profile expression may arise due to an inherently distinct working principles for both ST and SFG measurements. ST monitors the activities related to the displacement and re-arrangement of water molecules at the surface which impacts its ST values.<sup>121,122</sup> The adsorption of protein molecules at the interface can disrupt the interfacial water molecules and therefore reduce the surface free energy. Subsequently, the ST value would decrease and may continue as long as the adsorption of protein molecules is dominating at the surface. In contrast, the SFG signal response is based on the second-order nonlinear optical process, where the SFG signal strength relies on the number of molecules present at the interface and their net average orientation.<sup>33,109</sup> The SFG signal response starts showing up when the diffusion-induced adsorbed protein molecules carry a net polar orientation at the interface due to the protein adsorption and structural re-arrangement processes.

Conclusively, the diffusion process governs the BHp protein adsorption at the air-water interface, and the process can be thus summarized in a few sequential steps:

- (i) Diffusion of protein molecules from the bulk towards the subsurface region,
- (ii) Protein adsorption at the interface, and
- (iii) Molecular structural rearrangement through protein–protein and protein–interfacial water interactions.

The diffusion of native protein molecules towards the surface seems to ultimately control the complex rate of protein adsorption at the surface. In addition to the diffusion process, there are several other factors known to influence the adsorption and structural re-arrangement of protein at the air–water interface.<sup>136,169</sup> Elaborating the mechanism involved in protein adsorption scheme as stated above, the first step includes the migration of native protein molecules toward the subsurface (Figure 3.5A) and to get adsorbed at the interface by the influence of various forces, e.g., electrostatic interaction, hydrogen-bonding, van der Waals attraction hydrophobic hydration, and then consequently the protein molecules tend to rearrange their architecture (shown in Figure 3.5B).<sup>48,170</sup> Due to the intrinsic amphiphilic nature of protein molecules, they show a

higher affinity of adsorption towards the hydrophobic surface. The air-water interface is considered as a typical hydrophobic interface for the amphiphilic molecules.<sup>134-136</sup> The interfacial adsorption protein molecules leads to exposing off their hydrophobic residues towards the air, where they tend to displace the interfacial water molecules coexisting at the interface causing a disturbance in their native H-bonding arrangement. The occupied space by the hydrophobic entities enforces the interfacial water molecules to rearrange themselves.<sup>48,71,133,157</sup> Our findings suggested that this re-structuring observed in the interfacial water molecular network and the origin of strongly H-bonded water structure occurs at the expense of the weakly H-bonded network during the protein adsorption and its structural re-organization at the interface. Here, it is expected that the exposed hydrophilic residues of the protein molecules after the occurrence of its structural re-arrangement at the interface might have offered a suitable opportunity to the interfacial water molecules to build a strong H-bonded water network surrounding the protein molecules.<sup>48,170</sup> Similar observation were monitored by Strazdaite et al. where they found that the interfacial water molecules to show a stronger preference for molecular ordering at the hydrophobe-water interface than at the air-water interface.<sup>157</sup> Moreover, the signature of a strong hydrogen-bonded network was reported by Meister et al. at the ice-binding site of the protein molecules at the air-aqueous interface.<sup>71</sup>

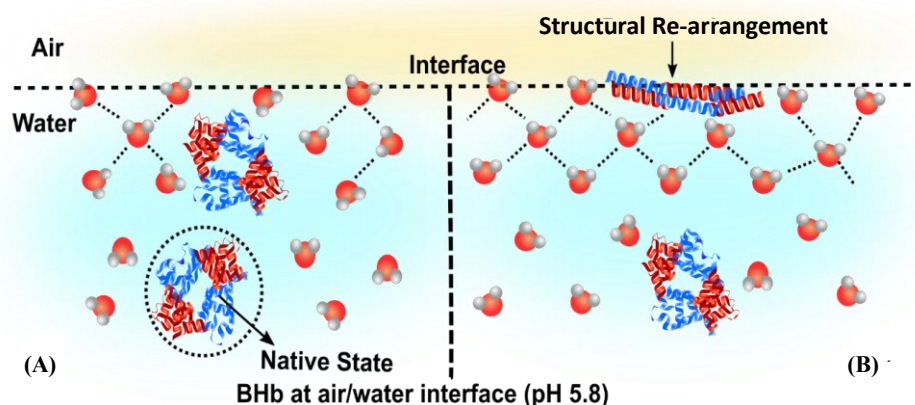


**Figure 3.5** Predicted model representation of the protein surface adsorption and structural re-arrangement process and its influence on the interfacial water molecular structure at the air-water interface at working pH of  $5.8 \pm 0.1$ . The size of molecular entities represented in this model does not represent the actual space occupied by them. Reprinted with permission from Chaudhary and Kaur et al. *Appl. Spectrosc.* **75**, 1497-1509 (2021).<sup>129</sup>

### **3.3.3 Conclusion**

In the present work, we have evaluated the BHp protein surface adsorption, structural re-structuring of the BHp protein molecules, and their impact on the H-bonding network of the interfacial water molecules at the air-water interface. We found a direct correlation among raising the bulk protein concentration and an enhancement in the protein adsorption process at the interfacial region. The protein adsorption process was also seen to strongly influence the H-bonded network of the interfacial water molecules. Subsequently, the evolution of CH- and OH-stretching modes at the air-water interface was probed in real-time with protein concentration variation. The in situ real-time SFG kinetics studies provided information about the induction time followed by fast and slow growth dynamics of the protein molecules during the adsorption process for different protein concentrations. There is an increase in the induction time with the decrease in the protein bulk concentration, and the same trend is observed for the value of characteristic time for the growth dynamics with the protein concentration. A synchronization in the protein adsorption kinetics process was monitored along with a variation in the H-bonding network of the interfacial water molecules to form a stronger H-bonded network at the cost of weakly H-bonded water molecules. The ST kinetics measurements further confirmed the surface propensity of the BHp protein molecules at the air-water interface, which is reflected by a decrement in the ST values as a variation of time and bulk protein concentration. The understanding presented in our work provides a detailed molecular-level insight about the protein adsorption process and its kinetics. This finding can be advantageous to understand various fundamental and complicated protein denaturation processes occurring at different interfaces.

## **3.4 Investigating the molecular structure of double-stranded DNA and the influence of hydrogen peroxide at the air-aqueous interface**

### **3.4.1 Background**

A double helical deoxyribonucleic acid (DNA) is the basic foundation of all living beings. It consists of a spirally wound polynucleotide chains arranged in an antiparallel fashion. Each nucleotide consists of a phosphate group facing outwards, a deoxyribose

sugar residue presents in the backbone and four different nucleic bases (adenine, guanine, cytosine and thymine) constituting its helical core.<sup>75,171</sup> Small local variations in the immediate neighborhood, i.e., hydration, ions, temperature, or presence of free radicals around the native B-form of DNA, ultimately lead to a large variety of global geometries.<sup>171</sup> Hence, the basic molecular nature of the DNA and its related physicochemical properties are crucial to examine to comprehend the basis of the molecular interaction and the changes in the DNA conformation in an aqueous media. The behavior of DNA can be analyzed via aggregation, precipitation, or adsorption processes majorly involving the nucleic bases of DNA, causing molecular phase-separation within the media. DNA condensation is useful to understand both the biological as well as for various applied systems.<sup>41,100,101,171</sup> DNA in physiological systems is usually associated with protein molecules that tend to affect the topology of DNA.<sup>41,171</sup> The existence of interfacial DNA is considered as a highly efficient machinery within the cell, capable of bulk phase-separation, denature, renature, or cyclize with a higher rate in the heterogenous than that in the homogenous environment.<sup>101</sup> This can be observed either through homogenous or bulk-phase studies or studying DNA molecules in heterogenous systems or at interfacial region. The condensed or dense states of DNA are usually obtained under the influence of ions, free radicals, polyelectrolytes, condensing agents, reduced molecular hydration or concentrated sample solutions.<sup>101,171,172</sup> A more reliable system for understanding the DNA condensed states would be to study it in heterogenous media i.e., at the interfaces, where the aggregated states adhere after undergoing the molecular phase-separation. Thus, DNA at interfaces provide a simple model system to understand how it perceives the heterogenous complexity and how the corresponding functionality of DNA gets modulated.

Early experiments were done by Frommer and Miller<sup>173</sup> in 1968 on E.coli [<sup>3</sup>H] DNA at air-water interface. It was apprehended that both the adsorption and interaction forces are too low to allow an appreciable osmotic pressure differences between the surface and the bulk phases, such that both the native and denatured DNA molecules negligibly affect the surface tension and potential. Later, Eickbush and Moudrianakis<sup>174</sup> investigated dsDNA adsorption at the air-water interface in presence of different chemical moieties. The interfacial activities of the adsorbed DNA via a carbon-grid were analysed using electron microscope and observed that the DNA adsorption is prompted in the presence of cations, intercalators, and polyelectrolytes. This adsorption is followed by the

formation of aggregates in the bulk, as a result, it is concluded the possibility of DNA adsorption at the interface majorly through the condensing associations via hydrophobic interactions.<sup>174</sup> Nevertheless, both these studies supported the non-existence of adsorbed DNA at the interface due to the native repulsive forces among the negatively charged DNA molecules, and associated the DNA interfacial adsorption with the presence of ions or salts. Another investigation by Douarche and co-workers<sup>101</sup> elucidated the phase-behavior of a single-stranded DNA (ssDNA) in presence of salts and as a function of hydration in water (H<sub>2</sub>O) and heavy water (D<sub>2</sub>O). It is attributed that the DNA interfacial adsorption and bulk aggregation to the electrostatic neutralization, mathematically calculated van der Waals forces, and DNA hydration process. Other research contributions in this direction were also made to understand DNA adsorption and DNA hybridization at the surface primarily using the tensiometry, adsorption isotherms, QCM, FTIR, or x-ray reflectivity.<sup>175-178</sup>

Reactive oxygen species (ROS) are widely known to impact the DNA structure. Hydrogen peroxide (H<sub>2</sub>O<sub>2</sub>) is one of the ROS species that is endogenously formed inside the cells during metabolism and results exogenously through the environment.<sup>102,179</sup> During the radiotherapy, chemotherapy, under stressful conditions (both intrinsic and environmental induced), cancer, ageing, etc., H<sub>2</sub>O<sub>2</sub> is formed in a significant amount.<sup>102,179,180</sup> From both experimental and simulation studies, H<sub>2</sub>O<sub>2</sub> is known to be the longest existing ROS species at the biological-level.<sup>106,180,181</sup> Under such conditions, H<sub>2</sub>O<sub>2</sub> forms single- or double-stranded breaks, or intramolecular associations among nucleic bases within the DNA molecule, which tends to impact the conformation and the fundamental activity of DNA.<sup>102,106,179,182,183</sup> Various ROS or H<sub>2</sub>O<sub>2</sub> formed during such processes also disrupt other biomolecular systems like lipids, proteins, and metabolites within the human body.<sup>179</sup> Yet, these biomolecules are replenished quickly during the native metabolic maintenance within the cell. Contrarily, DNA damage is tended to be more pronounced, and is difficult to recover its lost information. The existence of H<sub>2</sub>O<sub>2</sub> at the moist surfaces and water microdroplets has been recently explored at the water-solid surfaces and suggested its possible enrolment in the bacterial or viral modifications at the genetic level during seasonal changes.<sup>104,184</sup> Zare group reasoned out the formation of H<sub>2</sub>O<sub>2</sub> at moist surfaces to be the effect of an electron-transfer process which causes the liquid-solid contact electrification.<sup>104</sup> This approach is especially critical to investigate for designing optimum microfluidic-based device applications and bio-molecular sensor



surface fabrications by understanding the fundamental mechanisms occurring at the interface. It is known through certain atomistic-level simulation studies that the H<sub>2</sub>O<sub>2</sub> form a specific complexation with the nucleoside bases within the grooves and non-specific association with the backbone phosphate groups via oxygen atoms.<sup>106,182,183</sup> The complexation of backbone phosphates with H<sub>2</sub>O<sub>2</sub> was found to form stable interactions than with the surrounding water molecules.<sup>182</sup> Another study theoretically verifies the interaction of H<sub>2</sub>O<sub>2</sub> with nucleic bases and rationalized the blocking of base pair opening in presence of H<sub>2</sub>O<sub>2</sub> species, if the interaction energy of H<sub>2</sub>O<sub>2</sub> species with DNA happens to be larger than that of DNA with water.<sup>106,180</sup> All these theoretical interpretations, however, require an experimental support.

However, studies carried out till date on the conformational states of DNA in different perturbing system are relatively characterized in bulk environments including invasive or fluorescent-based approaches, where a net isotropic effect is observed by averaging the signal from a large group of molecules.<sup>102,183</sup> However, with the sum frequency generation vibration spectroscopy (SFG-VS), one can specifically probe the molecular underpinnings at the air-water interface with a scale of up to 1 nm, where most of the biological heterogeneity comes to effect. Several literature reports on DNA studies at the interface by employing SFG-VS have been discussed in chapter 1 (refer section 1.4.2). Recently, Perets et al.<sup>185</sup> presented the ssDNA and dsDNA signatures immobilized using three distinct methodologies at the air-glass and air-water interface by employing the chiral and achiral SFG-VS techniques. They localized DNA molecules at the air-water interface by hydrocarbon modification. Their results potentially revealed the label-free identification of DNA hybridization, and successfully distinguished the handedness of double helical structure, aromatic signatures, and the macroscopic chirality of DNA secondary structures. Local concentration impact has been known to be quite useful in understanding biomolecular adsorption at highly dense states and linked to understanding the pre-biotic chemistry.<sup>101,172,173,184</sup> In this study, we aim to investigate and report the characteristic features and molecular behavior of dsDNA at the air-aqueous interface without any structural modifications, as a function of concentration using SFG-VS tool. Subsequently, we have analyzed the competitive influence of H<sub>2</sub>O<sub>2</sub> and bio-molecular hydration over the behavior of the adsorbed dsDNA molecules at the air-aqueous interface, by varying H<sub>2</sub>O<sub>2</sub> concentration. In both the experimental investigations, dsDNA sample was prepared in the buffered solution at physiological pH conditions, mimicking

the DNA's native existence in the water-ionic solution inside the cell. This knowledge could help to seek an increase in the efficiency of their applications in evaluating the biological mechanism of its interaction with small molecules and in developing an efficient DNA conjugated sensor system.

### 3.4.2 Results and discussion

#### ➤ Concentration-dependent interfacial probing of dsDNA

The interfacial adsorption process of dsDNA molecules was evaluated using SFG-VS in a broad wavenumber region of 2800-3800  $\text{cm}^{-1}$  including information in both CH- and OH-stretch regions in three different polarization schemes (SSP, PPP, and SPS). The SFG spectra were acquired at two different concentrations of dsDNA i.e., 100 and 300 ppm prepared in 20 mM Tris-HCl buffer at pH 7.4 (mimicking physiological pH). The measurements were conducted immediately after solution preparation without waiting for surface equilibrium. The polarization-dependent SFG experimentation allows to gain the overall molecular behavior and its interfacial structural arrangement through the orientational evaluation of functional moieties predominantly occupying the interface. [83-85] The resultant data points of the obtained SFG spectra of different samples were fitted with the Lorentzian profile to access the peak positions and their relative amplitude values (fitting table provided in Appendix B). Priorly, the SFG spectra of pristine water and Tris-HCl buffer (pH 7.4) were taken as reference in all three polarization combinations. The peak assignments for the pristine water-air interface have been discussed in detail in section 3.3.2. Figure 3.6 (panel A-C) depicts no significant variations in the SFG intensity profile for Tris-HCl buffer sample with respect to the neat water spectrum. Although, an intensity variation at the free OH peak position is seen in the PPP polarization scheme for the Tris-HCl buffer in comparison with pristine water (panel B).

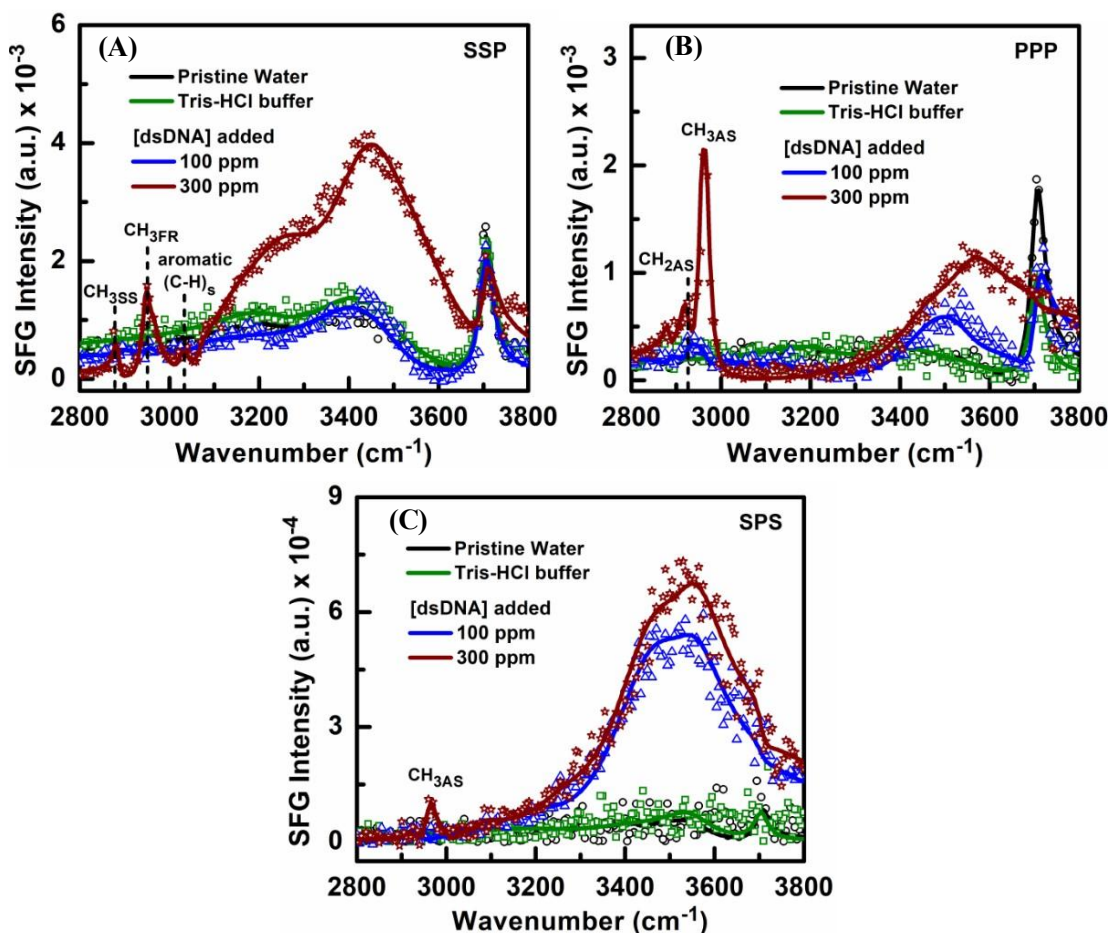


**Figure 3.6** SFG-VS spectra of pristine water, Tris-HCl buffer (at pH 7.4), and dsDNA solution at two concentrations (100 and 300 ppm) observed in (A) SSP, (B) PPP, and (C) SPS polarization schemes at the air-aqueous interface.

The SFG spectra for dsDNA at two distinct concentrations are also presented in Figure 3.6 (panels A-C). No CH-stretch features were seen for 100 ppm dsDNA concentration in SSP and SPS polarization schemes at the air-aqueous interface. However, a slight intensity rise is noticed in the PPP polarization mode with the peak centering at  $\sim 2965 \text{ cm}^{-1}$  depicting the methyl asymmetric stretch ( $\text{CH}_3\text{AS}$ ) feature.<sup>35,79</sup> On increasing the dsDNA bulk concentration three times (i.e., 300 ppm), marked variations are seen in the CH-stretch region ( $2800\text{-}3050 \text{ cm}^{-1}$ ) along with a huge enhancement observed in the OH-stretch region ( $3050\text{-}3600 \text{ cm}^{-1}$ ). The CH-stretch profile shows dominant features from the methyl moieties, which are representative of the methyl residues of thymine nucleic base or from some of the methylated nucleic base present in the salmon sperm dsDNA, used in this work.<sup>186</sup> The appearance of the peak positions at  $2885 \text{ cm}^{-1}$ ,  $2948 \text{ cm}^{-1}$ , and  $2965 \text{ cm}^{-1}$  are ascribed to methyl symmetric stretching ( $\text{CH}_3\text{SS}$ ), methyl fermi resonance ( $\text{CH}_3\text{FR}$ ), and the methyl asymmetric stretch ( $\text{CH}_3\text{AS}$ ) modes, respectively.<sup>35,79</sup> A minor contribution from  $2925 \text{ cm}^{-1}$  depicting the methylene

antisymmetric profile ( $\text{CH}_{2\text{AS}}$ ) is also considered in the spectral fitting. The asymmetric modes were clearly noticed here from the polarization-dependent analysis of dsDNA, depicting the beauty of the SFG vibrational spectroscopic analysis. The presence of vibrational modes from the aromatic ring structures of dsDNA (originating from the ring-structure of nucleic base and deoxy-ribose sugar ring) is also noticed with lesser intensity contribution in the aromatic stretch region from  $3000\text{-}3100\text{ cm}^{-1}$ . The corresponding peak positions at  $3025\text{ cm}^{-1}$ ,  $3042\text{ cm}^{-1}$ , and  $3070\text{ cm}^{-1}$  are assigned to  $\nu_{20\text{b}}$  ( $\text{C-H}$ )<sub>s</sub>,  $\nu_{7\text{a}}$  ( $\text{C-H}$ )<sub>s</sub>, and  $\nu_2$  ( $\text{C-H}$ )<sub>s</sub> modes, respectively.<sup>158-160,185</sup> The dominant presence of  $\text{CH}_{3\text{SS}}$  mode, with increasing concentration of dsDNA in an aqueous media, is an indication that the methyl entities of the dsDNA molecules are aligned along the surface normal, which is also supported by several studies performed on dsDNA at the interface.<sup>35,79,185</sup> The ordered alignment of methyl residues at the air-aqueous interface is also substantiated through the SPS polarization profile of 300 ppm dsDNA, where a very minute intensity of  $\text{CH}_{3\text{AS}}$  is seen, as SPS polarization combination is known to present the functional moieties with a parallel alignment with respect to the sample surface.<sup>111,187</sup> These interpretations suggest the occurrence of conformational-level changes in the dsDNA helical structure after they adsorb at the interface, such that the alkyl residues present inside the helical core of dsDNA structure gets exposed towards the air at the air-aqueous interface.<sup>35,79,101,174</sup> The observed CH-stretch profile of dsDNA depicts the concentration-dependent surface adsorption and conformational re-structuring of the dsDNA molecules, making the intrinsic methyl residues of DNA nucleic base to be highly ordered at the air-aqueous interface.

The OH-stretch region showcases an enhanced SFG intensity profile in SSP polarization scheme for 300 ppm dsDNA in both the strongly and weakly H-bonded water molecular structure, while a minimal perturbation is observed for 100 ppm dsDNA solution at  $3450\text{ cm}^{-1}$ , which is a representative of the weakly H-bonded water molecular structure (Figure 3.6A). The stronger SFG intensity seen for 300 ppm concentration suggests a field-dependent rise in the polar alignment of water dipoles due to the presence of charged moieties<sup>151,155</sup> of dsDNA at the interface, since the dsDNA is known to carry negative charge at pH 7.4 due to its phosphate backbone.<sup>75</sup> Contrary to the SSP polarization mode, both PPP and SPS show a significant enhancement at the higher wavenumber of the OH-stretch region with a peak intensity centered at  $\sim 3550\text{ cm}^{-1}$ , observed for 100 ppm dsDNA. Upon incrementing the dsDNA concentration to 300 ppm,

the intensity at  $3550\text{ cm}^{-1}$  simply gets increased. The enhanced profile at  $\sim 3550\text{ cm}^{-1}$  could possibly result due to the charge-dependent polar alignment of weakly coordinated water molecules.<sup>188</sup> Several studies have attributed the  $3550\text{ cm}^{-1}$  peak position to the water molecules that form weaker H-bonding associations with the hydrophobic residues, referred to as the hydrophobic hydration of the molecular entities.<sup>155,188-190</sup> Hydrophobic hydration plays a vital role in conducting key biological functions including protein folding, DNA helix stabilization, DNA-ligand binding, molecular phase transitioning, bilayer stability, etc.<sup>41,81,171,172,188,190</sup> It becomes quite prominent in SPS and PPP than in the SSP polarization spectra.<sup>188,189</sup> Hence, it is inferred from the polarization-dependent results of dsDNA as a function of concentration that the hydration profile of the dsDNA becomes the first level indicator of the dsDNA re-structuring or helical disruption at the air-aqueous interface. The enhanced intensity feature at  $3550\text{ cm}^{-1}$  hint towards the accessibility and rich association of the inner hydrophobic moieties of dsDNA with the surrounding water molecules. This feature positioned at  $3550\text{ cm}^{-1}$  is observed to be quite significant even before the alkyl features of dsDNA emerge at the air-aqueous interface.

Further, we could observe a slight reduction in the intensity of free OH at  $\sim 3705\text{ cm}^{-1}$  on introducing dsDNA in aqueous media in SSP and PPP spectra (Figure 3.6, panel A and B). This is representative of surface coverage by dsDNA molecules, which slightly affects the free OH distribution at the air-aqueous interface.<sup>8,133</sup> Here, we observe a considerable overlapping of the  $3705\text{ cm}^{-1}$  feature with the relatively lower frequencies at  $\sim 3550\text{ cm}^{-1}$  peak. This suggests the existence of heterogenous states of weakly H-bonded water molecules.<sup>8,133,188</sup>

#### ➤ **Impact of H<sub>2</sub>O<sub>2</sub> concentration on interfacial molecular structure of dsDNA**

Considering the maximal interfacial activity observed for 300 ppm dsDNA concentration at the air-aqueous interface, the impact of H<sub>2</sub>O<sub>2</sub> on the dsDNA interfacial structure was subsequently investigated. Here, we wanted to understand the competitive role of H<sub>2</sub>O<sub>2</sub> and water (H<sub>2</sub>O) molecules in influencing the interfacial molecular signature of dsDNA. Here, we would like to mention that the H<sub>2</sub>O<sub>2</sub> addition to the buffered dsDNA sample did not vary the solution pH value, primarily due to the buffering action of Tris-HCl buffer system.

Figure 3.7 depicts the SFG spectra of dsDNA (300 ppm) under the influence of varying concentrations of H<sub>2</sub>O<sub>2</sub>, i.e., 0.1 and 0.2 v/v%, in SSP (panel A) and PPP (panel B) polarization schemes. Since the methyl features were prominently visible in the SSP and PPP polarization schemes only for the pristine dsDNA solution (Figure 3.6), SPS polarization scheme has not been considered here for conducting the H<sub>2</sub>O<sub>2</sub>-based studies. On introducing H<sub>2</sub>O<sub>2</sub>, the CH-stretch region displayed a reduction in the methyl stretching modes at 2885 and 2942 cm<sup>-1</sup> (i.e., CH<sub>3</sub>SS and CH<sub>3</sub>FR, respectively) in the SSP spectra (panel A), which gets completely disappear when the 0.2 v/v% H<sub>2</sub>O<sub>2</sub> is added. Considering the drastic changes observed after introducing 0.2 v/v% H<sub>2</sub>O<sub>2</sub> to the dsDNA sample in SSP polarization scheme, its spectral signatures were also acquired in the PPP polarization mode. Here, the contribution from the CH<sub>3</sub>AS mode (at ~2965 cm<sup>-1</sup>) is still observed at the air-aqueous interface, while the methyl features were absent in SSP for the similar sample. It is important to mention here that the SSP and PPP polarization spectral acquisition has been performed consecutively and there has been no waiting period between the acquired spectra. On examining the OH-stretch region, the SSP spectra display an overall decrement in the OH-stretch intensity in the coordinated region without impacting free OH (panel A). Although the enhanced features in OH-stretch intensity does not get completely diminished as observed in case of the CH-stretch profile for dsDNA under the influence of 0.2 v/v% H<sub>2</sub>O<sub>2</sub>. Contrastingly, no marked changes were seen in the PPP OH-stretch profile at the higher wavenumber region centered at ~3550 cm<sup>-1</sup> with 0.2 v/v% of H<sub>2</sub>O<sub>2</sub> addition.

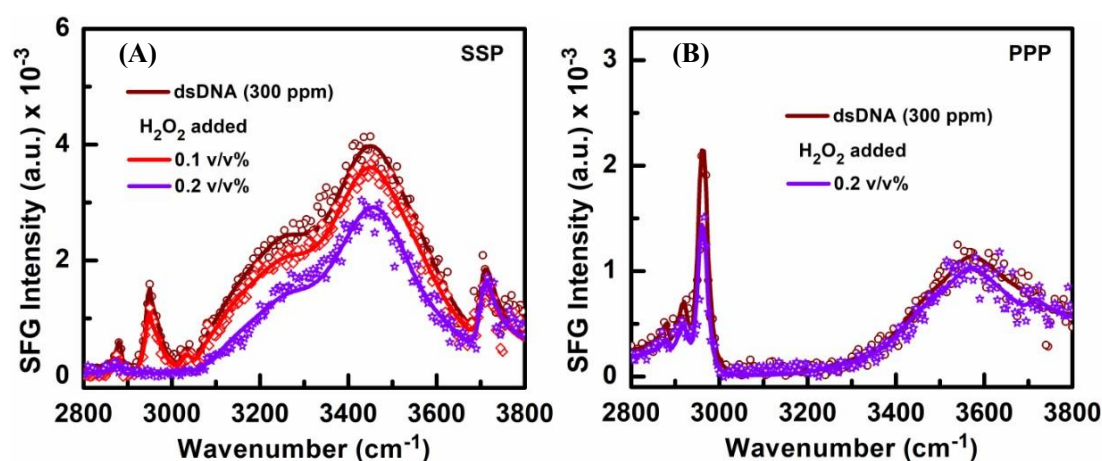


**Figure 3.7** Influence of hydrogen peroxide (H<sub>2</sub>O<sub>2</sub>) as a function of its volume concentration on the interfacial molecular features of dsDNA (300 ppm) in (A) SSP and (B) PPP polarization combinations at the air-aqueous interface.

Reviewing the CH- and OH-stretch regions of SSP and PPP polarization spectra, the significant differences observed in the dsDNA spectral profile on introducing H<sub>2</sub>O<sub>2</sub> suggest that the peroxide impacts the orientation of methyl groups of nucleic bases of dsDNA, while subtle variations are seen in the ordered water molecular structure at the air-aqueous interface. As per the polarization-selection rules,<sup>111</sup> the interpretation of the CH<sub>3AS</sub> in PPP and CH<sub>3SS</sub> in SSP spectra (Figure 3.7) reveals that the methyl groups seem to incline more towards the surface under the influence of H<sub>2</sub>O<sub>2</sub>. Peroxide, however, does not significantly impact the water molecule-DNA interaction (i.e., the hydrophobic hydration of dsDNA molecules assigned to ~3550 cm<sup>-1</sup>) and disrupts majorly the organization of dsDNA nucleic bases at the air-aqueous interface. This is equally supported by the diminished profile observed for the aromatic C-H stretch modes as seen from the SSP polarization spectra (panel A), while the hydration feature in the OH-stretch region observed at 3550 cm<sup>-1</sup> in PPP spectra (panel B) remains unaffected. In opposition, the OH-stretch profile in wavenumber range 3100-3600 cm<sup>-1</sup> in SSP polarization scheme (panel A) shows a slight reduction in the enhanced OH-stretch intensity. Conclusively, the influence of H<sub>2</sub>O<sub>2</sub> on the OH-stretch signature of dsDNA as seen in SSP and PPP spectra simultaneously depicts that, although the H<sub>2</sub>O<sub>2</sub> molecules do not affect the hydration profile of dsDNA molecules, they are able to perturb the charged moieties of dsDNA and the corresponding charge-based influence on the polar alignment of interfacial water molecules.

**Mechanism of H<sub>2</sub>O<sub>2</sub> interaction with dsDNA.** The molecular orientation changes observed through our results provided an experimental validation to the recently proposed hypothesis on the spatial configuration of nucleic base pairs complexing with H<sub>2</sub>O<sub>2</sub> and water molecules, given by Volkov group based on the atom-atom potential function method and DFT calculations.<sup>106,180,182</sup> The interaction energy comparison revealed that the H<sub>2</sub>O<sub>2</sub> forms more stable interactions with DNA phosphates than the water molecules.<sup>180,182</sup> However, with nucleic base pairs, the three potential complexation possibilities of H<sub>2</sub>O<sub>2</sub> and bases were exhibited in presence of water which blocks the DNA unzipping process. These include closed, pre-opened, and stretched configuration of base pairs while complexing with H<sub>2</sub>O<sub>2</sub> in the presence of water, where the pre-opened and stretched configuration of H<sub>2</sub>O<sub>2</sub>-base interactions were found to stabilize dsDNA better than water molecules. Their calculations showcased that the pre-opened

configuration arrange bases in out-of-plane configuration with respect to their original intact position.<sup>106</sup>

Our results depicted changes in the inclination of methyl groups of dsDNA bases towards the surface with H<sub>2</sub>O<sub>2</sub> addition, which signifies the possibility of a change in nucleic base configuration. Additionally, we here discuss the two ways of interaction of interfacial water molecules with dsDNA in presence of H<sub>2</sub>O<sub>2</sub>. The first way showcased that the H<sub>2</sub>O<sub>2</sub> does not impact the water molecular organization surrounding the hydrophobic moieties (nucleic bases or sugar backbone). The second state authenticates about the influence of H<sub>2</sub>O<sub>2</sub> on charged phosphate group arrangement of dsDNA backbone which is observed indirectly via lowering of the interfacial polar alignment of water molecules. This shows a distinct interactive tendency of water molecules with the charged backbone units of dsDNA in absence and presence of H<sub>2</sub>O<sub>2</sub>, which has not been presented before. Therefore, our results supported the association of H<sub>2</sub>O<sub>2</sub> with dsDNA molecules possibly in a pre-opened configuration, where it renders the methyl residues of bases to change their alignment with respect to the surface normal. From the OH-stretch analysis, we infer here that the H<sub>2</sub>O<sub>2</sub> molecules do not perturb or displace the hydrated water molecules surrounding nucleic bases and associates directly with the methyl residues of the bases of dsDNA molecules, successfully observed at the air-aqueous interface.

### 3.4.3 Conclusion

In this work, we have characterized the molecular signatures of dsDNA at physiological pH 7.4 at the air-aqueous interface as a function of dsDNA concentration (i.e., 100 and 300 ppm). Considering the significant features of dsDNA observed for 300 ppm, we subjected the dsDNA to evaluate the impact of hydrogen peroxide (H<sub>2</sub>O<sub>2</sub>) over its spatial configuration and the possibility of its competitive binding with dsDNA with respect to that of water. We have experimentally provided an insight towards the inclination of the alkyl groups towards the sample surface with H<sub>2</sub>O<sub>2</sub> addition. A distinct mechanistic impact of H<sub>2</sub>O<sub>2</sub>-dsDNA complexation over the water molecular structure is provided using SFG-VS, where the interfacial polar alignment of water molecules and the presence of the hydrated structure surrounding the macromolecular system are influenced differentially in presence of H<sub>2</sub>O<sub>2</sub>.



# **Characterization of molecularly imprinted polymer and its protein recognition ability using sum frequency generation vibrational spectroscopy**

In this chapter, we stepped further towards building and characterizing the coated polymer surfaces which are being optimally constructed as imprinted biomolecular recognition platform. Gaining the fundamental information of the interfacial expression of bovine hemoglobin (BHb) protein molecules at the pristine water-air interface, here, we have worked in the direction of developing a recognition system for BHb molecules. Keeping this in focus, a nature-inspired molecularly imprinted polymer (MIP) coating over simple glass slide surfaces was enrolled with a simple one-step procedure for BHb recognition, thus reducing the sensor integration step. MIPs provide a biomimetic approach to build robust artificial recognizing elements with similar functionality as that of physiological antibodies. They can be readily customized to develop a bio-/chemo-sensor for recognizing the molecule of choice. We have utilized the diverse functionality of the dopamine monomer for fabricating the polydopamine (PDA) thin-films and protein template imprinting. The molecular recognition mechanism of MIP surfaces relies predominantly on the functional group arrangement of underlying polymer matrix. Hence, extracting the molecular-level insight about the template imprinted and non-imprinted polymer (NIP) fabrication at each step could pave the way of developing our understanding towards designing efficient and reliable template recognition. To identify the molecular features predominance of the polymer film, vibrational sum frequency generation (VSFG) spectroscopy has been implemented. Optimizations of NIPs and MIPs polymerization time were carried out through VSFG spectral analysis to recognize the molecular groups crucial for template recognition and binding. The washing as well as consecutive binding of the template was analysed to substantiate the re-binding ability of the label-free imprinted polymer surfaces, which were successfully demonstrated using interface-specific VSFG spectroscopic tool.

## 4.1 Introduction

Many natural biological receptors, display an intricate level of complementarity towards their molecular targets. These showcase the sensing of molecules via the fundamental phenomena of molecular recognition which include antibody-antigen recognition or analyte detection by enzymes. However, their utility for industrial-scale chemical processing, as analyte separators, catalysts, or molecular sensing pose certain challenges in terms of their maintenance and production cost, conformational stability in non-native milieu, and versatile sensitivity of natural receptors towards the analyte.<sup>191-195</sup> Nevertheless, comprehending the basic physico-chemical processes of these bio-recognitions and implementing the understanding to create bio-mimicking receptor promises an immense growth in the bio-/chemo-sensing domain. Molecularly imprinted polymers (MIPs) are one of the alternatives widely recognized as “synthetic antibodies” analogous to the natural receptor’s selectivity and tunability for a template.<sup>191-195</sup> MIPs are quite robust in their structure, providing a storage endurance and a molecular memory which can be accordingly tailored in comparison to the natural receptors. As a result, they are potentially being involved for targeted drug delivery, molecular extraction, and selective analyte detection, where the molecular imprints are identified by using the conventional “lock and key” analogy.<sup>191-195</sup>

Imprinting of macromolecules viz., proteins happen to be quite cumbersome due their intrinsic three-dimensional structure and molecular flexibility which is required to stay consistent especially during the MIP re-binding procedure. This relies heavily on the underlying polymerizing moiety, which will determine an efficient capturing of the template protein molecules. Protein imprinting has gained a notable consideration due to its increased utility in bio-macromolecular recognition, separation, as well as for chemical agent analysis.<sup>191-195</sup> Generally, MIPs are synthesized by polymerization of a monomer in the presence of a cross-linker and template molecule. After the polymerization, the template molecule is removed from the polymer matrix, which results in cavities complimentary in shape and size of the target molecules. To improve the sensitivity and response-time towards the template, the MIP construction must bear an optimally thick films with dimension roughly around the template molecule diameter for convenient re-capturing of the template.<sup>193,196</sup> For an effective MIP film generation, dopamine (DA) monomer (chemically named 3,4-dihydroxyphenylalanine) which is a popular

neurotransmitter is rigorously being studied for developing various organic/inorganic coatings in the form of a polydopamine (PDA) polymer layer.<sup>197,198</sup> PDA is a nature inspired adhesive coating which is a native component of the secretion by mussels (a marine animal) that aids them in adhering to distinct surfaces.<sup>197,198</sup> Its monomeric unit ‘DA’ sustains both hydroxyl-rich catechol moiety and amine groups (see Figure 4.1 (A)) which makes PDA inherently hydrophilic and biocompatible. These molecular features assist PDA in adhering large number of substrates via coordination bonds and other weaker interactions to form active functional surfaces.<sup>198-201</sup> PDA is therefore considered for distinct application areas concerning its important properties (Figure 4.1 (B)). Moreover, due to the real-time polymerization of DA to form PDA films, the overall film thickness can be tuned readily. Because of its chief attributes, DA has gained precedence over several other monomers, to be utilized for building imprinted surfaces, particularly for protein molecules as templates.<sup>192,195,198,199,202-205</sup> During the polymerization of DA monomeric units, distinct intermediate species are formed in the course of PDA formation including a small number of non-cyclized, cyclized, protonated and non-protonated amines, and weakly bound dopamine units.<sup>201,205-208</sup> The proportionate occurrence of these intermediates is determined by the aqueous pH value, rate of molecular oxidation, free radical addition, ionic catalysts, and the time duration of the DA sample exposure to air.<sup>201,206-209</sup>

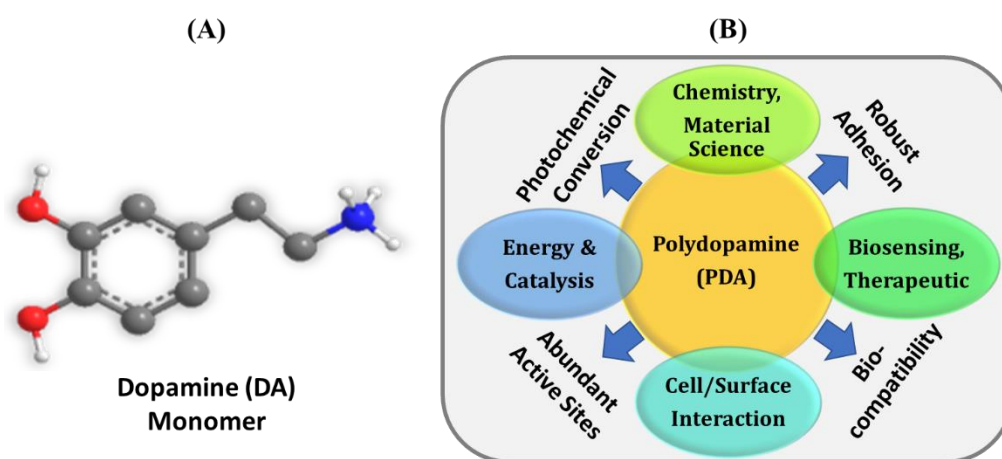


**Figure 4.1** (A) Chemical Structure of dopamine (DA) monomer (here only polar hydrogen atoms are shown for clarity purpose). (B) Illustration of the PDA properties and their relationship with domain-specific applications.

To investigate the potential functional moieties, present at the surface for optimal imprinting and recognition of template molecules, an interface-selective vibrational sum frequency generation (VSFG) spectroscopic tool has been employed in this work to probe

the air-polymer interface. Many studies have been pursued successfully in the past over the air-polymer film and air-polymer aqueous system interfaces by using VSFG spectroscopy, depicting its eminence in this domain area.<sup>12,195,210,211</sup> Here, we have characterized the prepared NIP and MIP thin-films coated on SiO<sub>2</sub> substrates for their ultimate implementation for protein template recognition. Bovine hemoglobin (BHb) has been considered as a model template protein molecule for the MIP-based molecular recognition and re-binding process. Interfacial dominance of the related functional moieties has been resonantly identified over the prepared NIP and MIP surfaces with varied polymerization time-duration. VSFG works on the fundamental principle of a second-order nonlinear spectroscopy for investigating the interfacial activity and the molecular specificity exclusively at the interface.<sup>12,195,210,211</sup> Till now there has been only one report by Oblies et al.<sup>195</sup> where interface-specific VSFG spectroscopic tool has been applied to study methacrylic acid-based MIP surfaces for detecting a drug template molecule, named metronidazole, emphasizing over the template recognition by the physisorption process. However, they enrolled an initiator and cross-linker for constructing template-targeting MIP surfaces. There are several other reports in the research community where the bulk-spectroscopic features of the hemoglobin (Hb) protein adsorption procedure have been identified over the coated PDA or PDA-mix film surfaces.<sup>212-214</sup> Studies in the direction of PDA-coated micro-/nanostructures have also been pursued for detecting Hb protein molecules primarily by using the bulk techniques.<sup>215,216</sup>

Our work approach involves the molecular-level exploration of the one-step PDA fabrication procedure upon varying polymerization time without incorporating any external free-radical initiator or coupling agent during the polymerization process. The PDA coatings were developed on the widely applicable silicon-dioxide (SiO<sub>2</sub>) substrates for the BHb protein molecule recognition. Both the NIPs and MIPs thin-films were analyzed quantitatively by VSFG with polymerization-time variation depicting the significant role of the polymerization-time in establishing the molecular intermediary species at the air-polymer interface. Our results demonstrated a successful imprinting of the PDA matrix at each step of binding, washing, and re-binding. This could not be descriptively confirmed in several studies performed by different researchers using conventional investigative tools like UV-Visible absorption spectroscopy, ellipsometry,

voltammetry, small-angle neutron scattering (SANS), X-ray photoelectron spectroscopy (XPS) and SPR measurements.<sup>192,198-200,203,204,209,216</sup>

## **4.2 Experimental Methods and Procedure**

### **4.2.1 Material Requirements**

Dopamine-HCl and Tris-HCl salt (pre-defined crystals) were purchased from Sigma-Aldrich Co., and used without any purification. All solvents and reagents were procured from Sigma-Aldrich Co. and MERCK. All glassware and microscopic glass (silicon-dioxide) slides were treated with piranha (concentrated H<sub>2</sub>SO<sub>4</sub>: 30% H<sub>2</sub>O<sub>2</sub> = 3:1, v/v) to remove organic immunities, and then rinsed thoroughly with water. All the sample solutions were prepared in millipore ultra-pure de-ionized water type-1 with the resistivity of 18.2 MΩ.cm and pH 5.70 ± 0.02 at 25°C.

### **4.2.2 Fabrication Procedure for NIPs and MIPs**

For conducting the polymer film fabrication process, a 2mg.mL<sup>-1</sup> solution of dopamine monomer was prepared in 10 mM Tris-HCl buffer solution maintained to pH 8 (schematic presented in Figure 4.2). The fabrication was done over the piranha-cleaned glass slides by vertically immersing the slides (to rule out aggregate formation during film deposition)<sup>192</sup> into the dopamine solution to form simple NIP films (panel A). Following the similar scheme, the MIP film fabrication was performed by additionally incorporating the BHb protein molecules (1 mg.mL<sup>-1</sup>) as template molecules, for their inclusion within the fabrication during dopamine polymerization within the buffer solution (panel B). This procedure and optimized concentration have been adopted from the work of Zhou and co-workers.<sup>215</sup> For both the NIP and MIP films, the time of dopamine polymerization to form PDA fabrication over glass substrates were varied, forming 3-, 6-, 9-, and 24-hours spinning duration of NIP and MIP films. The stirring of dopamine solution for film deposition was done with ~500 rpm speed over a magnetic stirrer using a magnetic bead. The coated surfaces were rigorously washed with de-ionized water to remove the unbound or loosely bound moieties.

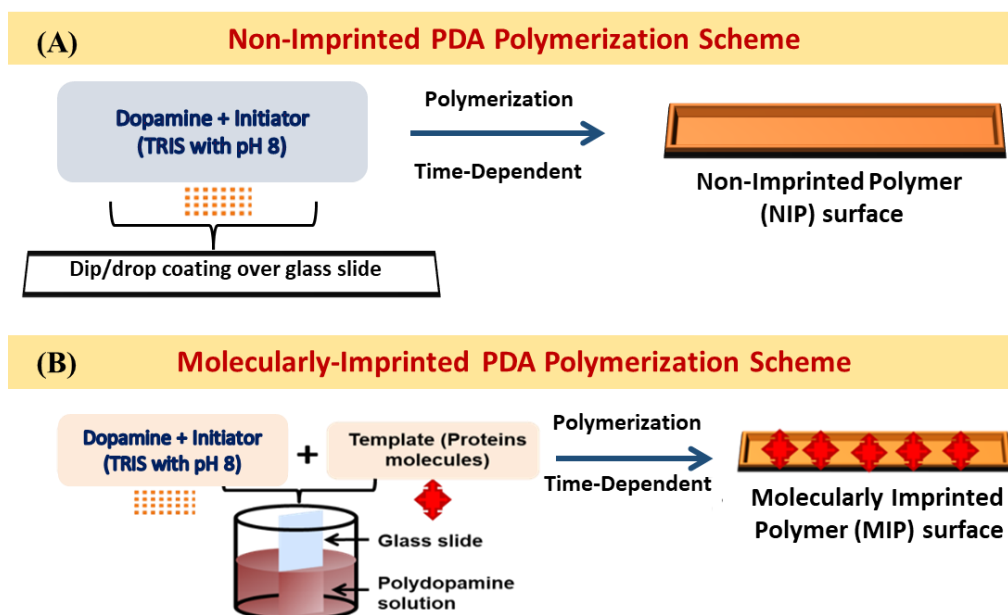


**Figure 4.2** Distinct fabrication schemes followed for (A) non-imprinted PDA polymerization, and (B) molecularly-imprinted PDA polymerization procedure.

#### 4.2.3 UV-Visible Spectrophotometer

The UV-Visible absorption measurements were observed for the residual solution after conducting the template re-binding experiments for MIP and NIP film using Shimadzu Spectrophotometer in wavelength range 300-800 nm.

#### 4.2.4 Atomic Force Microscopy (AFM)

The NIP film thickness evaluation was done via AFM (MultiMode 8, Bruker, USA) in a non-contact operating mode by the scratching method. With the tapping mode, the silicon tip of ~10 nm radius was used to make a fine scratch over the film surface and the measurements were done perpendicular to the scratched line. The obtained thickness values for the films prepared were analyzed by noting the height differences across the scratched line generated using a tweezer. The instrumental details can be seen in chapter 2 (section 2.6.3).

#### 4.2.5 Scanning Electron Microscopy (SEM)

SEM characterizations for NIP films were performed via SEM (JEOL, model 6610LV, Japan, 10 kV operational mode) at the scale of 2  $\mu\text{m}$ . Description on the same can be seen in chapter 2 (section 2.6.2).

#### 4.2.6 Sum Frequency Generation Vibrational Spectroscopy

Vibrational Sum Frequency Generation (VSFG) was used to characterize the NIP and MIP thin films and their template re-binding potential. The signal is optimized at  $2876\text{ cm}^{-1}$  of the CH-stretching region. Instrumental details and specifications have been provided in chapter 2 (section 2.2.2). The thin-films were analyzed at different spots for uniformity check. All the storage vials and glass slides were treated with piranha solution ( $\text{H}_2\text{SO}_4:\text{H}_2\text{O}_2$  in 3:1 ratio) at  $70^\circ\text{C}$  for 1 hour (hr) and subsequently washed with type-1 deionized water and dried prior to usage. The central reflected red guided beam from the film-coated glass surface was carefully kept at focus to pass the center of the iris across the focusing optics within the SFG spectrometer towards the monochromator for the SFG signal detection. The sample preparation and fabrication were performed at laboratory temperature ( $\sim 22^\circ\text{C}$ ). The SFG spectral fits were done by using the Lorentzian expression (details in chapter 2, section 2.2, equation 2.16). Spectra were acquired in SSP, PPP, and SPS polarization schemes. Data points for spectra were obtained by averaging 200 pulses per step with  $5\text{ cm}^{-1}$  step size in the range of  $2800\text{-}3000\text{ cm}^{-1}$  of IR wavenumber. The fitting values and parameters are tabulated in Appendix C.

### 4.3 Results and Discussion

The PDA polymerized films fabricated in their non-imprinted (NIPs) and template-imprinted (MIPs) version can be observed from Figure 4.2. Here, NIPs are considered as the controlled-film surfaces to identify the relative proportion of functional groups prominent at the air-polymer interface. Digital pictures of the fabricated PDA non-imprinted thin-films (NIPs) are represented in Figure 4.3 (A) displaying visible differences in the colour profiles of the deposited films (from light to dark brown) as a function of varying PDA polymerization duration (3-, 6-, and 24-hrs), shown in sub-panels I, II, and III respectively. It reflects an increase in the deposition of PDA over the  $\text{SiO}_2$  substrate with increasing polymerization duration. Initially, these PDA coated substrates were characterized for their topography and coated-film thickness using SEM and AFM respectively (Figure 4.3, panel B and C). Studies conducted by Lee et al.<sup>198</sup> revealed the formation of self-assembled coatings of PDA deposits over the substrate. On the other side, Su et al.<sup>217</sup> demonstrated the PDA nanoparticle formation by the simple solution shaking procedure. From our results of SEM imaging, the film growth on the

substrate is evident with increasing PDA polymerization duration under constant stirring of the aqueous media. The film thickness analysis by AFM in Figure 4.3 (C) showed the measured values to be ~9 nm, 15 nm, and 55 nm for the 3-, 6-, and 24-hrs polymerization duration (sub-panels I, II, and III in Figure 4.3 (C)), respectively. These observations were found to be in alignment with the results already reported.<sup>198</sup> The observed thickness values from AFM results are represented in a histogram profile in panel C (IV) of Figure 4.3 for clarity. These characterizations of NIP films depicted the formation of micro-/nano-particle self-polymerized coatings over the SiO<sub>2</sub> substrates which increase proportionately with respect to time-duration of substrate immersion and stirring within the buffered DA aqueous solution at pH 8.

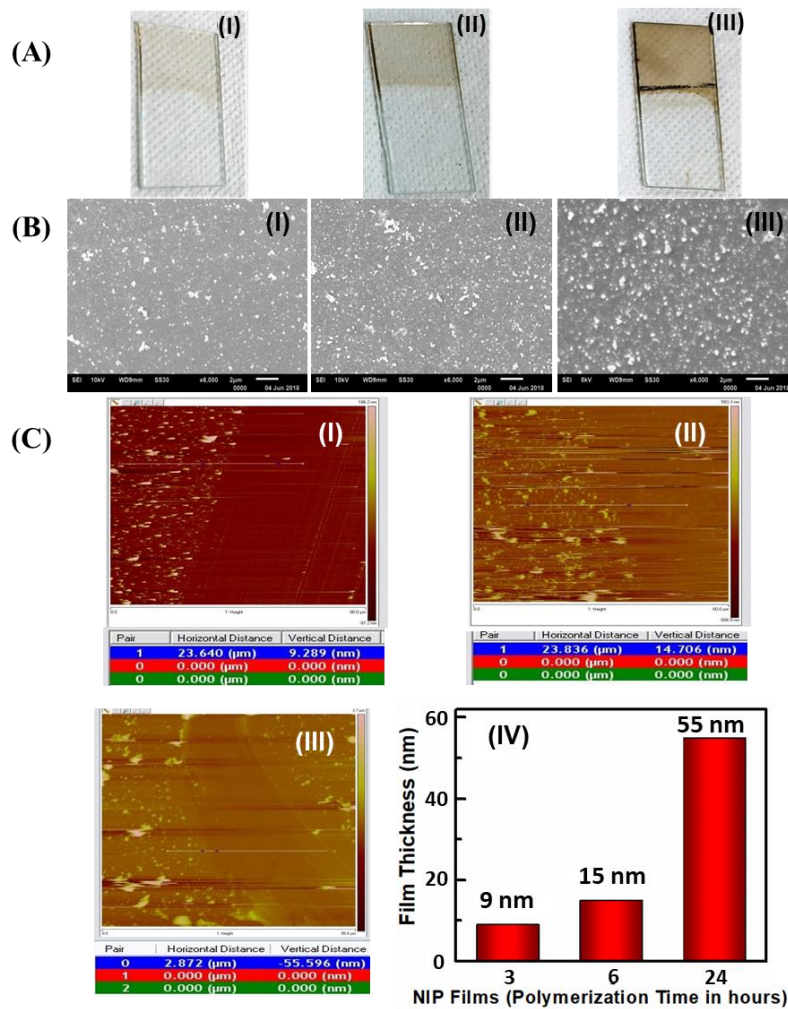


**Figure 4.3** (A) Digital images of PDA fabricated SiO<sub>2</sub> substrates (NIP films), (B) SEM imaging, and (C) Film thickness evaluation by AFM with distinct polymerization time durations of NIP for (I) 3-hrs, (II) 6-hrs, and (III) 24-hrs respectively. (C) Subpanel (IV) represents the histogram of the film thickness evaluated by AFM.



A lot of work is done in the course of understanding the polymerization scheme of DA to form PDA in the process.<sup>198,200-202,205,218</sup> As per the literature, PDA polymerization involves an initial step involving deprotonation of dihydroxyl moieties of DA under an alkaline oxidative aqueous condition. This generates a reactive specie DA-quinone, which subsequently re-arranges to form leukodopaminechrome and its further oxidation leads to the formation of 5,6-dihydroxyindole (DHI).<sup>198,200-202,205,218</sup> Additional oxidative coupling of DHI with other formed intermediates during the polymerization process results in the formation of PDA. The probable molecular structure of polymer formed after polymerization gets completed, is shown in Figure 4.4 (A) as per the literature.<sup>201,202,204,205</sup> Since the incorporation of Tris buffer is known to propel the intrinsic oxidation process of the DA monomers to form PDA,<sup>203</sup> we have prepared the DA solutions in Tris-HCl buffer system in our work. Literature reports that the DA monomers tend to project differential pKa values for its corresponding molecular units.<sup>206,219</sup> The first and second hydroxyl group of the catechol moiety bears pKa value of ~9.0 and 12 respectively, while the non-cyclized ammonium group has pKa ~10.5 value.<sup>206,219</sup> Thus, it is clear from this information that the aqueous conditions and polymerization duration will be primarily determining the concomitant molecular species to be formed after the PDA polymerization gets completed. We have worked at pH 8 for generating PDA-based thin-films over SiO<sub>2</sub> substrates, where we expect the presence of both the protonated as well as non-protonated amino groups<sup>209,216,220</sup> in addition to the cyclized imine structures forming an adhesive PDA film.<sup>201,205,207,208,219</sup> The non-protonated groups are more inclined to form an intramolecular cyclized product during PDA polymerization,<sup>209,220</sup> while the protonated functional moieties bear more propensity to interact via ionic interactions either with the underlying silanol groups of SiO<sub>2</sub> substrate or with the template molecules.<sup>216-219</sup>

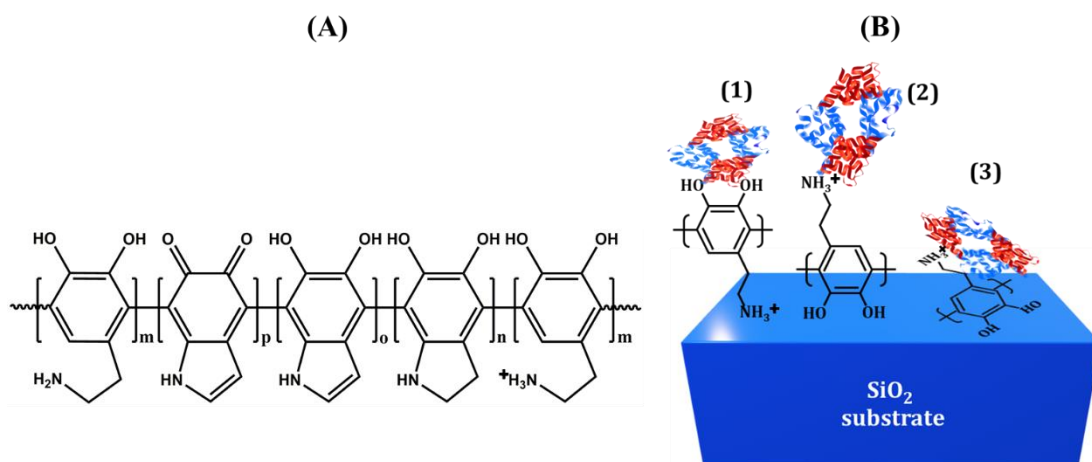


**Figure 4.4** (A) Plausible molecular structure of the polydopamine (PDA) formed after the polymerization from dopamine (DA) monomers. (B) Possible arrangements of the PDA fabrication over SiO<sub>2</sub> substrates and BHb protein association.

Hence, to prepare an effective functional surface for embedding and recognition of template molecules, it is crucial to identify that which functional moiety is actually residing and is active at the air-polymer interface, as depicted in Figure 4.4 (B) in the proposed model of PDA molecules arrangement and protein binding in possibly three different ways. Considering this, the VSFG spectroscopy has been employed to extract the molecular-level profile of NIP film fabrication initially for discerning the predominant functional groups at the air-NIP interface, and how their relative proportion varies with increasing PDA polymerization time. Across the literature it is known that the primary charged amine groups interact well with the aromatic rings, which aids in catechol-based cross-linking structures to form adhesive and robust PDA coatings.<sup>202,206,218,221</sup> In terms of interaction with analytes or template molecules, PDA coatings rich in quinones provide an excellent biomolecular immobilization via stacking and hydrophobic associations.<sup>213,222</sup> This signifies that an optimal presence of functional moieties is required for improved biomolecular embedding and recognition, that is highly governed by the time-scale of DA polymerization.<sup>200,206,209,218</sup> In this study we have worked upon this parameter, where, based on the relative observance of protonated and non-protonated groups from the SFG spectra of NIP, we were able to spot the favorable time-duration of PDA formation with maximum surface coverage of active binding groups.

Figure 4.5 (A) shows the fitted SFG spectral profile of NIPs with polymerization-time variation, observed in CH-stretch region. Here, the intense profile of features in CH-region is an indicator of the resonating modes exclusively present at the air-NIP interface. Since PDA consists largely of methylene residues and as per the proposed molecular

structure of PDA from the literature,<sup>201,202,204,205</sup> for our analysis in CH-region, we have referred the methylene groups attached to protonated amines as “protonated ethylamine groups”, while those attached to non-protonated free amine groups are assigned as “non-protonated ethylamine groups” for clarity. The protonation of molecular group causes perturbations in its molecular cloud arrangement which leads its neighbouring moieties to resonate comparatively at a higher wavenumber than the non-protonated counterparts.<sup>210,223,224</sup> Similar characteristic profile is observed for NIPs where the peak splitting of methylene symmetric stretch ( $\text{CH}_{2\text{SS}}$ ) contribution in VSFG spectra (Figure 4.5 (A)) occurs, with first peak centered at  $\sim 2858 \text{ cm}^{-1}$  ( $\text{P}_1$ ) and the second peak located at  $\sim 2876 \text{ cm}^{-1}$  ( $\text{P}_2$ ).  $\text{P}_1$  is the representative of the non-protonated ethylamines, while  $\text{P}_2$  attributes to protonated ethylamines.<sup>210,223,224</sup> An additional dominating peak centered at  $\sim 2922 \text{ cm}^{-1}$  is seen which is assigned to methylene anti-symmetric stretch ( $\text{CH}_{2\text{AS}}$ ) mode from non-protonated ethylamines (depicted as peak  $\text{P}_3$ ).<sup>210,223,224</sup> Through the spectral fitting (Appendix C), other minor contributions were also recognized at wavenumbers  $\sim 2904 \text{ cm}^{-1}$  (C-H stretch of catechol/cyclized five-membered ring structure),  $\sim 2939 \text{ cm}^{-1}$  (non-protonated  $\text{CH}_{2\text{FR}}$ ),  $\sim 2965 \text{ cm}^{-1}$  ( $\text{CH}_{2\text{AS}}$  from protonated ethylamine), and  $\sim 2996 \text{ cm}^{-1}$  (combination band from C- $\text{H}_{\text{AS}}$  stretch of catechol/cyclized unit).<sup>210,223-226</sup> However, here we will limit our discussion to the predominantly resonant features observed. The anti-symmetric modes were identified from the VSFG polarization-dependent selection rules by observing these modes in PPP polarization configuration for NIPs (Figure 4.5 (B)), as it is quite known that the symmetric vibrational modes are prominently observed in SSP polarization scheme while the anti-symmetric modes dominate the PPP configuration of the SFG spectra.<sup>223,224,227</sup>

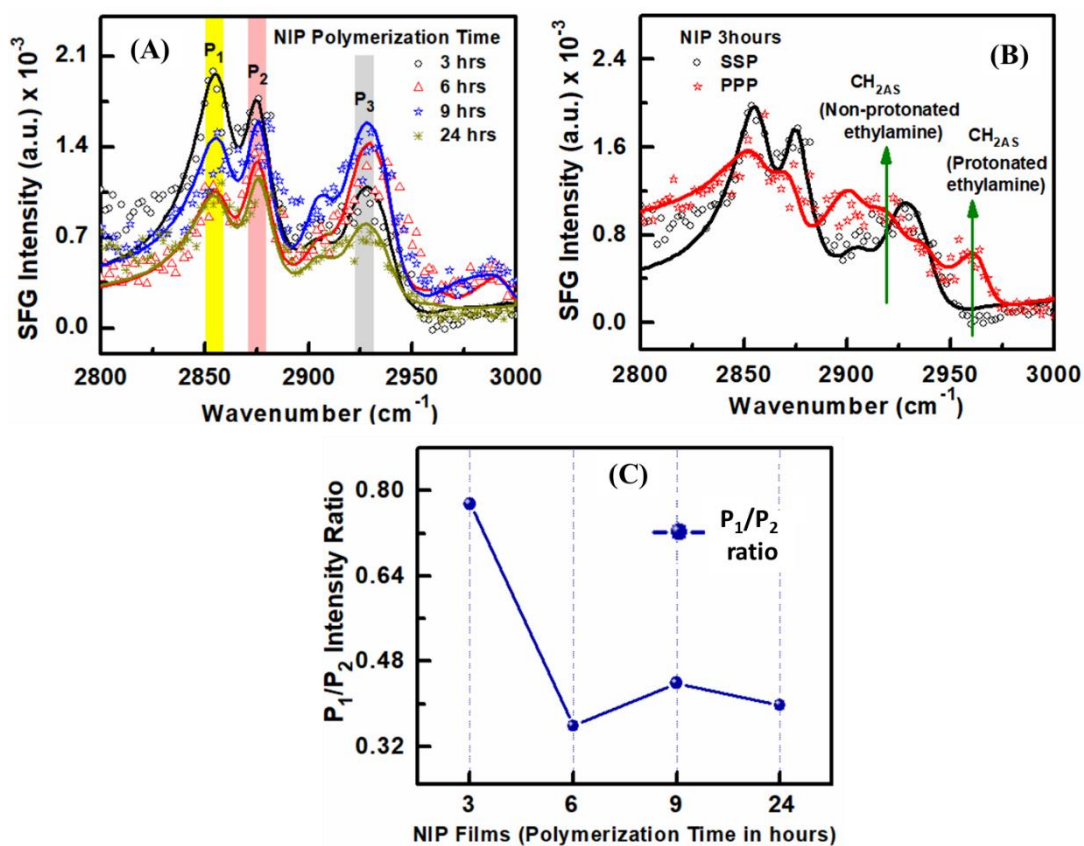


**Figure 4.5** (A) Fitted VSFG spectra of NIP films fabricated with 3-, 6-, 9-, and 24-hrs duration of polymerization. (B) SFG spectra of 3-hr NIP film in SSP and PPP polarization combinations. (C) Peak intensity ratios of P<sub>1</sub> and P<sub>2</sub> for the fitted SFG spectra of NIP films fabricated at distinct time-scales.

To analyze the functional group proportion, Figure 4.5 (C) quantitatively elaborates the VSFG intensity ratio profile among peaks P<sub>1</sub> and P<sub>2</sub>. It could be readily apprehended that the non-protonated ethylamine contribution (P<sub>1</sub>) dominated for 3-hr duration NIP film, while it was minimum in case of 6-hour duration NIP fabrication. Instead, for 6-hr NIP, relative proportion of protonated ethylamines (P<sub>2</sub>) dominates the spectrum (Figure 4.5 (A)). Moreover, as seen from Figure 4.5 (panel A), the contribution from the combination band of C-H<sub>AS</sub> stretch of catechol/cyclized unit also becomes prominent in comparison to other NIP durations. Thus, the relative balance of the catechol moieties and protonated functional groups are optimal in case of 6-hr duration of PDA polymerized NIP films. Several works in the literature performed to understand the PDA formation mechanism with polymerization-time variation also represent the similar observations, where higher number of protonated species could be found for durations near 6-hr.<sup>200,204,209</sup> These studies were evaluated through X-ray photoelectron spectroscopy and cyclic voltammetry.<sup>200,204,209</sup> Although the analyses from the interfacial

probing implemented in our study harmonizes well the observations from the literature,<sup>200,204,209</sup> interpretation from the SFG spectra offers a convenient and direct evidence of the resonating species distinctively along with the information about the aromatic-specie presence, with a notable structural sensitivity at the molecular-scale.

Following the interfacial analysis of NIPs, template molecule embedding and imprinting of PDA films were characterized as a function of polymerization time-duration to extract the information about the actively interacting surface. MIPs are fabricated by including BHB protein as template molecules along with the DA monomers for proceeding with the BHB-embedded-MIP polymerization for different time intervals. The MIP SFG spectra in Figure 4.6 (A) show tremendous contribution from the methyl features. This arises due to the fact that the BHB protein molecules bear a tetrameric assembly consisting of two  $\alpha$ -chains and two  $\beta$ -chains, which carries a net amount of 376 methyl ( $-\text{CH}_3-$ ) residues per protein molecule as a part of its aliphatic amino acid presence (structure from PDB 2QSP). This elucidates the dominance of  $-\text{CH}_3-$  features over the native ethylamine signatures from PDA due to BHB presence, as observed from the air-BHB interfacial spectra displayed in Figure 4.6 (B). The major resonating features in both BHB and MIP films are seen at  $2858\text{ cm}^{-1}$  ( $\text{CH}_2\text{ss}$ , ( $d^+$ )),  $2876\text{ cm}^{-1}$  ( $\text{CH}_3\text{ss}$ , ( $r^+$ )), and  $2939\text{ cm}^{-1}$  ( $\text{CH}_{3\text{FR}}$ , ( $r_{\text{FR}}$ )).<sup>67,228,229</sup> Subsidiary peaks, including  $2904\text{ cm}^{-1}$ ,  $2922\text{ cm}^{-1}$ ,  $2965\text{ cm}^{-1}$ , and  $2996\text{ cm}^{-1}$  attributed to methine C-H stretch,<sup>67,229</sup>  $\text{CH}_{2\text{AS}}$  ( $d^-$ ),<sup>229,230</sup>  $\text{CH}_{3\text{AS}}$  ( $r^-$ ),<sup>67,230</sup> and combination band of C-H stretch (from aromatic ring) modes<sup>225,226</sup> were also considered for spectral fitting analysis (see Appendix C). The anti-symmetric modes were considered from the PPP and SPS polarization combinations performed for BHB protein molecules using VSFG (Figure 4.6 (B)). Although the underlying contribution of PDA features (as observed for NIPs) cannot be excluded in the MIP SFG spectra, nevertheless, the overall intensity profile is indicative primarily of the methyl group features, which are being accounted here for further analysis of MIP thin-films with polymerization time variation. It is necessary to emphasize here that the observed highly intense SFG profile results due to the large-scale molecular ordering with the species predominantly facing perpendicularly towards the air. Therefore, to determine the ordering and alignment of the alkyl features of protein molecules upon imprinting the PDA fabricated at different time durations, the relative peak intensity ratios of  $\text{CH}_2\text{ss}/\text{CH}_3\text{ss}$  ( $d^+/r^+$  ratio) were observed. This could aid in qualitatively discerning the optimum time duration of polymerization such that the template-monomer associations are efficient to construct reliable imprinted

surfaces. Here,  $d^+/r^+$  ratio analysis is used to identify higher number embedded BHb protein molecules. Figure 4.6 (C) shows the  $\text{CH}_2\text{SS}/\text{CH}_3\text{SS}$  ratio to be minimum in case of 6-hr MIP film which was observed to be similar in value and features with the SFG spectra of pristine BHb film drop-casted over the  $\text{SiO}_2$  surface in SSP polarization mode. This  $d^+/r^+$  ratio analysis for MIPs indicates an aligned embedding of the BHb protein molecules along with the PDA fabrication. This alignment in the methyl group signatures could not be observed for other MIP fabrications at 3-, 9- and 24-hrs.

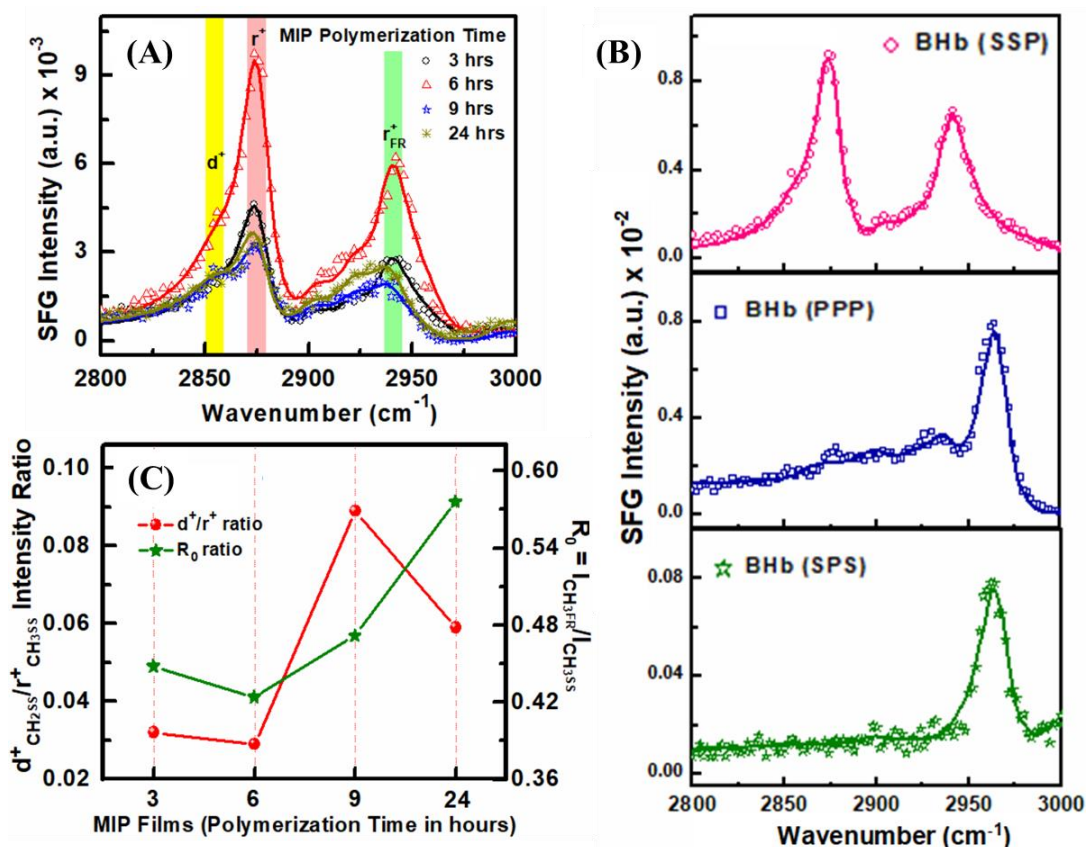


**Figure 4.6** (A) Fitted VSF profile of MIP thin films with polymerization duration of 3-, 6-, 9-, and 24-hours. (B) Polarization-dependent VSF spectra of BHb protein molecules fabricated as a thin-film over  $\text{SiO}_2$  substrate. (C) Peak intensity ratio trend of  $d^+/r^+$  ratio values and  $R_0$  ( $I_{\text{CH}_3\text{FR}}/I_{\text{CH}_3\text{SS}}$ ) ratio values observed for MIP fabrications of distinct polymerization durations.

Figure 4.6 (C) also incorporates the quantitative analysis from another prominent feature observed in MIP SFG spectra (in panel A) i.e., ratio of  $\text{CH}_3\text{FR}$  and  $\text{CH}_3\text{SS}$  mode as  $R_0$ . The fermi resonance (FR) signature basically dominates in the SFG spectra when there occurs a resonant coupling among the degenerate fundamental vibrational mode ( $\nu_1$ ) and the overtone mode ( $2\nu_2$ ) of the methyl vibrational frequency.<sup>231-233</sup> The FR emergence, thus, highly determines the net proportion of inter- and intra-molecular

interactions, and the impact on their strength due to nearby molecular environment.<sup>228,231-233</sup> Several groups have propelled their work in correlating the strengthening of inter-molecular forces with emergence of FR vibrational feature in SFG spectroscopy.<sup>228,231-233</sup> First initiated by Tian et al., the net intermolecular interactions were determined by experimentally quantifying the CH<sub>3FR</sub> and CH<sub>3SS</sub> mode ratios at both air-liquid and air-solid interfaces of developed phospholipid monolayers.<sup>228,231</sup> Subsequently, Premadasa et al. conducted a modelled experiment to understand the impact of chemical substitution and nature of polarity on the originating FR contribution from the polymeric molecular groups.<sup>232</sup> Recent work in this direction by Liu et al.<sup>233</sup> stated an inter-connective contribution of intermolecular forces which are actually responsible for the arrangement and distribution of ordered molecular groups to develop phosphate films over a substrate. They suggested the major role of van der Waal (vdW) forces in causing the superior molecular coverage and formation of ordered structures. These inter-molecular interactions are fundamentally generated from the attractive vdW forces and repulsive electrostatic forces.<sup>228,231-233</sup> Thus, all these studies implemented CH<sub>3FR</sub>/CH<sub>3SS</sub> ratio to be a direct representative of variations in inter-molecular association, where the relative impact of the attractive and repulsive forces could be identified. The above discussion exemplified that the CH<sub>3FR</sub>/CH<sub>3SS</sub> ratio decreases for molecular groups projecting maximum enrolment of vdW interactions while reduced contribution from electrostatic forces. Implementation of this information to our results where we analysed the evolution of CH<sub>3FR</sub>/CH<sub>3SS</sub> ratio (referred to 'R<sub>0</sub>' here) strengthened our inference about an increase in the number of inter-molecular associations via vdW forces while the electrostatic influence is minimum for the case of 6-hour polymerized MIP film. Here, at the working pH of 8, the minimum contribution from electrostatic forces indicates neutralization of net charges due to association among the positively charged amines of dopamine from PDA structures and negatively charged residues from Bhb protein molecules (which bear overall negative charge above its pI of 6.8).<sup>201,234</sup> Thus, the 6-hr MIP surface project neutralization of net charges at the surface after the completion of the fabrication procedure. Additionally, in coherence with the observations by Liu et al.,<sup>233</sup> our results also projected an ordered maximally intense methyl profile (as discerned through minimum d<sup>+</sup>/r<sup>+</sup> ratio value) for 6-hr MIP (panel A and C) aligned towards the air as a result of larger vdW interactions.

Through the thickness analysis of the NIP fabrications by AFM (Figure 4.3 (C)), the thickness of 6-hr polymerized fabrication results in a 15 nm thick film (Figure 4.3 (C), panel II and IV) which conveniently incorporates sufficient amount of BHB protein molecules bearing a molecular diameter of approximately 5.5 nm (according to its PDB 2QSP structure). VSFG provided the molecular insights about the predominance of the functional groups at the air-NIP interface (Figure 4.5), which assisted in effectively associating with the BHB molecules to form MIP surfaces (observed to be optimal for 6-hr duration) (Figure 4.6). Therefore, the deposition time of 6-hours was selected for the imprinting of BHB template molecules and further experimental characterizations.

The BHB template removal efficacy was screened for the optimized fabrication of MIP 6-hrs film using VSFG at the air-MIP interface. This was done by undertaking a series of 5 washing cycles of the 6-hr MIP film and its potential impact over the BHB removal and underlying imprinted polymer surface was evaluated. The washing solution for fabricated thin-films was prepared with 3% v/v of acetic acid with added 0.1% w/v of SDS. The fabricate films were stirred for 20 minutes each. Figure 4.7 represents the evolution of SFG profile of 6-hr MIP with subsequent washing cycles and how the BHB template removal impacts the MIP spectra. The spectra (in panel A) show a notable decrement in  $\text{CH}_{3\text{SS}}$  ( $r^+$ ,  $2876\text{ cm}^{-1}$ ) peak intensity contribution of the 6-hr MIP SFG profile (without washing). By quantitatively determining the  $d^+/r^+$  ratio profile to check for the relative contribution by  $\text{CH}_{3\text{SS}}$  feature (characteristic for BHB embedding), a striking rise is seen with the first washing step itself which then present smaller variations in the magnitude upon conducting subsequent washing steps (quantitative plot in Figure 4.7 (B)). This indicates that the template molecules are being promptly and considerably removed from the 6-hr MIP surface due to consecutive washing steps. Additionally, the  $\text{CH}_{3\text{FR}}$  feature ( $r^+_{\text{FR}}$ ,  $2939\text{ cm}^{-1}$ ) of 6-hour MIP film (panel A) with every washing cycle gets reduced in the magnitude of its intensity. However, in contrast to the distinct  $\text{CH}_{2\text{AS}}$  ( $P_3$ ,  $2922\text{ cm}^{-1}$ ) feature observed for NIP films (Figure 4.5 (A)), MIP films after systemic washing cycles still exhibit visible contribution from the  $\text{CH}_{3\text{FR}}$  peak ( $r^+_{\text{FR}}$ ,  $2939\text{ cm}^{-1}$ ) in the VSFG spectra (Figure 4.7 (A)). This projects that few residual BHB molecules could still be held within some of the MIP cavities. Despite this, considering the net magnitude of reduction in methyl features in SFG spectra, it can be stated reliably that a considerate amount of embedded BHB template molecules have been washed off the MIP surface leaving behind the cavities which structurally mimic the bound protein structure.



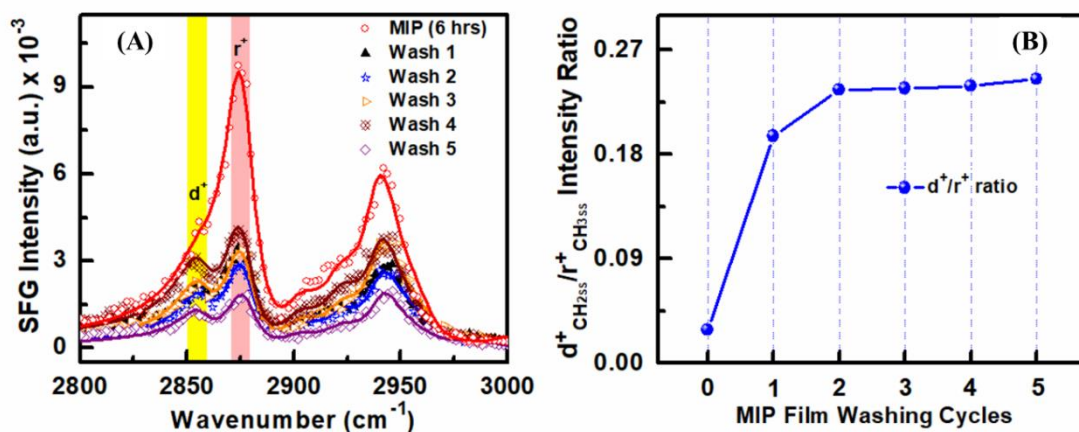


**Figure 4.7** (A) Fitted VSG spectra, and (B) peak intensity profile of  $d^+/r^+$  ( $\text{CH}_2\text{SS}/\text{CH}_3\text{SS}$ ) ratio values plotted for the 6-hrs MIP film evaluated after a sequence of washing cycles (in SSP polarization mode).

After undergoing systemic washing cycles (5 times) to remove the template molecules, the 6-hr MIP film bearing BHb sized imprints were inspected for their BHb re-binding potential. To conduct the re-binding process, the cavity bearing 6-hr MIP film was dipped into the  $0.5 \text{ mg}\cdot\text{mL}^{-1}$  BHb solution buffered with Tris-HCl buffer at pH 7.5 containing 0.01% SDS within the solution (referring here as the re-binding solution) and were kept under constant stirring for 120 minutes. This methodology has been adapted from Zhou et al.,<sup>215</sup> where considering lower BHb concentration for re-binding process than that chosen initially for MIP fabrication is essentially done since extracting all the bound BHb molecules is potentially difficult and harsh, and not much changes could be seen for higher BHb concentrations as reported by Zhou and coworkers.<sup>215</sup> In our work, the BHb re-binding of cavity-laden MIP evaluated using VSG (in Figure 4.8 (A)) shows a visible increment in the  $\text{CH}_3\text{SS}$  mode at  $2876 \text{ cm}^{-1}$  upon dispensing the cavity-laden 6-hr MIP into the BHb rebinding solution. Simultaneously, on plotting the  $d^+/r^+$  ratio values (as obtained after spectral fitting) shown in Figure 4.8 (B), the obtained value descends with respect to the cavity-laden MIP (without subjecting to BHb re-binding). The relative rise in  $\text{CH}_3\text{SS}$  ( $r^+$ ) contribution suggests presence of some bound form of BHb molecules. The observed results are the direct validation of the MIP-cavities memorizing and recognizing the template BHb molecules during the re-binding procedure.

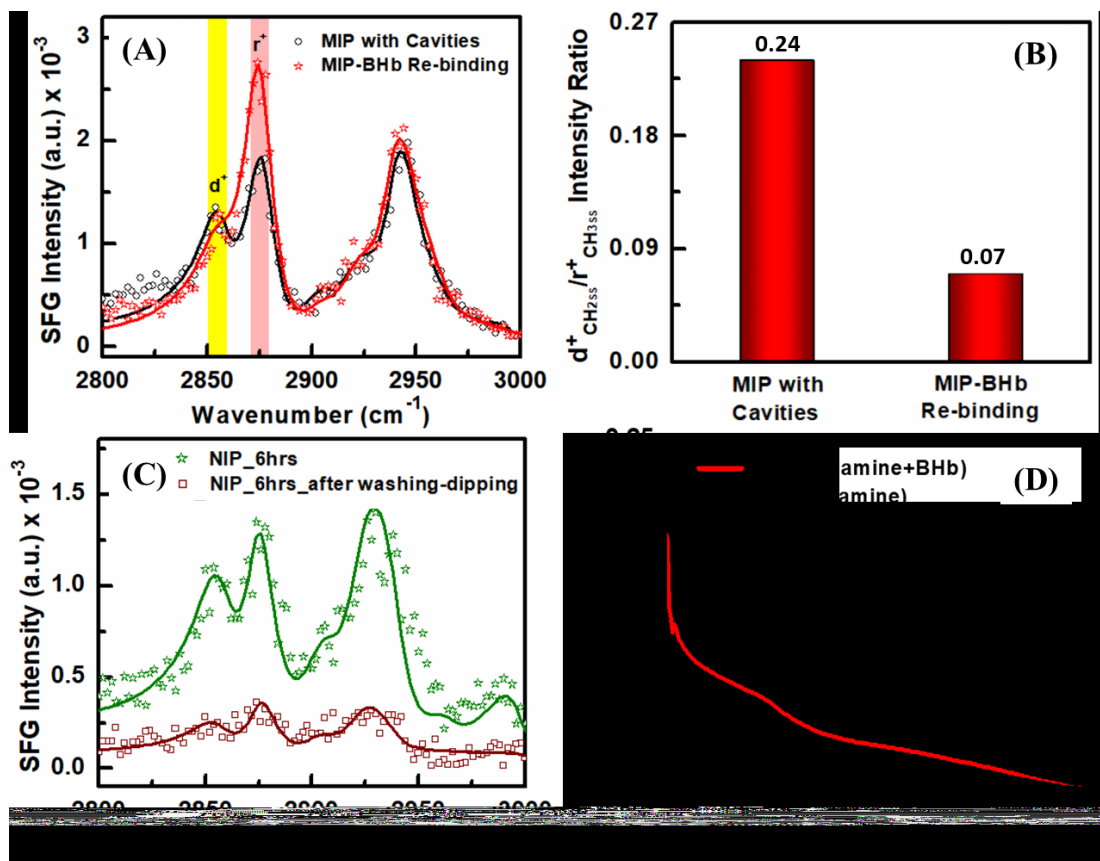


**Figure 4.8** (A) Fitted VSFG spectra, and (B) histogram profile of cavity bearing 6-hr MIP surface and after BHb-cavity re-binding. (C) Comparative VSFG profile of 6-hrs NIP fabrication before and after subjecting to systemic washing and BHb re-binding processes. (D) UV-Visible absorption spectra of the residual solution from 6-hrs NIP and MIP fabrications respectively after conducting the BHb re-binding experiment.

Similar procedure of the template washing and re-binding (as done for 6-hr MIP) was performed for the 6-hr NIP fabrication and were put through for interfacial analysis using VSFG (Figure 4.8 (C)). Here, no enhancements in the spectral intensity or resonant features were seen, turning down the possibility of any kind of molecular-level changes occurring after going through the similar re-binding procedure. Thus, from this investigation, the possibility of NIP washing and template binding after dipping it into the re-binding solution is eliminated. Hence, the interfacial evaluation of the re-binding potential via SFG displayed favorable re-binding of BHb over the cavity-bearing 6-hr MIP by simply probing the molecular vibrations at the air-polymer interface. Additionally, after carrying out MIP and NIP re-binding process, the residual BHb solution was collected and investigated indirectly for the efficacy of template re-binding process using UV-Visible absorbance spectroscopy (Figure 4.8 (D)) to discern any changes in the net BHb concentration within the re-binding solution. The observations

however showed very minute differences in the overall absorbance profile when re-bound 6-hr MIP and 6-hr NIP (after subjecting through similar washing and re-binding process) are compared. Thus, the UV-Visible absorption spectroscopy could only provide indirect evidence of the BHb re-binding with MIP. However, VSFG offered a detailed insight towards the resonant molecular features specifically at the interface of air-MIP interface as a direct indicator of the MIP re-binding and molecular recognition potential, without carrying out any kind of surface modifications or chemical/radical additives for optimal film fabrication and template binding.

Although, the contributing sum frequency intensity after BHb re-binding the MIP cavities (Figure 4.8) is considerably less than that seen in case of 6-hr polymerized MIP-BHb surface before template removal (Figure 4.6). This could probably arise by considering few factors which are vital for the template incorporation process: (1) since VSFG intensity is correlated directly with the molecular number and their surface orientation, randomization of BHb molecules might affect the signal; (2) BHb protein molecules favourably stay within the buffer solution than to completely fill the MIP cavities over the substrate; (3) the diffusion process of template molecules might require some energy-driven mechanism and therefore, larger BHb concentrations and increased contact time in the immersing solution may aid in better loading of MIP cavities; (4) the percentage of cavity formed and accessible to template molecules on MIP surface is less such that during re-binding, a limited number of BHb molecules are able to re-bind in comparison to the number of BHb moieties incorporated during MIP formation; or (5) MIP surface washing affected the polymeric cross-links and cavity morphology such that BHb molecules do not embed within their appropriately carved imprints on MIP surface. Henceforth, it will be worthwhile to address these elementary aspects to fine-tune the building-up of an effective imprinted surface for molecular-scale recognition for future prospects.

#### **4.4 Conclusion**

In summary, we have demonstrated the potential of SFG spectroscopy to devise and investigate a simple one step approach of MIP matrix formation and recognition of template protein (BHb) molecules, which is not achievable by limited surface sensitive tools. Here, the MIP matrices are directly fabricated on to the solid SiO<sub>2</sub> substrate

applicable for the designing of bio/chemo sensors. VSFG aided in deducing the interactive forces embracing the BHB recognition and re-binding process within the MIP cavities at the air-polymer interface. This fundamental molecular-scale probing of the interactive forces involved during polydopamine polymerization and how the functional moieties are varying preferentially at the interface could provide a vital understanding for designing and tailoring the future biomimetic fabrications based on adhesive polymers to construct MIP-based sensing platforms, which would aid in enhancing the overall sensing efficiency of distinct template molecules.

# Monitoring the protein-protein interactions mediated by tungsten disulfide quantum dots at the air-aqueous interface

In the present chapter, we progressed towards studying a more complex system in terms of protein-protein interactions (PPIs) in the presence and absence of transition-metal quantum dots ( $WS_2$ QDs) at air-aqueous interface. Protein-protein interactions (PPIs) are fundamental to biology and are being progressively investigated for various industrial and biomedical applications. However, to enhance their potentiality in technological/industrial domains, requirement of a mediator or an immobilization matrix proves to be helpful in mediating their working capacity. Transition metal dichalcogenides (TMDs) are one of the emerging materials bearing distinctive characteristics, which makes them a potent mediator. Among them, tungsten disulfide ( $WS_2$ , a TMD) possesses higher electronic as well as optical properties with higher electron carrier mobility, which makes it an effective material for conducting label-free sensing applications. Utilizing  $WS_2$ -based sensing devices with biomolecular interfacing demands their comprehensive investigation in modulating protein-protein associations at the molecular-scale, so as to obtain an improved performance for the  $WS_2$ -based materials. In the present work, we probed the significance of  $WS_2$  as quantum dots in supporting the antiferritin-ferritin proteins (taken as the model proteins) at the air-water interface using sum frequency generation vibration spectroscopy (SFG-VS). By observing the role of water molecules as a reporter of interactions, and a quantitative orientational analysis of alkyl groups in absence and presence of  $WS_2$  QDs, we conclusively state that the  $WS_2$  nanomaterial could potentially govern efficient PPIs.

## 5.1 Introduction

Proteins are widely recognized as work-horses of the cell, since they play a major part in several biological processes and interactions with other biomolecules and thus regulates the cellular functioning. Protein-protein interactions (PPIs) is one such

phenomena that is the essence of life and the basic forces (covalent or non-covalent forces) that govern their binding is being progressively investigated in various research domains like developing theragnostic,<sup>235</sup> biomolecular extraction procedures<sup>236</sup> as well as for developing and optimizing biosensors<sup>237</sup> with unprecedented capacities. Concerning the recognition/identification of PPIs, several different methodologies have been pursued such as co-immunoprecipitation (Co-IP) assay, gel electrophoresis, enzyme-linked immunosorbent assay (ELISA), fluorescence resonance energy transfer (FRET), mass spectrometry, flow cytometry, circular dichroism, and atomic force microscopy (AFM).<sup>18,236,238,239</sup> Out of all these, immunoassay procedures for PPI identification provides benefit related to the molecular selectivity, sensitivity, and instantaneous response towards the analyte. These properties are further strengthened in presence of a mediator or an immobilizing material, since PPIs tend to enroll several random non-specific interactions in their native milieu which are relatively weak and predispose them to loosen their attachment and ultimately break off from their position. Therefore, requirement of a strong mediator which is biocompatible and is also being widely used for sensing design applications is a necessary prerequisite for the evolution of bio-aided sensor designing in terms of sensitivity and selectivity.

Several immobilizing materials are known to aid in molecular recognition processes ranging from polymers, molecular dendrimers, silica, and various nano-dimensioned materials.<sup>240-242</sup> The transition metal dichalcogenides (TMDs), which include MoS<sub>2</sub>, WS<sub>2</sub> etc., gained significant importance in the research community due to their involvement in opto-electronics, photonics, sensing, electrocatalysis, etc.<sup>243,244</sup> Tungsten disulfide (WS<sub>2</sub>) is a newly evaluated material of choice for analytical and electronic devices due to their good charge carrier mobility, storage capacity, and structure-dependent electronic/optical properties.<sup>243,245,246</sup> Numerous studies have been directed related to WS<sub>2</sub> for biosensing applications, where they often encounter several different biomolecules and analytes for conducting a sensitive detection process.<sup>243,247-252</sup> The existing studies on PPIs using bulk-phase techniques built a crucial information about the protein-protein association strengthened and mediated by introducing organic molecules and/or osmolytes.<sup>241,253,254</sup> Nevertheless, the strengthening parameter among PPIs also involves the reorientation and reorganization of the biomolecular groups to project complimentary binding while associating with the immobilizing material.<sup>255,256</sup> The importance of the molecular orientation changes with antibody (Ab) concentration has

been explicitly studied by Saha et al.<sup>257</sup> where they evaluated the significance of antibody surface coverage in an appropriately oriented fashion over magnetic nanoparticle in determining the antigen (Ag) capturing activity and kinetics for efficient biosensing, using optical-based immunoassay procedure. However, there is a lack in the understanding about the molecular level associations which arise between the receptor and analyte during recognition, especially within the aqueous media where the strength and dynamics of interaction gets intricate.<sup>3</sup> Moreover, switching from the bulk expression towards the interface, the surface topography and chemical heterogeneity during molecular recognition become predominant and crucial to probe. Hence, it becomes necessary to explore the molecular-level details of PPI-WS<sub>2</sub> association to evaluate and improve the overall performance of WS<sub>2</sub> towards sensing applications.

As an interface-selective tool, SFG-VS has been successfully used in several studies to analyze the protein interfacial features and the molecular-level implications over the interfacial water network.<sup>38,57,65,229</sup> Xiao et al.<sup>65,258</sup> in their consecutive reports, worked upon TMD-based MoS<sub>2</sub> and WS<sub>2</sub> materials to understand the predominant role of the nature of molecular groups in defining the adsorption tendency of protein molecules over the TMD's surface. Boughton et al.<sup>259</sup> deduced the interfacial protein-protein complexation in real time which facilitated a 15° change in the protein's molecular orientation profile during PPIs over the model cell membrane. However, the molecular crowding aspect (by varying protein concentration) and the strengthening of PPIs upon interfacing with a quantum-sized nanomaterial (i.e., WS<sub>2</sub> QDs) in the aqueous environment is relatively unexplored in details. Additionally, studies concerning the implication of WS<sub>2</sub> as quantum dots (QDs) in PPIs regulation has not been explored yet. Here, using the SFG-VS, we have exploited the native complementarity of antibody and antigen protein molecules (denoted here as 'Ab' and 'Ag' respectively), where ferritin and antiferritin protein molecules are taken as model proteins in our work. Addition of WS<sub>2</sub> QDs was effective in reducing the overall tilt angle value of PPI's methyl groups by 12° as analyzed through interfacial SFG-VS studies. The results comprehensively depicted an enhanced protein-protein interaction in presence of WS<sub>2</sub> nanomaterial.

## 5.2 Experimental Methods and Procedure

### 5.2.1 Material Requirements

Anti-ferritin, a human antibody produced in rabbit, was obtained from Sigma-Aldrich (F5012) and ferritin antigen (source: human liver,  $\geq 95\%$ ) was procured from EastCoast Bio (LA066). These samples were utilized without any further modification and purification. All samples were prepared in Millipore ultra-pure water type-1 with a resistivity of  $18.2 \text{ M}\Omega\cdot\text{cm}$  and  $\text{pH } 5.8 \pm 0.1$  at  $22^\circ\text{C}$ . All glassware and sample cell used in the experiment were treated with piranha solution ( $\text{H}_2\text{SO}_4:\text{H}_2\text{O}_2$  in 3:1 ratio composition) and rinsed multiple times with Millipore water before their usage.

### 5.2.2 Synthesis and Preparation of $\text{WS}_2$ QDs

The  $\text{WS}_2$  QD sample was a generous gift from our collaborator Dr. Suman Singh, CSIR-CSIO, Chandigarh (India), for conducting the SFG experiments. The detailed synthesis, preparative, and characterization scheme of  $\text{WS}_2$  QDs has been reported by the collaborators in the literature.<sup>260</sup> Briefly, the 300 mg of  $\text{WS}_2$  nanosheets obtained in powder form were subjected to 30 minutes stirring at room temperature along with added 150 mg native-derived biosurfactant. It was then exposed to probe sonication for 3 hours and then centrifuged consecutively for 15 and 30 minutes at 6,500 and 10,000 rpm respectively to obtain the resultant  $\text{WS}_2$  QDs (schematically represented in Figure 5.1).

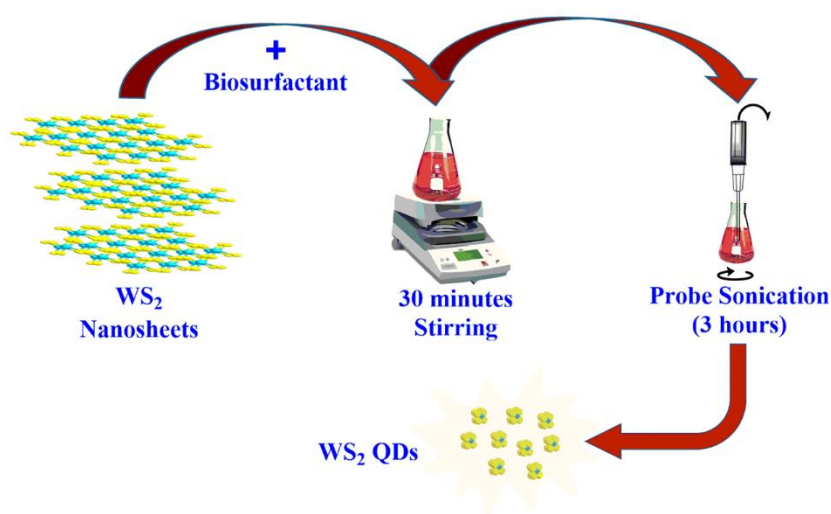


**Figure 5.1** Synthesis scheme for tungsten disulfide quantum dots ( $\text{WS}_2$  QDs).



### 5.2.3 Sum Frequency Generation Vibrational Spectroscopy (SFG-VS)

The current study has been performed using a commercial SFG spectrometer (Ekspla, Lithuania). The details of the experimental set up are provided in chapter 2 (section 2.2.2). The samples (7 mL in volume) taken in a Teflon cell of 45 mm in diameter for SFG-VS evaluation. Anti-ferritin antibody (Ab) was prepared at two concentrations i.e.,  $0.3 \mu\text{g}\cdot\text{mL}^{-1}$  and  $3 \mu\text{g}\cdot\text{mL}^{-1}$  in pristine water whereas ferritin antigen (Ag) was prepared at the concentration of  $0.3 \text{ ng}\cdot\text{mL}^{-1}$  and  $3 \text{ ng}\cdot\text{mL}^{-1}$ . WS<sub>2</sub> QDs are taken at concentration of  $0.25 \mu\text{g}\cdot\text{mL}^{-1}$  in pristine water for the current studies. The SFG spectra were acquired distinctly in two regions i.e., the CH-stretching region ( $2750\text{-}3050 \text{ cm}^{-1}$ ) and OH-stretching region ( $3050\text{-}3800 \text{ cm}^{-1}$ ). Experiments were performed in three polarization modes i.e., SSP, PPP, and SPS. where S and P denote electric field polarization of light to be perpendicular and parallel to the plane of incidence, respectively. The SPS polarization mode is considered only for CH-stretch region probing of molecular systems in this study. These polarization combinations depict the polarization mode of the output sum frequency, input visible, and input IR beam in sequence respectively. The spectral data was gathered with average of 200 pulses per step and  $2 \text{ cm}^{-1}$  step size in the C-H region, while  $5 \text{ cm}^{-1}$  step size was taken for O-H region probing. The experiments were performed at room temperature ( $\sim 22^\circ\text{C}$ ). The SFG spectra were evaluated and fitted using the Lorentzian expression (details can be seen in chapter 2, section 2.2, equation 2.16) and the orientation analysis of the molecular groups have been performed using relations elaborated in chapter 2, equation 2.20–2.25.

### 5.2.4 SFG-VS Data Analysis

The SFG intensity variations are directly linked to the average number density of molecules at the interface as well as their orientation with respect to the surface normal (refer chapter 2, section 2.2, equation 2.19). The SFG spectra are acquired in SSP, PPP, and SPS polarization schemes (SPS polarization spectrum of the samples) in CH-stretch region. Both the symmetric ( $\text{CH}_{3\text{SS}}$ ) and asymmetric ( $\text{CH}_{3\text{AS}}$ ) stretch modes were considered for terminal methyl orientation analysis by referring to the ratios of their amplitudes (obtained by spectral fitting analysis in CH-stretch region, values provided in Appendix D) in SSP and PPP polarization schemes respectively. After employing the

equation 2.20 and 2.23 (from section 2.2 in chapter 2), and considering the ‘R’ value to be 3 and  $\beta_{caa} \approx -\beta_{aac}$ ,<sup>111,113</sup> the following theoretical formula is derived:

$$\frac{\chi_{xxx,SS}^{(2)}}{\chi_{zzz,AS}^{(2)}} = \frac{-\{2\langle \cos \theta \rangle + \langle \cos^3 \theta \rangle\}}{6\{\langle \cos \theta \rangle - \langle \cos^3 \theta \rangle\}} \quad (5.1)$$

Using the theoretical equation (5.1), an orientation plot is obtained following the Gaussian distribution function. The variation in the angular distribution width ( $\sigma$ ) is taken from 0° to 60° for the analysis of the orientation angle of terminal methyl groups of proteins. The value obtained from the ratio of amplitude values of SSP and PPP symmetric and asymmetric stretches of sample spectra, respectively, is drawn as a horizontal line (represented here as dotted straight lines). The intersection points of the horizontal lines with the plotted theoretical curves provide the average orientation angle ( $\theta$ ) value or tilt angle value (in degrees) for the respective distribution width ( $\sigma$ ) of the terminal methyl residues of protein molecules.

### 5.3 Results and Discussion

Molecular recognition and the strength of interactive forces specifically at the interface can be readily identified by SFG-VS technique in an unprecedented way.<sup>38,57,65,187,258,259</sup> Here, we have investigated the potential of WS<sub>2</sub> QDs in mediating ferritin antigen (Ag) and anti-ferritin antibody (Ab) protein interactions (taken as a model system proteins) at the interface. Ferritin protein is ubiquitous in the living systems, known to buffer the net iron content within the body. The procured human liver ferritin (will be referred as ‘Ag’ ahead) is a full length 440 kDa serum protein molecule bearing 24 subunits with 21 kDa and 19 kDa H/L chain hybrids.<sup>261</sup> Its isoelectric point (IEP) is around 5.3 on pH unit scale, and at the experimental pH condition employed in this work i.e., 5.8 ± 0.1 pH value, it withholds an overall negative charge (constituted by 44 negative and 23 positively charged residues within a single subunit, in accordance with its sequence).<sup>261,262</sup> The complimentary anti-ferritin antibody (designated ahead as ‘Ab’) used here is a 183 amino acid sequence protein molecule with ~21 kDa of weight (UniProtKB accession number: P02794 for sequence). The IEP of Ab is calculated by ExPASy ProtParam tool (information adapted from Gasteiger et al.),<sup>263</sup> considering its

UniProt amino acid sequence, and is theoretically found to be  $\sim 5.31$ . The Ab molecules bear a net negative charge (a total of 31 negatively charged and 30 positively charged amino acid residues), hence, bearing a net single negative charge per Ab protein molecule at pH 5.8. Likewise, the WS<sub>2</sub> QDs tend to attain a negative charge at the studied pH conditions (optimally found from published work of the collaborators providing the prepared QDs sample).<sup>260</sup>

The SFG-VS experiments are initiated by acquiring the interfacial spectra of pristine water in SSP, PPP, and SPS polarization modes respectively, which is considered as the reference spectrum devoid of any foreign molecule or perturbations due to organic contamination. The polarization-dependent SFG experimentation allows to gain the overall molecular behavior and its interfacial structural arrangement through the orientational evaluation of functional moieties predominantly occupying the interface.<sup>111,113,187</sup> The resultant data points of the obtained SFG spectra of different samples were fitted with the Lorentzian profile to access the peak positions and their relative amplitude values (fitting tables provided in Appendix D). The interfacial VSFG probing of pristine water in different polarization modes is represented in Figure 5.2. As explained in chapter 3, the obtained interfacial profile of the water structure includes contribution from the lower frequency region positioned at  $\sim 3220\text{ cm}^{-1}$  (referred to strongly H-bonded) and a higher frequency region with relative peaks positioned at  $\sim 3450\text{ cm}^{-1}$  and  $\sim 3550\text{ cm}^{-1}$  (depicted as weakly H-bonded).<sup>146,152,189,264</sup> The prominent feature visible at  $\sim 3705\text{ cm}^{-1}$  is contributed by the interfacial free (dangling) O-H stretch mode projecting towards the air.<sup>146,152,189,264</sup> The H-bonding network in the OH-stretch region are usually prone to frequency shifts or amplitude changes owing to the perturbations in their H-bonding strength whenever any foreign constituent is added within the system, which can be directly observed through spectral analysis.<sup>146,149,152,189,264</sup> The absence of features in CH-stretch region depicts pristine nature of interfacial water molecules.

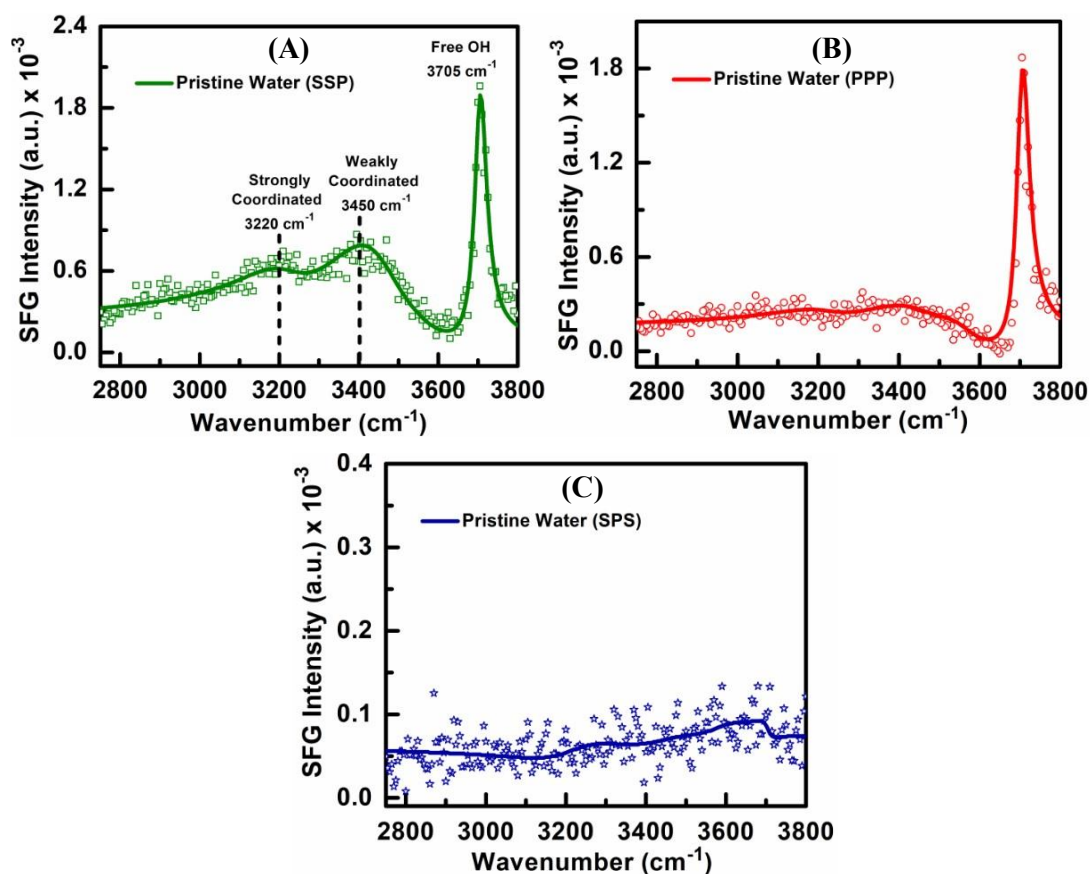


**Figure 5.2** VSFG spectra of pristine water-air interface in (A) SSP, (B) PPP, and (C) SPS polarization schemes.

Studies related to WS<sub>2</sub> QDs, Ab, and Ag were performed in appropriate combinations to acquire a clear and overall molecular picture behind the QD's influence towards the PPIs exclusively at the air-water interface. We have worked with Ab molecules in  $\mu\text{g.mL}^{-1}$  concentration and Ag molecules in  $\text{ng.mL}^{-1}$  concentration. Here, the reason behind selecting distinct concentration levels for Ab and Ag is that at this optimum ratio value, the Ab-Ag complexes displayed sensitive binding, which were confirmed from the electrochemical responses in terms of a significant variation in the measured current response, as represented in the previously published work of collaborators with the same molecular entities.<sup>260</sup> Moreover, Ab molecules used in our work consists of only a heavy chain domain which bears two-regions per Ab molecule for interacting with Ag protein. Instead, a single Ag protein molecule bear several identical Ab-specific binding locations or epitopes.<sup>261</sup> Hence, a higher concentration of Ab in comparison to Ag will offer an increased opportunity for Ag recognition. The protein molecules are considered in two sets of concentration combinations. First set (set-I) include lower concentration of Ab-Ag as  $0.3 \mu\text{g.mL}^{-1}$  and  $0.3 \text{ng.mL}^{-1}$  respectively, while second set (set-II) represent higher concentration of Ab-Ag as  $3 \mu\text{g.mL}^{-1}$  and  $3 \text{ng.mL}^{-1}$

respectively. The SFG-VS spectra are obtained distinctively in CH-stretch and OH-stretch mode, where the CH-region offers information about the hydrophobic moieties while the OH-stretch region embodies the imprints of the influence of molecular interactions over the interfacial water molecular structure, which will be separately discussed in this work.

### 5.3.1 Probing Characteristic Features of Protein and Impact of WS<sub>2</sub> QDs

To begin with, the interfacial characteristic expression of respective protein molecules (i.e., Ab and Ag) have been analyzed at the experimental pH of 5.8. The interaction of these respective protein molecules was then studied with WS<sub>2</sub> QDs to understand and observe the impact of these nanomaterials over the interfacial protein molecular arrangement.

**CH-stretch region:** Figure 5.3 represents the SFG spectra in CH-stretch region in SSP, PPP, and SPS polarization schemes of the characteristic features of protein molecules and the influence of WS<sub>2</sub> at air-aqueous interface. It demonstrates significant response from CH<sub>3</sub> symmetric stretch (CH<sub>3SS</sub>, r<sup>+</sup>) and CH<sub>3</sub> fermi-resonance (CH<sub>3FR</sub>, r<sup>+FR</sup>) modes located at ~2879 cm<sup>-1</sup> and ~2939 cm<sup>-1</sup>, respectively.<sup>33,56,146,189,229,265,266</sup> A weaker contribution at ~2857 cm<sup>-1</sup> and ~2920 cm<sup>-1</sup> is attributed to methylene symmetric stretch (CH<sub>2SS</sub>, d<sup>+</sup>) and asymmetric stretch (CH<sub>2AS</sub>, d<sup>-</sup>) respectively.<sup>33,56,146,189,265,266</sup> Although, minute contribution from d<sup>+</sup> and d<sup>-</sup> mode have also been considered during spectral fitting of all the samples in Figure 5.3 which suggests the presence of symmetry breaks in the alkyl structures of the adsorbed protein molecules making the methylene resonant transitions possible.<sup>33</sup> The peak positions at ~2959 cm<sup>-1</sup> and ~2976 cm<sup>-1</sup> are attributed to the CH<sub>3</sub> asymmetric stretch (CH<sub>3AS</sub>) out-plane (r<sup>-op</sup>) and in-plane (r<sup>-ip</sup>) modes.<sup>56,265,266</sup> We observed substantial signal from CH<sub>3SS</sub> (r<sup>+</sup>) and CH<sub>3FR</sub> (r<sup>+FR</sup>) modes in SSP polarization, while the PPP and SPS spectra is majorly dominated by the CH<sub>3AS</sub> out-plane stretch mode (r<sup>-op</sup>). Henceforth, in our discussion throughout this chapter, we will mainly focus on the predominant methyl features of CH<sub>3SS</sub>, CH<sub>3FR</sub> and CH<sub>3AS</sub> modes. Prominence of these methyl features depict an increased level of molecular alignment along the surface normal at the interface.

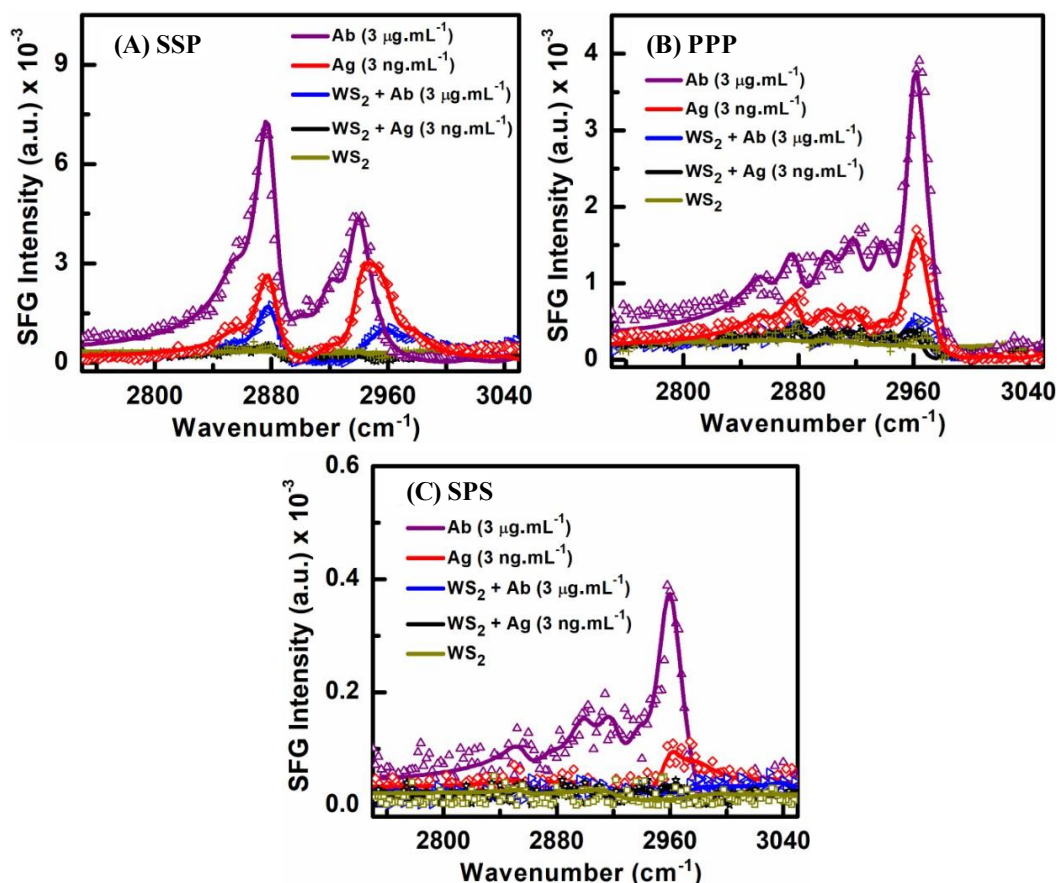


**Figure 5.3** VSFG spectra in CH-stretch region ( $2750\text{-}3050\text{ cm}^{-1}$ ) of individual proteins under pristine condition and in presence of  $\text{WS}_2$  QDs respectively at the higher protein concentration in (A) SSP, (B) PPP, and (C) SPS polarization schemes.

The observed peak intensities decrease in order of Ab, Ag,  $\text{WS}_2\text{-Ab}$ ,  $\text{WS}_2\text{-Ag}$  and  $\text{WS}_2$  in SSP, PPP, and SPS modes respectively (Figure 5.3). In SPS mode (panel C), no resonant mode of  $\text{CH}_3\text{AS}$  peak is seen for both  $\text{WS}_2\text{-Ab}$  and  $\text{WS}_2\text{-Ag}$ . As seen from panel A, the characteristic spectral features of Ab show a dominance of  $r^+$  and  $r^+_{\text{FR}}$  mode which indicates the interfacial molecular alignment of methyl groups along surface normal and the increased propensity of Ab protein molecules, which is inferred from several SFG-based studies.<sup>56,230,232</sup> Additionally, out of all the other samples demonstrated in panel A, B, and C, pristine Ab is seen to have negligible contribution from  $\text{CH}_3\text{AS}$  ( $r^-_{\text{ip}}$ ) mode in the SSP spectra while in PPP and SPS mode of Ab, the contribution from  $\text{CH}_3\text{AS}$  ( $r^-_{\text{op}}$ ) is predominant in addition to the overlapped  $r^-_{\text{ip}}$  mode. Contrarily, the characteristic SFG profile of Ag molecules in  $\text{ng.mL}^{-1}$  concentration display an overall reduced intensity than that observed for Ab (at  $\mu\text{g.mL}^{-1}$ ). The SSP profile of Ag also features  $\text{CH}_3\text{AS}$  mode, which points towards possibility of differential alignment of methyl groups of Ag molecules at the interface.<sup>267</sup> Several studies provide concomitant details about the protein binding with the substrate and the associated conformation acquired by the proteins

during the process.<sup>36,39,60,65,229,258,259</sup> Many experimental findings reinforce that the proteins bind to hydrophobic surfaces via adsorption, mainly through exposed aromatic residues.<sup>60,258,259,268,269</sup> WS<sub>2</sub> material has equally shown its potential to bind and interact with different protein and peptide molecules.<sup>60,258</sup> Sun et al. presented details about the amino acid specificity of WS<sub>2</sub>, displaying 100% attachment of cysteine and ~89% attachment of arginine amino acid to WS<sub>2</sub> nanosheets.<sup>247</sup> Li et al. utilized fluorescence assay to observe an enhanced binding of proteins to WS<sub>2</sub> via van der Waals (vdW) interactions with protein's aromatic amino acids and H-bonding of protein's hydrophilic groups with sulfur atoms of WS<sub>2</sub>.<sup>269</sup> Work by Xiao et al. deduced that the adsorption of proteins over the MoS<sub>2</sub>/WS<sub>2</sub> surface occurs precisely due to hydrophobic interactions instead of the exposed cysteine of different proteins.<sup>258</sup> This explicitly show the possible precedence of protein hydrophobic groups to associate with WS<sub>2</sub>. Accounting for the sequence of proteins in our work, Ab presents more number of hydrophobic moieties (due to concentration in  $\mu\text{g.mL}^{-1}$ ) than Ag (in  $\text{ng.mL}^{-1}$ ). Additionally, Ab protein carries 3 cysteine and 7 arginine residues while Ag protein has 9 arginine residues in its sequence with no cysteine molecule.<sup>262,270</sup> On that account, we targeted to understand the differential impact of WS<sub>2</sub> QD on the characteristic interfacial signatures of Ab and Ag protein molecules respectively. For pristine WS<sub>2</sub> QDs at air-aqueous interface, no direct spectral features in CH-stretch region were observed in its SFG spectrum (panel A, B, and C), which suggests the pristine nature of WS<sub>2</sub> sample at interface. With the introduction of WS<sub>2</sub> to the pristine Ab sample, drastic minimization in the overall characteristic spectral intensity of Ab is seen in both SSP and PPP polarizations, and gets vanished in SPS mode (panel C). Moreover, in SSP mode (panel A) distinct appearance of CH<sub>3</sub>AS ( $\nu_{\text{ip}}$ ) is also recognized for WS<sub>2</sub>-Ab which was absent in pristine Ab spectra. This suggests the possibility of molecular orientational changes in the methyl groups of Ab protein molecules which gets slightly tilted in parallel position i.e., towards the surface upon interacting with WS<sub>2</sub>. The SFG response from the WS<sub>2</sub>-Ag system gets completely diminished with respect to pristine Ag interfacial signature as seen in SSP and SPS modes, while in PPP spectra a weak intensity feature of CH<sub>3</sub>AS mode can be observed. Hence, it is revealed that the introduction of WS<sub>2</sub> QDs has disrupted the net molecular ordering of the respective alkyl chains of both the protein molecules (Ab and Ag) at the air-aqueous interface. In case of lower concentration of respective protein molecules with and without WS<sub>2</sub>, (Figure 5.4, panel A and B) performed in SSP and PPP mode, the VSFG profile shows no distinct resonant features for any of the protein molecule

combinations. Thus, the observed features for higher protein concentrations are indicative of the concentration-dependent surface coverage of protein molecules as known from literature<sup>56,60,188</sup> and observed in our preliminary work of chapter 3 (section 3.3).<sup>129</sup>

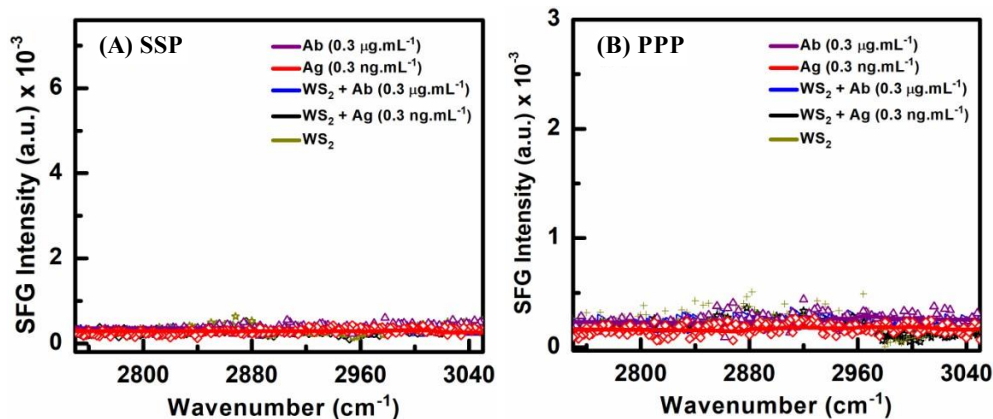


**Figure 5.4** VSFG spectra in CH-stretch region ( $2750\text{-}3050\text{ cm}^{-1}$ ) of individual proteins under pristine condition and in presence of  $\text{WS}_2$  QDs respectively at the lower protein concentration in (A) SSP and (B) PPP polarization schemes.

**OH-stretch region:** Figure 5.5 (panel A and B) showcase the characteristic influence of the Ab and Ag protein molecules, and respective proteins in presence of  $\text{WS}_2$  on the interfacial water structure in the OH-stretch region in SSP- and PPP-polarized schemes. In SSP mode (panel A), the Ab molecules display an overall diminishing OH-stretch profile with respect to the observed SFG spectra of pristine water. Here, a remarkable impact on the weakly H-bonded region is seen while the strongly H-bonded feature remains unaffected. This indicates a higher propensity of the stronger H-bonding population at the expense of weakly coordinated water molecules at the interface in the presence of Ab protein molecules. It may have enrolled the impact of protein's hydrophobic molecules in causing a structuring effect on the surrounding water molecules and hence, maintains the strongly coordinated H-bonds while disrupting the weakly coordinated H-bonding among the interfacial water molecules.<sup>71,157</sup> Conversely, Ag molecules show a huge enhancement in the OH-stretch spectra with significant contribution observed from the weakly coordinated OH-oscillators (centered at  $\sim 3450\text{ cm}^{-1}$ ). The stronger SFG intensity seen for Ag molecules suggests field-dependent rise in polar alignment of water dipoles due to the presence of charged moieties at the interface.<sup>38,146,188</sup> Also, since Ab is incorporated at a higher bulk concentration of  $\mu\text{g.mL}^{-1}$  relative to Ag (in  $\text{ng.mL}^{-1}$ ), a decreased OH-stretch signal reveals the disordered state of water dipoles at higher surface coverage of Ab molecules. These features are considered



to be the characteristic interfacial arrangement of respective protein molecules being studied here.

Primarily, the expression of WS<sub>2</sub> is deduced at the air-water interface which displayed perturbation exclusively on the free-OH peak intensity and the coordinated water structure is not influenced in that process (panel A and B). With the introduction of WS<sub>2</sub> QDs to protein solution, the overall SFG intensity in the OH-stretch region enhances for Ab while it gets lowered in its profile with respect to the pristine water spectrum for Ag (panel A). This is quite opposite to that observed for pristine Ab and Ag at the air-aqueous interface in the OH-stretch region in absence of WS<sub>2</sub> (panel A). Therefore, a reduced and an enhanced OH-stretch profile for WS<sub>2</sub>-Ag and WS<sub>2</sub>-Ab respectively, exhibits that the WS<sub>2</sub> potentially breaks the ordered H-bonding structure formed by Ag and builds an ordered water structure surrounding the Ab molecules at the interface.

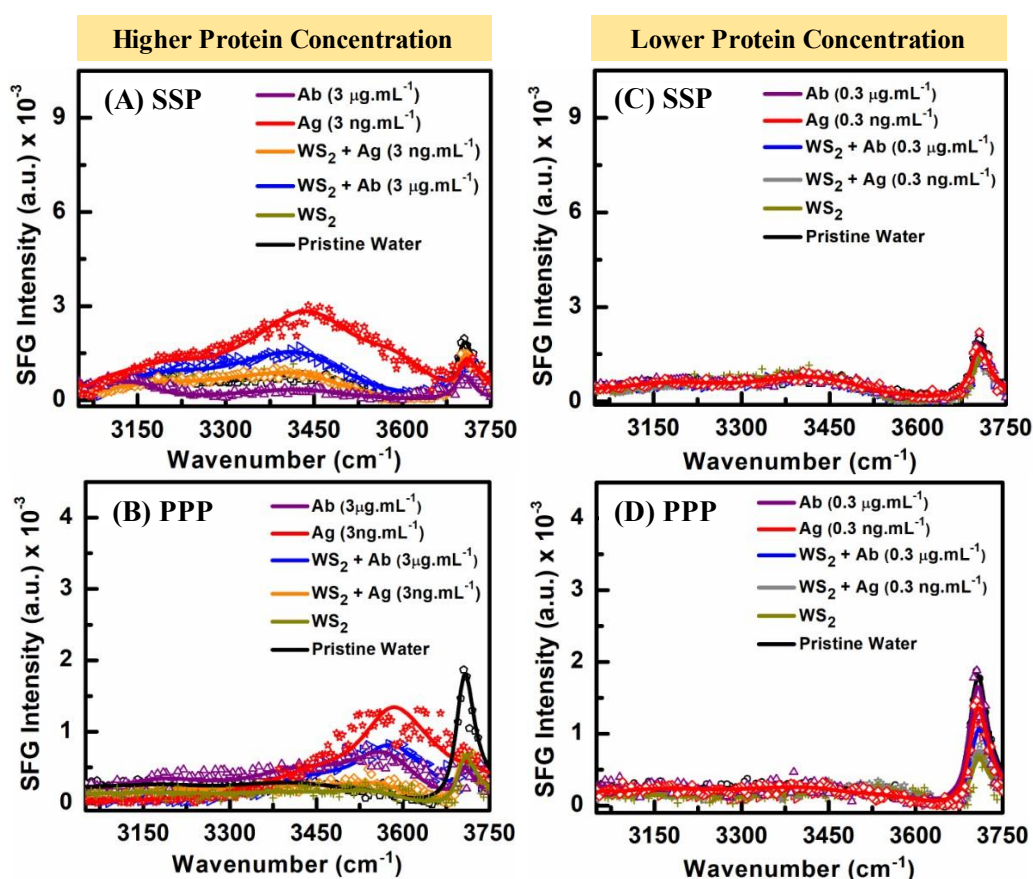


**Figure 5.5** Polarization-dependent VSG spectra in OH-stretch region (3050-3750 cm<sup>-1</sup>) of individual proteins under pristine condition and in presence of WS<sub>2</sub> QDs respectively at the higher (panel A and B) and lower (panel C and D) protein concentrations.

In case of PPP (panel B), there is an increased contribution from the OH-stretch intensity centered at ~3550 cm<sup>-1</sup> peak position. This assignment is widely ascribed to the

water molecules weakly bound to the hydrophobic residues of protein molecules, also referred to as hydrophobic hydration in several studies.<sup>188-190,264,271</sup> Nevertheless, the enhancement at  $\sim 3550\text{ cm}^{-1}$  peak can also be conferred by charge-dependent polar alignment of weakly coordinated water molecules.<sup>188</sup> Hydrophobic hydration plays a significant role in conducting several biological functions including protein folding, molecular phase transitioning, bilayer stability, etc.<sup>188-190,264,271</sup> It is distinctively apparent in PPP than in the SSP spectra. In SSP spectra (panel A), the  $3550\text{ cm}^{-1}$  peak is considered for the spectral fitting as it is observed to arise as a shoulder associated with the prominent  $3450\text{ cm}^{-1}$  peak, which suggests the presence of some weakly interacting water existing within the hydrophobic domains of protein molecules.<sup>188-190,264,271</sup> Panel B shows a higher  $3550\text{ cm}^{-1}$  intensity for Ag than Ab. This observation indicates that the molecular groups of Ab are present in confined state at the interface which is minimizing the access of inner hydrophobic domains to the water molecules.<sup>189,190,264</sup> On the other hand, Ag molecules are expected to acquire a rich association among their hydrophobic regions and the neighboring water molecules via weaker H-bonding.<sup>188-190,264</sup> Under the influence of  $\text{WS}_2$ , the  $3550\text{ cm}^{-1}$  feature subsides for Ag and remains invariable for Ab in PPP mode. Yet, in case of Ab here, a minimized contribution from strongly-coordinated feature (i.e.,  $3220\text{ cm}^{-1}$ ) is noticed which reflects change in water molecular orientation. This suggests that on introducing  $\text{WS}_2$ , the H-bonding among water molecules and hydrophobic moieties of Ag gets disrupted, while it does not impact the water molecular arrangement around Ab molecules, as observed from the PPP polarization scheme. Further, we could observe an overlapped feature of  $3705\text{ cm}^{-1}$  with the lower frequency  $\sim 3450\text{ cm}^{-1}$  and  $\sim 3550\text{ cm}^{-1}$  peak particularly for Ag and  $\text{WS}_2$ -Ab. This specifies the heterogeneity in the weaker H-coordination of water molecules with hydrophobic residues of protein molecules.<sup>188,189,264</sup> From panel A and B, the reduction of free OH feature at  $\sim 3705\text{ cm}^{-1}$  in intensity is apparent for all samples representing their respective molecular surface coverage. However, it does not completely diminish in intensity indicating the existence of residual free-OH groups at interface.

Re-evaluating the CH-OH stretch results in SSP and PPP mode (Figure 5.3 A-C and 5.5 A-B), it can be stipulated that although  $\text{WS}_2$  associates with hydrophobic residues of both the protein molecules, their association leave a distinct imprint over the interfacial water structure. It thereby represents a differential behavior of Ab and Ag in presence of  $\text{WS}_2$ . Introducing  $\text{WS}_2$  disrupts the ordered water structure for Ag while it makes an

ordered H-bonded structure and maintains the state of hydrophobic hydration exclusively for Ab protein molecules. In addition, for the case of lower protein concentration, for WS<sub>2</sub>-Ag and WS<sub>2</sub>-Ab samples, no significant variation is noticed in the OH-stretch region except a decrease in the free OH intensity which is a signature of molecular surface coverage (Figure 5.5, panel C and D).

### 5.3.2 Role WS<sub>2</sub> QDs in Steering PPIs with Varying Protein Concentration

The Ab and Ag protein molecules are naturally directed to form complementary associations with each other. Utilizing this property to our advantage, we aim to understand how WS<sub>2</sub> gets involved in steering the PPIs at the air-water interface. Furthermore, we investigated that how variation in the concentration of protein molecules alters the efficiency of WS<sub>2</sub> QDs in mediating PPIs at the air-water interface. For this, the experiments were performed with both lower (set-I) and higher (set-II) concentrations for Ab (0.3 and 3  $\mu\text{g.mL}^{-1}$ ) and Ag (0.3 and 3  $\text{ng.mL}^{-1}$ ) to understand the concentration-based impact.

**CH-stretch region:** Figure 5.6 demonstrates the SFG spectra of PPIs with lower (set-I) (panel A-C) and higher (set-II) (panel D-F) protein concentration combinations in presence and absence of WS<sub>2</sub> QDs in CH-stretch region in SSP, PPP, and SPS polarization schemes respectively. We observed similar methyl-stretch modes as mentioned previously. It is interesting to notice the influence of WS<sub>2</sub> QDs presence on the PPIs. Here, the changes are observed to be very substantial for set-I of PPIs in WS<sub>2</sub> QD presence (panel A-C). These molecular signatures were absent for the case of lower protein concentration for PPIs (Figure 5.6, panel A-C), pristine Ab, pristine Ag, and the respective individual proteins in presence of WS<sub>2</sub> QDs (Figure 5.4 and Figure 5.5 C-D) in the aqueous media. However, raising the protein concentration (i.e., set-II) under the influence of WS<sub>2</sub> QDs (at fixed concentration), leads to an increased contribution from  $r_{\text{FR}}^+$  with a relatively minor increment observed for  $r^+$  in SSP mode (panel D). Additionally, a contrasting behavior is noticed in the  $r^-$  mode in PPP and SPS spectra of two different protein concentration sets in WS<sub>2</sub> presence. For set-I PPI concentration (panel B-C), an emergence of  $r^-$  mode with WS<sub>2</sub> addition reveals an increased polar alignment of molecules making the molecules surface active. Besides, for set-II PPIs, an abrupt decrease in  $r^-$  mode is seen when WS<sub>2</sub> is added in PPP mode (panel E) while it increases slightly in SPS mode (panel F). This suggests that WS<sub>2</sub> is somewhat driving the

disruption in methyl group's alignment and tilting it more towards the surface normal as also evaluated from the SPS polarization scheme (panel F). Overall, these polarization-based SFG spectra of PPIs corroborate the likelihood of an active surface coverage and orientational changes of the methyl groups with respect to the surface normal which are favorably steered by WS<sub>2</sub> QDs, as perceived for both the concentration sets of protein molecules.

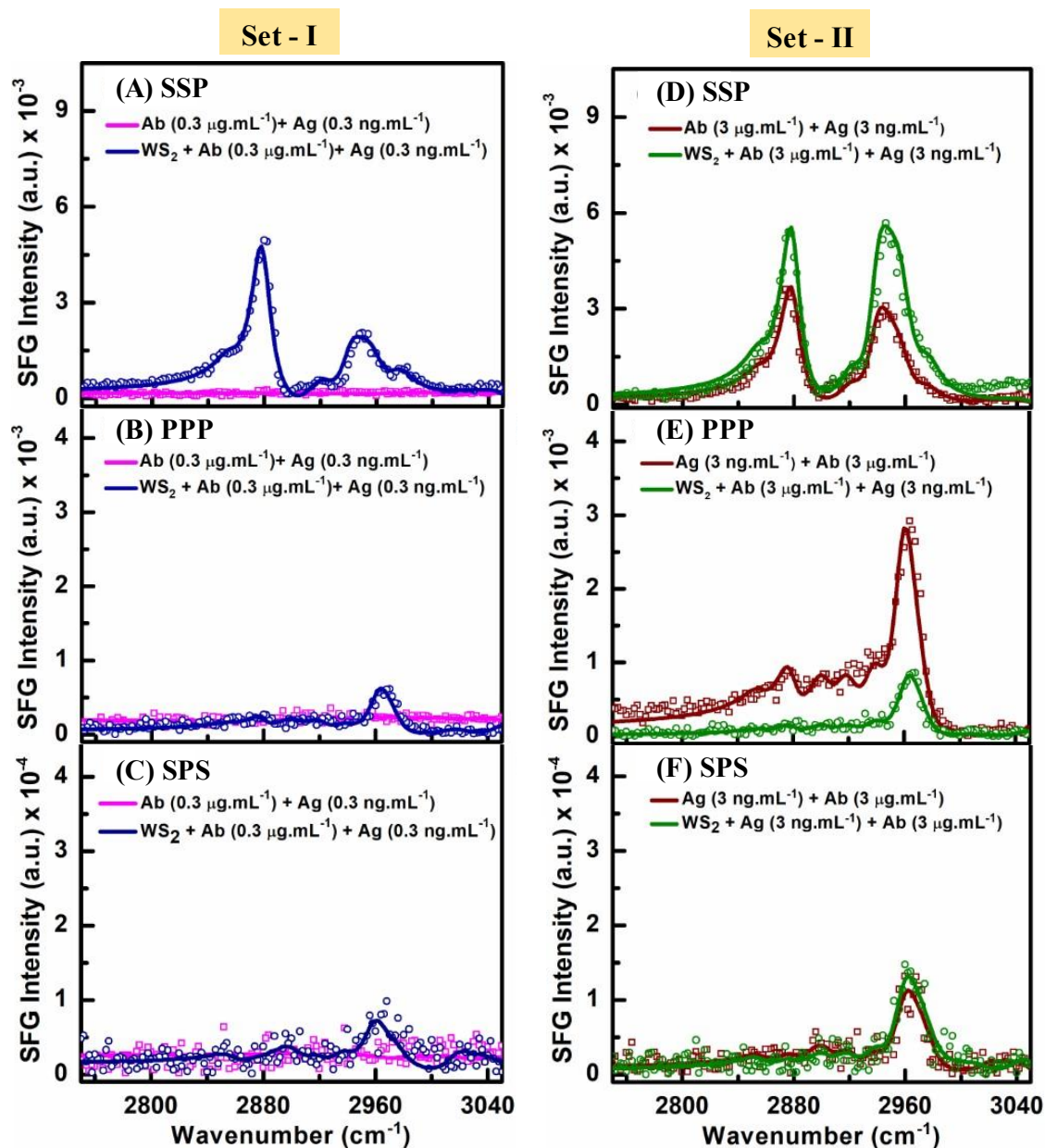


**Figure 5.6** Polarization-dependent VSFG spectra in CH-stretch region (2750-3050 cm<sup>-1</sup>) of lower (set-I) (panel A and B) and higher (set-II) (panel C and D) concentration combination of PPIs in absence and presence of WS<sub>2</sub> QDs.

Another aspect of WS<sub>2</sub>-PPIs is monitored in terms of protein molecular crowding effect on the PPI-mediation capacity of WS<sub>2</sub> QDs. This is clearly recognized through a

huge variation in the  $r^+_{FR}$  intensity as a function of protein concentration in SSP mode (panel A and D). The  $CH_3$  fermi resonance basically appears due to the splitting and overlapping of the  $r^+$  mode with the overtone of  $CH_3$  bending mode.<sup>228,232,272</sup> Hence, the fermi mode is quite sensitive towards nearby perturbations and molecular conformational changes.<sup>228,232,233,272</sup> Several reports have assigned the ratiometric value of  $r^+_{FR}/r^+$  modes to evaluate the degree of intermolecular interactions (i.e., electrostatic and vdW forces) due to an increased molecular concentration or surface pressure impact on molecular arrangement at the interface.<sup>228,272</sup> It is interpreted by these studies that an increased ratio value represents active enrolment of electrostatic forces among the interfacial molecular groups. With reference to this analysis, we observed the  $r^+_{FR}/r^+$  intensity ratio value of  $WS_2$ -PPIs for set-I and set-II protein concentration presented in SSP spectra (panel A and D) to be  $\sim 0.32$  and  $\sim 0.84$  respectively (obtained after spectral fitting data shown in Appendix D Table D1, histogram plot and values presented in Figure 5.7). Our interpretation suggests that increasing protein concentration under the influence of  $WS_2$  contributes largely towards the steric effects among the molecular groups. These steric interactions potentially influence the molecular orientation as well. This concept is convincingly supported by Saha et al.<sup>257</sup> where they demonstrated via immunoassay studies that an increased Ab density favors the out-of-plane Ab orientation due to PPI steric effects. In our results as well, we could identify a slight increment in  $r^-$  peak (representing  $r^-_{op}$  mode) in PPP and SPS spectra while comparing spectral features of  $WS_2$ -PPIs for two concentration sets (panel B-C and E-F). Hence, our results clearly illustrate that the  $WS_2$  QDs play an active role in rendering the molecular groups interface active for lower (set-I) protein molecules. On the other hand, for higher (set-II) protein concentration combination,  $WS_2$  may influence the net molecular arrangement of methyl groups via the steric effects and an increased electrostatic contribution at the interface.<sup>273,274</sup> This interpretation is further investigated by deducing the parameter of molecular orientation of terminal methyl groups, which will aid in evaluating the influence of  $WS_2$  over the molecular conformation during its interaction with Ab-Ag molecules as a function of protein concentration.

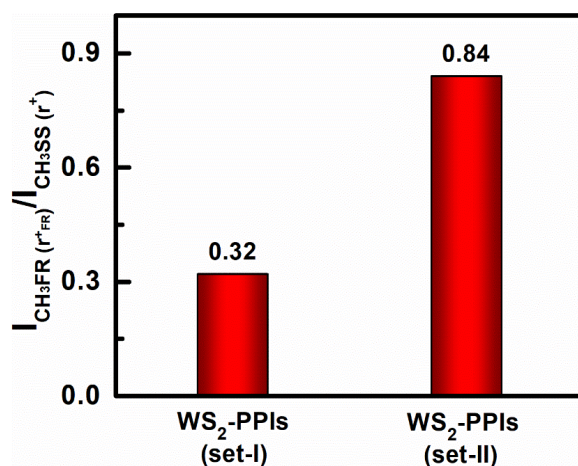


**Figure 5.7** A bar-graph representation of VSGF intensity ratio values of CH<sub>3</sub>FR ( $r^+_{FR}$ ) and CH<sub>3</sub>SS ( $r^+$ ) modes for lower (set-I) and higher (set-II) PPI concentration sets with WS<sub>2</sub> QDs.

**OH-stretch region:** Figure 5.8 shows the polarization-dependent OH-stretch region profile of PPIs at their lower (set-I) and higher (set-II) concentration combinations with and without WS<sub>2</sub> QDs. With WS<sub>2</sub> addition, the water molecules in the vicinity of set-I (panel A and B) and set-II (panel C and D) Ab-Ag concentration combinations acquire a net polar alignment at the interface by depicting an enhanced profile in coordinated OH-stretch region in coordinated region ( $3150-3500\text{ cm}^{-1}$ ) of SSP spectra. The PPP scheme showcase the impact of WS<sub>2</sub> in elevating the contribution from hydrophobic hydration feature at  $\sim 3550\text{ cm}^{-1}$ , which stems from WS<sub>2</sub> addition. The SFG profile seen in both SSP and PPP polarization schemes for set-I Ab-Ag on introducing WS<sub>2</sub>, however, become more pronounced when the Ab-Ag concentration is increased i.e., set-II Ab-Ag (panel C and D). This clearly depicts the concentration-dependent surface coverage of proteins and an increased field-strength at the interface, which impacts the polar alignment of interfacial water structure. In this scenario, the PPP spectra has been important in illustrating the role of WS<sub>2</sub> in upgrading the hydration state of Ab-Ag protein molecules. This is distinctively noticed for set-I Ab-Ag on introducing WS<sub>2</sub> (panel B), whereas in case of set-II Ab-Ag (panel D), the  $3550\text{ cm}^{-1}$  feature of Ab-Ag simply gets elevated under the influence of WS<sub>2</sub>. Simultaneously, the free-OH signal gets minimized for WS<sub>2</sub>-Ab-Ag (set-I), which is in an opposite trend to that of pristine Ab-Ag (set-I). For set-II proteins, the free-OH profile is found to be obscured with lower frequency regions (i.e.,  $3450\text{ cm}^{-1}$  and  $3550\text{ cm}^{-1}$ ) in SSP mode with WS<sub>2</sub> addition, suggesting the existence of heterogenous states of weakly H-bonded water molecules.



Consolidating the information attained from CH-OH-stretch region for PPIs in presence and absence of WS<sub>2</sub> (Figure 5.6 and 5.8), it is implied that WS<sub>2</sub> QDs have potentially increased the surface propensity of alkyl groups accompanied by a large number of intermolecular interactions. It simultaneously contributes towards enhancing the interfacial alignment of water dipoles in the vicinity of PPIs, as observed at the air-aqueous interface. Hence, the nano-bio combination displays an indispensable role of WS<sub>2</sub> QDs in mediating and making PPIs noticeable at the interface.

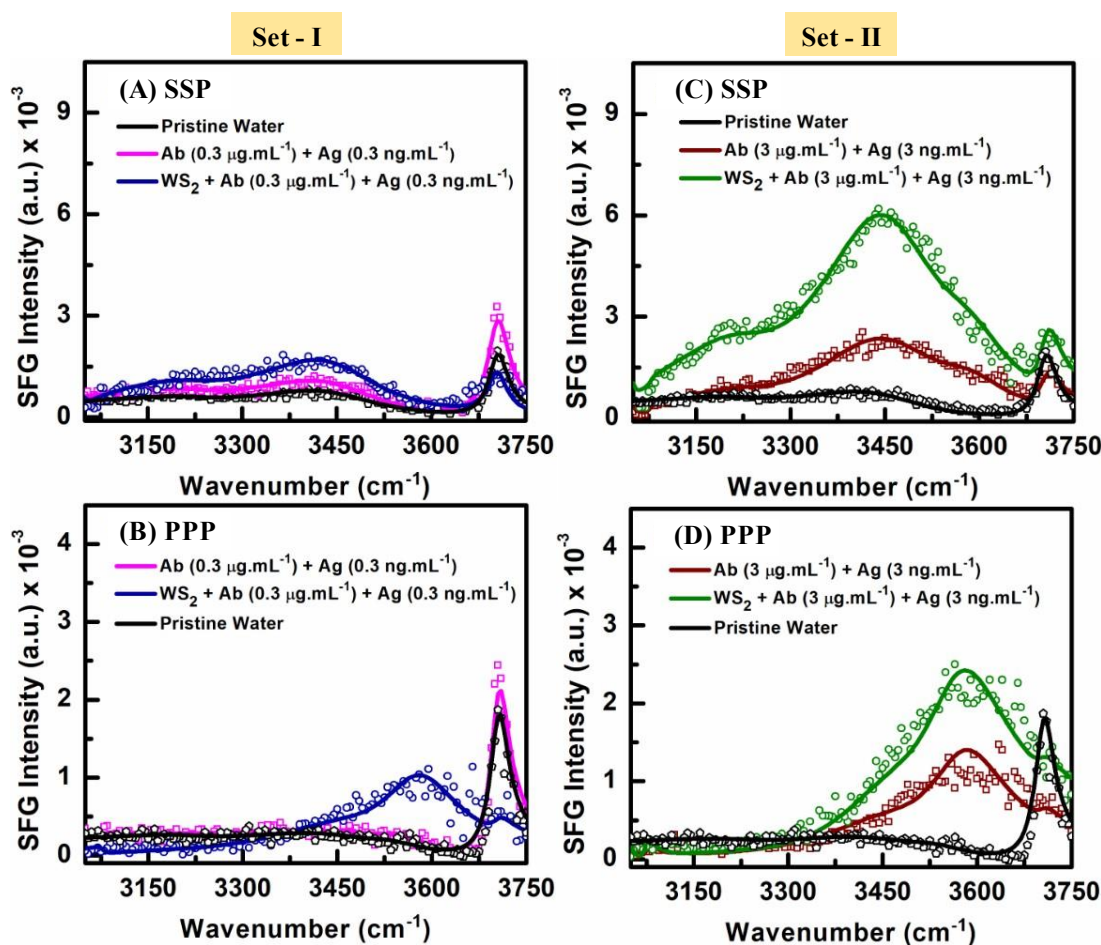


**Figure 5.8** Polarization-dependent VSGF spectra in OH-stretch region (3050-3750 cm<sup>-1</sup>) of lower (set-I) (panel A and B) and higher (set-II) (panel C and D) concentration combination of PPIs in absence and presence of WS<sub>2</sub> QDs.

### 5.3.3 Evaluating Methyl Tilt angle during bio-recognition in WS<sub>2</sub> QDs presence

To understand explicitly the role of WS<sub>2</sub> QDs in mediating PPIs, the parameter of molecular orientation of terminal methyl groups have been deduced, which could explicitly provide the measured values of changes appearing during PPIs as an implication of WS<sub>2</sub> QDs. The ratios of  $\chi_{SSP,SS}^{(2)}$  and  $\chi_{PPP,AS}^{(2)}$  were used for analysis. From

the intersection points in Figure 5.9 (panel A), it is noted that the PPIs acquire an average tilt angle ( $\theta$ ) value ranging from  $\sim 32^\circ$ - $41^\circ$  for an angular distribution ( $\sigma$ ) of  $0^\circ$ - $50^\circ$  and with  $\delta$ -distribution  $\theta$  value is observed at  $\sim 40^\circ$ . The introduction of  $\text{WS}_2$  QDs to set-II concentration PPIs greatly influence the average methyl tilt by shifting the angle value towards the lower range i.e.,  $\sim 11^\circ$ - $28^\circ$  with a  $\sigma$  of  $0^\circ$ - $20^\circ$ . With the  $\delta$ -distribution, their average tilt angle is observed to be  $\sim 28^\circ$ . Hence, the net shift in the tilt angle value was calculated to be  $\sim 12^\circ$  (based on  $\delta$ -distribution). This explicates the impact of  $\text{WS}_2$  QDs on the methyl groups to adopt smaller tilt angle values, making them aligned closer to the surface normal. Furthermore, the influence of protein concentration variation on the methyl group orientation is analyzed under the constant concentration of  $\text{WS}_2$ . The obtained experimental ratio intersects the theoretical values at the tilt angle transiting from  $\sim 12^\circ$ - $29^\circ$  for  $\sigma$  range ( $0^\circ$ - $20^\circ$ ) with an average angle value of  $29^\circ$  at  $\sigma = 0^\circ$  for set-I PPI concentration. For better clarity, the trend of corresponding  $\theta$  values at  $\sigma = 0^\circ$  have been plotted in panel B. While comparing the average  $\theta$  values of both the protein concentration sets with added  $\text{WS}_2$ , the nearly similar angular variation implies that the factor of protein concentration is not contributing dominantly towards molecular orientation changes. These experimental findings imply that the factor of protein concentration is unable to modify the molecular orientation of methyl groups and only participates in building the steric effects at the interface, as discussed in previous section. This aspect has also been investigated computationally in some studies where the concentration-dependent existence of steric and electrostatic effects was found to have minimal impact on the molecular orientation dynamics.<sup>274,275</sup> It is thus surmised that the observed SFG intensity variation in  $r^+$ ,  $r^+_{\text{FR}}$  and  $r^-$  (Figure 5.6) as a function of PPI concentration in  $\text{WS}_2$  presence is governed by the rise in number density of molecules and the resultant steric interactions occurring at the interface. Nevertheless, it can be emphasized that the  $\text{WS}_2$  QDs presence greatly influences the molecular features of PPIs at the air-aqueous interface.



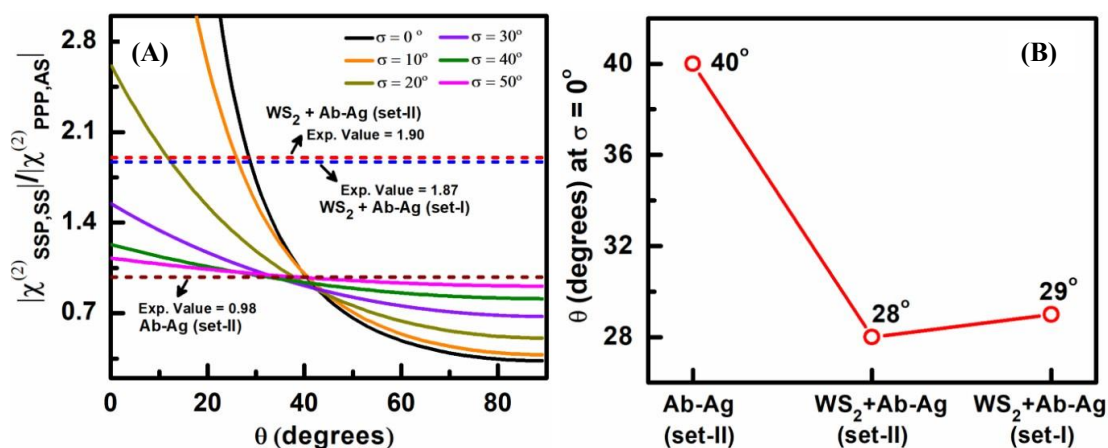


**Figure 5.9** (A) Theoretical plot of  $|\chi_{SSP,SS}^{(2)}|/|\chi_{PPP,AS}^{(2)}|$  ratios corresponding to the tilt angle ( $\theta$ ) values with the theoretical curves of the angular distribution width ( $\sigma$ ). (B) The trend of  $\theta$  variation at  $\sigma = 0^\circ$  (for  $\delta$ -distribution function) of the terminal methyl groups, as determined from the intersection points of the sample peak ratios obtained with the theoretical curve.

## 5.4 Conclusion

Considering the accelerated research on the application of nano-scaled particles in various domains, the study was performed to actually understand the role of tungsten disulfide quantum dots (WS<sub>2</sub> QDs) in facilitating the interaction between antigen-antibody at the air-aqueous interface by employing SFG-VS. Studying antigen-antibody association is essential from a research point of view as these aid in developing new assays for the ultimate improvement of several diagnostic and sensing procedures for undertaking sensitive and selective detection of biomolecules. The polarization-dependent SFG studies have been carried out for Ag, Ab and WS<sub>2</sub> QDs in particular combination schemes so as to deduce an overall molecular picture of the binding process. The SFG results explicitly showed an enhanced alkyl contribution at the interface for PPIs under the influence of WS<sub>2</sub>. This observation is well supported by the quantitative orientational analysis performed in this study to find the average tilt angle of the terminal methyl groups which displayed  $\sim 12^\circ$  reduction in the angle value when WS<sub>2</sub> is being introduced to the protein-protein complexes. Similarly, the OH stretch region showcased how water molecular arrangement gets perturbed with WS<sub>2</sub> addition to PPIs by greatly affecting their polar ordering at the interface (conclusively illustrated in Figure 5.10). Hence, the nano-bio complexes leave an imprint of their association by displaying a huge enhancement in the H-bonded profile relative to the PPIs. The impact of WS<sub>2</sub> as a function of PPI concentration combination clearly infers that increasing protein concentration majorly

contributes towards the steric interactions among the moieties without causing any significant alteration in the molecular orientation. These results summarize that the molecular interactions and conformation at the microscopic scale harmonize well with the average effect of the molecular binding at the macroscopic level. The work also substantiated the role of nano-dimensioned materials in enhancing the binding efficiencies by not only mediating the interactions but also building an oriented and ordered molecular conformation as an indicator of molecular-scale influence at the air-aqueous interface. Hence, employing the nano-dimensioned materials in designing the biosensing assay potentially proves to be one of the progressive domains of research.

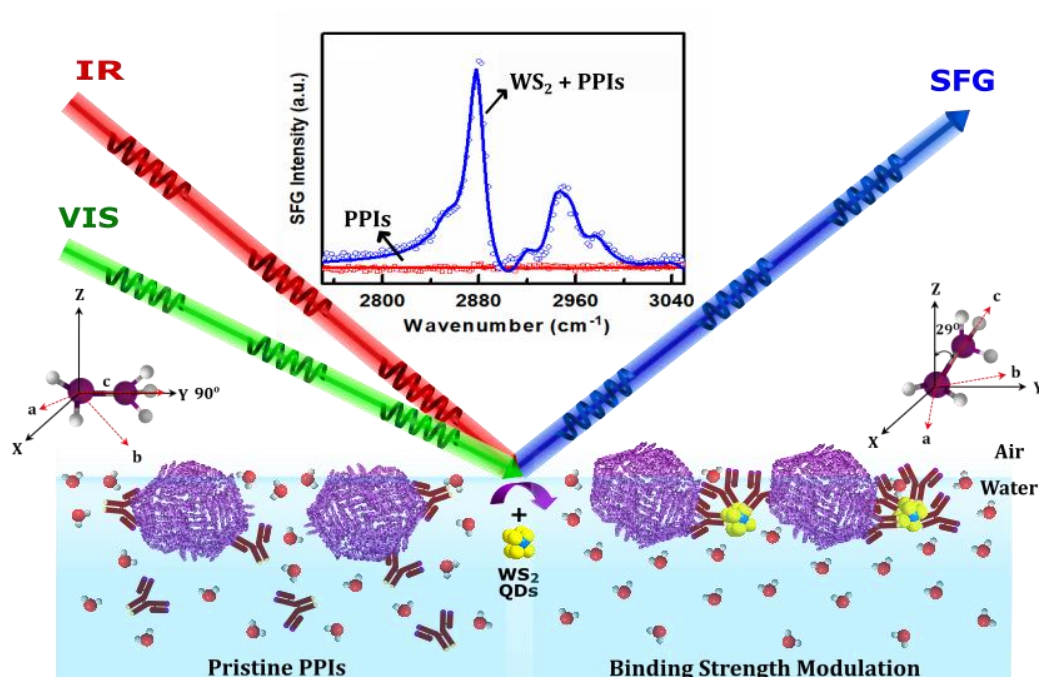


**Figure 5.10** Schematic illustration of PPIs in absence and presence of WS<sub>2</sub> QDs, showcasing the modulation in antibody and antigen binding strength, increased polar alignment of interfacial water molecules, and the observed molecular orientational changes of methyl residues, observed using SFG spectroscopy. This model represents the protein molecules at lower concentration combination, which tend to show surface propensity in presence of WS<sub>2</sub> QDs.

# Elucidating the molecular structure of hydrophobically modified polyethylenimine nanoparticles and its potential implication for DNA binding

This chapter involves the presentation of the research work performed over the surface characterization of the in-house synthesized polymeric organic nanoparticles and their behavior in presence of a biomacromolecule. Contrary to previously performed work, here we intend to understand how the structural modification of a commonly used biocompatible polymer influences its surface adsorbing behavior and could contribute during its interaction with a biomacromolecule. Considering the vast involvement of polyethylenimine (PEI) polymer as a broad-spectrum material in distinct fields such as in healthcare, sensing, optical devices, or material building, PEI is often actively directed to tune its physico-chemical properties by selective structural modifications. Additionally, its effective binding with DNA and its inclusion in DNA-based theragnostic and DNA delivery applications have raised its importance in the medical field. Constructing a nanoparticle version of PEI polymer is known to enhance its physico-chemical properties, while observing its impact after association with DNA could aid in understanding its potency for sensor designing or in microfabrication technologies. Here in our work, we have investigated a branched PEI polymer for the impact of the hydrophobic modification over its structural properties after forming its organic nanoparticles (ONPs). The studies have been evaluated in both bulk-phase via surface tensiometry, zeta-potential measurements and ATR-FTIR, and at the air-aqueous interface using VSFG spectroscopy. Part of this work has been published as: “Kaur et al. Langmuir, 38, 13456-13468, 2022”.<sup>276</sup>

## 6.1 Introduction

Constructing tunable surfaces/interfaces are in significant demand considering their applicability in domains such as designing biological scaffolds, theragnostic, anti-bacterial/anti-viral coatings, catalysis, organic electronics and dielectrics designing,

energy storage, etc.<sup>277-279</sup> Polymers offer attractive properties due to their important morphological features including molecular branching, and attached functional groups which provide efficient coating thickness, adhesiveness, flexibility, and chemical tunability for applicability.<sup>211,277,280</sup> As a result, polymers project minimal biofouling of the system, minimal interference from the surrounding molecules in the media, and biocompatibility along with good surface immobilization of the ligand.<sup>277</sup> Polyethylenimine (PEI) is one of the widely studied cationic polymeric material since it is largely enrolled in tissue engineering, environmental purposes, gene and drug delivery, and sensor surface fabrications especially in organic electronics to minimize the electrode work function for enhancing the detection efficiency.<sup>277-279</sup> Branched PEI (b-PEI) is a hydrophilic polymer bearing a larger proportion of secondary and tertiary amine groups that renders it a better conjugation property while sustaining higher positive charge density within the aqueous media.<sup>277</sup> The cationic nature of b-PEIs is preferentially utilized for binding oppositely charged moieties and has been widely used in DNA condensing applications.<sup>277,281-283</sup> Taking advantage of the charged side groups, b-PEI polymer is often modified structurally or chemically to enhance its response based on its applicability.<sup>277,279,284-287</sup> Among the wide range of modifications in use, hydrophobically substituted polymeric materials are in extensive demand as it aids in structurally assembling the polymer by balancing the charged state of polymers (like b-PEI) under physiological pH.<sup>279,284,285</sup> Conjugating hydrophobic group to the functional polymers enables superior analyte interaction and extraction mechanism.<sup>82,286,288</sup> It also improves the immobilizing or adsorbing features of the polymer with a secondary surface via hydrophobic interactions, impacting the working capacity of the underlying material for utility in micro-fabrication technologies.<sup>278,288</sup> Architectural changes of polymer brings about changes in the interfacial characteristics and behavior of the polymer. The study of an interfacial perturbation is indispensable for the utility of polymers for various surface science applications. Hydrophobically modified polymers in aqueous media are being widely used in pharmaceuticals, food and paper processing industries, medical sealants, etc.<sup>82,279,284-286</sup>

In recent times, the domain of nanoscience and nano-engineering has delivered a novelistic approach for material designing involved in various branches.<sup>284,285,287</sup> Preparing a nano-scale version of the b-PEI polymer could confer unique physico-chemical and biological properties which are distinct from the monomeric as well as the

macroscopic material with the similar chemical architecture.<sup>284,287,289</sup> Studies have been performed regarding hydrophobically modified PEIs involving primarily the bulk-sensitive approaches.<sup>277,279,284-286,290-292</sup> Tian et al.<sup>293</sup> studied the surface adsorption dynamics of PEG protected NPs to quantitatively understand the interfacial restructuring and adsorption rate of the self-assembled NPs in complex environment mainly using surface tensiometry. Synthesis of multicolored PEI polymeric particles have been pursued by certain research groups for DNA detection and cellular imaging applications.<sup>287,289,290</sup> These polymeric nanostructures primarily enroll organization and rearrangement of its functional moieties which classifies their surface and interfacial phenomena over the solid or in an aqueous medium. This governs certain fundamental properties like chemical reactivity, adhesion, wettability, and biocompatibility. Noting the significance of the confined nature of surface and interface, and its value in explicating the molecular behavior in the aqueous system, the sum frequency generation vibration spectroscopy (SFG-VS) poses to be a novel spectroscopic tool which selectively analyzes the interfacial molecular features bearing a non-centrosymmetric environment. In contrast to the conventional spectroscopic techniques, SFG-VS specifically characterizing the vibrational signatures of the functional groups present at the air-water interface.<sup>32,211</sup> Remarkable work has been done in the field of interfacial polymer science using SFG-VS covering different aspects related to the concentration or pH-dependent surface characterization of polymer functional groups present at discrete interfaces, in polymer-surfactant interactions, polymer blend studies, etc.<sup>211,280,294,295</sup>

The prime aim of this work is to explore (a) the tailoring of PEI polymer properties via hydrophobic modification, (b) understand the surface affinity and adsorption characteristics of the hydrophobically-modified PEI nanoparticles, and (c) to explore the nature of associations among the modified-PEI nanoparticles with dsDNA. In this work, 1,8-naphthalic anhydride (an organic acid) has been used for the aromatic conjugation of b-PEI via reflux technique. Naphthalimide offers strong electron-withdrawing ability and hydrophobicity upon functionalizing with b-PEI.<sup>285,290</sup> It's been largely used for developing chemosensors,<sup>296</sup> and logic operators.<sup>297</sup> Naphthalimide is also known to readily intercalate and incorporate within the DNA double helix via  $\pi$ - $\pi$  stacking interactions among the nucleic bases.<sup>285,290,298</sup> Hence, employing an aromatic structure for conjugation provides a substantial intercalating property, increased colloidal stability, and reduced steric hindrance probability which comparatively becomes higher in case of long

alkyl chain conjugation.<sup>286</sup> The work of Sarkar et al.<sup>285</sup> and Liang et al.<sup>290</sup> involved naphthalimide associated PEI nanoparticle or nanocarrier synthesis respectively but their synthesis procedure is quite cumbersome, involving additional modifications and sequential steps of reaction. This work involved development of the nano-self-assembly of naphthalimide modified polyethylenimine (NPEI) polymer was stimulated using ultrasonication to form NPEI-organic nanoparticles (NPEI-ONPs) in a simple one-step reaction procedure. The NPEI-ONPs were characterized for the surface adsorption behavior using SFG-VS and surface tension measurements by raising its bulk concentration. To elucidate the relevance of NPEI-ONPs towards the bio-medical and bio-sensor fabrications, binding associations among NPEI-ONPs and double-stranded DNA (dsDNA) were evaluated by both bulk-phase techniques (viscometry, thermal denaturation measurements, zeta ( $\zeta$ ) potential, ATR-FTIR spectroscopy) and interface-sensitive SFG-VS in this work. We emphasize here that, although the respective binding modes of b-PEI and NA with dsDNA are known from the literature,<sup>281,283,290,292,298</sup> however, a systematic investigation of aromatic-ring modified polymeric nanoparticles (NPEI-ONPs) and dsDNA interactions with a combination of bulk- and interface-specific spectroscopies is essentially absent. Our results qualitatively discuss about the conformational changes in dsDNA structure and the variation in physico-chemical properties of NPEI-ONPs at the molecular-scale, during NPEI-ONP and dsDNA interaction.

## **6.2 Experimental methods and procedure**

### **6.2.1 Material requirements**

1,8-naphthalic anhydride ( $\geq 98.0\%$ ), low molecular weight b-PEI (25 kDa), D<sub>2</sub>O (99.9%), low molecular weight Salmon sperm double-stranded DNA (stored at 4°C), and Tris-HCl salt (pre-defined crystals) purchased from Sigma-Aldrich Co., were used in their native state. All solvents and reagents were procured from Sigma-Aldrich Co. and MERCK.

### **6.2.2 Synthesis and preparation scheme of polymeric nanoparticles**

Low molecular weight branched PEI (25 kDa, 700 mg or 1.4 mM) polymer and 1,8-naphthalic anhydride (1 g) were solubilized in 20 mL of dry methanol in the round

bottom flask in presence of triethylamine ( $\text{Et}_3\text{N}$ ) as a catalyst. The solution mixture was then refluxed at  $120^\circ\text{C}$  for 24 hours duration over the magnetic stirrer (reaction scheme presented in Figure 6.1 (A)). A yellowish-brown colored end-product, thus formed, was washed rigorously with dry methanol so as to remove any unreacted part. The resultant solid product was cooled and dried under high-pressure conditions using a rotatory evaporator technique. The yellowish-brown colored product formed was subjected to  $^1\text{H}$  and  $^{13}\text{C}$  NMR characterization. The solubility of the compound was initially checked in varied solvents such as pristine water, methanol, acetonitrile, DMSO, tetrahydrofuran, and acetic acid. The compound readily solubilized in acetic acid. Therefore, NPEI-ONPs stock solution was prepared (as presented in Figure 6.1 (B)) by dropwise injecting the synthesized polymer (5 mg per 100 mL, prepared in-stock solution), priorly solubilized in acetic acid ( $\geq 99\%$ , 1.5% w/v), using micro-syringe under constant sonication for 10 minutes at  $25^\circ\text{C}$ . The stock solution was prepared in 20 mM Tris-HCl buffer and the pH of the final solution was set to 7.4 using 0.1 M HCl and the readings were monitored with a calibrated pH meter (Mettler Toledo S210-Basic). Accordingly, after ONP preparation, the net amount of acetic acid in a Tris-HCl buffer solution (pH 7.4) stays 0.02% v/v.

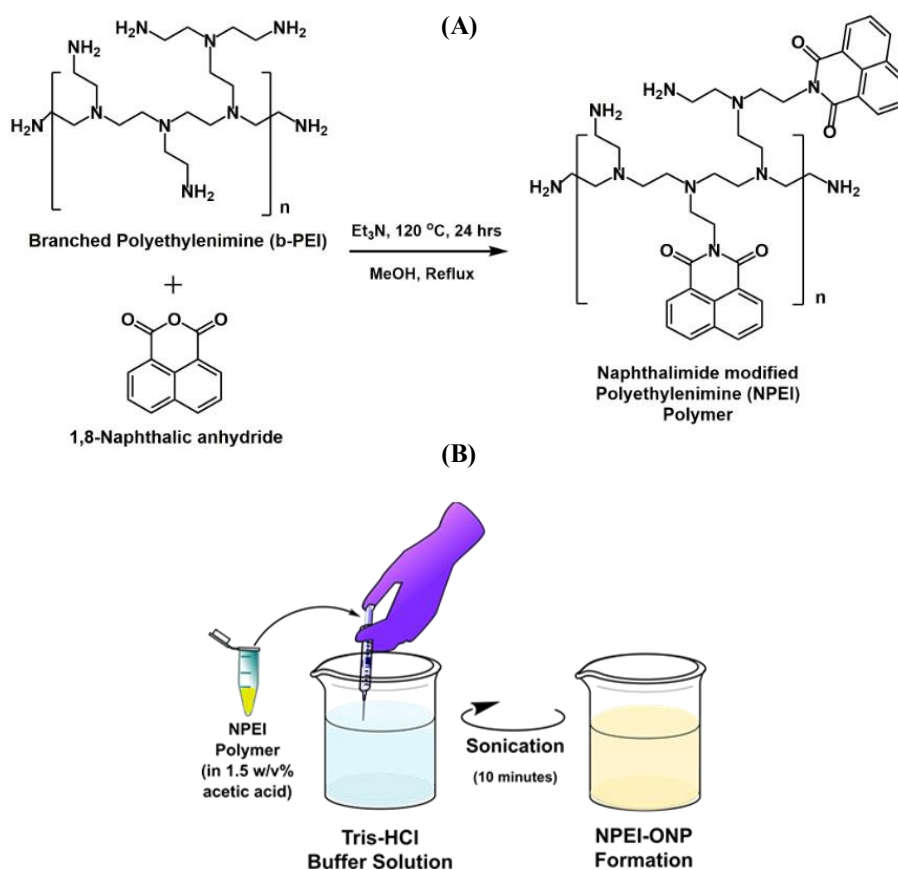


**Figure 6.1** (A) Reaction scheme of the synthesis of naphthalimide modified polyethylenimine (NPEI) polymer. (B) Pictorial illustration of the preparation of NPEI organic nanoparticles (NPEI-ONPs) in buffered solution. Reprinted with permission from Kaur et al., *Langmuir* **38**, 13456–13468 (2022). Copyright (2022) American Chemical Society.<sup>276</sup>

### 6.2.3 Surface tensiometry

The surface tensiometry is conducted by the Wilhelmy-plate technique using Biolin Scientific KSV NIMA LB apparatus. The platinum (Pt) plate used here is subjected to rigorous washing with ethanol, de-ionized water and then air-dried before usage. The surface tension value of pristine water is taken as a reference point for all the corresponding sample measurements done at room temperature  $\sim 22 \pm 1^\circ\text{C}$ . The samples were stabilized in a 45 mm diameter Teflon sample cell (with 7 mL capacity) before experimentation. The acquired surface tension values were averaged for five consecutive readings and plotted as a change in the sample surface tension with respect to pristine water.



#### **6.2.4 UV-Visible spectrophotometer**

DNA melting temperature ( $T_m$ ) profile was studied using Shimadzu Spectrophotometer equipped with a Peltier thermoregulator.  $T_m$  was analyzed through the absorbance profile of salmon sperm dsDNA at 260 nm with varying temperature under the absence and presence of ONPs at the ramp rate of  $1^\circ\text{C}\cdot\text{min}^{-1}$  in 20 mM Tris-HCl buffer (pH 7.4). The midpoint of the melting curve was assigned as the  $T_m$  value.

#### **6.2.5 Viscometry measurements**

A conventional Ostwald's viscometer was used to conduct viscometry measurements. The viscometer was held vertically in a thermostat at  $25^\circ\text{C}$ . The sample flow-time was measured with a digital stopwatch and tested three consecutive times for calculating the average time. The obtained values were plotted as  $(\eta/\eta_0)^{1/3}$  v/s [Compound]/[DNA] ratio. Here,  $\eta$  and  $\eta_0$  denotes the specific viscosity of salmon sperm dsDNA in the presence and absence of the NPEI-ONPs and their values were calculated using formula  $(t - t_b)/t_b$ , where 't' is the observed flow-time in the presence of the compound and  $t_b$  is the flow-time of the buffer alone.<sup>298</sup>

#### **6.2.6 Atomic force microscopy**

The AFM microscopic images were acquired for the NPEI-ONPs coated glass substrates in order to analyze the 2D morphology of the prepared nanoparticles. The instrumental and experimental details are mentioned in chapter 2 (section 2.6.3).

#### **6.2.7 Zeta-sizer and potentiometry measurements**

The size and potential measurements of synthesized NPEI-ONPs and their interaction with dsDNA were studied using Zetasizer Nano-ZS90 instrument (Malvern Panalytical Ltd.) at an applied voltage of 149 V. The instrumental details are provided in chapter 2 (section 2.5). For measurements of average potential values, NPEI-ONPs and dsDNA samples were prepared according to the concentration ratios of (0, 0.01, 0.05, 0.1, 0.15, 0.2, 0.25, 0.5, and 1) from the stock dsDNA titrating concentration of  $0.03 \text{ mg}\cdot\text{mL}^{-1}$ . The mean nanoparticle diameter was also recorded for these NPEI-dsDNA concentration ratios. Measurements were performed at working temperature of  $22^\circ\text{C}$  in triplicates and

averaged over 10 recorded values. The zeta potential measurements were formulated from the measured electrophoretic mobility of the particles in an aqueous media using Helmholtz-Smoluchowski approximation model (refer chapter 2, section 2.5).

### **6.2.8 ATR-FTIR vibrational spectroscopy**

The ATR-FTIR absorption spectrometer (Bruker Optics Tensor II) bearing a room temperature based deuterated L-alanine-doped triglycine sulfate (RT-DLaTGS) detector is employed in this work. The measurements were made at room temperature of  $\sim 22^{\circ}\text{C}$  utilizing ATRMax II variable angle horizontal ATR accessory from Pike technologies assembled with a trapezoidal ZnSe ATR crystal. Further details about the instrument are mentioned in chapter 2 (section 2.3.1). The spectral acquisition was done in range  $900$  to  $1800\text{ cm}^{-1}$  with the resolution of  $2\text{ cm}^{-1}$  and the data are averaged for 256 scans for  $0.5\text{ mL}$  sample volume. The data analysis and spectral treatment were carried out in the OPUS Version 7.5 Build software. A detailed protocol for spectral treatment and correction is provided in chapter 2 (section 2.3.1).

### **6.2.9 Sum frequency generation vibrational spectroscopy**

Vibrational Sum Frequency Generation (VSFG) was used to probe and characterize the interfacial properties of synthesized NPEI-ONPs at the interface with signal optimization done at  $3700\text{ cm}^{-1}$ . The instrumental details and specifications have been provided in chapter 2 (section 2.2.2). All the sample solutions were prepared in millipore ultra-pure de-ionized water type-1 with the resistivity of  $18.2\text{ M}\Omega\cdot\text{cm}$  and pH  $5.70 \pm 0.02$  at  $25^{\circ}\text{C}$ . The samples ( $7\text{ mL}$  in volume) taken in a Teflon cell for SFG-VS evaluation. Before experimentation, all storage vials and sample cell were subjected to piranha treatment ( $\text{H}_2\text{SO}_4:\text{H}_2\text{O}_2$  in 3:1 ratio) at  $70^{\circ}\text{C}$  for 1 hour and then intensely washed with type-1 deionized water and dried before use. Titration studies with salmon sperm dsDNA were performed with a standard stock solution of NPEI-ONPs ( $0.05\text{ mg}\cdot\text{mL}^{-1}$ ). Varying concentration of dsDNA is added from its stock solution ( $0.03\text{ mg}\cdot\text{mL}^{-1}$  in  $20\text{ mM}$  Tris-HCl buffer (pH 7.4) to fixed NPEI-ONP concentration ( $0.03\text{ mg}\cdot\text{mL}^{-1}$ ) solution. The prepared solution with different concentrations of dsDNA were gently mixed each time to ensure homogenous mixing and were kept for 10 minutes stabilization before spectral recording. The sample preparation protocols were done at room temperature ( $\sim 22^{\circ}\text{C}$ ). The SFG spectra were evaluated and fitted using the Lorentzian expression

(details can be seen in chapter 2, section 2.2, equation 2.16) and the fitted parameters and values for the results acquired in this chapter are presented in Appendix E (table E1-E4). The spectra were taken with SSP, and PPP polarization combinations. The data points for the spectrum were gathered with an average acquisition of 200 pulses per step with  $2\text{ cm}^{-1}$  step size. The spectra are acquired from range  $2800\text{--}3800\text{ cm}^{-1}$  of IR wavenumber.

### 6.3 Results and discussion

The synthesis of naphthalimide modified polyethylenimine (NPEI) polymer was conducted via reflux technique (which involves a continuous process of evaporation and condensation of the solvent within the round bottom flask under constant temperature). The resultant yellow-brown colored product was characterized with  $^1\text{H}$  NMR and  $^{13}\text{C}$  NMR spectrum (Figure 6.2 (A) and (B) respectively) which were recorded in  $\text{CDCl}_3$  (chemical shifts recorded in ppm with reference to tetramethylsilane as an internal standard) using JEOL JNM-ECS spectrometer operating at 400 MHz and 100 MHz for  $^1\text{H}$  NMR and  $^{13}\text{C}$  NMR respectively (for instrument details and analysis refer chapter 2, section 2.6.1). The NMR spectroscopic processing with the peaks designated for  $^1\text{H}$  NMR (Figure 6.2 (A)) (400 MHz,  $\text{CDCl}_3$ )  $\delta$  (ppm) include: broad feature 'f' denotes protons from naphthalimide rings,<sup>299</sup> peak 'e' denotes 7.24 (s, 1H,  $\text{CHCl}_3$ ),<sup>300</sup> peak 'd' attributes to methylene protons of (- $\text{CH}_2\text{-N-CO-}$ ) (4.1 ppm (s, 1H)),<sup>300</sup> peak 'c' and 'b' denoting 3.5 ppm (s, 1H) and 3.25 ppm (s, 1H) respectively depicts protons from methylene groups of (- $\text{CO-N-CH}_2\text{-CH}_2\text{-N-}$ ) from side chain of the complex,<sup>300,301</sup> peak 'a' represents the original contribution from protons of the  $\text{CH}_2$  groups of the PEI structure in region 2.4-2.9 ppm (s, 1H) of (- $\text{CH}_2\text{-CH}_2\text{-NH-}$ ).<sup>300,301</sup> The  $^{13}\text{C}$  NMR spectra (Figure 6.2 (B)) (100 MHz,  $\text{CDCl}_3$ )  $\delta$  (ppm) shows peaks at: 38.00, 39.79, 47.50, 48.82, 51.62, 52.96, 54.31 ppm, (collectively labelled as 'L') all denoting the feature from carbons of - $\text{CH}_2$  groups mainly from the nearby formed amide structures.<sup>300</sup> Peaks at 121.96 (peak 'N'), 126.77 (peak 'K'), 130.96 (peak 'P'), 133.75 (peak 'S') denote carbons from naphthalimide aromatic rings,<sup>302</sup> while the peak 'R' at 163.65 ppm arises due to carbon atoms of the carbonyl group.<sup>300,302</sup> Here, 77 ppm peak 'G' is assigned to carbon from  $\text{CDCl}_3$ .<sup>300</sup> These peak assignments are presented in the tabulated form (Table 6.1):

**Table 6.2**  $^1\text{H}$  and  $^{13}\text{C}$  NMR peak designations of NPEI polymer. Reprinted with permission from Kaur et al., *Langmuir* **38**, 13456–13468 (2022). Copyright (2022) American Chemical Society.<sup>276</sup>

Chemical Moiety	Probing Atomic Group	Peak Feature	Alphabetical Designations	Chemical Shift (ppm)
<b><math>^1\text{H}</math> NMR peak assignments</b>				
b-PEI chain	(-CH <sub>2</sub> -CH <sub>2</sub> -NH-)	Broad Singlet	a	2.4 – 2.9
	(-CH <sub>2</sub> -N-)	Singlet	b	3.25
NPEI side groups	(-CO-N-CH <sub>2</sub> -CH <sub>2</sub> -N-)	Singlet	c	3.5
	(-CO-N-CH <sub>2</sub> -)	Broad Singlet	d	4.1
Solvent	CHCl <sub>3</sub>	Singlet	e	7.24
Naphthalimide ring structure	-C <sub>6</sub> H <sub>5</sub>	Broad Singlet	f	7.5 – 8.25
<b><math>^{13}\text{C}</math> NMR peak assignments</b>				
NPEI side groups	(-CH <sub>2</sub> -N-CO-)	Broad Multiplet	L	38 – 54.31
Solvent	-CDCl <sub>3</sub>	Singlet	G	77
Naphthalimide ring structure	-C <sub>6</sub> H <sub>5</sub>	Singlet	N	121.96
	-C <sub>6</sub> H <sub>5</sub>	Singlet	K	126.77
	-C <sub>6</sub> H <sub>5</sub>	Singlet	P	130.96
	-C <sub>6</sub> H <sub>5</sub>	Singlet	S	133.75
Naphthalimide	-C=O	Singlet	R	163.65

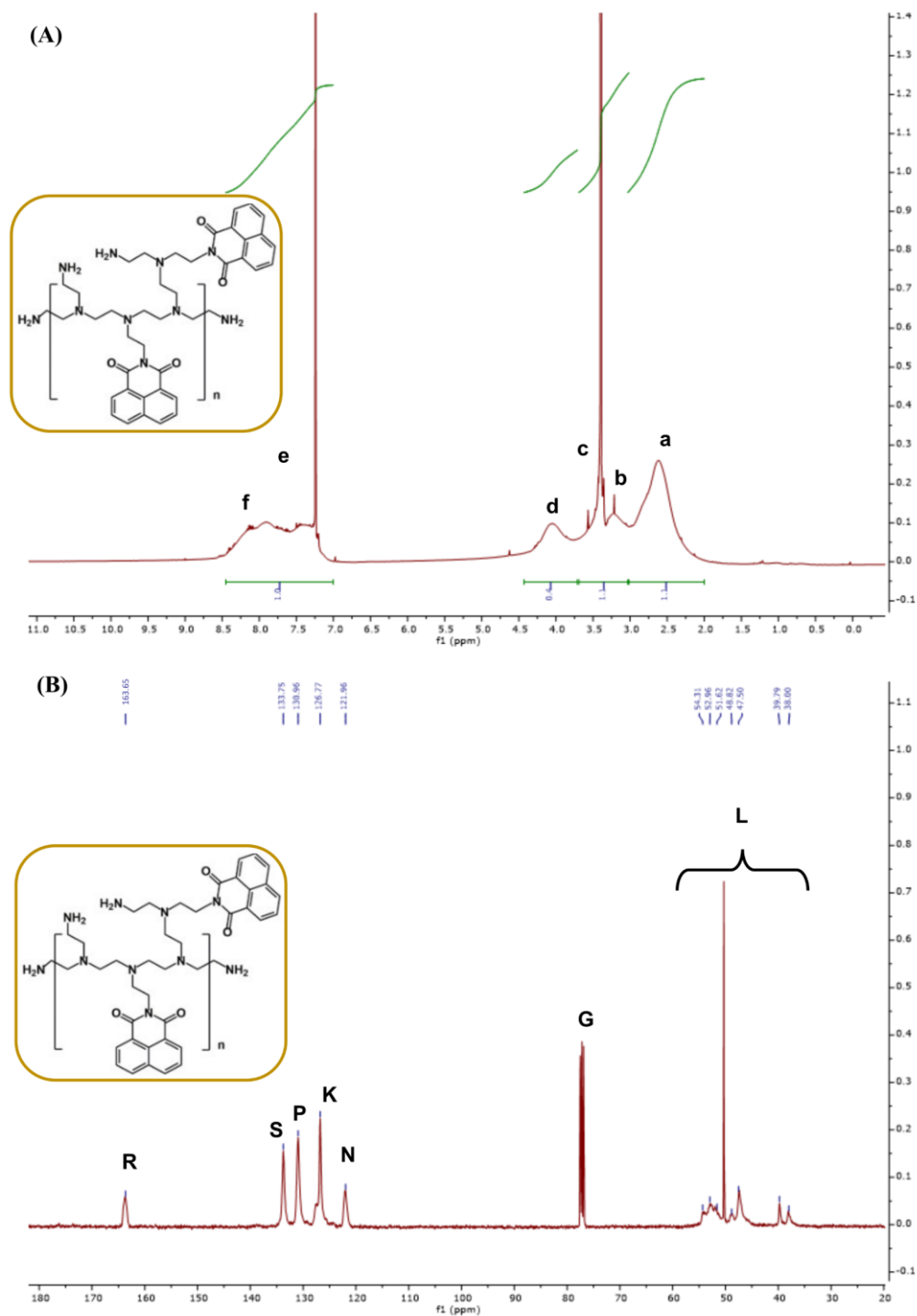


**Figure 6.2** (A)  $^1\text{H}$  NMR and (B)  $^{13}\text{C}$  NMR spectra in  $\text{CDCl}_3$  of the synthesized NPEI polymer. The chemical structure of NPEI polymer is provided along for clarity. Reprinted with permission from Kaur et al., *Langmuir* **38**, 13456–13468 (2022). Copyright (2022) American Chemical Society.<sup>276</sup>

The average particle size of the prepared NPEI-ONP solution was analyzed via dynamic light scattering (DLS) technique using Zetasizer Nano ZS90 instrument to be an average ~200 nm in range (shown in Figure 6.3 (A)), which relatively stayed consistent with different concentrations of NPEI-ONPs in the solution. Secondly, 2D AFM images

were obtained to visualize the morphology of NPEI-ONPs drop-casted over the glass substrate. Figure 6.3 (B) exhibit relatively circular form of particles being formed after the ultrasonication procedure. The zeta potential measurements of prepared NPEI-ONPs (shown in Figure 6.3 (C)) depicted a consistent profile with concentration variation with highly positive potential values above +30 mV. This implies that the prepared nanoparticles at different concentrations are quite stable with minimal aggregation probability.

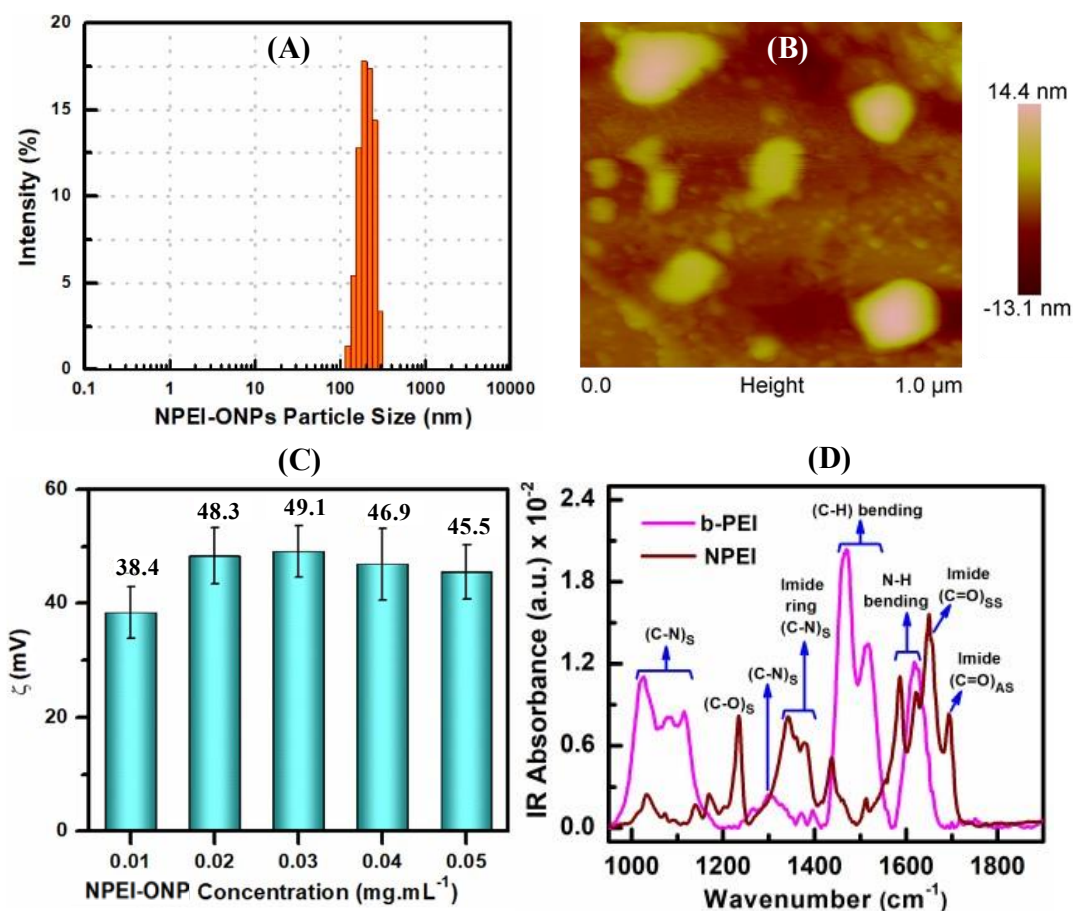


**Figure 6.3** (A) Histogram representation of the measured NPEI-ONP particle size. (B) Morphological determination by AFM imaging of the prepared NPEI-ONPs. (C) Zeta potential measurements with NPEI-ONP concentration variation. (D) ATR-FTIR absorbance profile of b-PEI polymer and prepared NPEI-ONPs in the aqueous media. Reprinted with permission from Kaur et al., *Langmuir* **38**, 13456–13468 (2022). Copyright (2022) American Chemical Society.<sup>276</sup>

The prepared NPEI-ONPs were also characterized using ATR-FTIR spectroscopy to deduce its molecular features. The ATR-FTIR absorbance profile of NPEI-ONPs and b-PEI polymer without any modifications is shown in Figure 6.3 panel D. The occurrence of C-N stretch bands in the NPEI product from the wavenumber range of 1349-1381 cm<sup>-1</sup> represents the dicarboximide formation.<sup>303</sup> The C-H bending modes (1469 and 1515 cm<sup>-1</sup>)

are quite prominent in b-PEI spectra as a signature of its backbone structure, which diminish evidently after the formation of the NPEI conjugate and shifts to 1440  $\text{cm}^{-1}$  peak position.<sup>304</sup> The division of a broad band at  $\sim 1620 \text{ cm}^{-1}$ , depicting N-H bending mode,<sup>305</sup> into four distinct peak positions implies the involvement of N-H modes of b-PEI in the conjugation process with 1,8-Naphthalic anhydride (NA) to form NPEI. The occurrence of imide (C=O) stretching modes (symmetric stretch: 1655  $\text{cm}^{-1}$ , asymmetric stretch: 1697  $\text{cm}^{-1}$ ) evidently validates the occurrence of modification of PEI amine groups by NA moieties.<sup>306,307</sup> The remaining peak designations have been elaborated in the Table 6.2 below.

**Table 6.3** ATR-FTIR absorption profile peak designations and assignments for b-PEI polymer and NPEI-ONPs in aqueous media. Reprinted with permission from Kaur et al., *Langmuir* **38**, 13456–13468 (2022). Copyright (2022) American Chemical Society.<sup>276</sup>

Sample	Wavenumber ( $\text{cm}^{-1}$ )	Assignment
<b>b-PEI</b>	1022 - 1114	(C-N) <sub>s</sub> <sup>284,304,308</sup>
	1302	
	1469 - 1515	C-H bending <sup>304</sup>
	1620	N-H bending <sup>305</sup>
<b>NPEI</b>	1238	(C-O) <sub>s</sub> of naphthalimide moiety <sup>309</sup>
	1349 - 1381	(C-N) <sub>s</sub> mode of imide ring <sup>304,305,308</sup>
	1440	C-H bending <sup>309</sup>
	1588	N-H bending of PEI <sup>284,285,304,308</sup>
	1624	N-H bending from PEI <sup>306</sup>
	1655	(C=O) <sub>ss</sub> mode of imide <sup>306,307</sup>
	1697	(C=O) <sub>as</sub> mode of imide <sup>306,307</sup>

### 6.3.1 Tensiometry measurements of NPEI-ONPs

The surface adsorption process of NPEI-ONPs with concentration variation is determined in terms of significant changes observed in the measured surface tension values (Figure 6.4 (A)). The surface tension process is a classical approach where the sequential adsorption of molecules is observed with rising bulk concentration that is plotted with the surface tension (ST) fluctuations. The obtained ST trend is generally segregated into three distinct regions.<sup>122,125</sup> On the same platform, our results show a decremental profile of surface tension with NPEI-ONP addition which initiates with a slow decline referred to region I, that is followed by a substantial drop (indicated as region II), which then becomes stagnant for higher bulk concentration. The region I extends up to 0.02 mg.mL<sup>-1</sup> NPEI-ONP concentration depicting a concentration build-up of nanoparticles at the surface. Region II presents a steep profile of ST decrement beyond 0.02 mg.mL<sup>-1</sup> suggesting an escalation in the molecular adsorption and hydrophobic group dominance of NPEI-ONPs at the surface. Finally, this decreasing trend subsides for NPEI-ONP concentration  $\geq 0.04$  mg.mL<sup>-1</sup>, indicating the maximum occupancy for ONPs has reached at the surface and no further decrease in ST profile could be seen. These ST results follow the Gibb's adsorption model for the ionic solutes, from where one can calculate the relative molecular surface excess ( $\Gamma'$ ) for NPEI-ONPs. The formulation is represented as:<sup>121,122,124,125</sup>

$$\Gamma' = -\frac{1}{nRT} \frac{\partial \gamma}{\partial \ln c_i} \quad (6.1)$$

Here,  $\gamma$  is the surface tension value,  $n$  is the adsorbate species number existing at the interface whose concentration is defined by  $c_i$  (referred to the mole ratio of solute ( $n_i$ ) and solvent ( $n_1$ ) for dilute solutions). Considering ionic solutes,  $n$  is taken to be 2 in above expression.<sup>121,124,125</sup> The molecular surface excess ( $\Gamma'$ ) in this expression is referred to the difference between the number of solute (ONP) molecules adsorbing to the surface with respect to those residing within the bulk-phase of the aqueous media. Hence, when an equal occupancy is reached for the solute molecules between the surface and bulk-phase, the formulated surface excess value for solute molecules gets minimized.<sup>121,124</sup> From the surface excess interpretation of our ST results (Figure 6.4 (B)), it is seen that the  $\Gamma'$  value show a rapid decline after 0.04 mg.mL<sup>-1</sup> concentration reaching a minimum value for 0.05 mg.mL<sup>-1</sup> ONP concentration. Thus, the ST and  $\Gamma'$  profile of NPEI-ONPs



provided clear information about the ONP concentration i.e.,  $0.04 \text{ mg.mL}^{-1}$  at which a complete surface coverage of ONP molecules is achieved.<sup>124</sup> This is partly analyzed by examining the difference in the adsorbate and bulk ONP concentration as observed and calculated through ST values and the resultant estimation of  $\Gamma'$ .

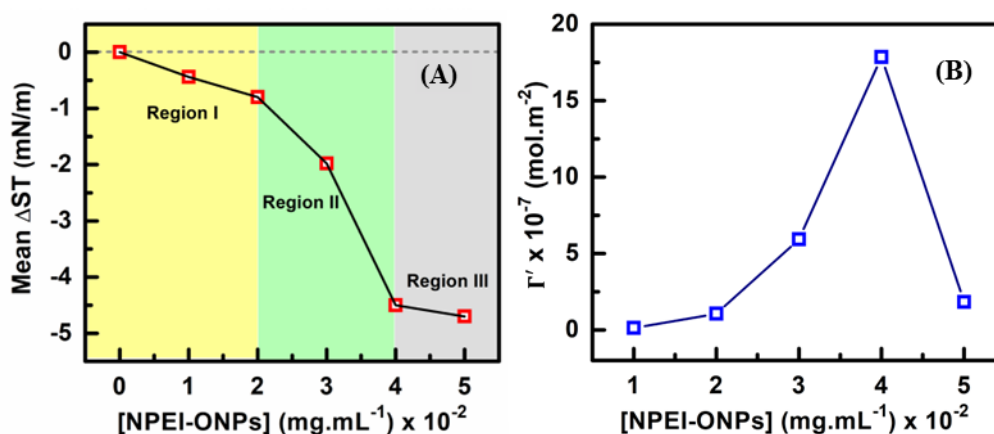


**Figure 6.4** Variations in the (A) mean surface tension of aqueous media, and (B) formulated molecular surface excess ( $\Gamma'$ ) plot as a function of NPEI-ONP concentration. Reprinted with permission from Kaur et al., *Langmuir* **38**, 13456–13468 (2022). Copyright (2022) American Chemical Society.<sup>276</sup>

### 6.3.2 Interfacial molecular expression of NPEI-ONPs

To analyze the possible surface/interfacial behavior and molecular signatures of prepared modified form of ONPs, the reactant molecular species utilized during the reaction scheme were studied first at the air-aqueous interface under the similar buffering strength by SFG-VS. Here, in order to understand the impact caused by the added molecular system, we have initially obtained the SFG spectra of the pristine water, Tris-HCl buffer and Tris-HCl buffer consisting of 0.02% v/v acetic acid (representing the ONP suspension media) as control spectra (see Figure 6.5). The main characteristic modes were identified (using Lorentzian fitting) at the lower wavenumber region centered at  $\sim 3225 \text{ cm}^{-1}$ , higher wavenumber region with peak contributions at  $\sim 3450 \text{ cm}^{-1}$  and  $\sim 3560 \text{ cm}^{-1}$  respectively, and the free dangling OH protruding towards the air that imparts a prominent distinguished narrow peak at  $3705 \text{ cm}^{-1}$  (Figure 6.5 (A)).<sup>146,152,189,264</sup> The lower and the higher wavenumber region showcase the inter- and intra-molecular hydrogen bonding among the water molecules.<sup>152,264</sup> The SFG spectra at the air-aqueous interface of the buffer system (in Figure 6.5 (B)) depicted no variations relative to the pristine water-air interface spectrum.

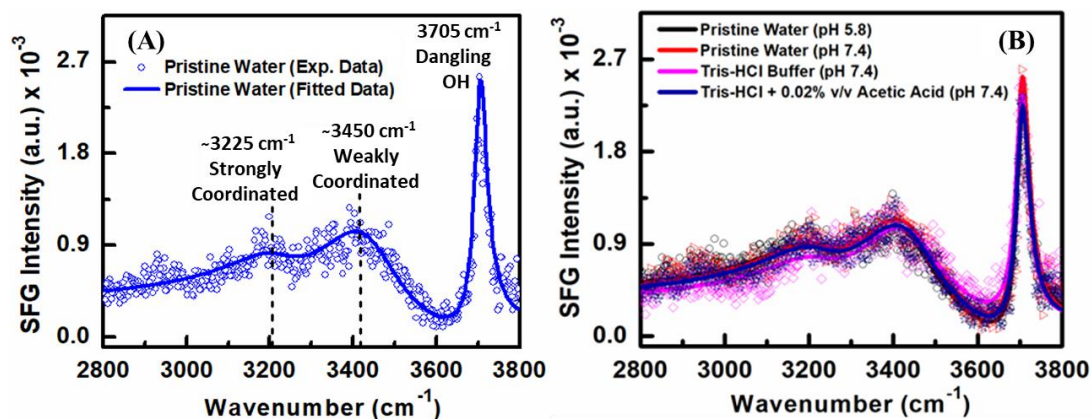


**Figure 6.5** (A) SFG spectrum of pristine water-air interface at pH 5.8 along with peak assignments. (B) Comparative sum frequency spectra of aqueous media taken for reference. Reprinted with permission from Kaur et al., *Langmuir* **38**, 13456–13468 (2022). Copyright (2022) American Chemical Society.<sup>276</sup>

The interfacial spectra of b-PEI polymer (1.4 mM, dissolved in Tris-HCl buffer with 0.02% v/v acetic acid at pH 7.4) did not show any contribution from the methylene moieties in CH-stretch region and amine groups of backbone and side chains in OH-stretch region. In this case, the overall hydrogen bonding strength among the water molecules is seen to reduce with a greater impact observed for the lower wavenumber region centered at  $\sim 3225\text{ cm}^{-1}$  (Figure 6.6 (A)). The b-PEI tends to sustain positive charge at pH 7.4 due to presence of positively charged amine ( $-\text{NH}_3^+$ ) terminal groups within its branched structure. The observed spectra show the tendency of b-PEI molecular groups to slightly disorder the water molecular structure at the interface.<sup>310,311</sup> The hydrophobic alkyl groups and side-chain amines might have arranged themselves along the surface plane or acquired a disordered state at the interface, rendering them SFG inactive in the SSP polarization mode of probing.<sup>310,311</sup> Similarly, the interfacial profile of 1,8-naphthalic anhydride (0.04  $\mu\text{M}$  dissolved in Tris-HCl buffer with similar composition) show no significant change in the profile of the hydrogen-bonded water molecular structure (Figure 6.6 (B)). The alkyl region ( $2800\text{--}3100\text{ cm}^{-1}$ ) did not present any signature of aromatic ring moiety, an attribute of the 1,8-naphthalic anhydride molecules. This indicates that the ring structure probably lie with a flat conformation at the air-water interface.<sup>294,312,313</sup> Monitoring the free O-H peak ( $3705\text{ cm}^{-1}$ ) of both b-PEI and 1,8-naphthalic anhydride (Figure 6.6) shows minute impact from molecular units and indicates their probable involvement with the free OH molecules at the interface.<sup>146,152,189,264</sup>

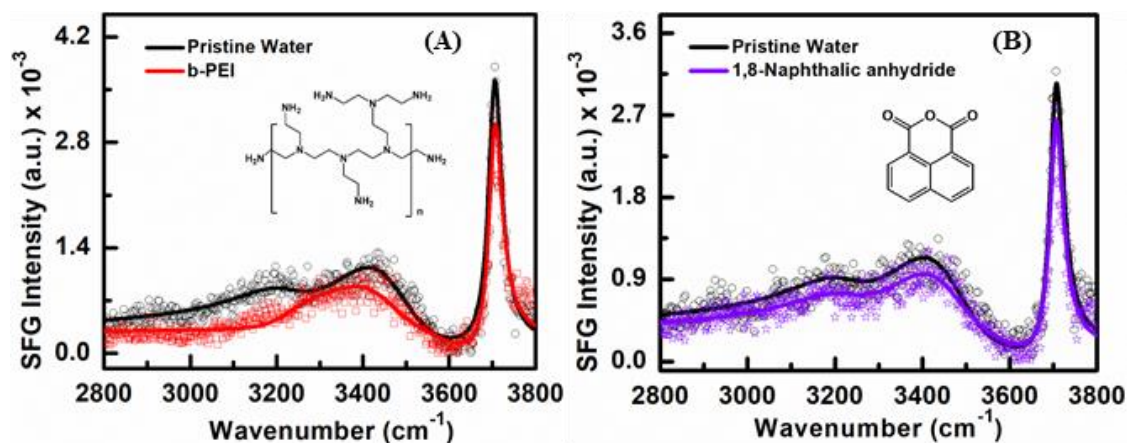


**Figure 6.6** SFG spectra in SSP polarization scheme for (A) b-PEI (1.4 mM) and (B) 1,8-naphthalic anhydride (0.04  $\mu\text{M}$ ). Solid lines are indicative of the fitted curve for the symbol-marked experimental data points. Reprinted with permission from Kaur et al., *Langmuir* **38**, 13456–13468 (2022). Copyright (2022) American Chemical Society.<sup>276</sup>

Conversely, the synthesized product (NPEI polymer) in its nanoparticle state shows predominant surface-active resonances both in CH-region and OH-region, as studied using SFG spectroscopy at the air-water interface. Figure 6.7 (panel A) shows the fitted SFG spectra of NPEI-ONPs at the air-aqueous interface as a function of its concentration in the media. The impact of NPEI-ONPs over the interfacial water molecular network is deduced from the magnitude of perturbations caused among the water molecules along with the occurrence of hydrophobic features of ONP moieties at the air-aqueous interface. Figure 6.7 (A) shows the C-H vibration modes in aromatic region (3000-3100  $\text{cm}^{-1}$ ) with emerging broad and low-intensity contribution from methylene symmetric ( $\text{CH}_{2\text{SS}}$ ) and anti-symmetric ( $\text{CH}_{2\text{AS}}$ ) resonances at 2856  $\text{cm}^{-1}$  and 2930  $\text{cm}^{-1}$  of b-PEI unit of NPEI-ONPs.<sup>280,295,314,315</sup> These features gradually appear upon increasing NPEI-ONP concentration. At NPEI-ONP concentration of 0.05  $\text{mg}\cdot\text{mL}^{-1}$ , the 3073  $\text{cm}^{-1}$  assigned as  $\nu_2$  mode of the aromatic C-H stretch, which emerges as a sharp intense feature along with a shoulder peak at 3005  $\text{cm}^{-1}$  referred to C=C from aromatic ring structure of naphthalimide moiety.<sup>158,294,312</sup>

The influence of NPEI-ONPs over the water molecular network is observed in the O-H stretching region in SSP polarization scheme from 3050  $\text{cm}^{-1}$  to 3800  $\text{cm}^{-1}$  (see Figure 6.7 (A)), where the NPEI-ONP concentration of 0.02  $\text{mg}\cdot\text{mL}^{-1}$  is seen to initially impact and enhance the weaker hydrogen bonding (H-bonding) coordination among water molecules (peak centering at 3450  $\text{cm}^{-1}$ ). For ONP concentrations  $>0.02$   $\text{mg}\cdot\text{mL}^{-1}$ , the spectral intensity for strongly coordinated H-bonds with peak centered at  $\sim 3225$   $\text{cm}^{-1}$  is

also raised. This could be observed from the plotted peak intensity ratios (after extracting values from Lorentzian fitting) among higher and lower wavenumbers centered at  $\sim 3450\text{ cm}^{-1}$  and  $\sim 3225\text{ cm}^{-1}$  in Figure 6.7 (B). This immediate surge in  $3225\text{ cm}^{-1}$  and an overall enhancement in water molecular coordination seen in the O-H stretch region later acquires a saturation state and does not rise significantly further, thus, decreasing the relative peak intensity ratio values drastically beyond  $0.02\text{ mg.mL}^{-1}$  ONP concentration (Figure 6.7 (B)). In contradiction to the observation from O-H stretch region, the C-H region resonant peaks with a predominant spectral intensity noted at  $3073\text{ cm}^{-1}$  rises in proportion with the amount of NPEI-ONPs added to the aqueous media (quantitatively represented in Figure 6.7 (C)). However, this enhancement at  $3073\text{ cm}^{-1}$  peak for varying ONP concentrations is lacking in PPP polarization mode (shown in Figure 6.7 (D)). Several studies have demonstrated the interfacial preference of hydrophobic moieties which dominantly point towards the air, as studied at different interfaces.<sup>48,71,133,157</sup> Therefore, it can be considered that the naphthalimide moieties of NPEI-ONPs initially lie in a flatter conformation at lower concentration but, acquire an ordered state due to rising molecular compactness with increasing NPEI-ONP concentration at air-aqueous interface with their hydrophobic groups predominantly covering the surface upon increasing concentration. The disappearing free O-H peak with concentration rise further validates an increase in the molecular surface coverage.<sup>146,152,189,264</sup>

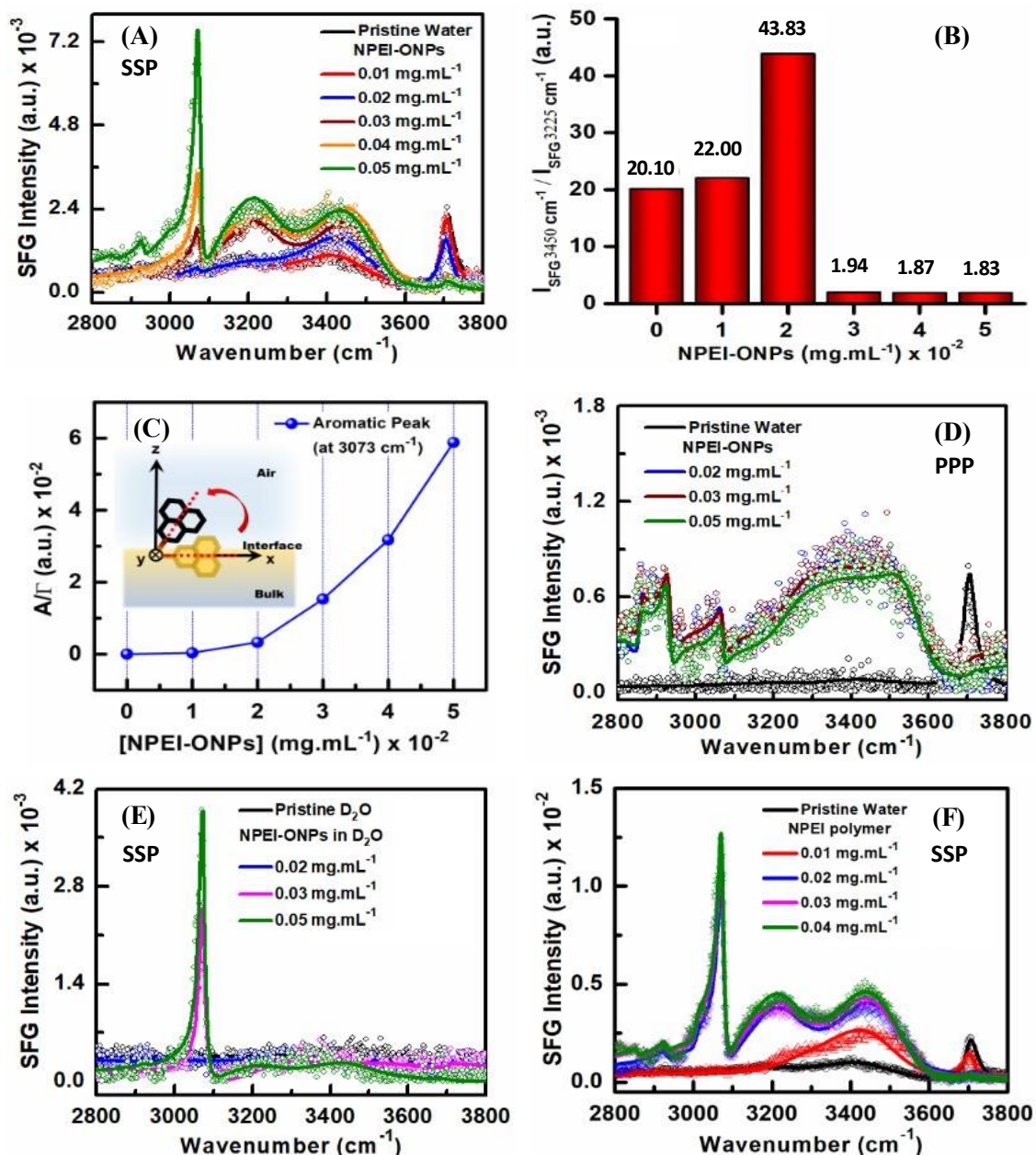


**Figure 6.7** (A) Sum frequency spectra of NPEI-ONPs as a function of concentration variation at air-aqueous interface, (B) represent histogram profile of  $3450\text{ cm}^{-1}$  and  $3225\text{ cm}^{-1}$  peak intensity ratios, and (C) depicts peak amplitude variation at  $3073\text{ cm}^{-1}$  aromatic peak feature, in SSP polarization combination with inset illustrating aromatic ring ordering. (D) SFG spectra of NPEI-ONPs at selective concentrations in PPP polarization scheme. (E) SFG spectra of NPEI-ONPs prepared in buffered  $\text{D}_2\text{O}$  media for selective concentrations. (F) Concentration-dependent profile of NPEI polymer in buffer system. In SFG spectra, the solid lines depict fitting lines of the experimental data points represented in symbols. Reprinted with permission from Kaur et al., *Langmuir* **38**, 13456–13468 (2022). Copyright (2022) American Chemical Society.<sup>276</sup>

From above discussion, it could be conferred that the NPEI-ONP surface adsorption ensues with perturbation and enhancement in the O-H stretch profile. Many studies link this observation with perturbations in the average alignment of water

molecules due to the presence of charged moieties nearby.<sup>133,146,264</sup> The b-PEI polyelectrolyte stays cationic from pH in range of 2-10 due to its positively charged amine end groups.<sup>277</sup> Here, two possibilities could be considered for the enhanced O-H stretch profile. It could either occur by perturbation of water molecular alignment affected by charged amine and amide groups from the PEI backbone of NPEI-ONPs or N-H stretching modes are constructively interfering as an overlapped resonant signal in region 3100-3600  $\text{cm}^{-1}$ .<sup>162</sup> To explicitly distinguish between the two possibilities, NPEI-ONPs were prepared and evaluated in buffered  $\text{D}_2\text{O}$  at three selective concentrations. As shown in Figure 6.7 (panel E), no resonating profile is observed in the O-H stretch region of the ONP profile. An aromatic feature at 3073  $\text{cm}^{-1}$  remains invariable with slight variation in the peak intensity that appears probably due to minimized interference from neighboring O-H stretch signal within the spectra. The N-H stretch mode, usually identified around  $\sim 3150 \text{ cm}^{-1}$  and  $\sim 3300 \text{ cm}^{-1}$ ,<sup>162</sup> is negligible in the NPEI-ONPs spectra in  $\text{D}_2\text{O}$ . However, the probability of N-D formation could not be ruled out as it could arise overlapped in the O-D stretch region as N-D stretch mode. Referring to the Meister et al.,<sup>162</sup> a less intense broad signal from N-H stretch mode could be notified in the spectra in the O-H stretch region simply at air-aqueous interface. Contrarily, our results for three NPEI-ONP concentrations in  $\text{D}_2\text{O}$ , indicates no N-H stretch contribution. Therefore, we are considering the enhanced O-H stretch profile to be primarily contributed by an increased alignment of interfacial water molecules in the vicinity of charge moieties. The nanoparticle dissolution in  $\text{D}_2\text{O}$  system, however, removes the signal interference from OH-stretch enhancement noticed in  $\text{H}_2\text{O}$  based aqueous media, which leads to a clear evaluation of the aromatic mode from NPEI-ONPs with concentration. Henceforth, based on the NPEI-ONP profile in  $\text{D}_2\text{O}$  system, we decided to rule out the inclusion of amine side-chain contribution to the interfacial SFG spectra, and have analyzed the ONP surface adsorption in terms of its influence over the interfacial water molecular network with ONP concentration variation.

In order to rule out the possibility of sonication induced structural changes that might incur to the synthesized NPEI polymer undergoing the procedure of nanoparticle synthesis, the NPEI polymer in its native form without subjecting to sonication, was dissolved directly in 1.5% w/v acetic acid and then rigorously mixed in Tris-HCl buffer solution (pH 7.4). Its surface characterization in solubilized native polymer form done by SFG shows a similar profile as obtained by its nanoparticles at the air-water interface



(Figure 6.7 (F)). This verifies that even after sonication, the structural features of NPEI polymer remain stable and the conjugation formed from b-PEI and naphthalic anhydride reactants make NPEI polymer naturally disposed to surface activity. Association of b-PEI with 1,8-Naphthalic anhydride at its end-group sites during the chemical synthesis of NPEI polymer results in the loss of positively charged  $-\text{NH}_3^+$  at few random sites where naphthalic anhydride conjugates to form naphthalimide. This reaction provides hydrophobic character to the compound and henceforth lowers the solubility of the formed complexed structure within the bulk aqueous solution. This enhances the adsorption process at the interface, rendering it SFG active.

**Culmination of surface tensiometry and SFG-VS observations:** Both studies projected a comprehensive view of the attained molecular surface excess and formation of ONP monolayer at the interface, where the hydrophobic interactions are contributing towards the naphthalimide rearrangement, and consequently the aromatic peak evolution is observed through interfacial SFG spectra. Surface tensiometry, however, only projects the ONP surface adsorption impact which becomes steady beyond certain bulk concentration since additional ONP adsorption towards the surface gets hindered at higher concentration, as calculated from the surface excess assessment of NPEI-ONPs. While, SFG-VS explicitly provided a molecular-level information about the adsorption process along with their possible re-arrangement at a microscopic level. SFG spectral results offer deeper insights towards the molecular re-organizations which could still occur for the maximally covered surface by ONP molecules and their impact over the neighboring water structure. This potentially explains about the ongoing fundamental steric interactions during inter-molecular associations and their assembly at the air-aqueous interface which could be identified only via SFG-VS. The possible molecular behavior of NPEI-ONPs is represented pictorially in Figure 6.8.

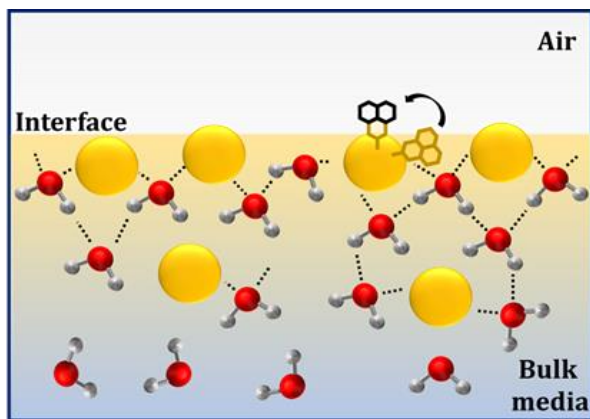


**Figure 6.8** Pictorial illustration of the possible NPEI-ONP molecular behavior at the air-aqueous interface.

### 6.3.3 Probing NPEI-ONPs interaction with dsDNA

The DNA detection is of fundamental importance in the area of research, medicine and healthcare, and in several device applications.<sup>281,283,290,298,316</sup> Several methodologies are being used for identifying DNA which include a variety of inorganic and organic nanoparticles.<sup>82,290</sup> The inorganic nanoparticles tend to bear higher hydrophobicity and require additives or surface modifications to enhance its water dissolution.<sup>82</sup> Organic nanoparticles, however, are biocompatible, show better solubility, readily immobilize, and are convenient to modify.<sup>82</sup> Due to cationic nature, b-PEIs readily condenses dsDNA molecules via electrostatic interactions,<sup>281,282,289</sup> while the naphthalimide moieties act by intercalating within the double helical structure of dsDNA predominantly through  $\pi$ - $\pi$  stacking interactions among the nucleic bases.<sup>290,298,301</sup> Utilizing these characteristics of the parent compounds, the synthesized NPEI-ONPs were assessed for dsDNA binding capacity in both bulk-phase and at interface. We propose here that the hybridized product NPEI offer a large surface area to volume ratio in its nanoparticle version, and thus the overall binding modes of the NPEI-ONPs with dsDNA possibly upgrades. The chemical structure of prepared positively charged NPEI-ONPs as well as negatively charged dsDNA at pH 7.4 in Tris-buffered media are provided in Figure 6.9, panel A and B respectively, for clarity. Considering the NPEI-ONP surface coverage observed beyond  $0.03 \text{ mg.mL}^{-1}$  concentration, for conducting binding studies with DNA, we have utilized the  $0.03 \text{ mg.mL}^{-1}$  concentration of NPEI-ONPs ahead.



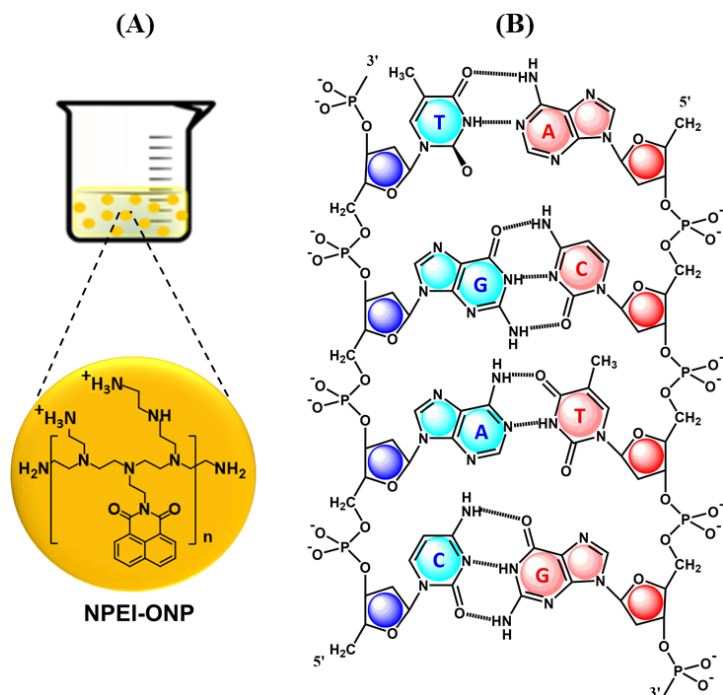


**Figure 6.9** Chemical structure of (A) prepared NPEI-ONPs and (B) dsDNA.<sup>276,281</sup>

**Viscometry measurements.** The hydrodynamic profile of the solutions containing dsDNA with and without ONPs were monitored by viscosity measurements. Viscometry analysis provides information about the intercalative binding state of the compound within the double helical DNA structure. Intercalation creates stiffness, lengthening, and unwinding of the double helix which causes a relative increase in the sample viscosity.<sup>298,317</sup> Our results (shown in Figure 6.10 (A)), however, indicates a relatively lowered viscosity profile for dsDNA with NPEI-ONP addition, in comparison to the viscosity of pristine dsDNA solution. Due to the possibility of the NPEI to condense dsDNA molecules via its b-PEI unit through attractive electrostatic interactions,<sup>281,282</sup> the average molecular distribution per unit volume of the aqueous media could decrease in number. The aromatic structure of attached naphthalimide moiety further aids in improving the overall binding strength. This could result in decreasing profile of viscosity for dsDNA after introducing NPEI-ONP.

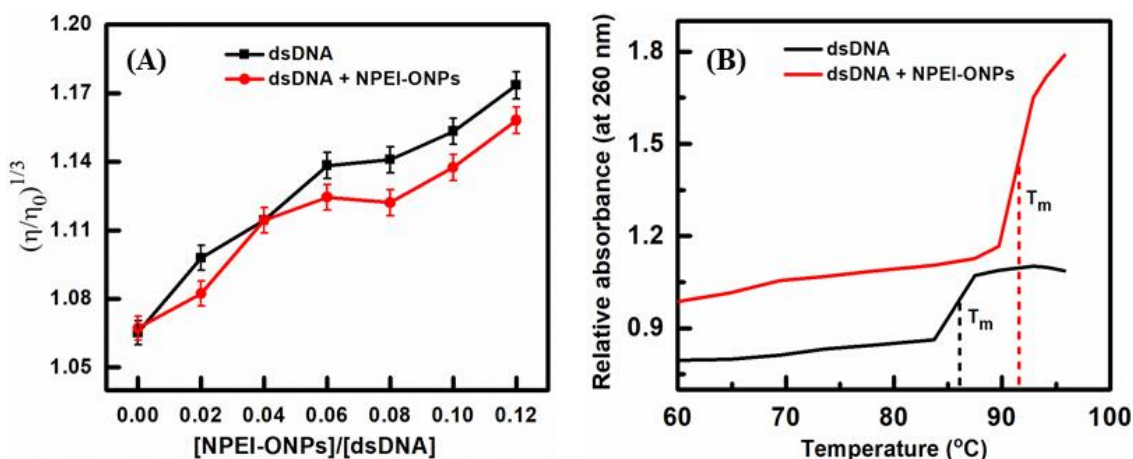


**Figure 6.10** (A) Viscosity measurements of dsDNA in pristine conditions and under NPEI-ONP influence added to fixed dsDNA concentration. (B) The melting temperature ( $T_m$ ) profile of dsDNA observed at its characteristic 260 nm absorbance wavelength with and without NPEI-ONP addition to aqueous media. Reprinted with permission from Kaur et al., *Langmuir* **38**, 13456–13468 (2022). Copyright (2022) American Chemical Society.<sup>276</sup>

**Thermal denaturation studies.** The stability of the dsDNA helical structure is analyzed via thermal denaturation curves attained using UV-Visible spectrophotometer equipped with a thermoregulator. The studies were conducted in the absence and presence of NPEI-ONPs (see Figure 6.10 (B)). Since the intercalative binding mode is known to stabilize the helical conformation of dsDNA while the covalent association destabilizes it,<sup>298,317</sup> we could readily identify the mode of dsDNA-compound interaction. Through these studies, the melting temperature ( $T_m$ ) profile for low molecular weight dsDNA of salmon sperm (measured at  $\lambda_{\text{max}}$  of 260 nm) is identified to be at 87.5 $^{\circ}\text{C}$ . On the other hand,  $T_m$  value of dsDNA under NPEI-ONP influence rises by 5 $^{\circ}\text{C}$ . This variation in profile suggests that the dsDNA gets increasingly stabilized in presence of ONPs primarily via non-covalent intercalative interactions among the nucleic bases of dsDNA and naphthalimide moiety of NPEI-ONPs.

**Zeta-sizer and potentiometric studies.** Owing to the positive and negative charge density carried by NPEI-ONPs and dsDNA respectively, their associations can be suitably inspected through observing the dispersive media stability which is governed by the inter-particle interactions as well as the charge on particle surface. Henceforth, here we have targeted to evaluate the particle size and impact on the charge of ONPs under the influence of dsDNA. The average charge carried by the particle is identified via an indirect measure of particle mobility under an externally applied electric field, which is used to theoretically obtain the zeta potential ( $\zeta$ ) values/charge of the nanoparticles within

the aqueous media.<sup>128</sup> Further description about the theory is provided in chapter 2 (section 2.5). Thus,  $\zeta$  measurements rely on the extension of charged functional groups of the particle within its diffused boundary layer. Fig. 6.11 represents the observations attained for the ONP-dsDNA interaction over the nanoparticle size,  $\zeta$ , and conductivity ( $\sigma$ ) of the association. Here, Panel A shows the nanoparticle size distribution with dsDNA addition. It depicts that the size distribution of NPEI-ONPs become broader with dsDNA addition. The broadening in the size distribution of ONPs represents that the dsDNA gets loosely bound with ONPs.<sup>318</sup> This leads to the formation of a larger diameter of the NPEI-ONPs and dsDNA complex in the dispersive media. Bellettini et al.<sup>292</sup> reported a comparative study on DNA condensing capabilities of PEI and alkylated PEI, respectively. In their work, PEIs are found to be more potent in forming strong interactions and small-sized complexes with DNA than the alkylated PEIs. They attributed this observation to the possible intrachain steric hindrance contributed by the attached alkyl groups. In our study as well, the particle size measurements of b-PEI and dsDNA complexes were also evaluated. However, our results (data not shown) depicted the formation of unstable heterogenous complexes with size of varied diameters and large aggregates. The observation is contrary to the particle size observed for the aromatic ring-modified PEI nanoparticles (NPEI-ONPs) and dsDNA complexes which were relatively stable and signifies the benefit of the NPEI-ONPs over b-PEIs in condensing the dsDNA molecules.

Panel B of Figure 6.11 presents the  $\zeta$  potential observations of ONPs under dsDNA influence in terms of their coupled effective charge.<sup>126,128,318</sup> The electrophoretic mobility plot (Figure 6.10 (D)) presented the same pattern of  $\zeta$  potential curve for same experiment. Significant variations in the positive  $\zeta$  value of pristine ONPs could be notified readily from the  $\zeta$ -potential graph with dsDNA addition to the ONP-based aqueous media (Figure 6.11 (C)). Various studies have demonstrated this decrement to be associated with the shielding effect by the oppositely charged molecules, forming a macromolecular corona at the boundaries of the nanoparticle.<sup>126,128,292,318</sup> For increasing amount of dsDNA concentration added, the  $\zeta$ -potential value becomes highly negative in magnitude projecting the prevalence of strong repulsive forces among the acquired negatively charged of ONP-dsDNA coupled systems with added dsDNA molecules.<sup>126,128,318</sup> This suggested the formation of a stable dispersive media. While, lower  $\zeta$  values near zero are usually referred to broad particle sizes.<sup>126,128,318</sup> The similar

observation was also noticed by Bellettini et al.,<sup>292</sup> where the aggregates and coacervation of the PEI and DNA complexes are formed as the concentration of DNA is raised and with an overall  $\zeta$ -potential of the aqueous media approaching near-zero value. Hence, it can be inferred from the observation that the reversal of  $\zeta$ -potential values of NPEI-ONPs is caused by the shielding effect of dsDNA, which increases with the dsDNA addition and creates a macromolecular corona at the boundaries of the nanoparticle surface.<sup>126,128,318</sup> Further, the conductivity ( $\sigma$ ) of nanoparticles in aqueous media is analyzed (Figure 6.11, panel E) which mainly arises as a result of conjugation or attractive forces among molecular groups (i.e., electrostatic and hydrophobic). Here, a sudden rise in ' $\sigma$ ' value is ascribed to the stacked structure formation of ONPs with dsDNA. Some reports support this interpretation where the rising  $\sigma$  value is analogized with the structural-level transitions of dsDNA to acquire a more compact form observed during the DNA-surfactant interactions in their studies.<sup>319,320</sup> A consecutive fall off in  $\sigma$  value, nevertheless, indicates an elevated ionic strength of the media (as observed from the highly negative  $\zeta$  values)<sup>128,319,320</sup> beyond [dsDNA]/[NPEI-ONP] concentration ratio value of 1 in the aqueous suspension. Collectively, the findings from Figure 7 substantiated the impact of dsDNA on the physico-chemical properties of NPEI-ONPs.

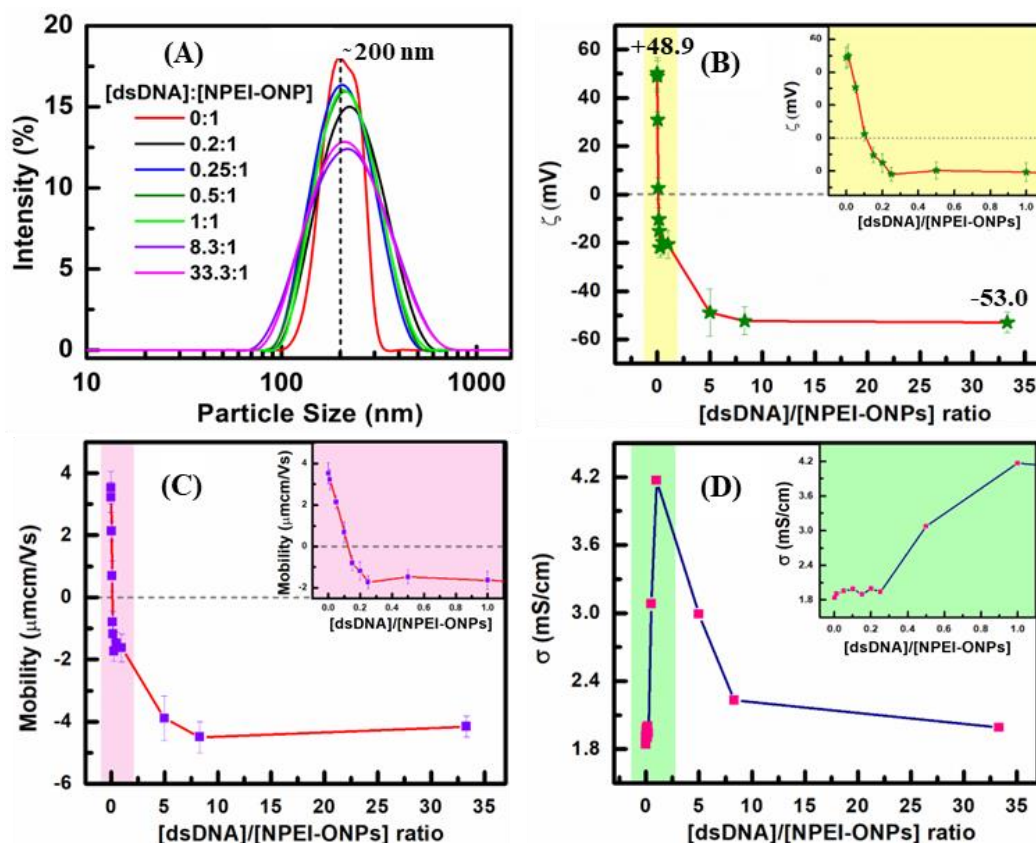


**Figure 6.11** (A) Mean particle size evaluation, (C)  $\zeta$ -potential and (D) electrophoretic mobility measurements, and (E) conductivity ( $\sigma$ ) analysis of NPEI-ONPs, compared with respect to dsDNA and ONP concentration ratios. Reprinted with permission from Kaur et al., *Langmuir* **38**, 13456–13468 (2022). Copyright (2022) American Chemical Society.<sup>276</sup>

**ATR-FTIR vibrational spectroscopic studies.** So far, with different conventional approaches, we broadly examined how the ONPs and dsDNA influence each other's conformational and physical properties. Advancing for in-depth investigation, ATR-FTIR spectroscopy is employed to identify the molecular-level impact of the ONP-dsDNA association. ATR-FTIR spectroscopic technique ably examines the vibrational perturbations within the depth scale of few micrometers from the crystal surface towards the bulk aqueous media under study.<sup>29,30,114</sup> These feature-level changes are discerned via intensity fluctuations, peak shifting, and new peak emergence which highlights the changes in the chemical structure and vibrational patterns in lieu of inter-molecular interactions. The ATR-FTIR absorption spectra were attained for NPEI-ONPs (fixed 0.03 mg.mL<sup>-1</sup> concentration), dsDNA (0.03–1 mg.mL<sup>-1</sup>), and their mixed solutions in fingerprint region (900-1300 cm<sup>-1</sup>), and CH- and OH-region (2700-3800 cm<sup>-1</sup>) (see Figure 6.12). Here, we have conducted the experiments by considering dsDNA concentration in the higher range i.e., for 0.03, 0.1, and 1 mg.mL<sup>-1</sup>, as the lower concentration values of dsDNA were rendering a lower signal-to-noise ratio which was

difficult for any conclusive discussion. The prominent peak feature observed for NPEI-ONPs is centered at  $\sim 1238 \text{ cm}^{-1}$  which is assigned to C-O symmetric stretch [(C-O)<sub>ss</sub>] from naphthalimide moiety.<sup>309</sup> The dsDNA sample shows characteristic profile of B-conformational form which include peaks at  $\sim 967 \text{ cm}^{-1}$  for coupled phosphodiester stretch or deoxyribose stretching,<sup>321-323</sup> an overlapped region with peaks at  $\sim 1068 \text{ cm}^{-1}$  (C-O stretch of sugar ring) and another at  $\sim 1090 \text{ cm}^{-1}$  assigned to the symmetric  $\text{PO}^{2-}$  stretch, and  $\sim 1220 \text{ cm}^{-1}$  peak designated to asymmetric stretch mode of  $\text{PO}^{2-}$ .<sup>321-323</sup> From Figure 6.12, it is readily visible that the deoxyribose C-Os ( $1064 \text{ cm}^{-1}$ ) majorly gets affected as its intensity gets reduced with ONP addition for each concentration of dsDNA (panel A to C). In addition to the intensity, the peak position is seen to be shifted towards the lower wavenumber side to  $\sim 1054 \text{ cm}^{-1}$  which is probably arising due to direct association among b-PEI unit of ONPs and deoxyribose sugar of dsDNA backbone.<sup>321-323</sup> This indicates weakening of the C-O bond of sugar residues and the possibility of their simultaneous involvement with other functional group during interaction with NPEI-ONPs. Furthermore, the arousal of new peak feature at  $1010 \text{ cm}^{-1}$  ascribed to asymmetric C-O-C stretch mode [(C-O-C)<sub>AS</sub>] depicts and supports the involvement of sugar C-O groups in a new type of bonding.<sup>322,323</sup> The secondary peak at  $\sim 1090 \text{ cm}^{-1}$  of ( $\text{PO}^{2-}$ )<sub>ss</sub> also reduces in intensity and showcase blue shift to  $\sim 1111 \text{ cm}^{-1}$  broad feature, which suggests the propensity of phosphodiester bridges of dsDNA backbone becoming more free after interacting with ONPs.<sup>321,322</sup> The  $\sim 1220 \text{ cm}^{-1}$  peak position for ( $\text{PO}^{2-}$ )<sub>AS</sub> is usually referred as an indicator of the hydration or dehydration processes occurring for the phosphoric groups of dsDNA.<sup>321-323</sup> An increasing intensity for this peak position at higher dsDNA concentration hints towards the impact on the hydration state of DNA molecules with NPEI-ONP addition. The CH- and OH-region (panel D) depicts increased contribution from the methyl groups and N-H/O-H stretching modes for the ONP-dsDNA mixed aqueous media, with more methyl features observed for lower DNA concentration added. Hence, at lower dsDNA concentration hydrophobic forces (intercalative forces) are playing a dominant role, while with higher concentration of dsDNA electrostatic forces shows more impact. These results substantiated the alteration in the fundamental vibrational patterns of dsDNA in presence of NPEI-ONPs in bulk aqueous media.

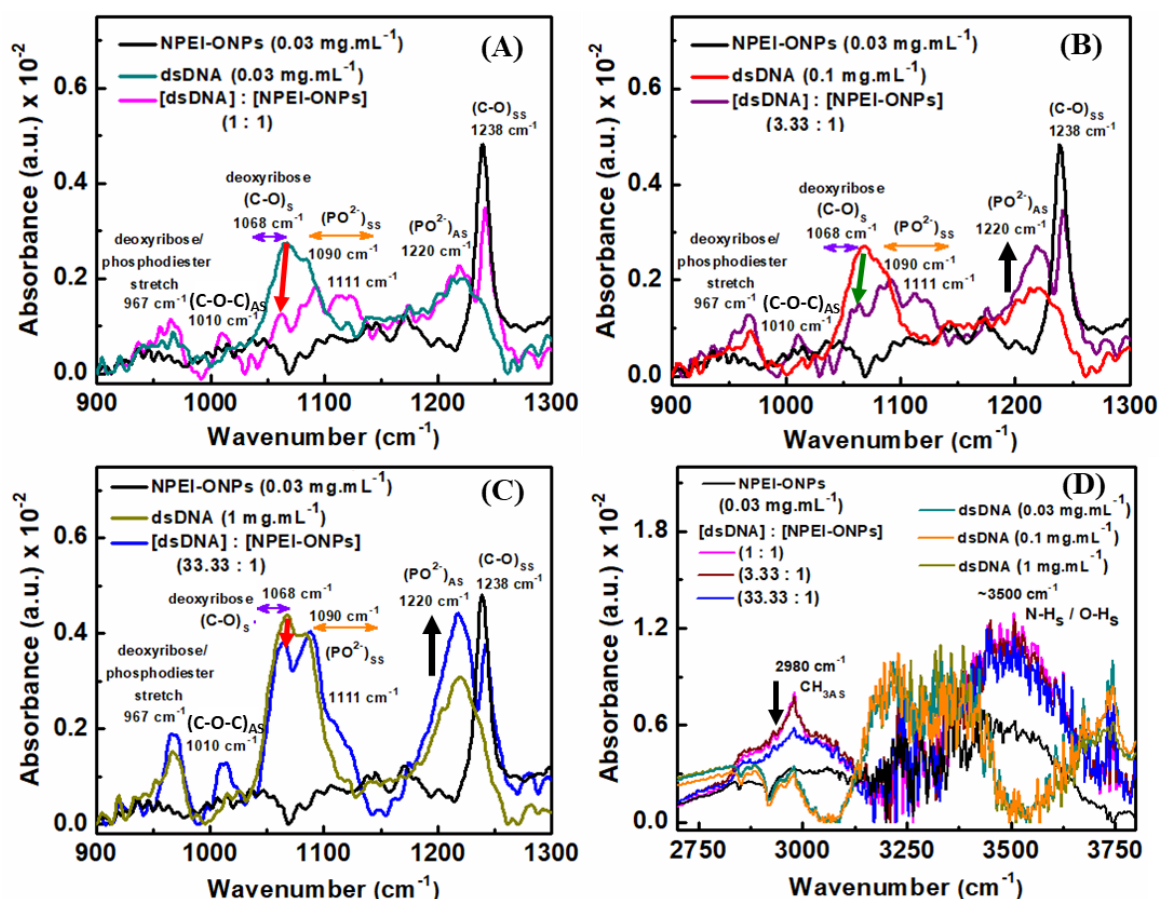
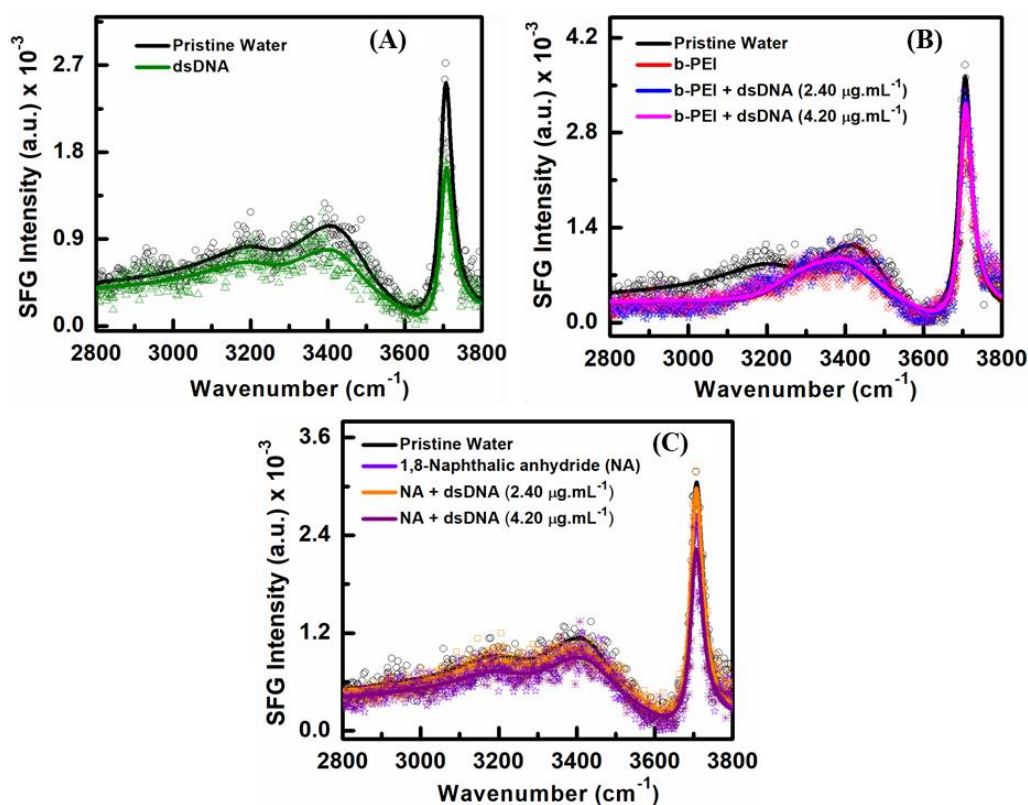


**Figure 6.12** ATR-FTIR absorbance spectra in bending region (900-1300  $\text{cm}^{-1}$ ) of dsDNA and NPEI-ONP with concentration ratios (A) 1:1, (B) 3.33:1, and (C) 33.33:1. (D) ATR-FTIR spectra in CH- and OH-region (2700-3800  $\text{cm}^{-1}$ ) of NPEI-ONPs, DNA, and their respective concentration ratios. Arrows depicts variations in intensity and peak shifting. Reprinted with permission from Kaur et al., *Langmuir* **38**, 13456–13468 (2022). Copyright (2022) American Chemical Society.<sup>276</sup>

**SFG-VS investigations at air-aqueous interface.** Investigating the interfacial organization and dynamics of molecular groups is essential for deploying the sample for several surface science applications.<sup>36,62,185,195,211,229,264,266,311,324</sup> The aqueous interfaces provide additional details about the interfacial water molecular structure and the influence of molecular interactions over the coordination/H-bonding network. Prior to studying the molecular interactions, the dsDNA molecules were studied at the air-aqueous interface under pristine conditions. Structurally, DNA carries negatively charged phosphate groups ( $\text{PO}_4^{2-}$ ), cyclic ring-structures of sugar and methyl groups. The SFG spectrum of dsDNA with the standard stock concentration of  $0.03 \text{ mg.mL}^{-1}$  is considered as reference at the air-water interface (Figure 6.13 (A)), where no significant perturbation was noticed for dsDNA with respect to the pristine water. This probably arises due to the attainment of centrosymmetry by the dsDNA functional groups at the interface.<sup>68,311,313</sup> There is an



overall decrease in the SFG intensity observed in the OH-stretch and free OH-stretch region in the presence of dsDNA. Due to already known preference of PEI and naphthalic anhydride units for dsDNA binding and intercalation, some preliminary experiments were done with b-PEI and 1,8-naphthalic anhydride respectively in the vicinity of dsDNA at the air-aqueous interface. Nevertheless, no surface activity/interfacial perturbations were seen in the acquired SFG spectra (Figure 6.13 (B and C)).



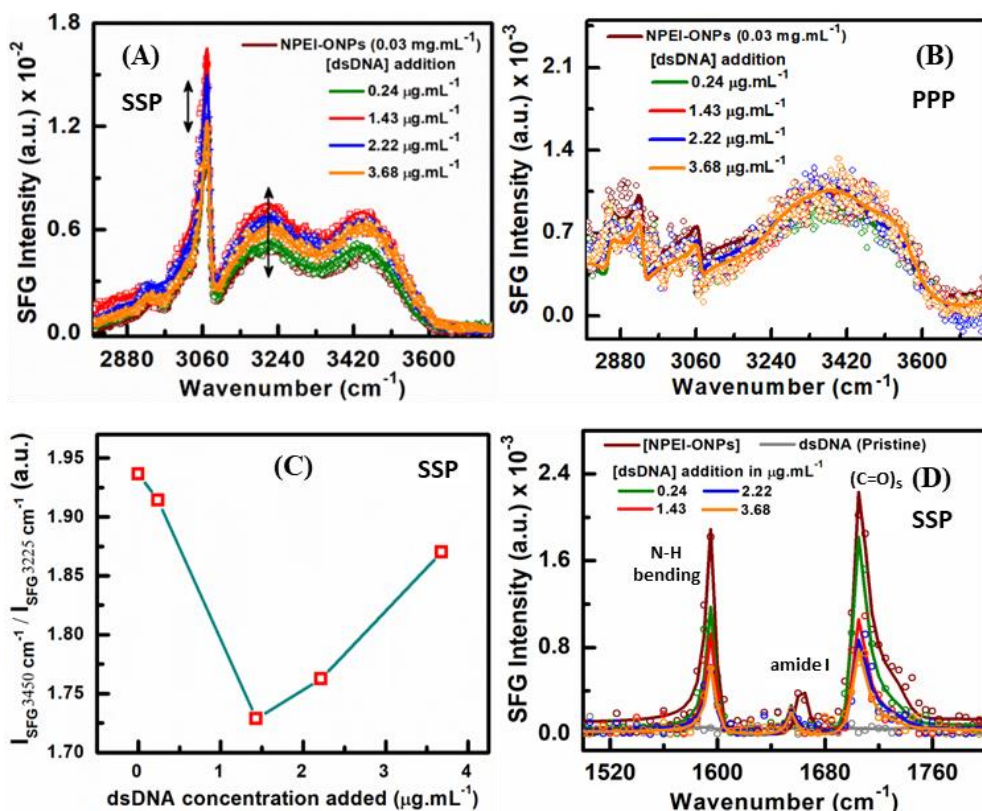
**Figure 6.13** Sum frequency spectra of (A) dsDNA ( $0.03 \text{ mg.mL}^{-1}$ ) comparative to pristine water, (B) b-PEI (at  $1.4 \text{ mM}$  concentration) and (C) 1,8-naphthalic anhydride (NA,  $0.04 \text{ }\mu\text{M}$ ) with dsDNA concentration variation respectively in SSP polarization scheme. Solid lines represent fitted lines of experimental data points denoted in symbol form. Reprinted with permission from Kaur et al., *Langmuir* **38**, 13456–13468 (2022). Copyright (2022) American Chemical Society.<sup>276</sup>

Figure 6.14 represents the influence of dsDNA addition over NPEI-ONP interfacial adsorption tendency, observed for fixed ONP aqueous concentration by SFG-VS at pH 7.4 in SSP and PPP polarization schemes (panel A and B). Here, we have worked with lower concentration values of dsDNA in  $\mu\text{g.mL}^{-1}$  to conduct the titration studies with NPEI-ONPs, since the addition of higher dsDNA concentration  $>3.68 \text{ }\mu\text{g.mL}^{-1}$  engendered sample aggregation, which was not suitable for the interface-based experiments at the air-aqueous interface. Here, in SSP mode (panel A), it can be interpreted that with only  $\mu\text{g}$  level increment in dsDNA concentration within fixed ONP



concentration leads to enhancement in both OH-stretching coordinated region and the aromatic peak at  $3073\text{ cm}^{-1}$  from  $0.24\text{-}1.43\text{ }\mu\text{g.mL}^{-1}$  added concentration. Then, further increment in dsDNA concentration from  $2.22\text{ to }3.68\text{ }\mu\text{g.mL}^{-1}$  causes an overall reduction in the observed signal strength in both the OH- and aromatic-stretch regions. Contrary to SSP mode, SFG spectra in PPP polarization scheme for NPEI-ONPs with dsDNA addition show no alteration in the spectral profile (panel B). In addition, the OH-stretch region of the ssp polarization profile (panel A) has also been evaluated in terms of the relative contribution of the weakly (centered  $\sim 3450\text{ cm}^{-1}$ ) and strongly (centered  $\sim 3225\text{ cm}^{-1}$ ) H-bonded water molecules respectively (panel C). The plot in panel C is constructed by considering the intensity values for  $3450$  and  $3225\text{ cm}^{-1}$  wavenumber, which have been attained through the Lorentzian curve fitting of SFG spectra shown in panel A. We are able to observe a moderate variation in the spectral profile of NPEI-ONPs with dsDNA addition. So, it can be inferred from the ratiometric plot (panel C) that dsDNA influences minutely the relative H-bonding strength among the interfacial water molecules. The data presented a discrete wobbling in the OH-stretch intensity ratio profile indicating that the DNA addition is plainly influencing the interfacial adsorption tendency and molecular packing of NPEI-ONPs, already adhered at the air-aqueous interface.

In order to gather more insight into the impact of dsDNA presence on the interfacial structure of NPEI-ONPs, we have carried out the SFG experiments in the bending mode region ( $1500\text{-}1800\text{ cm}^{-1}$ ). Figure 6.14 (panel D) showcases the Lorentzian-fitted SFG plots of pristine dsDNA, NPEI-ONPs, and NPEI-ONPs with dsDNA addition in the bending region. The spectral signature shows two strong peak features at  $1596\text{ cm}^{-1}$  (assigned as N-H bending mode) and  $1704\text{ cm}^{-1}$  (attributed to C=O stretch), which are characteristic of PEI and naphthalimide moieties of pristine NPEI-ONPs.<sup>230,324,325</sup> The changes in the characteristic peak intensity profile of N-H bending and C=O stretch with consecutive dsDNA addition suggest that the interaction of dsDNA with NPEI-ONPs indeed perturbs the interfacial signature of NPEI-ONPs. We also noticed a clear shift in position and decrement in intensity of the amide I ( $\sim 1662\text{ cm}^{-1}$ ) on introducing dsDNA, which is a characteristic feature of naphthalimide moieties of NPEI-ONPs.<sup>230,324,325</sup> The above observations, demonstrated in Figure 6.14, reveals that the dsDNA addition causes structural changes in the NPEI-ONPs at the air-aqueous interface.



**Figure 6.14** SFG spectra of NPEI-ONPs with increasing dsDNA concentration in  $\mu\text{g.mL}^{-1}$  in (A) SSP and (B) PPP polarization schemes in CH- and OH-stretch region. (C) Intensity ratio plot of fitted data peaks centred at  $\sim 3450\text{ cm}^{-1}$  and  $\sim 3225\text{ cm}^{-1}$  wavenumber value with added dsDNA of fitted SSP polarization data. (D) SFG spectra in bending mode region (in ssp polarization scheme) for NPEI-ONPs with varying dsDNA concentration at the air-aqueous interface. Pristine dsDNA spectra at  $3.68\text{ }\mu\text{g.mL}^{-1}$  concentration is shown for reference. Reprinted with permission from Kaur et al., *Langmuir* **38**, 13456–13468 (2022). Copyright (2022) American Chemical Society.<sup>276</sup>

## 6.4 Conclusion

The current work aims to understand the implication of aromatic hydrophobic modifications of the branched PEI (b-PEI) polymer, and further regulating its physico-chemical properties by preparing its nanoparticles. In our study, 1,8-Naphthalic anhydride has been used for conducting b-PEI modification by a single-step synthesis procedure. We addressed the molecular behavior of NPEI-ONPs with concentration variation at the air-aqueous interface by using SFG-VS, and is further complemented with surface tensiometry investigations. The results presented an increased surface activity for b-PEIs after its hydrophobic modification which simultaneously impacts the H-bonding coordination and molecular alignment at the interface. SFG-VS provides additional molecular scale information which could not be discerned from surface tension

measurements. For the purpose of applying NPEI-ONPs in biological applications, initial experiments were carried out in the vicinity of dsDNA to understand the primary binding modes and their impact over the physico-chemical profile of both the molecular systems. The bulk-sensitive (viscometry,  $T_m$ ,  $\zeta$ , ATR-FTIR) investigations projected transition in the conformational state of dsDNA making it compact, while the physical parameters of ONPs get majorly affected during interaction. The interfacial examination for dsDNA added at  $\mu\text{g.mL}^{-1}$  level show modulations largely over the molecular packing of NPEI-ONPs already adsorbed at the air-aqueous interface. We have also observed the structural changes in the NPEI-ONPs under the influence of dsDNA as discerned from the SFG data in the bending mode region. The pictorial representation is summarized in Figure 6.15 below. In lieu of significant connection of modified polymers with the bio-diagnostics and device surface coating applications, the current work of in-house hydrophobically modified nanoparticles could offer an added value towards other biomolecular interfacial investigations as well, both in aqueous-phase or as a solid-supported framework.

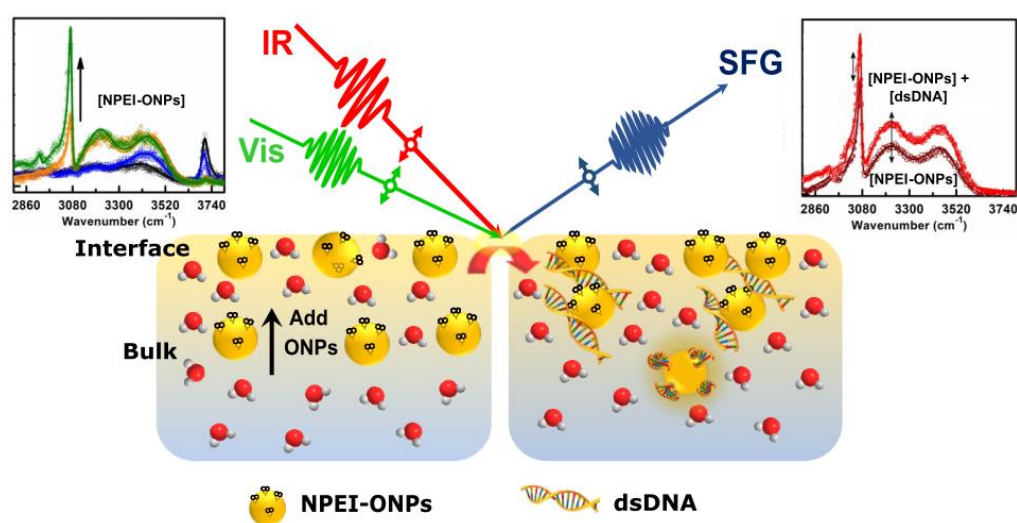


**Figure 6.15** Characterizing the molecular-level activities of hydrophobically modified polymeric nanoparticles as a variation of its concentration and under the influence of double-stranded DNA at the air-aqueous interface. Reprinted with permission from Kaur et al., *Langmuir* **38**, 13456–13468 (2022). Copyright (2022) American Chemical Society.<sup>276</sup>



## Chapter 7

### Conclusion

This chapter summarizes the research work performed and discussed in the preceding chapters of this thesis. An interface-dependent resonant molecular probing is regarded to be the essence of our work, since the active molecular/functional groups are mostly projected at the surface/interface and decides the overall activity at the macroscopic-level. In the introductory Chapter 1, we have outlined the ubiquity and significance of interfaces with associated literature in understanding the key molecular interactions, chemical reactions, and various natural phenomena. The fine-tuning of interfacial properties and dynamics is known to be governed by the interplay of different intermolecular forces such as electrostatic, van der Waals, hydrophobic-hydrophilic interactions, and hydrogen bonding. Thus, an interface-specific resonant probing of molecules is the essence of our work, as the active functional groups projecting at the surface/interface tend to determine the overall activity of the system at the macro-level at the modeled air-aqueous and air-solid interfaces. Understanding the structural organization of the basic biomolecules is highly important for their consideration as a programmable material in distinct device and surface coating applications for analyte recognition, where most of these biomolecules appear at the air-water interface. However, due to the extent of structural lability of biomolecules, we framed our work in the direction of exploring how their association with a nature-derived bio-mimetics and nanomaterials (inorganic and organic) could pave the way towards their robust applicability as programmable material or substrate fabrications. Information about the biomolecular and bio-nano-dependent impact over the water molecular networking is also determined at the aqueous interface.

In addition to evaluating the interfacial regime, integrating the complementary results via bulk-specific or linear optical tools further consolidates the fundamental understanding of the interfacial behavior of complex systems occurring during nano-bio associations. The fundamental theory and experimental details have been elaboratively discussed in Chapter 2 of the thesis, providing the intricacies and physics behind the

actual molecular-level analysis conducted in our work using different spectroscopic tools and methodologies.

Subsequently, we have addressed different research problems and conducted experimental work to probe and interconnect the biomolecular behavior and nano-bio associations at the interface in a broader perspective, where the following conclusions have been extracted from the work performed and are presented point-wise below:

[1] From Chapter 3, we initiated our studies with the investigation of bio-macromolecular adsorption at the air-water interface, which could aid in designing optimal microfabrication and micropatterning technologies involving biomolecules. The following conclusions were made:

- BHb proteins showcased the interfacial occurrence of their hydrocarbon features to be synchronized with the perturbations of interfacial H-bonding strength of water molecules. We observed a fast and slow growth of the protein adsorption process depicting the diffusion of protein towards the surface and the re-arrangement of its functional moieties at the interface, respectively. The results illustrated that the low bulk concentration of proteins renders substantial protein unfolding at the surface/interface, while higher bulk concentration and surface coverage leads to increased protein-protein interactions which causes BHb molecules to remain partially folded.
- For dsDNA at the air-aqueous interface, we have experimentally provided insight towards dsDNA and H<sub>2</sub>O<sub>2</sub> interaction depicting the inclination of alkyl groups towards the sample surface and a distinct influence on the interfacial polar alignment of water molecules and the hydrated water structure around dsDNA in the presence of H<sub>2</sub>O<sub>2</sub>.

[2] Subsequent work in Chapter 4 is performed on the recognition of BHb protein molecules using the molecular topology of imprinted surfaces, which were substantiated using the label-free SFG-VS technique. Here, the memory of the imprinted surface is potentiated as an antibody-mimicking device by observing simply the molecular vibrational features through SFG-VS. This approach has not been conducted before based on intricate molecular-details of the bio-mimetic substrate with a macromolecule-based surface imprinting, using interface-sensitive spectroscopy.

- [3] Further, in Chapter 5, we headed towards utilizing nanomaterials to elucidate the strengthening of interactions among the biomolecules. The complex macromolecular interactions among the antibody and antigen protein molecules are investigated in the presence of inorganic semi-conductor-based tungsten disulfide quantum dots (WS<sub>2</sub>QDs) at the air-water interface. Our results exhibited the mediation of antibody-antigen interactions by QDs. This is well-supported by analyzing the methyl group alignment at the interface in absence and presence of the QDs which was found to reduce by  $\sim 12^\circ$  in presence of QDs. Raising the concentrations of antibody and antigen protein molecules did not influence the methyl tilt angle, instead it was found to contribute more towards an increase in the extent of intermolecular interactions among the molecular groups at the air-water interface.
- [4] Our last Chapter 6 is targeted to elucidate the surface adsorbing behavior of in-house synthesized hydrophobically-modified polyethylenimine (PEI) nanoparticles. The hydrophobic functionalization was performed using an aromatic group (i.e., naphthalic anhydride) which rendered the nanoparticles to be highly surface-active. Their concentration-dependent surface packing was evaluated and their further implication for binding dsDNA molecules was investigated using a combination of interface- and bulk-specific techniques. The modified nanoparticles were found to be more potent than the un-modified PEIs in binding and condensing dsDNA molecules as exhibited by bulk characterizations. The interface-specific SFG analysis demonstrated that the hydrophobically-modified PEI nanoparticles impacted the structural organization of these nanoparticles already adhered at the interface. This understanding is crucial in employing aromatic-moiety dependent hydrophobic modifications for designing fabrications and their potential interactions with different biomacromolecules.
- [5] Additionally, from our studies, a crucial information regarding the water molecules acting as an indirect reporter of key molecular interactions or interfacial adsorption process under investigations has been provided. This understanding could aid in considering the water molecule as a potential manipulator during the process.

## 7.1 Scope of research work

The present thesis work encompasses the importance of interfaces in decoding the molecular-scale phenomena involving phase-separation, surface tensiometry

perturbations, surface adsorption propensity, molecular kinetics, understanding binding interactions at interface, surface density, molecular orientation, and the role of the surrounding environment in modulating the molecular structure. Our main aim is to study these processes with minimal modification procedures and under pristine conditions without utilizing strong perturbates. These parameters are crucial in utilizing biomolecules or employing nano-bio complexes to develop fine-tuned functional surfaces/interfaces, which could be potentially characterized by the label-free detection approach of SFG-VS technique.

## 7.2 Future prospects

Our work could offer a significant contribution towards the rapidly growing domains of bio-mimicking systems, soft functional materials, micro-fluidic device fabrications and biomolecular sensing applications. The current thesis work presented the importance of studying the interaction mechanisms at interfaces and the broad perspective where SFG-VS could be utilized to extract the molecular-level information in rich detail. Nevertheless, the research work presented in the current thesis holds the door open for further investigations and could be carry-forward to explore the following aspects:

- [1] How different reactive-oxygen species could interact differently with dsDNA and protein molecules and the corresponding influence on the interfacial water structure? Some preliminary studies have already been performed where a differential behavior of protein molecules and dsDNA has been seen at the air-water interface in the presence of hydrogen peroxide.
- [2] The developed molecularly-imprinted polymer substrates can be considered for further optimizations for competitive-binding studies with other interfering molecules to authenticate their memory and develop an efficient bio-mimicking sensing substrates.
- [3] The home-developed hydrophobically-modified PEI nanoparticles can be considered for substrate coating and probing their direct interactions with different biomolecules in the aqueous media under the free flow conditions.

Our work, thus offer an exploratory research domain in the area of interfacial science, which could be evaluated in a variety of experimental sets further.



## References

- (1). West, A. Surfaces and Basics From Surface Science, Thermodynamics of Interfaces and Kinetics. In *Interface Science and Technology*, Elsevier, Vol. 21; 2018;pp 1-47.
- (2). Butt, H.-J.; Graf, K.; Kappl, M. *Physics and chemistry of interfaces*. Third ed.; John Wiley & Sons, 2013.
- (3). Fernández, A. Interfacial Physics for Water in Biology. In *Physics at the Biomolecular Interface*, Springer, 2016;pp 1-46.
- (4). Cahen, D.; Kahn, A.; Umbach, E. Energetics of molecular interfaces. *Mater. Today* **2005**, *8*, 32-41.
- (5). Alberti, S.; Dormann, D. Liquid-liquid phase separation in disease. *Annu. Rev. Genet.* **2019**, *53*, 171-194.
- (6). Gomes, B. S.; Simões, B.; Mendes, P. M. The increasing dynamic, functional complexity of bio-interface materials. *Nat. Rev. Chem.* **2018**, *2*, 1-15.
- (7). King, M. D.; Rennie, A. R.; Thompson, K. C.; Fisher, F. N.; Dong, C. C.; Thomas, R. K.; Pfrang, C.; Hughes, A. V. Oxidation of oleic acid at the air–water interface and its potential effects on cloud critical supersaturations. *Phys. Chem. Chem. Phys.* **2009**, *11*, 7699-7707.
- (8). Engelhardt, K.; Rumpel, A.; Walter, J.; Dombrowski, J.; Kulozik, U.; Braunschweig, B. r.; Peukert, W. Protein adsorption at the electrified air–water interface: implications on foam stability. *Langmuir* **2012**, *28*, 7780-7787.
- (9). Brocca, P.; Saponaro, A.; Introini, B.; Rondelli, V.; Pannuzzo, M.; Raciti, D.; Corti, M.; Raudino, A. Protein adsorption at the air–water interface by a charge sensing interferometric technique. *Langmuir* **2019**, *35*, 16087-16100.
- (10). Steckl, A. J. DNA—a new material for photonics? *Nat. Photonics* **2007**, *1*, 3-5.
- (11). Mok, J.; Mindrinos, M. N.; Davis, R. W.; Javanmard, M. Digital microfluidic assay for protein detection. *Proc. Natl. Acad. Sci.* **2014**, *111*, 2110-2115.
- (12). Kaur, H.; Tomar, D.; Kaur, H.; Rana, B.; Chaudhary, S.; Jena, K. C. Sum-Frequency Generation Vibrational Spectroscopy: A Nonlinear Optical Tool to Probe the Polymer Interfaces. In *Advances in Spectroscopy: Molecules to Materials*, Springer, 2019;pp 39-55.
- (13). Franceschetti, G.; Grossi, M. *Homeland security technology challenges: from sensing and encrypting to mining and modeling*. Artech House, 2008.
- (14). Liao, Z.; Lampe, J. W.; Ayyaswamy, P. S.; Eckmann, D. M.; Dmochowski, I. J. Protein assembly at the air–water interface studied by fluorescence microscopy. *Langmuir* **2011**, *27*, 12775-12781.
- (15). Sharafeldin, M.; Davis, J. J. Characterising the biosensing interface. *Anal. Chim. Acta* **2022**, *1216*, 339759.
- (16). Gaudin, T.; Rotureau, P.; Pezron, I.; Fayet, G. Investigating the impact of sugar-based surfactants structure on surface tension at critical micelle concentration with structure-property relationships. *J. Colloid Interface Sci.* **2018**, *516*, 162-171.
- (17). Nakano, K.; Yoshitake, T.; Yamashita, Y.; Bowden, E. F. Cytochrome c self-assembly on alkanethiol monolayer electrodes as characterized by AFM, IR, QCM, and direct electrochemistry. *Langmuir* **2007**, *23*, 6270-6275.
- (18). Müller, D. J.; Dufrene, Y. F. Atomic force microscopy as a multifunctional molecular toolbox in nanobiotechnology. *Nat. Nanotechnol.* **2008**, *3*, 261-269.
- (19). Pajkossy, T.; Jurczakowski, R. Electrochemical impedance spectroscopy in interfacial studies. *Curr. Opin. Electrochem.* **2017**, *1*, 53-58.

- (20). Wu, J.; Zhou, R.; Radjenovic, P. M.; Liu, S.; Wu, D.; Li, J.; Mao, B.; Yan, J. Electrochemical impedance spectroscopy and Raman spectroscopy studies on electrochemical interface between Au (111) electrode and ethaline deep eutectic solvent. *Electrochim. Acta* **2021**, 390, 138859.
- (21). Bakhtiar, R. Surface plasmon resonance spectroscopy: a versatile technique in a biochemist's toolbox. *J. Chem. Educ.* **2013**, 90, 203-209.
- (22). Caballero-Quintana, I.; Romero-Borja, D.; Maldonado, J.-L.; Nicasio-Collazo, J.; Amargós-Reyes, O.; Jiménez-González, A. Interfacial energetic level mapping and nano-ordering of small molecule/fullerene organic solar cells by scanning tunneling microscopy and spectroscopy. *J. Nanomater.* **2020**, 10, 427.
- (23). Castner, D. G.; Ratner, B. D. Biomedical surface science: Foundations to frontiers. *Surf. Sci.* **2002**, 500, 28-60.
- (24). Pasche, S.; De Paul, S. M.; Vörös, J.; Spencer, N. D.; Textor, M. Poly (l-lysine)-g raft-poly (ethylene glycol) assembled monolayers on niobium oxide surfaces: A quantitative study of the influence of polymer interfacial architecture on resistance to protein adsorption by ToF-SIMS and in situ OWLS. *Langmuir* **2003**, 19, 9216-9225.
- (25). Yang, L.; Zhu, Z.; Yu, X. Y.; Rodek, E.; Saraf, L.; Thevuthasan, T.; Cowin, J. P. In situ SEM and ToF-SIMS analysis of IgG conjugated gold nanoparticles at aqueous surfaces. *Surf. Interface Anal.* **2014**, 46, 224-228.
- (26). Jablonski, E. L.; Lenhart, J. L.; Sambasivan, S.; Fischer, D. A.; Jones, R. L.; Lin, E. K.; Wu, W. I.; Goldfarb, D. L.; Temple, K.; Angelopoulos, M. NEXAFS measurements of the surface chemistry of chemically amplified photoresists, *In AIP Conf. Proc.*,
- (27). Lee, C.-Y.; Gamble, L. J.; Grainger, D. W.; Castner, D. G. Mixed DNA/oligo (ethylene glycol) functionalized gold surfaces improve DNA hybridization in complex media. *Biointerphases* **2006**, 1, 82-92.
- (28). Tomar, D.; Chaudhary, S.; Jena, K. C. Self-assembly of l-phenylalanine amino acid: electrostatic induced hindrance of fibril formation. *RSC Adv.* **2019**, 9, 12596-12605.
- (29). Tomar, D.; Kaur, H.; Kaur, H.; Rana, B.; Talegaonkar, K.; Maharana, V.; Jena, K. C. ATR-FTIR Spectroscopy and Its Relevance to Probe the Molecular-Level Interactions Between Amino Acids and Metal-Oxide Nanoparticles at Solid/Aqueous Interface. In *Advances in Spectroscopy: Molecules to Materials*, Singh, D. K.; Das, S.; Materny, A., Eds. Springer, Vol. 236; 2019;pp 3-21.
- (30). Kaur, H.; Rana, B.; Tomar, D.; Kaur, S.; Jena, K. C. Fundamentals of ATR-FTIR Spectroscopy and Its Role for Probing In-Situ Molecular-Level Interactions. In *Modern Techniques of Spectroscopy*, Springer, 2021;pp 3-37.
- (31). Jena, K. C.; Hore, D. K. Water structure at solid surfaces and its implications for biomolecule adsorption. *Phys. Chem. Chem. Phys.* **2010**, 12, 14383-14404.
- (32). Roy, S.; Covert, P. A.; Jarisz, T. A.; Chan, C.; Hore, D. K. Surface–bulk vibrational correlation spectroscopy. *Anal. Chem.* **2016**, 88, 4682-4691.
- (33). Lambert, A. G.; Davies, P. B.; Neivandt, D. J. Implementing the theory of sum frequency generation vibrational spectroscopy: a tutorial review. *Appl. Spectrosc. Rev.* **2005**, 40, 103-145.
- (34). Roy, S.; Covert, P. A.; FitzGerald, W. R.; Hore, D. K. Biomolecular structure at solid–liquid interfaces as revealed by nonlinear optical spectroscopy. *Chem. Rev.* **2014**, 114, 8388-8415.
- (35). Howell, C.; Schmidt, R.; Kurz, V.; Koelsch, P. Sum-frequency-generation spectroscopy of DNA films in air and aqueous environments. *Biointerphases* **2008**, 3, FC47-FC51.

- (36). Dreesen, L.; Sartenaer, Y.; Humbert, C.; Mani, A. A.; Lemaire, J.-J.; Méthivier, C.; Pradier, C.-M.; Thiry, P.; Peremans, A. Sum-frequency generation spectroscopy applied to model biosensors systems. *Thin Solid Films* **2004**, 464, 373-378.
- (37). Fellows, A. P.; Casford, M. T.; Davies, P. B. Orientation analysis of sum frequency generation spectra of di-chain phospholipids: Effect of the second acyl chain. *AIP Adv.* **2021**, 11, 045119.
- (38). Robertson, E. J.; Olivier, G. K.; Qian, M.; Proulx, C.; Zuckermann, R. N.; Richmond, G. L. Assembly and molecular order of two-dimensional peptoid nanosheets through the oil–water interface. *Proc. Natl. Acad. Sci.* **2014**, 111, 13284-13289.
- (39). Lis, D.; Cecchet, F. Unique Vibrational Features as a Direct Probe of Specific Antigen–Antibody Recognition at the Surface of a Solid-Supported Hybrid Lipid Bilayer. *Chem. Phys. Chem.* **2016**, 17, 2645-2649.
- (40). Boeynaems, S.; Alberti, S.; Fawzi, N. L.; Mittag, T.; Polymenidou, M.; Rousseau, F.; Schymkowitz, J.; Shorter, J.; Wolozin, B.; Van Den Bosch, L. Protein phase separation: a new phase in cell biology. *Trends Cell Biol.* **2018**, 28, 420-435.
- (41). Shakya, A.; King, J. T. DNA local-flexibility-dependent assembly of phase-separated liquid droplets. *Biophys. J.* **2018**, 115, 1840-1847.
- (42). Goussous, S.; Fellows, A.; Casford, M.; Davies, P. A time domain study of surfactin penetrating a phospholipid monolayer at the air-water interface investigated using sum frequency generation spectroscopy, infrared reflection absorption spectroscopy, and AFM-nano infrared microscopy. *Biochim. Biophys. Acta. Biomembr.* **2019**, 1861, 1568-1578.
- (43). Prabha, S.; Arya, G.; Chandra, R.; Ahmed, B.; Nimesh, S. Effect of size on biological properties of nanoparticles employed in gene delivery. *Artif. Cells Nanomed. Biotechnol.* **2016**, 44, 83-91.
- (44). Nel, A. E.; Mädler, L.; Velegol, D.; Xia, T.; Hoek, E.; Somasundaran, P.; Klaessig, F.; Castranova, V.; Thompson, M. Understanding biophysicochemical interactions at the nano–bio interface. *Nat. Mater.* **2009**, 8, 543-557.
- (45). Briggs, B. D.; Knecht, M. R. Nanotechnology meets biology: peptide-based methods for the fabrication of functional materials. *J. Phys. Chem. Lett.* **2012**, 3, 405-418.
- (46). Schloss, A. C.; Liu, W.; Williams, D. M.; Kaufman, G.; Hendrickson, H. P.; Rudsteyn, B.; Fu, L.; Wang, H.; Batista, V. S.; Osuji, C. Fabrication of modularly functionalizable microcapsules using protein-based technologies. *ACS Biomater. Sci. Eng.* **2016**, 2, 1856-1861.
- (47). Ball, P. Water as an active constituent in cell biology. *Chem. Rev.* **2008**, 108, 74-108.
- (48). Chandler, D. Interfaces and the driving force of hydrophobic assembly. *Nature* **2005**, 437, 640-647.
- (49). Crick, F.; Anderson, P. W. *What Mad Pursuit: A personal view of scientific discovery*. Purnyang, 1991.
- (50). Wang, Z.; Fu, L.; Ma, G.; Yan, E. C. Broad-Bandwidth Chiral Sum Frequency Generation Spectroscopy for Probing the Kinetics of Proteins at Interfaces. *Langmuir* **2015**, 31, 11384-11398.
- (51). Lautenbach, V.; Hosseinpour, S.; Peukert, W. Isoelectric point of proteins at hydrophobic interfaces. *Front. Chem.* **2021**, 602.
- (52). Meister, K.; Bäumer, A.; Szilvay, G. R.; Paananen, A.; Bakker, H. J. Self-assembly and conformational changes of hydrophobin classes at the air–water interface. *J. Phys. Chem. Lett.* **2016**, 7, 4067-4071.

- (53). Hosseinpour, S.; Roeters, S. J.; Bonn, M.; Peukert, W.; Woutersen, S.; Weidner, T. Structure and dynamics of interfacial peptides and proteins from vibrational sum-frequency generation spectroscopy. *Chem. Rev.* **2020**, *120*, 3420-3465.
- (54). Wang, J.; Buck, S. M.; Chen, Z. The effect of surface coverage on conformation changes of bovine serum albumin molecules at the air–solution interface detected by sum frequency generation vibrational spectroscopy. *Analyst* **2003**, *128*, 773-778.
- (55). Wang, J.; Buck, S. M.; Even, M. A.; Chen, Z. Molecular responses of proteins at different interfacial environments detected by sum frequency generation vibrational spectroscopy. *J. Am. Chem. Soc.* **2002**, *124*, 13302-13305.
- (56). Wang, J.; Buck, S. M.; Chen, Z. Sum frequency generation vibrational spectroscopy studies on protein adsorption. *J. Phys. Chem. B* **2002**, *106*, 11666-11672.
- (57). Li, Y.; Pan, D.; Nashine, V.; Deshmukh, S.; Vig, B.; Chen, Z. Understanding protein-interface interactions of a fusion protein at silicone oil-water interface probed by sum frequency generation vibrational spectroscopy. *J. Pharm. Sci.* **2018**, *107*, 682-689.
- (58). Perera, H. G.; Lu, T.; Fu, L.; Zhang, J.; Chen, Z. Probing the Interfacial Interactions of Monoclonal and Bispecific Antibodies at the Silicone Oil–Aqueous Solution Interface by Using Sum Frequency Generation Vibrational Spectroscopy. *Langmuir* **2019**, *35*, 14339-14347.
- (59). Wang, J.; Paszti, Z.; Even, M. A.; Chen, Z. Interpretation of sum frequency generation vibrational spectra of interfacial proteins by the thin film model. *J. Phys. Chem. B* **2004**, *108*, 3625-3632.
- (60). Kim, J.; Somorjai, G. A. Molecular packing of lysozyme, fibrinogen, and bovine serum albumin on hydrophilic and hydrophobic surfaces studied by infrared– visible sum frequency generation and fluorescence microscopy. *J. Am. Chem. Soc.* **2003**, *125*, 3150-3158.
- (61). Mitropoulos, V.; Mütze, A.; Fischer, P. Mechanical properties of protein adsorption layers at the air/water and oil/water interface: A comparison in light of the thermodynamical stability of proteins. *Adv. Colloid Interface Sci.* **2014**, *206*, 195-206.
- (62). Goussous, S.; Casford, M.; Murphy, A.; Salmond, G.; Leeper, F.; Davies, P. Structure of the fundamental lipopeptide surfactin at the air/water interface investigated by sum frequency generation spectroscopy. *J. Phys. Chem. B* **2017**, *121*, 5072-5077.
- (63). Yang, P.; Boughton, A.; Homan, K. T.; Tesmer, J. J.; Chen, Z. Membrane orientation of Gaiβ1γ2 and Gβ1γ2 determined via combined vibrational spectroscopic studies. *J. Am. Chem. Soc.* **2013**, *135*, 5044-5051.
- (64). Phillips, D. C.; York, R. L.; Mermut, O.; McCrea, K. R.; Ward, R. S.; Somorjai, G. A. Side chain, chain length, and sequence effects on amphiphilic peptide adsorption at hydrophobic and hydrophilic surfaces studied by sum-frequency generation vibrational spectroscopy and quartz crystal microbalance. *J. pHYS. Chem. C* **2007**, *111*, 255-261.
- (65). Xiao, M.; Wei, S.; Li, Y.; Jasensky, J.; Chen, J.; Brooks, C. L.; Chen, Z. Molecular interactions between single layered MoS<sub>2</sub> and biological molecules. *Chem. Sci.* **2018**, *9*, 1769-1773.
- (66). Engelhardt, K.; Lexis, M.; Gochev, G.; Konnerth, C.; Miller, R.; Willenbacher, N.; Peukert, W.; Braunschweig, B. r. pH effects on the molecular structure of β-lactoglobulin modified air–water interfaces and its impact on foam rheology. *Langmuir* **2013**, *29*, 11646-11655.
- (67). Devineau, S.; Inoue, K. I.; Kusaka, R.; Urashima, S. H.; Nihonyanagi, S.; Baigl, D.; Tsuneshige, A.; Tahara, T. Change of the isoelectric point of hemoglobin at the air/water interface probed by the orientational flip-flop of water molecules. *Phys. Chem. Chem. Phys.* **2017**, *19*, 10292-10300.

- (68). Alamdari, S.; Roeters, S. J.; Golbek, T. W.; Schmäser, L.; Weidner, T.; Pfaendtner, J. Orientation and conformation of proteins at the air–water interface determined from integrative molecular dynamics simulations and sum frequency generation spectroscopy. *Langmuir* **2020**, *36*, 11855-11865.
- (69). York, R. L.; Mermut, O.; Phillips, D. C.; McCrea, K. R.; Ward, R. S.; Somorjai, G. A. Influence of ionic strength on the adsorption of a model peptide on hydrophilic silica and hydrophobic polystyrene surfaces: Insight from SFG vibrational spectroscopy. *J. Phys. Chem. C* **2007**, *111*, 8866-8871.
- (70). Li, Y.; Ogorzalek, T. L.; Wei, S.; Zhang, X.; Yang, P.; Jasensky, J.; Brooks, C. L.; Marsh, E. N. G.; Chen, Z. Effect of immobilization site on the orientation and activity of surface-tethered enzymes. *Phys. Chem. Chem. Phys.* **2018**, *20*, 1021-1029.
- (71). Meister, K.; Strazdaite, S.; DeVries, A. L.; Lotze, S.; Olijve, L. L.; Voets, I. K.; Bakker, H. J. Observation of ice-like water layers at an aqueous protein surface. *Proc. Natl. Acad. Sci.* **2014**, *111*, 17732-17736.
- (72). Jung, S.-Y.; Lim, S.-M.; Albertorio, F.; Kim, G.; Gurau, M. C.; Yang, R. D.; Holden, M. A.; Cremer, P. S. The Vroman effect: a molecular level description of fibrinogen displacement. *J. Am. Chem. Soc.* **2003**, *125*, 12782-12786.
- (73). Li, Y.; Shrestha, M.; Luo, M.; Sit, I.; Song, M.; Grassian, V. H.; Xiong, W. Salting up of proteins at the air/water interface. *Langmuir* **2019**, *35*, 13815-13820.
- (74). Bulard, E.; Fontaine-Aupart, M.-P.; Dubost, H.; Zheng, W.; Bellon-Fontaine, M.-N. I.; Herry, J.-M.; Bourguignon, B. Competition of bovine serum albumin adsorption and bacterial adhesion onto surface-grafted ODT: in situ study by vibrational SFG and fluorescence confocal microscopy. *Langmuir* **2012**, *28*, 17001-17010.
- (75). Watson, J. D.; Crick, F. H. Molecular structure of nucleic acids: a structure for deoxyribose nucleic acid. *Nature* **1953**, *171*, 737-738.
- (76). Sartenaer, Y.; Tourillon, G.; Dreesen, L.; Lis, D.; Mani, A. A.; Thiry, P. A.; Peremans, A. Sum-frequency generation spectroscopy of DNA monolayers. *Biosens. Bioelectron.* **2007**, *22*, 2179-2183.
- (77). Howell, C.; Zhao, J.; Koelsch, P.; Zharnikov, M. Hybridization in ssDNA films—a multi-technique spectroscopy study. *Phys. Chem. Chem. Phys.* **2011**, *13*, 15512-15522.
- (78). Asanuma, H.; Noguchi, H.; Uosaki, K.; Yu, H.-Z. Metal cation-induced deformation of DNA self-assembled monolayers on silicon: vibrational sum frequency generation spectroscopy. *J. Am. Chem. Soc.* **2008**, *130*, 8016-8022.
- (79). Walter, S. R.; Young, K. L.; Holland, J. G.; Gieseck, R. L.; Mirkin, C. A.; Geiger, F. M. Counting the number of magnesium ions bound to the surface-immobilized thymine oligonucleotides that comprise spherical nucleic acids. *J. Am. Chem. Soc.* **2013**, *135*, 17339-17348.
- (80). Li, Z.; Weeraman, C. N.; Azam, M. S.; Osman, E.; Gibbs-Davis, J. M. The thermal reorganization of DNA immobilized at the silica/buffer interface: a vibrational sum frequency generation investigation. *Phys. Chem. Chem. Phys.* **2015**, *17*, 12452-12457.
- (81). McDermott, M. L.; Vanselous, H.; Corcelli, S. A.; Petersen, P. B. DNA's chiral spine of hydration. *ACS Cent. Sci.* **2017**, *3*, 708-714.
- (82). Gericke, M.; Schulze, P.; Heinze, T. Nanoparticles based on hydrophobic polysaccharide derivatives—formation principles, characterization techniques, and biomedical applications. *Macromol. Biosci.* **2020**, *20*, 1900415.
- (83). Modena, M. M.; Rühle, B.; Burg, T. P.; Wuttke, S. Nanoparticle characterization: what to measure? *Adv. Mater.* **2019**, *31*, 1901556.
- (84). Wang, C.-y.; Groenzin, H.; Shultz, M. J. Molecular species on nanoparticulate anatase TiO<sub>2</sub> film detected by sum frequency generation: Trace hydrocarbons and hydroxyl groups. *Langmuir* **2003**, *19*, 7330-7334.

- (85). Hosseinpour, S.; Tang, F.; Wang, F.; Livingstone, R. A.; Schlegel, S. J.; Ohto, T.; Bonn, M.; Nagata, Y.; Backus, E. H. Chemisorbed and physisorbed water at the TiO<sub>2</sub>/water interface. *J. Phys. Chem. Lett.* **2017**, *8*, 2195-2199.
- (86). Weeraman, C.; Yatawara, A. K.; Bordenyuk, A. N.; Benderskii, A. V. Effect of nanoscale geometry on molecular conformation: Vibrational sum-frequency generation of alkanethiols on gold nanoparticles. *J. Am. Chem. Soc.* **2006**, *128*, 14244-14245.
- (87). Lu, Z.; Karakoti, A.; Velarde, L.; Wang, W.; Yang, P.; Thevuthasan, S.; Wang, H. F. Dissociative binding of carboxylic acid ligand on nanoceria surface in aqueous solution: a joint in situ spectroscopic characterization and first-principles study. *J. Phys. Chem. C* **2013**, *117*, 24329-24338.
- (88). Watson, B. R.; Ma, Y.-Z.; Cahill, J. F.; Doughty, B.; Calhoun, T. R. Probing ligand removal and ordering at quantum dot surfaces using vibrational sum frequency generation spectroscopy. *J. Colloid Interface Sci.* **2019**, *537*, 389-395.
- (89). Holman, J.; Ye, S.; Neivandt, D. J.; Davies, P. B. Studying nanoparticle-induced structural changes within fatty acid multilayer films using sum frequency generation vibrational spectroscopy. *J. Am. Chem. Soc.* **2004**, *126*, 14322-14323.
- (90). Toledo-Fuentes, X.; Lis, D.; Cecchet, F. Structural changes to lipid bilayers and their surrounding water upon interaction with functionalized gold nanoparticles. *J. Phys. Chem. C* **2016**, *120*, 21399-21409.
- (91). Hu, P.; Qian, W.; Liu, B.; Pichan, C.; Chen, Z. Molecular interactions between gold nanoparticles and model cell membranes: a study of nanoparticle surface charge effect. *J. Phys. Chem. C* **2016**, *120*, 22718-22729.
- (92). Lan, F.; Ma, S.; Yang, Q.; Xie, L.; Wu, Y.; Gu, Z. Polydopamine-based superparamagnetic molecularly imprinted polymer nanospheres for efficient protein recognition. *Colloids Surf. B Biointerfaces* **2014**, *123*, 213-218.
- (93). Sit, I.; Sagisaka, S.; Grassian, V. H. Nucleotide adsorption on iron (III) oxide nanoparticle surfaces: insights into nano-geo-bio interactions through vibrational spectroscopy. *Langmuir* **2020**, *36*, 15501-15513.
- (94). Schneider, T.; Jahr, N.; Jatschka, J.; Csaki, A.; Stranik, O.; Fritzsche, W. Localized surface plasmon resonance (LSPR) study of DNA hybridization at single nanoparticle transducers. *J. Nanopart. Res.* **2013**, *15*, 1-10.
- (95). Laptinskiy, K. A.; Burikov, S. A.; Vervald, A. M.; Dolenko, T. A. Coherent anti-stokes Raman spectroscopy of nanodiamond-lysozyme interactions in water. *Laser Phys.* **2021**, *31*, 065702.
- (96). Shourni, S.; Javadi, A.; Hosseinpour, N.; Bahramian, A.; Raoufi, M. Characterization of protein corona formation on nanoparticles via the analysis of dynamic interfacial properties: Bovine serum albumin-silica particle interaction. *Colloids Surf. A: Physicochem. Eng. Aspects* **2022**, *638*, 128273.
- (97). He, M.; Zhang, W.; Liu, Z.; Zhou, L.; Cai, X.; Li, R.; Pan, Y.; Wang, F. The interfacial interactions of nanomaterials with human serum albumin. *Anal. Bioanal. Chem.* **2022**, *414*, 4677-4684.
- (98). Benbow, N.; Rozenberga, L.; McQuillan, A. J.; Krasowska, M.; Beattie, D. ATR FTIR Study of the Interaction of TiO<sub>2</sub> Nanoparticle Films with  $\beta$ -Lactoglobulin and Bile Salts. *Langmuir* **2021**, *37*, 13278-13290.
- (99). Tourillon, G.; Dreesen, L.; Volcke, C.; Sartenaer, Y.; Thiry, P. A.; Peremans, A. Close-packed array of gold nanoparticles and sum frequency generation spectroscopy in total internal reflection: a platform for studying biomolecules and biosensors. *J. Mater. Sci.* **2009**, *44*, 6805-6810.

- (100). Petit, C. A.; Carbeck, J. D. Combing of molecules in microchannels (COMMIC): a method for micropatterning and orienting stretched molecules of DNA on a surface. *Nano Lett.* **2003**, 3, 1141-1146.
- (101). Douarache, C.; Sikorav, J.-L.; Goldar, A. Aggregation and Adsorption at the Air-Water Interface of Bacteriophage  $\phi$ X174 Single-Stranded DNA. *Biophys. J.* **2008**, 94, 134-146.
- (102). Lee, J.; Kim, Y.; Lim, S.; Jo, K. Single-molecule visualization of ROS-induced DNA damage in large DNA molecules. *Analyst* **2016**, 141, 847-852.
- (103). Pangotra, D.; Csepei, L.-I.; Roth, A.; de León, C. P.; Sieber, V.; Vieira, L. Anodic production of hydrogen peroxide using commercial carbon materials. *Appl. Catal. B Environ.* **2022**, 303, 120848.
- (104). Chen, B.; Xia, Y.; He, R.; Sang, H.; Zhang, W.; Li, J.; Chen, L.; Wang, P.; Guo, S.; Yin, Y. Water–solid contact electrification causes hydrogen peroxide production from hydroxyl radical recombination in sprayed microdroplets. *Proc. Natl. Acad. Sci.* **2022**, 119, e2209056119.
- (105). Ward, J.; Evans, J.; Limoli, C.; Calabro-Jones, P. Radiation and hydrogen peroxide induced free radical damage to DNA. *Br. J. Cancer Suppl.* **1987**, 8, 105-112.
- (106). Zdorevskyi, O.; Volkov, S. N. The possibility of blocking the process of DNA base pairs opening by hydrogen peroxide. *Ukr. J. Phys.* **2019**, 64, 500-508.
- (107). Boyd, R. W. *Nonlinear optics*. Fourth ed.; Academic press, 2020.
- (108). He, G.; Liu, S. H. *Physics of nonlinear optics*. World Scientific, 1999.
- (109). Pickering, J. D.; Bregnhøj, M.; Chatterley, A. S.; Rasmussen, M. H.; Strunge, K.; Weidner, T. Tutorials in vibrational sum frequency generation spectroscopy. I. The foundations. *Biointerphases* **2022**, 17, 011201.
- (110). Gan, W.; Wu, D.; Zhang, Z.; Feng, R. R.; Wang, H. F. Polarization and experimental configuration analyses of sum frequency generation vibrational spectra, structure, and orientational motion of the air/water interface. *J. Chem. Phys.* **2006**, 124, 114705.
- (111). Wang, H. F.; Gan, W.; Lu, R.; Rao, Y.; Wu, B. H. Quantitative spectral and orientational analysis in surface sum frequency generation vibrational spectroscopy (SFG-VS). *Int. Rev. Phys. Chem.* **2005**, 24, 191-256.
- (112). Tyrode, E.; Johnson, C. M.; Baldelli, S.; Leygraf, C.; Rutland, M. W. A vibrational sum frequency spectroscopy study of the liquid– gas interface of acetic acid– water mixtures: 2. Orientation analysis. *J. Phys. Chem. B* **2005**, 109, 329-341.
- (113). Hong, Y.; Zhou, H.; Qian, W.; Zuo, B.; Wang, X. Impact of the  $\alpha$ -Methyl Group ( $\alpha$ -CH<sub>3</sub>) on the Aggregation States and Interfacial Isotherms of Poly (acrylates) Monolayers at the Water Surface. *J. Phys. Chem. C* **2017**, 121, 19816-19827.
- (114). Mudunkotuwa, I. A.; Al Minshid, A.; Grassian, V. H. ATR-FTIR spectroscopy as a tool to probe surface adsorption on nanoparticles at the liquid–solid interface in environmentally and biologically relevant media. *Analyst* **2014**, 139, 870-881.
- (115). Hind, A. R.; Bhargava, S. K.; McKinnon, A. At the solid/liquid interface: FTIR/ATR—the tool of choice. *Adv. Colloid Interface Sci.* **2001**, 93, 91-114.
- (116). Barth, A. Infrared spectroscopy of proteins. *Biochim. Biophys. Acta. Bioenerg.* **2007**, 1767, 1073-1101.
- (117). Perez-Guaita, D.; Richardson, Z.; Heraud, P.; Wood, B. Quantification and identification of microproteinuria using ultrafiltration and ATR-FTIR spectroscopy. *Anal. Chem.* **2020**, 92, 2409-2416.
- (118). Milosevic, M. *Internal reflection and ATR spectroscopy*. First ed.; John Wiley & Sons, Inc., Hoboken, NJ, 2012.

- (119). Griffiths, P. R. Fourier transform infrared spectrometry. *Science* **1983**, 222, 297-302.
- (120). Yang, H.; Yang, S.; Kong, J.; Dong, A.; Yu, S. Obtaining information about protein secondary structures in aqueous solution using Fourier transform IR spectroscopy. *Nat. Protoc.* **2015**, 10, 382-396.
- (121). Chattoraj, D. *Adsorption and the Gibbs surface excess*. Springer Science & Business Media, 2012.
- (122). Rosen, M. J.; Kunjappu, J. T. *Surfactants and interfacial phenomena*. Fourth ed.; John Wiley & Sons, 2012.
- (123). Hua, X.; Frechette, J.; Bevan, M. A. Nanoparticle adsorption dynamics at fluid interfaces. *Soft Matter* **2018**, 14, 3818-3828.
- (124). Rao, Y.; Li, X.; Lei, X.; Jockusch, S.; George, M. W.; Turro, N. J.; Eiseenthal, K. B. Observations of interfacial population and organization of surfactants with sum frequency generation and surface tension. *J. Phys. Chem. C* **2011**, 115, 12064-12067.
- (125). Shahir, A. A.; Nguyen, K. T.; Nguyen, A. V. A sum-frequency generation spectroscopic study of the Gibbs analysis paradox: monolayer or sub-monolayer adsorption? *Phys. Chem. Phys. Chem.* **2016**, 18, 8794-8805.
- (126). Lowry, G. V.; Hill, R. J.; Harper, S.; Rawle, A. F.; Hendren, C. O.; Klaessig, F.; Nobbmann, U.; Sayre, P.; Rumble, J. Guidance to improve the scientific value of zeta-potential measurements in nanoEHS. *Environ. Sci.: Nano* **2016**, 3, 953-965.
- (127). Yang, F.; Wu, W.; Chen, S.; Gan, W. The ionic strength dependent zeta potential at the surface of hexadecane droplets in water and the corresponding interfacial adsorption of surfactants. *Soft Matter* **2017**, 13, 638-646.
- (128). Sharma, V.; Chotia, C.; Ganesan, V.; Okram, G. S. Influence of particle size and dielectric environment on the dispersion behaviour and surface plasmon in nickel nanoparticles. *Phys. Chem. Phys. Chem.* **2017**, 19, 14096-14106.
- (129). Chaudhary, S.; Kaur, H.; Kaur, H.; Rana, B.; Tomar, D.; Jena, K. C. Probing the Bovine Hemoglobin Adsorption Process and its Influence on Interfacial Water Structure at the Air–Water Interface. *Appl. Spectrosc.* **2021**, 75, 1497-1509.
- (130). Tzannis, S. T.; Hrushesky, W. J.; Wood, P. A.; Przybycien, T. M. Adsorption of a formulated protein on a drug delivery device surface. *J. Colloid Interface Sci.* **1997**, 189, 216-228.
- (131). Banerjee, I.; Pangule, R. C.; Kane, R. S. Antifouling coatings: recent developments in the design of surfaces that prevent fouling by proteins, bacteria, and marine organisms. *Adv. Mater.* **2011**, 23, 690-718.
- (132). Jesionowski, T.; Zdarta, J.; Krajewska, B. Enzyme immobilization by adsorption: A review. *Adsorption* **2014**, 20, 801-821.
- (133). Engelhardt, K.; Peukert, W.; Braunschweig, B. Vibrational sum-frequency generation at protein modified air–water interfaces: Effects of molecular structure and surface charging. *Curr. Opin. Colloid Interface Sci.* **2014**, 19, 207-215.
- (134). Bellissent-Funel, M.-C.; Hassanali, A.; Havenith, M.; Henchman, R.; Pohl, P.; Sterpone, F.; Van Der Spoel, D.; Xu, Y.; Garcia, A. E. Water determines the structure and dynamics of proteins. *Chem. Rev.* **2016**, 116, 7673-7697.
- (135). van Oss, C. J.; Giese, R. F.; Docoslis, A. Hyperhydrophobicity of the water-air interface. *J. Dispersion Sci. Technol.* **2005**, 26, 585-590.
- (136). Yano, Y. F. Kinetics of protein unfolding at interfaces. *J. Phys.: Condens. Matter* **2012**, 24, 503101.
- (137). Chaplin, M. Do we underestimate the importance of water in cell biology? *Nat. Rev. Mol. Cell Biol.* **2006**, 7, 861-866.



- (138). Bulone, D.; San Biagio, P.; Palma-Vittorelli, M.; Palma, M. The role of water in hemoglobin function and stability. *Science* **1993**, *259*, 1335-1336.
- (139). Levy, Y.; Onuchic, J. N. Water mediation in protein folding and molecular recognition. *Annu. Rev. Biophys. Biomol. Struct.* **2006**, *35*, 389-415.
- (140). Chen, S.; Li, L.; Zhao, C.; Zheng, J. Surface hydration: Principles and applications toward low-fouling/nonfouling biomaterials. *Polymer* **2010**, *51*, 5283-5293.
- (141). Ahmad, M.; Gu, W.; Geyer, T.; Helms, V. Adhesive water networks facilitate binding of protein interfaces. *Nat. Commun.* **2011**, *2*, 1-7.
- (142). Wei, Q.; Becherer, T.; Angioletti-Uberti, S.; Dzubiella, J.; Wischke, C.; Neffe, A. T.; Lendlein, A.; Ballauff, M.; Haag, R. Protein interactions with polymer coatings and biomaterials. *Angew. Chem. Int. Ed.* **2014**, *53*, 8004-8031.
- (143). Petralli-Mallow, T.; Plant, A. L.; Lewis, M.; Hicks, J. Cytochrome c at model membrane surfaces: exploration via second harmonic generation-circular dichroism and surface-enhanced resonance raman spectroscopy. *Langmuir* **2000**, *16*, 5960-5966.
- (144). Goobes, G.; Stayton, P. S.; Drobny, G. P. Solid state NMR studies of molecular recognition at protein-mineral interfaces. *Prog. Nucl. Magn. Reson. Spectrosc.* **2007**, *50*, 71.
- (145). Shang, L.; Wang, Y.; Jiang, J.; Dong, S. pH-dependent protein conformational changes in albumin: gold nanoparticle bioconjugates: a spectroscopic study. *Langmuir* **2007**, *23*, 2714-2721.
- (146). Engelhardt, K.; Weichsel, U.; Kraft, E.; Segets, D.; Peukert, W.; Braunschweig, B. r. Mixed layers of  $\beta$ -lactoglobulin and SDS at air-water interfaces with tunable intermolecular interactions. *J. Phys. Chem. B* **2014**, *118*, 4098-4105.
- (147). Russev, S. C.; Arguirov, T. V.; Gurkov, T. D.  $\beta$ -Casein adsorption kinetics on air-water and oil-water interfaces studied by ellipsometry. *Colloids Surf. B Biointerfaces* **2000**, *19*, 89-100.
- (148). Kim, J.; Cremer, P. S. IR-visible SFG investigations of interfacial water structure upon polyelectrolyte adsorption at the solid/liquid interface. *J. Am. Chem. Soc.* **2000**, *122*, 12371-12372.
- (149). Scatena, L.; Brown, M.; Richmond, G. Water at hydrophobic surfaces: weak hydrogen bonding and strong orientation effects. *Science* **2001**, *292*, 908-912.
- (150). Raymond, E. A.; Richmond, G. L. Probing the molecular structure and bonding of the surface of aqueous salt solutions. *J. Phys. Chem. B* **2004**, *108*, 5051-5059.
- (151). Walker, D. S.; Hore, D. K.; Richmond, G. L. Understanding the population, coordination, and orientation of water species contributing to the nonlinear optical spectroscopy of the vapor-water interface through molecular dynamics simulations. *J. Phys. Chem. B* **2006**, *110*, 20451-20459.
- (152). Sovago, M.; Campen, R. K.; Wurfel, G. W.; Müller, M.; Bakker, H. J.; Bonn, M. Vibrational response of hydrogen-bonded interfacial water is dominated by intramolecular coupling. *Phys. Rev. Lett.* **2008**, *100*, 173901.
- (153). Nagata, Y.; Mukamel, S. Vibrational sum-frequency generation spectroscopy at the water/lipid interface: molecular dynamics simulation study. *J. Am. Chem. Soc.* **2010**, *132*, 6434-6442.
- (154). Chen, X.; Hua, W.; Huang, Z.; Allen, H. C. Interfacial water structure associated with phospholipid membranes studied by phase-sensitive vibrational sum frequency generation spectroscopy. *J. Am. Chem. Soc.* **2010**, *132*, 11336-11342.
- (155). Mondal, J. A.; Nihonyanagi, S.; Yamaguchi, S.; Tahara, T. Structure and orientation of water at charged lipid monolayer/water interfaces probed by heterodyne-detected vibrational sum frequency generation spectroscopy. *J. Am. Chem. Soc.* **2010**, *132*, 10656-10657.

- (156). Ahmed, M.; Namboodiri, V.; Singh, A. K.; Mondal, J. A. On the intermolecular vibrational coupling, hydrogen bonding, and librational freedom of water in the hydration shell of mono- and bivalent anions. *J. Chem. Phys.* **2014**, *141*, 164708.
- (157). Strazdaite, S.; Versluis, J.; Backus, E. H.; Bakker, H. J. Enhanced ordering of water at hydrophobic surfaces. *J. Chem. Phys.* **2014**, *140*, 054711.
- (158). Hommel, E. L.; Allen, H. C. 1-methyl naphthalene reorientation at the air–liquid interface upon water saturation studied by vibrational broad bandwidth sum frequency generation spectroscopy. *J. Phys. Chem. B* **2003**, *107*, 10823-10828.
- (159). Hommel, E. L.; Allen, H. C. The air–liquid interface of benzene, toluene, m-xylene, and mesitylene: a sum frequency, Raman, and infrared spectroscopic study. *Analyst* **2003**, *128*, 750-755.
- (160). Lu, X.; Spanninga, S. A.; Kristalyn, C. B.; Chen, Z. Surface orientation of phenyl groups in poly (sodium 4-styrenesulfonate) and in poly (sodium 4-styrenesulfonate): poly (3, 4-ethylenedioxythiophene) mixture examined by sum frequency generation vibrational spectroscopy. *Langmuir* **2010**, *26*, 14231-14235.
- (161). Fu, L.; Xiao, D.; Wang, Z.; Batista, V. S.; Yan, E. C. Chiral sum frequency generation for in situ probing proton exchange in antiparallel  $\beta$ -sheets at interfaces. *J. Am. Chem. Soc.* **2013**, *135*, 3592-3598.
- (162). Meister, K.; Paananen, A.; Bakker, H. Identification of the response of protein N–H vibrations in vibrational sum-frequency generation spectroscopy of aqueous protein films. *Phys. Chem. Phys. Chem.* **2017**, *19*, 10804-10807.
- (163). Lu, J. Neutron reflection study of globular protein adsorption at planar interfaces. *Annu. Rep. Prog. Chem. Sect. C* **1999**, *95*, 3-46.
- (164). Holt, S. A.; McGillivray, D. J.; Poon, S.; White, J. W. Protein deformation and surfactancy at an interface. *J. Phys. Chem. B* **2000**, *104*, 7431-7438.
- (165). Santos, J. H.; Matsuda, N.; Qi, Z.-m.; Yoshida, T.; Takatsu, A.; Kato, K. Adsorption behavior of cytochrome c, myoglobin and hemoglobin in a quartz surface probed using slab optical waveguide (SOWG) spectroscopy. *Anal. Sci.* **2003**, *19*, 199-204.
- (166). Lu, J.; Su, T.; Thomas, R. Structural conformation of bovine serum albumin layers at the air–water interface studied by neutron reflection. *J. Colloid Interface Sci.* **1999**, *213*, 426-437.
- (167). Lu, J.; Su, T.; Penfold, J. Adsorption of serum albumins at the air/water interface. *Langmuir* **1999**, *15*, 6975-6983.
- (168). Saha, A.; Upadhyaya, H. P.; Kumar, A.; Choudhury, S.; Naik, P. D. Sum-Frequency Generation Spectroscopy of an Adsorbed Monolayer of Mixed Surfactants at an Air–Water Interface. *J. Phys. Chem. C* **2014**, *118*, 3145-3155.
- (169). Longeville, S.; Stingaciu, L.-R. Hemoglobin diffusion and the dynamics of oxygen capture by red blood cells. *Sci. Rep.* **2017**, *7*, 1-10.
- (170). Urahata, S.; Canuto, S. Monte Carlo study of the temperature dependence of the hydrophobic hydration of benzene. *J. Chem. Phys. Lett.* **1999**, *313*, 235-240.
- (171). Wood, B. R. The importance of hydration and DNA conformation in interpreting infrared spectra of cells and tissues. *Chem. Soc. Rev.* **2016**, *45*, 1980-1998.
- (172). Domínguez, C. M.; Ramos, D.; Mendieta-Moreno, J. I.; Fierro, J. L.; Mendieta, J.; Tamayo, J.; Calleja, M. Effect of water-DNA interactions on elastic properties of DNA self-assembled monolayers. *Sci. Rep.* **2017**, *7*, 1-8.
- (173). Frommer, M.; Miller, I. Adsorption of DNA at the air-water interface. *J. Phys. Chem.* **1968**, *72*, 2862-2866.
- (174). Eickbush, T. H.; Moudrianakis, E. N. A mechanism for the entrapment of DNA at an air-water interface. *Biophys. J.* **1977**, *18*, 275-288.

- (175). Chatteraj, D.; Mitra, A. Adsorption of DNA at solid–water interfaces and DNA–surfactant binding interaction in aqueous media. *Curr. Sci.* **2009**, 1430-1438.
- (176). Sastry, M.; Ramakrishnan, V.; Pattarkine, M.; Gole, A.; Ganesh, K. Hybridization of DNA by sequential immobilization of oligonucleotides at the air– water interface. *Langmuir* **2000**, 16, 9142-9146.
- (177). Shimomura, M.; Nakamura, F.; Ijio, K.; Taketsuna, H.; Tanaka, M.; Nakamura, H.; Hasebe, K. Two-Dimensional DNA-Mimetic Molecular Organizations at the Air–Water Interface. *J. Am. Chem. Soc.* **1997**, 119, 2341-2342.
- (178). Douarche, C.; Cortès, R.; Henry de Villeneuve, C.; Roser, S.; Braslau, A. DNA adsorption at functionalized Si/buffer interfaces studied by x-ray reflectivity. *J. Chem. Phys.* **2008**, 128, 06B610.
- (179). Gough, D.; Cotter, T. Hydrogen peroxide: a Jekyll and Hyde signalling molecule. *Cell Death Dis.* **2011**, 2, e213-e213.
- (180). Volkov, S. N. On possible role of hydrogen peroxide molecules in ion beam therapy of cancer cells. *J. Low Temp. Phys.* **2021**, 47, 214-219.
- (181). Kreipl, M. S.; Friedland, W.; Paretzke, H. G. Time-and space-resolved Monte Carlo study of water radiolysis for photon, electron and ion irradiation. *Radiat. Environ. Biophys.* **2009**, 48, 11-20.
- (182). Perepelytsya, S.; Uličný, J.; Volkov, S. N. Molecular dynamics study of the competitive binding of hydrogen peroxide and water molecules with DNA phosphate groups. *Eur. Biophys. J.* **2021**, 50, 759-770.
- (183). Kobierski, J.; Lipiec, E. DNA structure change induced by guanosine radicals–A theoretical and spectroscopic study of proton radiation damage. *J. Mol. Struct.* **2019**, 1178, 162-168.
- (184). Lee, J. K.; Han, H. S.; Chaikasetsin, S.; Marron, D. P.; Waymouth, R. M.; Prinz, F. B.; Zare, R. N. Condensing water vapor to droplets generates hydrogen peroxide. *Proc. Natl. Acad. Sci.* **2020**, 117, 30934-30941.
- (185). Perets, E. A.; Olesen, K. B.; Yan, E. C. Chiral Sum Frequency Generation Spectroscopy Detects Double-Helix DNA at Interfaces. *Langmuir* **2022**.
- (186). Schoen, A.; Cooks, R.; Wiebers, J. Modified bases characterized in intact DNA by mass-analyzed ion kinetic energy spectrometry. *Science* **1979**, 203, 1249-1251.
- (187). Chen, X.; Clarke, M. L.; Wang, J.; Chen, Z. Sum frequency generation vibrational spectroscopy studies on molecular conformation and orientation of biological molecules at interfaces. *Int. J. Mod. Phys. B* **2005**, 19, 691-713.
- (188). Wren, S. N.; Gordon, B. P.; Valley, N. A.; McWilliams, L. E.; Richmond, G. L. Hydration, orientation, and conformation of methylglyoxal at the air–water interface. *J. Phys. Chem. A* **2015**, 119, 6391-6403.
- (189). Tyrode, E.; Johnson, C. M.; Kumpulainen, A.; Rutland, M. W.; Claesson, P. M. Hydration state of nonionic surfactant monolayers at the liquid/vapor interface: Structure determination by vibrational sum frequency spectroscopy. *J. Am. Chem. Soc.* **2005**, 127, 16848-16859.
- (190). Johnson, C. M.; Baldelli, S. Vibrational sum frequency spectroscopy studies of the influence of solutes and phospholipids at vapor/water interfaces relevant to biological and environmental systems. *Chem. Rev.* **2014**, 114, 8416-8446.
- (191). Lavignac, N.; Allender, C. J.; Brain, K. R. Current status of molecularly imprinted polymers as alternatives to antibodies in sorbent assays. *Anal. Chim. Acta* **2004**, 510, 139-145.
- (192). Li, L.; Yang, L.; Xing, Z.; Lu, X.; Kan, X. Surface molecularly imprinted polymers-based electrochemical sensor for bovine hemoglobin recognition. *Analyst* **2013**, 138, 6962-6968.

- (193). Kalecki, J.; Iskierko, Z.; Cieplak, M.; Sharma, P. S. Oriented immobilization of protein templates: a new trend in surface imprinting. *ACS Sens.* **2020**, *5*, 3710-3720.
- (194). Schirhagl, R. Bioapplications for molecularly imprinted polymers. *Anal. Chem.* **2014**, *86*, 250-261.
- (195). Obiles, R.; Premadasa, U. I.; Cudia, P.; Erasquin, U. J.; Berger, J. M.; Martinez, I. S.; Cimatu, K. L. A. Insights on the Molecular Characteristics of Molecularly Imprinted Polymers as Monitored by Sum Frequency Generation Spectroscopy. *Langmuir* **2019**, *36*, 180-193.
- (196). Xu, J.; Ambrosini, S.; Tamahkar, E.; Rossi, C.; Haupt, K.; Tse Sum Bui, B. Toward a universal method for preparing molecularly imprinted polymer nanoparticles with antibody-like affinity for proteins. *Biomacromol.* **2016**, *17*, 345-353.
- (197). Dabrowski, M.; Lach, P.; Cieplak, M.; Kutner, W. Nanostructured molecularly imprinted polymers for protein chemosensing. *Biosens. Bioelectron.* **2018**, *102*, 17-26.
- (198). Lee, H.; Dellatore, S. M.; Miller, W. M.; Messersmith, P. B. Mussel-inspired surface chemistry for multifunctional coatings. *Science* **2007**, *318*, 426-430.
- (199). Pop-Georgievski, O.; Verreault, D.; Diesner, M.-O.; Proks, V.; Heissler, S.; Rypáček, F. e.; Koelsch, P. Nonfouling poly (ethylene oxide) layers end-tethered to polydopamine. *Langmuir* **2012**, *28*, 14273-14283.
- (200). Zangmeister, R. A.; Morris, T. A.; Tarlov, M. J. Characterization of polydopamine thin films deposited at short times by autoxidation of dopamine. *Langmuir* **2013**, *29*, 8619-8628.
- (201). Salomäki, M.; Marttila, L.; Kivelä, H.; Ouvinen, T.; Lukkari, J. Effects of pH and oxidants on the first steps of polydopamine formation: a thermodynamic approach. *J. Phys. Chem. B* **2018**, *122*, 6314-6327.
- (202). Liu, Y.; Ai, K.; Lu, L. Polydopamine and its derivative materials: synthesis and promising applications in energy, environmental, and biomedical fields. *Chem. Rev.* **2014**, *114*, 5057-5115.
- (203). Della Vecchia, N. F.; Luchini, A.; Napolitano, A.; D'Errico, G.; Vitiello, G.; Szekely, N.; d'Ischia, M.; Paduano, L. Tris buffer modulates polydopamine growth, aggregation, and paramagnetic properties. *Langmuir* **2014**, *30*, 9811-9818.
- (204). Ding, Y.; Weng, L.-T.; Yang, M.; Yang, Z.; Lu, X.; Huang, N.; Leng, Y. Insights into the aggregation/deposition and structure of a polydopamine film. *Langmuir* **2014**, *30*, 12258-12269.
- (205). Liebscher, J. r.; Mrówczyński, R.; Scheidt, H. A.; Filip, C.; Hädäde, N. D.; Turcu, R.; Bende, A.; Beck, S. Structure of polydopamine: a never-ending story? *Langmuir* **2013**, *29*, 10539-10548.
- (206). Barclay, T. G.; Hegab, H. M.; Clarke, S. R.; Ginic-Markovic, M. Versatile surface modification using polydopamine and related polycatecholamines: Chemistry, structure, and applications. *Adv. Mater. Interfaces* **2017**, *4*, 1601192.
- (207). Umek, N.; Geršak, B.; Vintar, N.; Šoštarič, M.; Mavri, J. Dopamine autoxidation is controlled by acidic pH. *Front. Mol. Neurosci.* **2018**, *11*, 467.
- (208). Umek, N. Cyclization step of noradrenaline and adrenaline autoxidation: a quantum chemical study. *RSC Adv.* **2020**, *10*, 16650-16658.
- (209). Ponzio, F.; Ball, V. Persistence of dopamine and small oxidation products thereof in oxygenated dopamine solutions and in "polydopamine" films. *Colloids Surf. A: Physicochem. Eng. Aspects* **2014**, *443*, 540-543.
- (210). Xu, M.; Liu, D.; Allen, H. C. Ethylenediamine at air/liquid and air/silica interfaces: protonation versus hydrogen bonding investigated by sum frequency generation spectroscopy. *J. Environ. Sci. Technol.* **2006**, *40*, 1566-1572.

- (211). Lu, X.; Zhang, C.; Ulrich, N.; Xiao, M.; Ma, Y.-H.; Chen, Z. Studying polymer surfaces and interfaces with sum frequency generation vibrational spectroscopy. *Anal. Chem.* **2017**, *89*, 466-489.
- (212). Bernsmann, F.; Frisch, B.; Ringwald, C.; Ball, V. Protein adsorption on dopamine–melanin films: Role of electrostatic interactions inferred from  $\zeta$ -potential measurements versus chemisorption. *J. Colloid Interface Sci.* **2010**, *344*, 54-60.
- (213). Luo, R.; Tang, L.; Wang, J.; Zhao, Y.; Tu, Q.; Weng, Y.; Shen, R.; Huang, N. Improved immobilization of biomolecules to quinone-rich polydopamine for efficient surface functionalization. *Colloids Surf. B Biointerfaces* **2013**, *106*, 66-73.
- (214). Almeida, L. C.; Frade, T.; Correia, R. D.; Niu, Y.; Jin, G.; Correia, J. P.; Viana, A. S. Electrosynthesis of polydopamine-ethanolamine films for the development of immunosensing interfaces. *Sci. Rep.* **2021**, *11*, 1-12.
- (215). Zhou, W.-H.; Lu, C.-H.; Guo, X.-C.; Chen, F.-R.; Yang, H.-H.; Wang, X.-R. Mussel-inspired molecularly imprinted polymer coating superparamagnetic nanoparticles for protein recognition. *J. Mater. Chem.* **2010**, *20*, 880-883.
- (216). Lamaoui, A.; Palacios-Santander, J. M.; Amine, A.; Cubillana-Aguilera, L. Molecularly imprinted polymers based on polydopamine: Assessment of non-specific adsorption. *Microchem. J.* **2021**, *164*, 106043.
- (217). Su, L.; Yu, Y.; Zhao, Y.; Liang, F.; Zhang, X. Strong antibacterial polydopamine coatings prepared by a shaking-assisted method. *Sci. Rep.* **2016**, *6*, 1-8.
- (218). Ball, V.; Del Frari, D.; Toniazzo, V.; Ruch, D. Kinetics of polydopamine film deposition as a function of pH and dopamine concentration: Insights in the polydopamine deposition mechanism. *J. Colloid Interface Sci.* **2012**, *386*, 366-372.
- (219). Schindler, S.; Aguiló-Aguayo, N.; Dornbierer, U.; Bechtold, T. Anodic Coating of 1.4622 Stainless Steel with Polydopamine by Repetitive Cyclic Voltammetry and Galvanostatic Deposition. *Ind. Eng. Chem. Res.* **2019**, *59*, 236-244.
- (220). Ouyang, R.; Lei, J.; Ju, H. Artificial receptor-functionalized nanoshell: facile preparation, fast separation and specific protein recognition. *Nanotechnology* **2010**, *21*, 185502.
- (221). Lim, C.; Huang, J.; Kim, S.; Lee, H.; Zeng, H.; Hwang, D. S. Nanomechanics of poly (catecholamine) coatings in aqueous solutions. *Angew. Chem. Int. Ed.* **2016**, *55*, 3342-3346.
- (222). Saiz Poseu, J.; Mancebo Aracil, J.; Nador, F. G.; Busque, F.; Ruiz Molina, D. The Chemistry behind Catechol-Based Adhesion. *Angew. Chem. Int. Ed.* **2018**, *58*, 696-714.
- (223). Lu, R.; Gan, W.; Wu, B. H.; Chen, H.; Wang, H. F. Vibrational polarization spectroscopy of CH stretching modes of the methylene group at the vapor/liquid interfaces with sum frequency generation. *J. Phys. Chem. B* **2004**, *108*, 7297-7306.
- (224). McWilliams, L. E.; Valley, N. A.; Wren, S. N.; Richmond, G. L. A means to an interface: investigating monoethanolamine behavior at an aqueous surface. *Phys. Chem. Chem. Phys.* **2015**, *17*, 21458-21469.
- (225). Reva, I.; Stepanian, S.; Plokhotnichenko, A.; Radchenko, E.; Sheina, G.; Blagoi, Y. P. Infrared matrix isolation studies of amino acids. Molecular structure of proline. *J. Mol. Struct.* **1994**, *318*, 1-13.
- (226). Holinga, G. J.; York, R. L.; Onorato, R. M.; Thompson, C. M.; Webb, N. E.; Yoon, A. P.; Somorjai, G. A. An SFG study of interfacial amino acids at the hydrophilic SiO<sub>2</sub> and hydrophobic deuterated polystyrene surfaces. *J. Am. Chem. Soc.* **2011**, *133*, 6243-6253.
- (227). Weidner, T.; Castner, D. G. SFG analysis of surface bound proteins: a route towards structure determination. *Phys. Chem. Chem. Phys.* **2013**, *15*, 12516-12524.

- (228). Tian, K.; Ye, S. Fermi Resonant Interaction of the Tailed Methyl Groups of Langmuir Monolayer at the Air/Water Interface during Phase Transition. *J. Phys. Chem. C* **2015**, 119, 25394-25400.
- (229). Ge, A.; Seo, J.-H.; Qiao, L.; Yui, N.; Ye, S. Structural reorganization and fibrinogen adsorption behaviors on the polyrotaxane surfaces investigated by sum frequency generation spectroscopy. *ACS Appl. Mater. Interfaces* **2015**, 7, 22709-22718.
- (230). Liu, W.; Fu, L.; Wang, Z.; Sohrabpour, Z.; Li, X.; Liu, Y.; Wang, H.-f.; Yan, E. C. Two dimensional crowding effects on protein folding at interfaces observed by chiral vibrational sum frequency generation spectroscopy. *Phys. Chem. Phys. Chem.* **2018**, 20, 22421-22426.
- (231). Tian, K.; Zhang, B.; Ye, S.; Luo, Y. Intermolecular interactions at the interface quantified by surface-sensitive second-order Fermi resonant signals. *J. Phys. Chem. C* **2015**, 119, 16587-16595.
- (232). Premadasa, U. I.; Adhikari, N. M.; Cimat, K. L. A. Molecular Insights into the Role of Electronic Substituents on the Chemical Environment of the  $\text{-CH}_3$  and  $\text{>C=O}$  Groups of Neat Liquid Monomers Using Sum Frequency Generation Spectroscopy. *J. Phys. Chem. C* **2019**, 123, 28201-28209.
- (233). Liu, Z.; Liu, M.; Liu, Y.; Zhang, C.; Wang, X.; Ma, L.; Cai, H.; Cheng, Q. Molecular arrangement mechanisms within phosphate films on Ti6Al4V regulated by intermolecular forces based on sum frequency generation vibrational spectroscopy. *Appl. Surf. Sci.* **2020**, 521, 146364.
- (234). Liu, Z.; Li, P.; Bian, W.; Yu, J.; Zhan, J. Revealing the role of oxidation state in interaction between nitro/amino-derived particulate matter and blood proteins. *Sci. Rep.* **2016**, 6, 1-9.
- (235). Punia, K.; Kronenberg, J. B.; Montclare, J. K. Protein biomaterials for theranostic applications. *Mol. Syst. Des. Eng.* **2019**, 4, 1074-1094.
- (236). Morris, J. H.; Knudsen, G. M.; Verschueren, E.; Johnson, J. R.; Cimermanic, P.; Greninger, A. L.; Pico, A. R. Affinity purification–mass spectrometry and network analysis to understand protein-protein interactions. *Nat. Protoc.* **2014**, 9, 2539-2554.
- (237). Jönsson, U.; Fågerstam, L.; Ivarsson, B.; Johnsson, B.; Karlsson, R.; Lundh, K.; Löfås, S.; Persson, B.; Roos, H.; Rönnberg, I. Real-time biospecific interaction analysis using surface plasmon resonance and a sensor chip technology. *Biotechniques* **1991**, 11, 620-627.
- (238). Martial, B.; Lefèvre, T.; Buffeteau, T.; Auger, M. Vibrational circular dichroism reveals supramolecular chirality inversion of  $\alpha$ -synuclein peptide assemblies upon interactions with anionic membranes. *ACS Nano* **2019**, 13, 3232-3242.
- (239). Park, S.-H.; Ko, W.; Lee, H. S.; Shin, I. Analysis of protein–protein interaction in a single live cell by using a FRET system based on genetic code expansion technology. *J. Am. Chem. Soc.* **2019**, 141, 4273-4281.
- (240). Wongkaew, N.; Simsek, M.; Griesche, C.; Bäumner, A. J. Functional nanomaterials and nanostructures enhancing electrochemical biosensors and lab-on-a-chip performances: recent progress, applications, and future perspective. *Chem. Rev.* **2018**, 119, 120-194.
- (241). Mogaki, R.; Okuro, K.; Ueki, R.; Sando, S.; Aida, T. Molecular Glue that Spatiotemporally Turns on Protein–Protein Interactions. *J. Am. Chem. Soc.* **2019**, 141, 8035-8040.
- (242). Qin, J.; Li, X.; Cao, L.; Du, S.; Wang, W.; Yao, S. Q. Competition-based universal photonic crystal biosensors by using antibody–antigen interaction. *J. Am. Chem. Soc.* **2019**, 142, 417-423.

- (243). Parlak, O.; Seshadri, P.; Lundström, I.; Turner, A. P.; Tiwari, A. Two-Dimensional Gold-Tungsten Disulphide Bio-Interface for High-Throughput Electrocatalytic Nano-Bioreactors. *Adv. Mater. Interfaces* **2014**, *1*, 1400136.
- (244). Ouyang, Q.; Zeng, S.; Jiang, L.; Hong, L.; Xu, G.; Dinh, X.-Q.; Qian, J.; He, S.; Qu, J.; Coquet, P. Sensitivity enhancement of transition metal dichalcogenides/silicon nanostructure-based surface plasmon resonance biosensor. *Sci. Rep.* **2016**, *6*, 1-13.
- (245). Batool, S.; Idrees, M.; Javed, M. S.; Saleem, M.; Kong, J. Engaging tailored capacity of layered WS<sub>2</sub> via sulphur bonding coupled with polyetherimide (WS<sub>2</sub>@ NC) nanocomposite for high power and improved lithium-ion storage. *Mater. Chem. Phys.* **2020**, *246*, 122832.
- (246). Hu, Y.; Huang, Y.; Tan, C.; Zhang, X.; Lu, Q.; Sindoro, M.; Huang, X.; Huang, W.; Wang, L.; Zhang, H. Two-dimensional transition metal dichalcogenide nanomaterials for biosensing applications. *Mater. Chem. Front.* **2017**, *1*, 24-36.
- (247). Sun, X.; Fan, J.; Fu, C.; Yao, L.; Zhao, S.; Wang, J.; Xiao, J. WS<sub>2</sub> and MoS<sub>2</sub> biosensing platforms using peptides as probe biomolecules. *Sci. Rep.* **2017**, *7*, 1-8.
- (248). Duan, X.; Liu, Q.; Wang, G.; Su, X. WS<sub>2</sub> quantum dots as a sensitive fluorescence probe for the detection of glucose. *J. Lumin.* **2019**, *207*, 491-496.
- (249). Gupta, R.; Valappil, M. O.; Sakthivel, A.; Mathur, A.; Pundir, C. S.; Murugavel, K.; Narang, J.; Alwarappan, S. Tungsten disulfide quantum dots based disposable paper based lab on a chip for specific meningitis DNA detection. *J. Electrochem. Soc.* **2020**, *167*, 107501.
- (250). Kim, M.-J.; Jeon, S.-J.; Kang, T. W.; Ju, J.-M.; Yim, D.; Kim, H.-I.; Park, J. H.; Kim, J.-H. 2H-WS<sub>2</sub> quantum dots produced by modulating the dimension and phase of 1T-nanosheets for antibody-free optical sensing of neurotransmitters. *ACS Appl. Mater. Interfaces* **2017**, *9*, 12316-12323.
- (251). Yan, Y.; Zhang, C.; Gu, W.; Ding, C.; Li, X.; Xian, Y. Facile synthesis of water-soluble WS<sub>2</sub> quantum dots for turn-on fluorescent measurement of lipoic acid. *J. Phys. Chem. C* **2016**, *120*, 12170-12177.
- (252). Zhao, X.; He, D.; Wang, Y.; Fu, C. Facile fabrication of tungsten disulfide quantum dots (WS<sub>2</sub> QDs) as effective probes for fluorescence detection of dopamine (DA). *Mater. Chem. Phys.* **2018**, *207*, 130-134.
- (253). Rydeen, A. E.; Brustad, E. M.; Pielak, G. J. Osmolytes and protein-protein interactions. *J. Am. Chem. Soc.* **2018**, *140*, 7441-7444.
- (254). Watkins, A. M.; Bonneau, R.; Arora, P. S. Side-chain conformational preferences govern protein-protein interactions. *J. Am. Chem. Soc.* **2016**, *138*, 10386-10389.
- (255). Cédric, V.; Yves, C.; André, P. Sum-frequency Generation Spectroscopy in Biosensors Technology. In *Biosens: Emerging Materials and Application*, Serra, P. A., Ed. IntechOpen, 2011.
- (256). Matysiak-Brynda, E.; Wagner, B.; Bystrzejewski, M.; Grudzinski, I. P.; Nowicka, A. M. The importance of antibody orientation in the electrochemical detection of ferritin. *Biosens. Bioelectron.* **2018**, *109*, 83-89.
- (257). Saha, B.; Evers, T. H.; Prins, M. W. How antibody surface coverage on nanoparticles determines the activity and kinetics of antigen capturing for biosensing. *Anal. Chem.* **2014**, *86*, 8158-8166.
- (258). Xiao, M.; Wei, S.; Chen, J.; Tian, J.; Brooks III, C. L.; Marsh, E. N. G.; Chen, Z. Molecular mechanisms of interactions between monolayered transition metal dichalcogenides and biological molecules. *J. Am. Chem. Soc.* **2019**, *141*, 9980-9988.
- (259). Boughton, A. P.; Yang, P.; Tesmer, V. M.; Ding, B.; Tesmer, J. J.; Chen, Z. Heterotrimeric G protein  $\beta$  1  $\gamma$  2 subunits change orientation upon complex formation

with G protein-coupled receptor kinase 2 (GRK2) on a model membrane. *Proc. Natl. Acad. Sci.* **2011**, 108, E667-E673.

(260). Garg, M.; Chatterjee, M.; Sharma, A. L.; Singh, S. Label-free approach for electrochemical ferritin sensing using biosurfactant stabilized tungsten disulfide quantum dots. *Biosens. Bioelectron.* **2020**, 151, 111979.

(261). Allen, S.; Chen, X.; Davies, J.; Davies, M. C.; Dawkes, A. C.; Edwards, J. C.; Roberts, C. J.; Sefton, J.; Tendler, S. J.; Williams, P. M. Detection of antigen– antibody binding events with the atomic force microscope. *Biochemistry* **1997**, 36, 7457-7463.

(262). Kazakbaeva, K. M.; Buglanov, A.; Bakhranov, S. Isolation, purification, and characterization of ferritin from human liver. *Chem. Nat. Compd.* **1986**, 22, 90-93.

(263). Gasteiger, E.; Hoogland, C.; Gattiker, A.; Wilkins, M. R.; Appel, R. D.; Bairoch, A. Protein identification and analysis tools on the ExpASy server. In *The proteomics protocols handbook*, Walker, J. M., Ed. Humana Press, 2005; pp 571-607.

(264). Mondal, J. A.; Nihonyanagi, S.; Yamaguchi, S.; Tahara, T. Three distinct water structures at a zwitterionic lipid/water interface revealed by heterodyne-detected vibrational sum frequency generation. *J. Am. Chem. Soc.* **2012**, 134, 7842-7850.

(265). Ji, N.; Shen, Y. R. Sum frequency vibrational spectroscopy of leucine molecules adsorbed at air–water interface. *J. Chem. Phys.* **2004**, 120, 7107-7112.

(266). Bordenyuk, A. N.; Weeraman, C.; Yatawara, A.; Jayathilake, H. D.; Stiopkin, I.; Liu, Y.; Benderskii, A. V. Vibrational sum frequency generation spectroscopy of dodecanethiol on metal nanoparticles. *J. Phys. Chem. C* **2007**, 111, 8925-8933.

(267). Ye, S.; Majumdar, P.; Chisholm, B.; Stafslie, S.; Chen, Z. Antifouling and antimicrobial mechanism of tethered quaternary ammonium salts in a cross-linked poly (dimethylsiloxane) matrix studied using sum frequency generation vibrational spectroscopy. *Langmuir* **2010**, 26, 16455-16462.

(268). Guan, G.; Zhang, S.; Liu, S.; Cai, Y.; Low, M.; Teng, C. P.; Phang, I. Y.; Cheng, Y.; Duei, K. L.; Srinivasan, B. M. Protein induces layer-by-layer exfoliation of transition metal dichalcogenides. *J. Am. Chem. Soc.* **2015**, 137, 6152-6155.

(269). Li, M.; Zhao, A.; Dong, K.; Li, W.; Ren, J.; Qu, X. Chemically exfoliated WS<sub>2</sub> nanosheets efficiently inhibit amyloid  $\beta$ -peptide aggregation and can be used for photothermal treatment of Alzheimer's disease. *Nano Res.* **2015**, 8, 3216-3227.

(270). Jutz, G. n.; van Rijn, P.; Santos Miranda, B.; Böker, A. Ferritin: a versatile building block for bionanotechnology. *Chem. Rev.* **2015**, 115, 1653-1701.

(271). Feng, R.-R.; Guo, Y.; Wang, H.-F. Reorientation of the “free OH” group in the top-most layer of air/water interface of sodium fluoride aqueous solution probed with sum-frequency generation vibrational spectroscopy. *J. Chem. Phys.* **2014**, 141, 18C507.

(272). Bui, T. T.; Colón, L. A.; Velarde, L. Intermolecular Interactions at the Silica–Liquid Interface Modulate the Fermi Resonance Coupling in Surface Methanol. *J. Phys. Chem. Lett.* **2021**, 12, 5695-5702.

(273). Sin, J.-S.; Jang, Y.-M.; Kim, C.-H.; Kim, H.-C. Steric effect of water molecule clusters on electrostatic interaction and electroosmotic transport in aqueous electrolytes: A mean-field approach. *AIP Adv.* **2018**, 8, 105222.

(274). Karnes, J. J.; Benjamin, I. Deconstructing the Local Intermolecular Ordering and Dynamics of Liquid Chloroform and Bromoform. *J. Phys. Chem. B* **2021**, 125, 3629-3637.

(275). Pothoczki, S.; Ottochian, A.; Rovira-Esteva, M.; Pardo, L.; Tamarit, J. L.; Cuello, G. Role of steric and electrostatic effects in the short-range order of quasitetrahedral molecular liquids. *Phys. Rev. B* **2012**, 85, 014202.



- (276). Kaur, H.; Verma, M.; Kaur, S.; Rana, B.; Singh, N.; Jena, K. C. Elucidating the Molecular Structure of Hydrophobically Modified Polyethylenimine Nanoparticles and Its Potential Implications for DNA Binding. *Langmuir* **2022**, *38*, 13456-13468.
- (277). Jäger, M.; Schubert, S.; Ochrimenko, S.; Fischer, D.; Schubert, U. S. Branched and linear poly (ethylene imine)-based conjugates: synthetic modification, characterization, and application. *Chem. Soc. Rev.* **2012**, *41*, 4755-4767.
- (278). Zhou, Y.; Fuentes-Hernandez, C.; Shim, J.; Meyer, J.; Giordano, A. J.; Li, H.; Winget, P.; Papadopoulos, T.; Cheun, H.; Kim, J. A universal method to produce low-work function electrodes for organic electronics. *Science* **2012**, *336*, 327-332.
- (279). Zhang, H.; Xie, L.; Shen, X.; Shang, T.; Luo, R.; Li, X.; You, T.; Wang, J.; Huang, N.; Wang, Y. Catechol/polyethyleneimine conversion coating with enhanced corrosion protection of magnesium alloys: potential applications for vascular implants. *J. Mater. Chem. B* **2018**, *6*, 6936-6949.
- (280). Xiao, M.; Mohler, C.; Tucker, C.; Walther, B.; Lu, X.; Chen, Z. Structures and adhesion properties at polyethylene/silica and polyethylene/nylon interfaces. *Langmuir* **2018**, *34*, 6194-6204.
- (281). Perevyazko, I. Y.; Bauer, M.; Pavlov, G. M.; Hoepfner, S.; Schubert, S.; Fischer, D.; Schubert, U. S. Polyelectrolyte complexes of DNA and linear PEI: formation, composition and properties. *Langmuir* **2012**, *28*, 16167-16176.
- (282). Kondinskaia, D. A.; Gurtovenko, A. A. Supramolecular complexes of DNA with cationic polymers: The effect of polymer concentration. *Polymer* **2018**, *142*, 277-284.
- (283). Molnar, M. M.; Liddell, S. C.; Wadkins, R. M. Effects of polyamine binding on the stability of DNA i-motif structures. *ACS Omega* **2019**, *4*, 8967-8973.
- (284). Ma, C.; Zhang, X.; Yang, L.; Wu, Y.; Liu, H.; Zhang, X.; Wei, Y. Preparation of fluorescent organic nanoparticles from polyethylenimine and sucrose for cell imaging. *Mater. Sci. Eng. C* **2016**, *68*, 37-42.
- (285). Sarkar, K.; Meka, S. R. K.; Madras, G.; Chatterjee, K. A self-assembling polycationic nanocarrier that exhibits exceptional gene transfection efficiency. *RSC Adv.* **2015**, *5*, 91619-91632.
- (286). Liu, Z.; Zhang, Z.; Zhou, C.; Jiao, Y. Hydrophobic modifications of cationic polymers for gene delivery. *Prog. Polym. Sci.* **2010**, *35*, 1144-1162.
- (287). Ling, Y.; Qu, F.; Zhou, Q.; Li, T.; Gao, Z. F.; Lei, J. L.; Li, N. B.; Luo, H. Q. Diverse states and properties of polymer nanoparticles and gel formed by polyethyleneimine and aldehydes and analytical applications. *Anal. Chem.* **2015**, *87*, 8679-8686.
- (288). Ahmad, N.; Leo, C.; Ahmad, A.; Ramli, W. Membranes with great hydrophobicity: a review on preparation and characterization. *Sep. Purif. Rev.* **2015**, *44*, 109-134.
- (289). Sahiner, N. Preparation of poly (ethylene imine) particles for versatile applications. *Colloids Surf. A Physicochem. Eng. Asp.* **2013**, *433*, 212-218.
- (290). Liang, S.; Yu, H.; Xiang, J.; Yang, W.; Chen, X.; Liu, Y.; Gao, C.; Yan, G. New naphthalimide modified polyethylenimine nanoparticles as fluorescent probe for DNA detection. *Spectrochim. Acta A Mol. Biomol. Spectrosc.* **2012**, *97*, 359-365.
- (291). Tian, H.; Xiong, W.; Wei, J.; Wang, Y.; Chen, X.; Jing, X.; Zhu, Q. Gene transfection of hyperbranched PEI grafted by hydrophobic amino acid segment PBLG. *Biomaterials* **2007**, *28*, 2899-2907.
- (292). Bellettini, I. C.; Fayad, S. J.; Machado, V. G.; Minatti, E. Properties of polyplexes formed through interaction between hydrophobically-modified poly (ethylene imine) s and calf thymus DNA in aqueous solution. *Soft Matter* **2017**, *13*, 2609-2619.

- (293). Tian, C.; Feng, J.; Prud'homme, R. K. Adsorption dynamics of polymeric nanoparticles at an air-water interface with addition of surfactants. *J. Colloid Interface Sci.* **2020**, *575*, 416-424.
- (294). Lu, X.; Han, J.; Shephard, N.; Rhodes, S.; Martin, A. D.; Li, D.; Xue, G.; Chen, Z. Phenolic resin surface restructuring upon exposure to humid air: A sum frequency generation vibrational spectroscopic study. *J. Phys. Chem. B* **2009**, *113*, 12944-12951.
- (295). Zhang, C.; Wu, F.-G.; Hu, P.; Chen, Z. Interaction of polyethylenimine with model cell membranes studied by linear and nonlinear spectroscopic techniques. *J. Phys. Chem. C* **2014**, *118*, 12195-12205.
- (296). Choi, S.; Park, C. S.; Kwon, O. S.; Giong, H.-K.; Lee, J.-S.; Ha, T. H.; Lee, C.-S. Structural effects of naphthalimide-based fluorescent sensor for hydrogen sulfide and imaging in live zebrafish. *Sci. Rep.* **2016**, *6*, 1-10.
- (297). Pischel, U.; Uzunova, V. D.; Remón, P.; Nau, W. M. Supramolecular logic with macrocyclic input and competitive reset. *Chem. Comm.* **2010**, *46*, 2635-2637.
- (298). Verma, M.; Kaur, N.; Singh, N. Naphthalimide-based DNA-coupled hybrid assembly for sensing dipicolinic acid: a biomarker for bacillus anthracis spores. *Langmuir* **2018**, *34*, 6591-6600.
- (299). Sáfar, G. A.; Malachias, A.; Magalhães-Paniago, R.; Martins, D. C.; Idemori, Y. M. Unravelling the molecular structure and packing of a planar molecule by combining nuclear magnetic resonance and scanning tunneling microscopy. *Phys. Chem. Chem. Phys.* **2013**, *15*, 20691-20697.
- (300). Idris, S. A.; Mkhathresh, O. A.; Heatley, F. Assignment of <sup>1</sup>H NMR spectrum and investigation of oxidative degradation of poly (ethylenimine) using <sup>1</sup>H and <sup>13</sup>C 1-D and 2-D NMR. *Polym. Int.* **2006**, *55*, 1040-1048.
- (301). Wang, Y.-Q.; Su, J.; Wu, F.; Lu, P.; Yuan, L.-F.; Yuan, W.-E.; Sheng, J.; Jin, T. Biscarbamate cross-linked polyethylenimine derivative with low molecular weight, low cytotoxicity, and high efficiency for gene delivery. *Int. J. Nanomed.* **2012**, *7*, 693.
- (302). Grzesiak, W.; Brycki, B. Synthesis, FTIR, <sup>13</sup>C-NMR and Temperature-Dependent <sup>1</sup>H NMR Characteristics of Bis-naphthalimide Derivatives. *Molecules* **2012**, *17*, 12427-12448.
- (303). Pulido-Reyes, G.; Martín, E.; Coronado, J. G.; Leganes, F.; Rosal, R.; Fernandez-Pinas, F. Physicochemical and biological interactions between cerium oxide nanoparticles and a 1, 8-naphthalimide derivative. *J. Photochem. Photobiol. B* **2017**, *172*, 61-69.
- (304). Kasprzak, A.; Popławska, M.; Bystrzejewski, M.; Łabędź, O.; Grudziński, I. P. Conjugation of polyethylenimine and its derivatives to carbon-encapsulated iron nanoparticles. *RSC Adv.* **2015**, *5*, 85556-85567.
- (305). Tan, M.; Feng, Y.; Wang, H.; Zhang, L.; Khan, M.; Guo, J.; Chen, Q.; Liu, J. Immobilized bioactive agents onto polyurethane surface with heparin and phosphorylcholine group. *Macromol. Res.* **2013**, *21*, 541-549.
- (306). Korzec, M.; Malarz, K.; Mrozek-Wilczkiewicz, A.; Rzycka-Korzec, R.; Schab-Balcerzak, E.; Polański, J. Live cell imaging by 3-imino-(2-phenol)-1, 8-naphthalimides: The effect of ex vivo hydrolysis. *Spectrochim. Acta A Mol. Biomol. Spectrosc.* **2020**, *238*, 118442.
- (307). Dimov, S. M.; Georgiev, N. I.; Asiri, A. M.; Bojinov, V. B. Synthesis and sensor activity of a PET-based 1, 8-naphthalimide probe for Zn<sup>2+</sup> and pH determination. *J. Fluoresc.* **2014**, *24*, 1621-1628.
- (308). Lindén, J. B.; Larsson, M.; Kaur, S.; Skinner, W. M.; Miklavcic, S. J.; Nann, T.; Kempson, I. M.; Nydén, M. Polyethyleneimine for copper absorption II: kinetics, selectivity and efficiency from seawater. *RSC Adv.* **2015**, *5*, 51883-51890.

- (309). Lin, S.-Y.; Cheng, W.-T.; Wei, Y.-S.; Lin, H.-L. DSC-FTIR microspectroscopy used to investigate the heat-induced intramolecular cyclic anhydride formation between Eudragit E and PVA copolymer. *Polym. J.* **2011**, *43*, 577-580.
- (310). Windsor, R.; Neivandt, D. J.; Davies, P. B. Temperature and pH effects on the coadsorption of sodium dodecyl sulfate and poly (ethylenimine). *Langmuir* **2002**, *18*, 2199-2204.
- (311). Windsor, R.; Neivandt, D. J.; Davies, P. B. Adsorption of sodium dodecyl sulfate in the presence of poly (ethylenimine) and sodium chloride studied using sum frequency vibrational spectroscopy. *Langmuir* **2001**, *17*, 7306-7312.
- (312). Lu, X.; Myers, J. N.; Chen, Z. Molecular ordering of phenyl groups at the buried polystyrene/metal interface. *Langmuir* **2014**, *30*, 9418-9422.
- (313). Kawaguchi, T.; Shiratori, K.; Henmi, Y.; Ishiyama, T.; Morita, A. Mechanisms of sum frequency generation from liquid benzene: Symmetry breaking at interface and bulk contribution. *J. Phys. Chem. C* **2012**, *116*, 13169-13182.
- (314). Zhang, D.; Shen, Y.; Somorjai, G. A. Studies of surface structures and compositions of polyethylene and polypropylene by IR+ visible sum frequency vibrational spectroscopy. *J. Chem. Phys. Lett.* **1997**, *281*, 394-400.
- (315). Lott, G. A.; King, M. D.; Hill, M. W.; Scatena, L. F. Effects of relative humidity on the surface and bulk structures of linear polyethylenimine thin films. *J. Phys. Chem. C* **2014**, *118*, 17686-17698.
- (316). Jones, M. R.; Seeman, N. C.; Mirkin, C. A. Programmable materials and the nature of the DNA bond. *Science* **2015**, *347*, 1260901.
- (317). Villarreal, W.; Colina-Vegas, L.; Visbal, G.; Corona, O.; Correa, R. S.; Ellena, J.; Cominetti, M. R.; Batista, A. A.; Navarro, M. Copper (I)-phosphine polypyridyl complexes: synthesis, characterization, DNA/HSA binding study, and antiproliferative activity. *Inorg. Chem.* **2017**, *56*, 3781-3793.
- (318). Guan, X.; Guo, Z.; Wang, T.; Lin, L.; Chen, J.; Tian, H.; Chen, X. A pH-responsive detachable PEG shielding strategy for gene delivery system in cancer therapy. *Biomacromol.* **2017**, *18*, 1342-1349.
- (319). Alatorre Meda, M.; Taboada, P.; Hartl, F.; Wagner, T.; Freis, M.; Rodríguez, J. R. The influence of chitosan valence on the complexation and transfection of DNA: The weaker the DNA-chitosan binding the higher the transfection efficiency. *Colloids Surf. B Biointerfaces* **2011**, *82*, 54-62.
- (320). Dias, R. S.; Magno, L. M.; Valente, A. J.; Das, D.; Das, P. K.; Maiti, S.; Miguel, M. G.; Lindman, B. r. Interaction between DNA and cationic surfactants: effect of DNA conformation and surfactant headgroup. *J. Phys. Chem. B* **2008**, *112*, 14446-14452.
- (321). Braun, C. S.; Vetro, J. A.; Tomalia, D. A.; Koe, G. S.; Koe, J. G.; Middaugh, C. R. Structure/function relationships of polyamidoamine/DNA dendrimers as gene delivery vehicles. *J. Pharm. Sci.* **2005**, *94*, 423-436.
- (322). Muntean, C. M.; Stefan, R.; Bindea, M.; Cozma, V. Fourier transform infrared spectroscopy of DNA from *Borrelia burgdorferi* sensu lato and *Ixodes ricinus* ticks. *Spectrochim. Acta Part A: Mol. Biomol. Spectrosc.* **2013**, *110*, 185-192.
- (323). Banyay, M.; Sarkar, M.; Gräslund, A. A library of IR bands of nucleic acids in solution. *Biophys. Chem.* **2003**, *104*, 477-488.
- (324). Ye, S.; Nguyen, K. T.; Chen, Z. Interactions of alamethicin with model cell membranes investigated using sum frequency generation vibrational spectroscopy in real time in situ. *J. Phys. Chem. B* **2010**, *114*, 3334-3340.
- (325). Andre, J. S.; Grant, J.; Greyson, E.; Chen, X.; Tucker, C.; Drumright, R.; Mohler, C.; Chen, Z. Molecular Interactions between Amino Silane Adhesion Promoter and Acrylic Polymer Adhesive at Buried Silica Interfaces. *Langmuir* **2022**, *38*, 6180-6190.



## Appendix A

**Table A1.** Fitting parameters for the OH-stretch region of the SFG spectra at air/water interface at various BHb protein concentrations, corresponding to Figure 3.1, panel A.

System	Pristine Water		BHb								Mode Assignment	
			1 ppm		5 ppm	10 ppm		100 ppm		800 ppm		
$ \chi_{NR}^{(2)} $ (a.u.)	0.01		0.01		0.01	0.01		0.01		0.00		
$\Gamma_v$ (cm <sup>-1</sup> )	$\omega_v$ (cm <sup>-1</sup> )	$ A_v $ (a.u.)	$\omega_v$	$ A_v $	$ A_v $	$\omega_v$	$ A_v $	$\omega_v$	$ A_v $	$ A_v $		
<b>100</b>	<b>3225</b>	0.56	<b>3225</b>	0.21	0.78	<b>3270</b>	2.23	<b>3160</b>	2.40	3.26		Strong H-bonding
<b>125</b>	<b>3450</b>	3.19	<b>3450</b>	2.91	2.62	<b>3450</b>	1.49	<b>3450</b>	0.09	2.50		Weak H-bonding
<b>70</b>	<b>3550</b>	0.06	<b>3550</b>	0.16	0.32	<b>3580</b>	1.15	<b>3580</b>	0.41	0.02		Weak H-bonding
<b>19</b>	<b>3705</b>	0.98	<b>3705</b>	0.98	1.06	<b>3705</b>	0.60	<b>3705</b>	0.39	0.47	Free OH	

**Table A2.** Fitting parameters of the SFG spectra at air/water and air/D<sub>2</sub>O interfaces for 10 ppm BHb protein concentration, depicting Figure 3.1, panel C.

System		BHb in H <sub>2</sub> O	BHb in D <sub>2</sub> O	Mode Assignment
$ \chi_{NR}^{(2)} $ (a.u.)		0.00	0.01	
$\omega_v$ (cm <sup>-1</sup> )	$\Gamma_v$ (cm <sup>-1</sup> )	$ A_v $ (a.u.)	$ A_v $ (a.u.)	
<b>3005</b>	<b>12</b>	0.02	0.03	2v (C=C) <sub>s</sub>
<b>3041</b>	<b>11</b>	0.05	0.00	v (=CH) <sub>20a</sub>
<b>3064</b>	<b>11</b>	0.18	0.16	v (=CH) <sub>20b</sub>
<b>3160</b>	<b>100</b>	3.06	0.35	Strong H-bonding

**Table A3.** Fitting parameters for the CH-stretch region of the SFG spectra at air/water interface at various BHp protein concentrations for Figure 3.1, panel D.

System		BHp						Mode Assignment
		1 ppm	5 ppm	10 ppm	30 ppm	100 ppm	800 ppm	
$ \chi_{\text{NR}}^{(2)} $ (a.u.)		0.01	0.01	0.01	0.00	0.00	0.00	
$\omega_{\nu}$ (cm <sup>-1</sup> )	$\Gamma_{\nu}$ (cm <sup>-1</sup> )	$ A_{\nu} $ (a.u.)	$ A_{\nu} $	$ A_{\nu} $	$ A_{\nu} $	$ A_{\nu} $	$ A_{\nu} $	
<b>2850</b>	<b>10</b>	0.00	0.00	0.01	0.03	0.05	0.05	CH <sub>2</sub> ss
<b>2876</b>	<b>8</b>	0.00	0.00	0.02	0.34	0.46	0.63	CH <sub>3</sub> ss
<b>2904</b>	<b>10</b>	0.00	0.00	0.02	0.12	0.17	0.17	methine CHs
<b>2920</b>	<b>11</b>	0.00	0.00	0.01	0.18	0.24	0.25	CH <sub>2</sub> as
<b>2939</b>	<b>11</b>	0.00	0.00	0.07	0.32	0.42	0.49	CH <sub>2</sub> FR
<b>2985</b>	<b>12</b>	0.00	0.01	0.04	0.05	0.09	0.11	CH <sub>3</sub> as
<b>3005</b>	<b>12</b>	0.01	0.02	0.04	0.08	0.13	0.14	2 $\nu$ (C=C)s
<b>3041</b>	<b>11</b>	0.01	0.01	0.02	0.13	0.15	0.16	$\nu$ (=CH) <sub>20a</sub>
<b>3055</b>	<b>11</b>	0.00	0.00	0.04	0.31	0.37	0.46	$\nu$ (=CH) <sub>20b</sub>

**Table A4.** SFG fitting parameters for time-dependent OH-stretch region evolution for 5 ppm BHp protein concentration at air/water interface of Figure 3.2, panel A.

System	Pristine Water		BHp (5 ppm)						
			0 min		28 min	56 min		84 min	
$ \chi_{\text{NR}}^{(2)} $ (a.u.)	0.01		0.02		0.02	0.02		0.00	
$\Gamma_{\nu}$ (cm <sup>-1</sup> )	$\omega_{\nu}$ (cm <sup>-1</sup> )	$ A_{\nu} $ (a.u.)	$\omega_{\nu}$ (cm <sup>-1</sup> )	$ A_{\nu} $	$ A_{\nu} $	$\omega_{\nu}$ (cm <sup>-1</sup> )	$ A_{\nu} $	$\omega_{\nu}$ (cm <sup>-1</sup> )	$ A_{\nu} $
<b>100</b>	<b>3225</b>	0.56	<b>3225</b>	0.50	0.27	<b>3330</b>	0.52	<b>3160</b>	3.90
<b>125</b>	<b>3450</b>	3.19	<b>3450</b>	2.27	2.45	<b>3450</b>	2.31	<b>3450</b>	1.86
<b>70</b>	<b>3550</b>	0.09	<b>3580</b>	0.89	0.77	<b>3580</b>	0.81	<b>3580</b>	0.55
<b>19</b>	<b>3705</b>	0.98	<b>3705</b>	1.05	1.10	<b>3705</b>	1.07	<b>3705</b>	0.8

**Table A5.** SFG fitting parameters for time-dependent OH-stretch region evolution for 10 ppm BHB protein concentration at air/water interface of Figure 3.2, panel B.

System	Pristine Water		BHB (10 ppm)							
			0 min		21 min		42 min		63 min	84 min
$ \chi_{\text{NR}}^{(2)} $ (a.u.)	0.01		0.01		0.00		0.00		0.00	0.01
$\Gamma_{\nu}$ ( $\text{cm}^{-1}$ )	$\omega_{\nu}$ ( $\text{cm}^{-1}$ )	$ A_{\nu} $ (a.u.)	$\omega_{\nu}$ ( $\text{cm}^{-1}$ )	$ A_{\nu} $	$ A_{\nu} $	$\omega_{\nu}$ ( $\text{cm}^{-1}$ )	$ A_{\nu} $	$ A_{\nu} $	$ A_{\nu} $	
<b>100</b>	<b>3225</b>	0.53	<b>3225</b>	0.22	3.47	<b>3160</b>	3.51	3.71	3.83	
<b>125</b>	<b>3450</b>	3.10	<b>3450</b>	1.67	1.59	<b>3450</b>	1.59	1.61	2.33	
<b>70</b>	<b>3550</b>	0.05	<b>3580</b>	0.91	0.79	<b>3580</b>	0.59	0.53	0.11	
<b>19</b>	<b>3705</b>	0.93	<b>3705</b>	0.92	0.68	<b>3705</b>	0.61	0.59	0.58	





## Appendix B

**Table B1.** Data Fitting parameters of the SFG profile of sample references, dsDNA as a function of concentration, and the concentration-dependent influence of H<sub>2</sub>O<sub>2</sub> on dsDNA molecular signatures, studied at air-aqueous interface, for Figures 3.6 and 3.7.

System		Pristine Water			Tris-HCl (pH 7.4)		
		SSP	PPP	SPS	SSP	PPP	SPS
$ \chi_{NR}^{(2)} $ (a.u.)		0.02	0.01	0.01	0.02	0.01	0.01
$\omega_v$ (cm <sup>-1</sup> )	$\Gamma_v$ (cm <sup>-1</sup> )	$ A_v $ (a.u.)	$ A_v $	$ A_v $	$ A_v $	$ A_v $	$ A_v $
<b>3225</b>	<b>100</b>	0.66	0.24	0.09	0.78	0.58	0.11
<b>3450</b>	<b>125</b>	3.69	1.03	0.29	3.83	1.57	0.29
<b>3550</b>	<b>70</b>	0.09	0.61	0.39	0.27	0.36	0.49
<b>3705</b>	<b>19</b>	1.05	0.85	0.19	1.04	0.65	0.19

**Table B2.** Fitting parameters of the polarization-dependent SFG profile of dsDNA as a function of concentration at air-aqueous interface, for Figure 3.6.

System		dsDNA							Peak Assignments
		0.1 mg.mL <sup>-1</sup>			0.3 mg.mL <sup>-1</sup>				
		SSP	PPP	SPS	$\omega_v$ (cm <sup>-1</sup> )	SSP	PPP	SPS	
$ \chi_{NR}^{(2)} $ (a.u.)		0.02	0.02	0.01			0.01	0.02	0.01
$\omega_v$ (cm <sup>-1</sup> )	$\Gamma_v$ (cm <sup>-1</sup> )	$ A_v $ (a.u.)	$ A_v $	$ A_v $		$ A_v $	$ A_v $	$ A_v $	
<b>2885</b>	<b>7</b>	0.02	0.02	0.01	<b>2885</b>	0.13	0.04	0.01	CH <sub>3</sub> SS
<b>2925</b>	<b>12</b>	0.00	0.04	0.04	<b>2925</b>	0.03	0.13	0.04	CH <sub>2</sub> AS
<b>2948</b>	<b>10</b>	0.01	0.01	0.01	<b>2948</b>	0.55	0.09	0.01	CH <sub>3</sub> FR
<b>2965</b>	<b>15</b>	0.02	0.07	0.01	<b>2965</b>	0.68	0.74	0.18	CH <sub>3</sub> AS
<b>3025</b>	<b>12</b>	0.01	0.02	0.01	<b>3025</b>	0.09	0.04	0.03	$\nu_{20b}$ (C-H) <sub>S</sub>
<b>3042</b>	<b>12</b>	0.00	0.00	0.01	<b>3042</b>	0.05	0.05	0.02	$\nu_{7a}$ (C-H) <sub>S</sub>
<b>3070</b>	<b>20</b>	0.04	0.00	0.01	<b>3070</b>	0.11	0.00	0.05	$\nu_2$ (C-H) <sub>S</sub>
<b>3100</b>	<b>70</b>	0.04	0.00	0.03	<b>3100</b>	1.00	0.01	0.12	(N-H) <sub>S</sub>
<b>3200</b>	<b>100</b>	0.27	0.36	0.38	<b>3270</b>	1.92	0.42	0.39	Strong H-bonding
<b>3450</b>	<b>125</b>	4.07	2.11	2.44	<b>3450</b>	7.14	2.38	2.52	Weak H-bonding
<b>3550</b>	<b>70</b>	0.25	0.49	0.39	<b>3550</b>	0.40	0.63	0.48	Weak H-bonding
<b>3705</b>	<b>19</b>	0.97	0.35	0.02	<b>3705</b>	0.33	0.03	0.05	Free OH

**Table B3.** Fitting parameters of the polarization-dependent SFG profile for the concentration-dependent influence of H<sub>2</sub>O<sub>2</sub> on dsDNA (0.03 mg.mL<sup>-1</sup>) molecular signatures at air-aqueous interface, for Figure 3.7.

System		dsDNA (0.03 mg.mL <sup>-1</sup> ) + H <sub>2</sub> O <sub>2</sub>		
		0.1 v/v % H <sub>2</sub> O <sub>2</sub>		0.2 v/v % H <sub>2</sub> O <sub>2</sub>
		SSP		SSP
$ \chi_{NR}^{(2)} $ (a.u.)		0.00	0.01	0.02
$\omega_v$ (cm <sup>-1</sup> )	$\Gamma_v$ (cm <sup>-1</sup> )	$ A_v $ (a.u.)	$ A_v $	$ A_v $
2885	7	0.08	0.06	0.03
2925	12	0.02	0.01	0.10
2948	10	0.47	0.03	0.08
2965	15	0.58	0.01	0.60
3025	12	0.08	0.02	0.03
3042	12	0.02	0.01	0.03
3070	20	0.08	0.02	0.00
3100	70	0.98	0.72	0.01
3270	100	1.58	1.50	0.37
3450	125	6.92	6.41	2.30
3550	70	0.31	0.27	0.62
3705	19	0.30	0.36	0.04

## Appendix C

**Table C1.** NIP films as a variation of polymerization time in SSP polarization mode, for Figure 4.5, panel A.

System	NIP Films								Peak Assignments
	3 hours		6 hours		9 hours		24 hours		
$ \chi_{NR}^{(2)} $ (a.u.)	0.02		0.01		0.02		0.01		
$\omega_v$ ( $\text{cm}^{-1}$ )	$\Gamma_v$ ( $\text{cm}^{-1}$ )	$ A_v $ (a.u.)	$\Gamma_v$ ( $\text{cm}^{-1}$ )	$ A_v $ (a.u.)	$\Gamma_v$ ( $\text{cm}^{-1}$ )	$ A_v $ (a.u.)	$\Gamma_v$ ( $\text{cm}^{-1}$ )	$ A_v $ (a.u.)	
<b>2858</b>	<b>11.5</b>	0.36	<b>12</b>	0.24	<b>12</b>	0.29	<b>12</b>	0.24	CH <sub>2</sub> ss (non-protonated ethylamine)
<b>2876</b>	<b>9</b>	0.32	<b>8.8</b>	0.29	<b>8.5</b>	0.31	<b>8.8</b>	0.28	CH <sub>2</sub> ss (protonated ethylamine)
<b>2904</b>	<b>12</b>	0.30	<b>12</b>	0.29	<b>11</b>	0.32	<b>12</b>	0.27	CHs
<b>2922</b>	<b>13</b>	0.27	<b>13</b>	0.31	<b>13</b>	0.21	<b>13</b>	0.21	CH <sub>2</sub> as (non-protonated ethylamine)
<b>2939</b>	<b>11</b>	0.22	<b>11</b>	0.24	<b>12</b>	0.23	<b>12</b>	0.13	CH <sub>2</sub> FR (non-protonated ethylamine)
<b>2965</b>	<b>10</b>	0.01	<b>10</b>	0.04	<b>10</b>	0.02	<b>10</b>	0.01	CH <sub>2</sub> as (protonated ethylamine)
<b>2996</b>	<b>11</b>	0.01	<b>11</b>	0.16	<b>11</b>	0.08	<b>11</b>	0.01	Combination band of C-H <sub>As</sub> stretch from cyclized five-membered ring structure
<b>P<sub>1</sub>/P<sub>2</sub> ratio ±0.02</b>	0.78		0.36		0.44		0.39		

**Table C2.** MIP films as a variation of polymerization time in SSP polarization mode for Figure 4.6, panel A.

System		MIP Films						Peak Assignments
		3 hours	6 hours	9 hours		24 hours		
$ \chi_{NR}^{(2)} $ (a.u.)		0.01	0.01	0.01		0.01		CH <sub>2</sub> ss (d <sup>+</sup> ) CH <sub>3</sub> ss (r <sup>+</sup> ) methine CHs CH <sub>2</sub> as (d <sup>-</sup> ) CH <sub>3</sub> FR (r <sup>+</sup> <sub>FR</sub> ) CH <sub>3</sub> as (r <sup>-</sup> ) C-H combination band from aromatic ring structure
$\omega_v$ (cm <sup>-1</sup> )	$\Gamma_v$ (cm <sup>-1</sup> )	$ A_v $ (a.u.)	$ A_v $	$\Gamma_v$ (cm <sup>-1</sup> )	$ A_v $	$\Gamma_v$ (cm <sup>-1</sup> )	$ A_v $	
2858	12	0.12	0.17	11	0.14	11	0.12	
2876	9	0.50	0.74	10	0.41	9.5	0.42	
2904	12	0.18	0.25	12	0.18	12	0.18	
2922	13	0.28	0.38	14	0.32	13	0.35	
2939	11	0.41	0.59	12	0.34	11.5	0.39	
2965	10	0.09	0.13	10	0.09	10	0.05	
2996	11	0.22	0.08	11	0.17	11	0.25	
<b>d<sup>+</sup>/r<sup>+</sup> ratio ±0.001</b>		0.03	0.03	0.09		0.06		
<b>R<sub>0</sub> = r<sup>+</sup><sub>FR</sub>/r<sup>+</sup> ±0.01</b>		0.45	0.42	0.47		0.58		

**Table C3.** BHb film (polarization-dependent) parameters, for Figure 4.6, panel B.

System		BHb (1 mg.mL <sup>-1</sup> )			Peak Assignments
		SSP	PPP	SPS	
$ \chi_{NR}^{(2)} $ (a.u.)		0.00	0.03	0.01	CH <sub>2</sub> ss (d <sup>+</sup> ) CH <sub>3</sub> ss (r <sup>+</sup> ) methine CHs CH <sub>2</sub> as (d <sup>-</sup> ) CH <sub>3</sub> FR (r <sup>+</sup> <sub>FR</sub> ) CH <sub>3</sub> as (r <sup>-</sup> ) C-H combination band from aromatic ring structure
$\omega_v$ (cm <sup>-1</sup> )	$\Gamma_v$ (cm <sup>-1</sup> )	$ A_v $ (a.u.)	$ A_v $	$ A_v $	
2858	12	0.16	0.05	0.01	
2876	9	0.74	0.02	0.00	
2904	12	0.24	0.11	0.02	
2922	13	0.27	0.09	0.02	
2939	11	0.65	0.20	0.00	
2965	10	0.01	0.72	0.29	
2996	11	0.06	0.00	-0.19	
<b>d<sup>+</sup>/r<sup>+</sup> ratio ±0.001</b>		0.03			

**Table C4.** Washing steps of 6-hour polymerized MIP film in SSP polarization mode, for Figure 4.7, panel A.

System		MIP Film 6 hours	Wash 1		Wash 2		Wash 3	Wash 4		Wash 5	
$ \chi_{NR}^{(2)} $ (a.u.)		0.01	0.01		0.01		0.01	0.01		0.01	
$\omega_v$ ( $\text{cm}^{-1}$ )	$\Gamma_v$ ( $\text{cm}^{-1}$ )	$ A_v $ (a.u.)	$\Gamma_v$ ( $\text{cm}^{-1}$ )	$ A_v $	$\Gamma_v$ ( $\text{cm}^{-1}$ )	$ A_v $	$ A_v $	$\Gamma_v$ ( $\text{cm}^{-1}$ )	$ A_v $	$\Gamma_v$ ( $\text{cm}^{-1}$ )	$ A_v $
<b>2858</b>	<b>12</b>	0.17	<b>10.5</b>	0.22	<b>9.5</b>	0.21	0.22	<b>9.8</b>	0.24	<b>9</b>	0.15
<b>2876</b>	<b>9</b>	0.74	<b>8.8</b>	0.42	<b>8.8</b>	0.38	0.41	<b>8.8</b>	0.44	<b>8.8</b>	0.30
<b>2904</b>	<b>12</b>	0.25	<b>11</b>	0.17	<b>11</b>	0.18	0.19	<b>11</b>	0.21	<b>11</b>	0.13
<b>2922</b>	<b>13</b>	0.38	<b>13</b>	0.30	<b>13</b>	0.29	0.32	<b>13</b>	0.39	<b>13</b>	0.23
<b>2939</b>	<b>11</b>	0.59	<b>11</b>	0.39	<b>10</b>	0.36	0.43	<b>10</b>	0.43	<b>10</b>	0.32
<b>2965</b>	<b>10</b>	0.13	<b>10</b>	0.07	<b>10</b>	0.09	0.12	<b>10</b>	0.11	<b>10</b>	0.03
<b>2996</b>	<b>11</b>	0.08	<b>11</b>	0.13	<b>11</b>	0.13	0.16	<b>11</b>	0.19	<b>11</b>	0.11
<b>d<sup>+</sup>/r<sup>+</sup> ratio ±0.01</b>		0.03	0.19		0.24		0.24	0.24		0.25	

**Table C5.** MIP (6-hour) polymerized film with cavities and after BHb re-binding in SSP polarization scheme, for Figure 4.8, panel A.

System	MIP with Cavities		MIP-BHb Rebinding	
$ \chi_{NR}^{(2)} $ (a.u.)	0.01		0.01	
$\omega_v$ ( $\text{cm}^{-1}$ )	$\Gamma_v$ ( $\text{cm}^{-1}$ )	$ A_v $ (a.u.)	$\Gamma_v$ ( $\text{cm}^{-1}$ )	$ A_v $
<b>2858</b>	<b>9</b>	0.15	<b>11</b>	0.13
<b>2876</b>	<b>8.8</b>	0.30	<b>8.8</b>	0.39
<b>2904</b>	<b>11</b>	0.13	<b>12</b>	0.10
<b>2922</b>	<b>13</b>	0.23	<b>13</b>	0.21
<b>2939</b>	<b>10</b>	0.32	<b>11</b>	0.37
<b>2965</b>	<b>10</b>	0.03	<b>10</b>	0.04
<b>2996</b>	<b>11</b>	0.11	<b>11</b>	0.02
<b>d<sup>+</sup>/r<sup>+</sup> ratio ±0.01</b>	0.25		0.07	

**Table C6.** NIP (6-hour) polymerized film after washing-dipping in BHb protein solution in SSP polarization scheme, for Figure 4.8, panel C.

Sample	$ \chi_{NR}^{(2)} $ (a.u.)	$\omega_v$ ( $\text{cm}^{-1}$ )	$ A_v $ (a.u.)	$\Gamma_v$ ( $\text{cm}^{-1}$ )	Peak Assignment	$P_1/P_2$ ratio $\pm 0.01$
<b>NIP (6- hours) after washing and dipping</b>	0.01	2858	0.10	12	CH <sub>2</sub> ss (non-protonated ethylamine)	0.20
		2876	0.17	8.8	CH <sub>2</sub> ss (protonated ethylamine)	
		2904	0.14	12	CHs	
		2922	0.16	13	CH <sub>2</sub> as (non-protonated ethylamine)	
		2939	0.05	11	CH <sub>2</sub> FR (non-protonated ethylamine)	
		2965	0.00	10	CH <sub>2</sub> as (protonated ethylamine)	
		2996	0.01	11	Combination band of C-H <sub>AS</sub> stretch from cyclized five-membered ring structure	

## Appendix D

**Table D1.** SFG fitting parameters of CH region of lower protein concentration in SSP polarization mode.

System		SSP							Peak Assignment
		Ab (0.3 $\mu\text{g.m L}^{-1}$ )	Ag (0.3 $\text{ng.m L}^{-1}$ )	Ag (0.3 $\text{ng.mL}^{-1}$ ) + Ab (0.3 $\mu\text{g.mL}^{-1}$ )	WS <sub>2</sub> (0.25 $\mu\text{g.m L}^{-1}$ )	WS <sub>2</sub> + Ab (0.3 $\mu\text{g.m L}^{-1}$ )	WS <sub>2</sub> + Ag (0.3 $\text{ng.m L}^{-1}$ )	WS <sub>2</sub> + Ag (0.3 $\text{ng.mL}^{-1}$ ) + Ab (0.3 $\mu\text{g.mL}^{-1}$ )	
$ \chi_{\text{NR}}^{(2)} $ (a.u.)		0.02	0.02	0.01	0.02	0.02	0.02	0.01	
$\omega_{\text{v}}$ ( $\text{cm}^{-1}$ )	$\Gamma_{\text{v}}$ ( $\text{cm}^{-1}$ )	$ A_{\text{v}} $ (a.u.)	$ A_{\text{v}} $	$ A_{\text{v}} $	$ A_{\text{v}} $	$ A_{\text{v}} $	$ A_{\text{v}} $	$ A_{\text{v}} $	
2857	10	0.00	0.00	0.00	0.00	0.00	0.00	0.09	CH <sub>2</sub> SS
2879	9	0.00	0.00	0.00	0.03	0.02	0.02	0.57	CH <sub>3</sub> SS
2902	11	0.00	0.00	0.00	0.00	0.00	0.00	0.05	alkyl CHs
2920	11	0.00	0.00	0.00	0.00	0.00	0.00	0.02	CH <sub>2</sub> as
2939	10	0.00	0.00	0.00	0.01	0.01	0.01	0.36	CH <sub>3</sub> FR
2959	11	0.00	0.00	0.00	0.00	0.00	0.00	0.34	CH <sub>3</sub> as (out-plane)
2976	12	0.01	0.01	0.01	0.01	0.01	0.01	0.28	CH <sub>2</sub> as (in-plane)
3015	13	0.00	0.02	0.00	0.00	0.01	0.00	0.02	2v (C=C)s
3047	10	0.00	0.00	0.00	0.00	0.00	0.00	0.08	v (=CH) <sub>20a</sub>

**Table D2.** SFG fitting parameters of CH region of higher protein concentration in SSP polarization mode.

System		SSP					Peak Assignment	
		Ab (3 $\mu\text{g.m L}^{-1}$ )	Ag (3 $\text{ng.m L}^{-1}$ )	Ag (3 $\text{ng.mL}^{-1}$ ) + Ab (3 $\mu\text{g.mL}^{-1}$ )	WS <sub>2</sub> + Ab (3 $\mu\text{g.mL}^{-1}$ )	WS <sub>2</sub> + Ag (3 $\text{ng.mL}^{-1}$ )		WS <sub>2</sub> + Ag (3 $\text{ng.mL}^{-1}$ ) + Ab (3 $\mu\text{g.mL}^{-1}$ )
$ \chi_{\text{NR}}^{(2)} $ (a.u.)		0.01	0.01	0.01	0.01	0.01	0.01	
$\omega_{\text{v}}$ ( $\text{cm}^{-1}$ )	$\Gamma_{\text{v}}$ ( $\text{cm}^{-1}$ )	$ A_{\text{v}} $ (a.u.)	$ A_{\text{v}} $	$ A_{\text{v}} $	$ A_{\text{v}} $	$ A_{\text{v}} $	$ A_{\text{v}} $	
2857	10	0.12	0.07	0.07	0.06	0.01	0.10	

<b>2879</b>	<b>9</b>	0.63	0.42	0.50	0.35	0.08	0.61
<b>2902</b>	<b>11</b>	0.17	0.01	0.01	0.01	0.02	0.05
<b>2920</b>	<b>11</b>	0.32	0.16	0.17	0.04	0.01	0.24
<b>2939</b>	<b>10</b>	0.54	0.49	0.49	0.19	0.03	0.62
<b>2959</b>	<b>11</b>	0.04	0.46	0.38	0.31	0.01	0.60
<b>2976</b>	<b>12</b>	0.01	0.29	0.22	0.26	0.00	0.34
<b>3015</b>	<b>13</b>	0.09	0.01	0.05	0.04	0.01	0.01
<b>3047</b>	<b>10</b>	0.08	0.06	0.05	0.14	0.04	0.05

**Table D3.** SFG fitting parameters of CH region of lower protein concentration in PPP polarization mode.

System		PPP							Peak Assignment
		Ab (0.3 $\mu\text{g.m L}^{-1}$ )	Ag (0.3 $\text{ng.m L}^{-1}$ )	Ag (0.3 $\text{ng.mL}^{-1}$ ) + Ab (0.3 $\mu\text{g.mL}^{-1}$ )	WS <sub>2</sub> (0.25 $\mu\text{g.mL}^{-1}$ )	WS <sub>2</sub> + Ab (0.3 $\mu\text{g.m L}^{-1}$ )	WS <sub>2</sub> + Ag (0.3 $\text{ng.m L}^{-1}$ )	WS <sub>2</sub> + Ag (0.3 $\text{ng.mL}^{-1}$ ) + Ab (0.3 $\mu\text{g.mL}^{-1}$ )	
$ \chi_{\text{NR}}^{(2)} $ (a.u.)		0.02	0.01	0.01	0.02	0.02	0.01	0.01	
$\omega_{\text{v}}$ ( $\text{cm}^{-1}$ )	$\Gamma_{\text{v}}$ ( $\text{cm}^{-1}$ )	$ A_{\text{v}} $ (a.u.)	$ A_{\text{v}} $	$ A_{\text{v}} $	$ A_{\text{v}} $	$ A_{\text{v}} $	$ A_{\text{v}} $	$ A_{\text{v}} $	
<b>2857</b>	<b>10</b>	0.00	0.00	0.00	0.00	0.00	0.00	0.02	CH <sub>2</sub> ss
<b>2879</b>	<b>9</b>	0.01	0.01	0.01	0.01	0.00	0.01	0.06	CH <sub>3</sub> ss
<b>2902</b>	<b>11</b>	0.00	0.01	0.01	0.01	0.00	0.01	0.07	alkyl CHs
<b>2920</b>	<b>11</b>	0.01	0.00	0.01	0.02	0.00	0.02	0.09	CH <sub>2</sub> as
<b>2939</b>	<b>10</b>	0.01	0.00	0.00	0.01	0.00	0.01	0.06	CH <sub>3</sub> FR
<b>2959</b>	<b>11</b>	0.01	0.01	0.01	0.01	0.03	0.04	0.30	CH <sub>3</sub> as (out-plane)
<b>2976</b>	<b>12</b>	0.00	0.00	0.00	0.00	0.00	0.05	0.19	CH <sub>2</sub> as (in-plane)
<b>3015</b>	<b>13</b>	0.00	0.01	0.01	0.01	0.00	0.00	0.09	2v (C=C)s
<b>3047</b>	<b>10</b>	0.00	0.00	0.01	0.01	0.00	0.00	0.07	v (=CH) <sub>20a</sub>



**Table D4.** SFG fitting parameters of CH region of higher protein concentration in PPP polarization mode.

System		PPP					
		Ab (3 $\mu\text{g.m L}^{-1}$ )	Ag (3 $\text{ng.m L}^{-1}$ )	Ag (3 $\text{ng.mL}^{-1}$ ) + Ab (3 $\mu\text{g.mL}^{-1}$ )	WS <sub>2</sub> + Ab (3 $\mu\text{g.mL}^{-1}$ )	WS <sub>2</sub> + Ag (3 $\text{ng.mL}^{-1}$ )	WS <sub>2</sub> + Ag (3 $\text{ng.mL}^{-1}$ ) + Ab (3 $\mu\text{g.mL}^{-1}$ )
$ \chi_{\text{NR}}^{(2)} $ (a.u.)		0.01	0.01	0.01	0.01	0.01	0.00
$\omega_{\text{v}}$ ( $\text{cm}^{-1}$ )	$\Gamma_{\text{v}}$ ( $\text{cm}^{-1}$ )	$ A_{\text{v}} $ (a.u.)	$ A_{\text{v}} $	$ A_{\text{v}} $	$ A_{\text{v}} $	$ A_{\text{v}} $	$ A_{\text{v}} $
<b>2857</b>	<b>10</b>	0.07	0.05	0.05	0.02	0.01	0.02
<b>2879</b>	<b>9</b>	0.13	0.11	0.13	0.07	0.04	0.05
<b>2902</b>	<b>11</b>	0.17	0.12	0.15	0.05	0.03	0.07
<b>2920</b>	<b>11</b>	0.25	0.16	0.17	0.09	0.08	0.07
<b>2939</b>	<b>10</b>	0.24	0.09	0.17	0.09	0.05	0.08
<b>2959</b>	<b>11</b>	0.52	0.46	0.51	0.28	0.24	0.32
<b>2976</b>	<b>12</b>	0.25	0.19	0.24	0.17	0.15	0.19
<b>3015</b>	<b>13</b>	0.10	0.09	0.09	0.02	0.02	0.04
<b>3047</b>	<b>10</b>	0.09	0.05	0.09	0.02	0.00	0.08

**Table D5.** SFG fitting parameters of polarization-dependent SFG spectra of pristine water and pristine WS<sub>2</sub> QDs in OH-stretch region.

System		SSP		PPP		Peak Assignments
		Pristine Water	WS <sub>2</sub> (0.25 $\mu\text{g.mL}^{-1}$ )	Pristine Water	WS <sub>2</sub> (0.25 $\mu\text{g.mL}^{-1}$ )	
$ \chi_{\text{NR}}^{(2)} $ (a.u.)		0.01	0.01	0.01	0.01	
$\omega_{\text{v}}$ ( $\text{cm}^{-1}$ )	$\Gamma_{\text{v}}$ ( $\text{cm}^{-1}$ )	$ A_{\text{v}} $ (a.u.)	$ A_{\text{v}} $	$ A_{\text{v}} $	$ A_{\text{v}} $	
<b>3220</b>	<b>100</b>	0.54	0.30	0.25	0.13	Strong H-bonding
<b>3450</b>	<b>125</b>	3.01	3.16	1.15	0.29	Weak H-bonding
<b>3550</b>	<b>70</b>	0.11	0.10	0.56	0.75	Weak H-bonding
<b>3705</b>	<b>19</b>	0.92	0.78	0.86	0.53	Free OH

**Table D6.** SFG fitting parameters of OH-stretch region of lower protein concentration in SSP polarization mode.

System		SSP								Peak Assignment
		Ab (0.3 $\mu\text{g.m L}^{-1}$ )		Ag (0.3 $\text{ng.m L}^{-1}$ )	Ag (0.3 $\text{ng.mL}^{-1}$ ) + Ab (0.3 $\mu\text{g.mL}^{-1}$ )	WS <sub>2</sub> + Ab (0.3 $\mu\text{g.m L}^{-1}$ )	WS <sub>2</sub> + Ag (0.3 $\text{ng.m L}^{-1}$ )	WS <sub>2</sub> + Ag (0.3 $\text{ng.mL}^{-1}$ ) + Ab (0.3 $\mu\text{g.mL}^{-1}$ )		
$ \chi_{\text{NR}}^{(2)} $ (a.u.)		0.01		0.01	0.02	0.01	0.01	0.02		
$\omega_{\text{v}}$ ( $\text{cm}^{-1}$ )	$\Gamma_{\text{v}}$ ( $\text{cm}^{-1}$ )	$ A_{\text{v}} $ (a.u.)	$\omega_{\text{v}}$ ( $\text{cm}^{-1}$ )	$\Gamma_{\text{v}}$ ( $\text{cm}^{-1}$ )	$ A_{\text{v}} $	$ A_{\text{v}} $	$ A_{\text{v}} $	$ A_{\text{v}} $	$ A_{\text{v}} $	
<b>3076</b>	<b>9</b>	0.00	<b>3076</b>	<b>9</b>	0.01	0.01	0.03	0.06	0.00	$\nu$ (=CH) <sub>2</sub>
<b>3170</b>	<b>60</b>	0.79	<b>3220</b>	<b>100</b>	0.62	0.66	0.41	0.49	0.75	Strong H-bonding
<b>3450</b>	<b>125</b>	3.01	<b>3450</b>	<b>125</b>	3.28	3.67	2.93	2.89	4.62	Weak H-bonding
<b>3550</b>	<b>70</b>	0.03	<b>3550</b>	<b>70</b>	0.01	0.01	0.01	0.01	0.14	Weak H-bonding
<b>3705</b>	<b>19</b>	0.89	<b>3705</b>	<b>19</b>	0.97	1.25	0.81	0.81	0.85	Free OH

**Table D7.** SFG fitting parameters of OH-stretch region of higher protein concentration in SSP polarization mode.

System		SSP								
		Ab (3 $\mu\text{g.m L}^{-1}$ )		Ag (3 $\text{ng.m L}^{-1}$ )	Ag (3 $\text{ng.mL}^{-1}$ ) + Ab (3 $\mu\text{g.mL}^{-1}$ )	WS <sub>2</sub> + Ab (3 $\mu\text{g.m L}^{-1}$ )	WS <sub>2</sub> + Ag (3 $\text{ng.m L}^{-1}$ )	WS <sub>2</sub> + Ag (3 $\text{ng.mL}^{-1}$ ) + Ab (3 $\mu\text{g.mL}^{-1}$ )		
$ \chi_{\text{NR}}^{(2)} $ (a.u.)		0.01		0.01	0.00	0.02	0.02	0.01		
$\omega_{\text{v}}$ ( $\text{cm}^{-1}$ )	$\Gamma_{\text{v}}$ ( $\text{cm}^{-1}$ )	$ A_{\text{v}} $ (a.u.)	$\omega_{\text{v}}$ ( $\text{cm}^{-1}$ )	$\Gamma_{\text{v}}$ ( $\text{cm}^{-1}$ )	$ A_{\text{v}} $	$ A_{\text{v}} $	$ A_{\text{v}} $	$ A_{\text{v}} $	$ A_{\text{v}} $	
<b>3076</b>	<b>9</b>	0.06	<b>3076</b>	<b>9</b>	0.01	0.05	0.03	0.06	0.02	
<b>3170</b>	<b>60</b>	0.78	<b>3220</b>	<b>100</b>	0.93	0.80	0.61	0.30	1.54	
<b>3450</b>	<b>125</b>	1.93	<b>3450</b>	<b>125</b>	5.92	5.53	4.32	3.12	8.98	
<b>3550</b>	<b>70</b>	0.07	<b>3550</b>	<b>70</b>	0.93	0.79	0.07	0.00	0.85	
<b>3705</b>	<b>19</b>	0.47	<b>3705</b>	<b>19</b>	0.33	0.33	0.82	0.81	0.41	

**Table D8.** SFG fitting parameters of OH-stretch region of lower protein concentration in PPP polarization mode.

System		PPP							
		Ab (0.3 $\mu\text{g.m}$ $\text{L}^{-1}$ )			Ag (0.3 $\text{ng.m}$ $\text{L}^{-1}$ )	Ag (0.3 $\text{ng.mL}^{-1}$ ) + Ab (0.3 $\mu\text{g.mL}^{-1}$ )	WS <sub>2</sub> + Ab (0.3 $\mu\text{g.mL}^{-1}$ )	WS <sub>2</sub> + Ag (0.3 $\text{ng.mL}^{-1}$ )	WS <sub>2</sub> + Ag (0.3 $\text{ng.mL}^{-1}$ ) + Ab (0.3 $\mu\text{g.mL}^{-1}$ )
$ \chi_{\text{NR}}^{(2)} $ (a.u.)		0.01			0.01	0.01	0.01	0.01	0.00
$\omega_{\text{v}}$ ( $\text{cm}^{-1}$ )	$\Gamma_{\text{v}}$ ( $\text{cm}^{-1}$ )	$ A_{\text{v}} $ (a.u.)	$\omega_{\text{v}}$ ( $\text{cm}^{-1}$ )	$\Gamma_{\text{v}}$ ( $\text{cm}^{-1}$ )	$ A_{\text{v}} $	$ A_{\text{v}} $	$ A_{\text{v}} $	$ A_{\text{v}} $	$ A_{\text{v}} $
3076	9	0.00	3076	9	0.01	0.00	0.01	0.01	0.04
3170	60	0.25	3220	100	0.23	0.05	0.24	0.12	0.03
3450	125	1.19	3450	125	1.04	0.70	0.16	0.11	1.55
3550	70	0.54	3550	70	0.56	0.91	0.77	0.98	1.88
3705	19	0.84	3705	19	0.76	0.94	0.65	0.57	0.09

**Table D9.** SFG fitting parameters of OH-stretch region of higher protein concentration in PPP polarization mode.

System		PPP							
		Ab (3 $\mu\text{g.m}$ $\text{L}^{-1}$ )			Ag (3 $\text{ng.m}$ $\text{L}^{-1}$ )	Ag (3 $\text{ng.mL}^{-1}$ ) + Ab (3 $\mu\text{g.mL}^{-1}$ )	WS <sub>2</sub> + Ab (3 $\mu\text{g.m}$ $\text{L}^{-1}$ )	WS <sub>2</sub> + Ag (3 $\text{ng.m}$ $\text{L}^{-1}$ )	WS <sub>2</sub> + Ag (3 $\text{ng.mL}^{-1}$ ) + Ab (3 $\mu\text{g.mL}^{-1}$ )
$ \chi_{\text{NR}}^{(2)} $ (a.u.)		0.01			0.00	0.00	0.00	0.01	0.01
$\omega_{\text{v}}$ ( $\text{cm}^{-1}$ )	$\Gamma_{\text{v}}$ ( $\text{cm}^{-1}$ )	$ A_{\text{v}} $ (a.u.)	$\omega_{\text{v}}$ ( $\text{cm}^{-1}$ )	$\Gamma_{\text{v}}$ ( $\text{cm}^{-1}$ )	$ A_{\text{v}} $	$ A_{\text{v}} $	$ A_{\text{v}} $	$ A_{\text{v}} $	$ A_{\text{v}} $
3076	9	0.02	3076	9	0.02	0.07	0.04	0.00	0.14
3170	60	0.57	3220	100	0.03	0.04	0.02	0.13	0.25
3450	125	1.45	3450	125	1.79	1.89	1.49	0.51	2.52
3550	70	1.49	3550	70	2.07	2.10	1.65	1.02	2.56
3705	19	0.26	3705	19	0.03	0.06	0.17	0.57	0.05

**Table D10.** The experimental values of  $|A_q/\Gamma_q|$  ratios for  $|\chi_{ssp,ss}^{(2)}/\chi_{ppp,as}^{(2)}|$  combination as per fitted parameters and methyl group tilt angles at the air-polymer interface with  $\delta$ - and Gaussian distributions for Ab and Ag molecules in absence and presence of WS<sub>2</sub> QDs.

System	$ A_q/\Gamma_q $ for $ \chi_{ssp,ss}^{(2)}/\chi_{ppp,as}^{(2)} $	Tilt Angle ( $\delta$ -distribution)	Tilt Angle (Gaussian-distribution)	Gaussian-distribution Width ( $\sigma$ )
Ag (3 ng.mL <sup>-1</sup> ) + Ab (3 $\mu$ g.mL <sup>-1</sup> )	0.98	40.30°	32.30°-69.80°	0°-60°
WS <sub>2</sub> + Ag (3 ng.mL <sup>-1</sup> ) + Ab (3 $\mu$ g.mL <sup>-1</sup> )	1.90	28.50°	11.80°-28.50°	0°-20°
WS <sub>2</sub> + Ag (0.3 ng.mL <sup>-1</sup> ) + Ab (0.3 $\mu$ g.mL <sup>-1</sup> )	1.87	28.80°	12.40°-28.80°	0°-20°

## Appendix E

**Table E1.** Fitting parameters of standard reference samples which contains pristine water at two different pH and buffer solution (SSP polarization scheme) in CH- and OH-stretch region.

System		Pristine Water	Water (pH 7.4)	Tris-HCl buffer (pH 7.4)	Tris-HCl buffer + Acetic acid (0.02 v/v%) (pH 7.4)	Peak Assignments
$ \chi_{NR}^{(2)} $ (a.u.)		0.02	0.02	0.01	0.02	
$\omega_v$ (cm <sup>-1</sup> )	$\Gamma_v$ (cm <sup>-1</sup> )	$ A_v $ (a.u.)	$ A_v $	$ A_v $	$ A_v $	
<b>3225</b>	<b>100</b>	0.58	0.63	0.56	0.63	Strong H-bonding
<b>3450</b>	<b>125</b>	3.25	3.52	3.45	3.41	Weak H-bonding
<b>3550</b>	<b>70</b>	0.19	0.22	0.18	0.21	Weak H-bonding
<b>3705</b>	<b>19</b>	1.00	1.07	1.02	1.01	Free OH

**Table E2.** Fitting parameters of the NPEI-ONP concentration series varying from 0.01 to 0.05 mg.mL<sup>-1</sup> (SSP polarization scheme) in CH- and OH-stretch region.

System		NPEI-ONPs						Peak Assignment
		0.01 mg.mL <sup>-1</sup>	0.02 mg.mL <sup>-1</sup>	$\omega_v$ (cm <sup>-1</sup> )	0.03 mg.mL <sup>-1</sup>	0.04 mg.mL <sup>-1</sup>	0.05 mg.mL <sup>-1</sup>	
$ \chi_{NR}^{(2)} $ (a.u.)		0.02	0.01			0.01	0.01	0.01
$\omega_v$ (cm <sup>-1</sup> )	$\Gamma_v$ (cm <sup>-1</sup> )	$ A_v $ (a.u.)	$ A_v $		$ A_v $	$ A_v $	$ A_v $	
<b>2856</b>	<b>13</b>	0.00	0.00	<b>2856</b>	0.03	0.01	0.04	CH <sub>2</sub> ss
<b>2930</b>	<b>8</b>	0.02	0.02	<b>2930</b>	0.03	0.01	0.05	CH <sub>2</sub> as
<b>3005</b>	<b>13</b>	0.04	0.05	<b>3005</b>	0.01	0.01	0.03	2v (C=C)s
<b>3073</b>	<b>8.5</b>	0.00	0.02	<b>3073</b>	0.13	0.27	0.50	v (=CH) <sub>2</sub>
<b>3225</b>	<b>100</b>	0.60	0.59	<b>3230</b>	2.98	3.29	3.35	Strongly coordinated H-bonding

<b>3450</b>	<b>125</b>	3.49	4.87	<b>3445</b>	5.19	5.63	5.68	Weakly coordinated H-bonding
<b>3560</b>	<b>70</b>	0.19	0.33	<b>3560</b>	0.90	0.92	0.92	Weakly coordinated H-bonding
<b>3705</b>	<b>19</b>	0.99	0.87	<b>3705</b>	0.18	0.16	0.16	Free OH
<b>I<sub>SFG</sub> (3450 cm<sup>-1</sup>/3225 cm<sup>-1</sup>)</b>		22.03	43.83		1.94	1.87	1.83	

**Table E3.** Fitting parameters of the NPEI-ONP with varying dsDNA concentration series (SSP polarization scheme) in CH- and OH-stretch region.

System		NPEI-ONPs (0.03 mg.m L <sup>-1</sup> )	NPEI-ONPs (0.03 mg.mL <sup>-1</sup> ) + dsDNA					Peak Assignment
			dsDNA (0.24 μg.mL <sup>-1</sup> )	dsDNA (1.43 μg.mL <sup>-1</sup> )	dsDNA (2.22 μg.mL <sup>-1</sup> )	dsDNA (3.68 μg.mL <sup>-1</sup> )		
χ <sub>NR</sub> <sup>(2)</sup>   (a.u.)		0.02		0.02	0.02	0.02	0.01	
ω <sub>v</sub> (cm <sup>-1</sup> )	Γ <sub>v</sub> (cm <sup>-1</sup> )	A <sub>v</sub>   (a.u.)	Γ <sub>v</sub> (cm <sup>-1</sup> )	A <sub>v</sub>	A <sub>v</sub>	A <sub>v</sub>	A <sub>v</sub>	
<b>2856</b>	<b>13</b>	0.00	<b>13</b>	0.03	0.07	0.01	0.00	CH <sub>2</sub> ss
<b>2930</b>	<b>8</b>	0.02	<b>8</b>	0.03	0.05	0.05	0.03	CH <sub>2</sub> as
<b>3005</b>	<b>13</b>	0.07	<b>13</b>	0.07	0.14	0.07	0.07	2ν (C=C)s
<b>3073</b>	<b>9</b>	0.61	<b>9</b>	0.61	0.70	0.67	0.59	ν (=CH) <sub>2</sub>
<b>3230</b>	<b>100</b>	5.01	<b>100</b>	5.15	6.38	6.07	5.80	Strongly coordinated H-bonding
<b>3445</b>	<b>126.5</b>	8.01	<b>125</b>	8.09	9.53	9.15	9.01	Weakly coordinated H-bonding
<b>3560</b>	<b>70</b>	1.50	<b>70</b>	1.50	1.92	1.91	1.75	Weakly coordinated H-bonding
<b>3705</b>	<b>19</b>	0.03	<b>19</b>	0.02	0.03	0.05	0.05	Free OH
<b>I<sub>SFG</sub> (3450 cm<sup>-1</sup>/3225 cm<sup>-1</sup>)</b>		1.94		1.91	1.73	1.76	1.87	

**Table E4:** Fitting parameters of the NPEI-ONP with varying dsDNA concentration series (SSP polarization scheme) in bending mode region.

System		NPEI-ONPs 0.03 mg.mL <sup>-1</sup>	NPEI-ONPs (0.03 mg.mL <sup>-1</sup> ) + dsDNA				Peak Assignment
			dsDNA (0.24 μg.mL <sup>-1</sup> )	dsDNA (1.43 μg.mL <sup>-1</sup> )	dsDNA (2.22 μg.mL <sup>-1</sup> )	dsDNA (3.68 μg.mL <sup>-1</sup> )	
$ \chi_{NR}^{(2)} $ (a.u.)		0.01	0.01	0.01	0.01	0.01	
$\omega_v$ (cm <sup>-1</sup> )	$\Gamma_v$ (cm <sup>-1</sup> )	$ A_v $ (a.u.)	$ A_v $	$ A_v $	$ A_v $	$ A_v $	
<b>1596</b>	<b>4</b>	0.17	0.14	0.12	0.10	0.10	N-H bending
<b>1655</b>	<b>4</b>	0.09	0.06	0.06	0.06	0.06	amide I
<b>1704</b>	<b>6</b>	0.27	0.25	0.19	0.17	0.16	(C=O) <sub>s</sub>
<b>1740</b>	<b>13</b>	0.09	0.05	0.05	0.05	0.02	(C=O) <sub>s</sub>





## List of publications

### ♣ Peer reviewed journals

- [1] **Harsharan Kaur**, Meenakshi Verma, Sarabjeet Kaur, Bhawna Rana, Narinder Singh, and Kailash C. Jena. Elucidating the Molecular Structure of Hydrophobically-Modified Polyethylenimine Nanoparticles and Its Potential Implication for DNA Binding. *Langmuir*, **2022**, Vol. 38, 13456-13468.
- [2] Harpreet Kaur, Shilpi Chaudhary, **Harsharan Kaur**, Monika Chaudhary, Kailash C. Jena. Hydrolysis and Condensation of Tetraethyl Orthosilicate at the Air-Aqueous Interface: Implications for Silica Nanoparticle Formation. *ACS Applied Nano Materials*, **2022**, Vol. 5, 411-422.
- [3] Shilpi Chaudhary\*, **Harsharan Kaur**\*, Harpreet Kaur, Bhawna Rana, Deepak Tomar, Kailash C. Jena. Probing the Bovine Hemoglobin Adsorption Process and its Influence on Interfacial Water Structure at Air/Water Interface. *Applied Spectroscopy*, **2021**, Vol. 75, 1497-1509. **\*Equal Contribution**.
- [4] **Harsharan Kaur**, Mayank Garg, Deepak Tomar, Suman Singh, and Kailash C. Jena. Probing the Role of Tungsten Disulfide Quantum Dots in Specific Protein-Protein Interactions at Air-Water Interface. **Submitted to Nano-Micro Letters (Under Review)**.
- [5] Shilpi Chaudhary\*, **Harsharan Kaur**\*, Harpreet Kaur, and Kailash C. Jena. Recognition of Bovine Hemoglobin Protein on Molecularly Imprinted Polymer Surfaces using Nonlinear Vibrational Spectroscopy. **Submitted to Applied Physics Letters (Under Review)**. **\*Equal Contribution**.

### ♣ Book Chapters

- [1] **Harsharan Kaur**, Bhawna Rana, Deepak Tomar, Sarabjeet Kaur, and Kailash C. Jena. Fundamentals of ATR-FTIR Spectroscopy and Its Role for Probing In-Situ Molecular-Level Interactions, in *Modern Techniques of Spectroscopy: Basics, Instrumentation, and Applications*. (Springer Nature, Singapore, 2021), Vol. 13, 3-37.

- [2] Harpreet Kaur, Deepak Tomar, **Harsharan Kaur**, Bhawna Rana, Shilpi Chaudhary, and Kailash C. Jena. Sum-Frequency Generation Vibrational Spectroscopy: A Nonlinear Optical Tool to Probe the Polymer Interfaces, in *Advances in Spectroscopy: Molecules to Materials*. (Springer Nature, Singapore, **2019**), Vol. 236, pp. 39-55.
- [3] Deepak Tomar, Harpreet Kaur, **Harsharan Kaur**, Bhawna Rana, Krutika Talegaonkar, Vivek Maharana, Kailash C. Jena. ATR-FTIR Spectroscopy and Its Relevance to Probe the Molecular-Level Interactions Between Amino Acids and Metal-Oxide Nanoparticles at Solid/Aqueous Interface, in *Advances in Spectroscopy: Molecules to Materials*. (Springer Nature, Singapore, **2019**), Vol. 236, pp. 3–21.

## Conferences/Seminars/Workshops

### ♣ Presentations in Conferences

[1] Poster Presentation

**H. Kaur**, N. Singh, and K. C. Jena, “Probing Interfacial Structure of Polyethylenimine Derivative by Nonlinear Vibrational Spectroscopy”, Trombay Symposium on Radiation and Photochemistry (TSRP–2018), organized by Bhabha Atomic Research Centre (BARC), Mumbai, January 3<sup>rd</sup> – 7<sup>th</sup>, 2018.

[2] Poster Presentation

**H. Kaur**, M. Verma, N. Singh, and K. C. Jena, “Understanding the Bulk and Interfacial DNA Recognition Properties of Polyethylenimine Derivative”, Research Conclave - 2018 held at Indian Institute of Technology Ropar, April 21<sup>st</sup>, 2018. (*Har Gobind Khurana Award for Best Poster Presentation*).

[3] Oral Presentation

**H. Kaur**, M. Verma, N. Singh, and K. C. Jena, “Unravelling the Bulk and Interfacial Behavior of DNA Binding by Polyethylenimine Derivative”, National Conference on Advances in Spectroscopy: Molecules to Materials (NCASMM), organized by Department of Physics, IITRAM, Ahmedabad, October 4<sup>th</sup> – 6<sup>th</sup>, 2018. (*Best Oral Award*).

[4] Poster Presentation

**H. Kaur**, M. Verma, N. Singh, and K. C. Jena, “Elucidating the Interfacial Molecular Structure of Hydrophobically-Modified Polyethylenimine Nanoparticles and their DNA Binding Properties”, UK-India Interdisciplinary Workshop on Advanced Biomaterials and Biosensors, organized by Indian Institute of Technology Ropar. November 13<sup>th</sup> – 15<sup>th</sup>, 2018.

[5] Poster Presentation

**H. Kaur**, M. Verma, N. Singh, and K. C. Jena, “Monitoring the Molecular Rearrangement of Polyethylenimine Derivative in the Presence of DNA at Air-Water Interface by using Nonlinear Optical Laser Spectroscopy”, 7<sup>th</sup> International Conference on Perspectives in Vibrational Spectroscopy (ICOPVS-2018)”, organized by Bhabha Atomic Research Centre (BARC), Mumbai. November 25<sup>th</sup> – 29<sup>th</sup>, 2018.

[6] Poster Presentation

**H. Kaur** and K. C. Jena, “Investigating Tungsten Disulfide Mediated Protein-Protein Interactions at Air-Aqueous Interface Studied by Sum Frequency Generation Vibrational Spectroscopy”, National Symposium on Light-Matter Interaction (NSLIMI-2019), organized by Department of Physics, Indian Institute of Technology Madras, Chennai. December 26<sup>th</sup>, 2019.

[7] Poster Presentation

**H. Kaur**, M. Garg, S. Singh, and K. C. Jena, “Interaction of Protein Molecules at Air-Aqueous Interface in the Presence of Transition Metal Dichalcogenides Studied by Nonlinear Vibrational Spectroscopy”, 8<sup>th</sup> International Conference on Perspectives in Vibrational Spectroscopy (ICOPVS-2020)”, organized by Jawaharlal Nehru Centre of Advanced Scientific Research (JNCASR). February 24<sup>th</sup> – 28<sup>th</sup>, 2020.

[8] Flash Poster Presentation

**H. Kaur**, M. Garg, S. Singh, and K. C. Jena, “Exploring the Protein-Protein Associations and their Modulation in Presence of Tungsten Disulfide using Sum Frequency Generation Vibrational Spectroscopy”, 11<sup>th</sup> International Conference on Advanced Vibrational Spectroscopy (ICAVS-2021), organized by Jagiellonian University, Karakow, Poland. August 23<sup>rd</sup> – 26<sup>th</sup>, 2021. Online Mode.

### ♣ Symposium/Workshops/Courses Attended

[1] Participation in UK-India Interdisciplinary Workshop on “Advanced Biomaterials and Biosensors” organized at Indian Institute of Technology Ropar, Rupnagar (INDIA). (November 13<sup>th</sup> - 15<sup>th</sup>, 2018).

[2] Participated in the online symposium “Virtual Symposium on Emerging Areas of Photonics” to Celebrate International Day of Light - May 16, 2020, Jointly Organized by The National Academy of Sciences India (NASI) - Delhi Chapter and The Optical Society of India. (May 16<sup>th</sup>, 2020)

[3] Participation in GIAN (Global Initiative of Academic Networks) course on “Theory of Surface Nonlinear Spectroscopy” organized at Indian Institute of Technology Ropar, Rupnagar (INDIA). (September 26<sup>th</sup> – 30<sup>th</sup>, 2022).

## Bio-Data of Author

### ♣ Personal details

Name	: Harsharan Kaur
Gender	: Female
Nationality	: Indian
E-mail	: harsharan.kaur@iitrpr.ac.in ; harsharankaur2008@gmail.com
Residential Address	: #5740-A, Sector-38 West, Chandigarh (U.T.), India, Pin Code - 160036
Permanent Address	: Same as residential address

### ♣ Research Interests/Area of Research

- Linear and Non-linear Spectroscopy
- Sum Frequency Generation Vibrational Spectroscopy
- Interfacial Molecular Activities of Biomolecules in Aqueous Media
- Interfacial and Bulk Characterizations of Nanomaterials
- Thin-Film Fabrications
- Experimental Molecular Biology
- Nano-Bio Interactions and Sensing Applications

### ♣ Additional Research Experience

- Thesis completion in the partial fulfillment for the Degree of M.Sc. (Honors), Biophysics, on “Standardization of Metallothionein Isolation from Rat Liver and their Mass Spectrometric Analysis”. Successfully defended and submitted on 31st July 2015.
- Participated in Particle Induced X-Ray Emission (PIXE) experiments of biological samples carried out at Institute of Physics (IOP), Bhubaneswar, supported by UGC-DAE, Kolkata (INDIA). (31<sup>st</sup> July – 8<sup>th</sup> August, 2015).

## ♣ Technical Skills

- Sum Frequency Generation Vibrational Spectroscopy
- Fourier Transform Infrared Spectroscopy (FTIR) and Attenuated Total Reflectance (ATR) FTIR vibrational spectroscopy
- Handling of FTIR micro-spectroscopy
- Langmuir Blodgett for monolayer formation of lipid and Surface tension measurements by Wilhelmy plate method
- Dynamic Light Scattering (DLS) and Zeta-potentiometry
- Scanning Electron Microscopy (SEM)
- UV-Visible Absorption Spectroscopy
- Fluorescence Emission Spectroscopy
- Circular Dichroism Spectroscopy
- Sodium Dodecyl Sulphate Poly-Acrylamide Gel Electrophoresis (SDS-PAGE)
- Hands-on experience of Dextran-based Gel Chromatographic Column for Protein Extraction

## ♣ Teaching Experience

- Teaching Assistantship for Post-Graduate Course (MTech.):  
BML604 (Biomedical Engineering Lab) – Introduction to Advanced Biology,  
from August 2017 – December 2017.